# NEUTRINO-NUCLEUS NEUTRAL CURRENT ELASTIC INTERACTIONS MEASUREMENT IN MINIBOONE

by

Denis Perevalov

A DISSERTATION

Submitted in partial fullfillment of the requirements
for the degree of Doctor of Philosophy
in the Department of Physics and Astronomy
in the Graduate School of
The University of Alabama

TUSCALOOSA, ALABAMA

2009

© Copyright by Denis Perevalov 2009 ALL RIGHTS RESERVED

# Abstract

The MiniBooNE experiment at the Fermi National Accelerator Laboratory (Fermilab) was designed to search for $\nu_\mu \rightarrow \nu_e$ neutrino oscillations at $\Delta m^2 \sim 1$ eV$^2$ using an intense neutrino flux with an average energy $E_\nu \sim 700$ MeV. From 2002 to 2009 MiniBooNE has accumulated more than $1.0\times10^{21}$ protons on target (POT) in both neutrino and antineutrino modes. MiniBooNE provides a perfect platform for detailed measurements of exclusive and semiinclusive neutrino cross-sections, for which MiniBooNE has the largest samples of events up to date, such as neutral current elastic (NCE), neutral current $\pi^0$, charged current quasi-elastic (CCQE), charged current $\pi^+$, and other channels. These measured cross-sections, in turn, allow to improve the knowledge of nucleon structure.

This thesis is devoted to the study of NCE interactions. Neutrino-nucleus neutral current elastic scattering ($\nu N \rightarrow \nu N$) accounts for about 18% of all neutrino interactions in MiniBooNE. Using a high-statistics, high purity sample of NCE interactions in MiniBooNE, the flux-averaged NCE differential cross-section has been measured and is being reported here.

Further study of the NCE cross-section allowed for probing the structure of nuclei. The main interest in the NCE cross-section is that it may be sensitive to the strange quark contribution to the nucleon spin ,$\Delta s$, this however requires a separation of NCE proton ($\nu p \rightarrow \nu p$) from NCE neutron ($\nu n \rightarrow \nu n$) events, which in general is a challenging task. MiniBooNE uses a Cherenkov detector, which imposes restrictions on the measured nucleon kinematic variables, mainly due to the impossibility to reconstruct the nucleon direction below the Cherenkov threshold. However, at kinetic energies above this threshold MiniBooNE is able to identify NCE proton events that do not experience final state interactions (FSI). These events were used for the $\Delta s$ measurement. In this thesis MiniBooNE reports the NCE (n+p) cross-section, the measurement of the axial mass, $M_A$, and the $\Delta s$ parameter from the NCE data.

# List of Abbreviations

| | |
|---|---|
| ADC | Analog-to-digital converter |
| BNB | Booster neutrino beamline |
| CC | Charged current |
| CCQE | Neutrino-nucleon charge current quasi-elastic ($\nu_l + n \rightarrow l^- + p$) |
| CCPi+ | Neutrino-nucleon charge current $\pi^+$ production ($\nu_l + n \rightarrow l^- + \pi^+ + n$) |
| CERN | European Organization for Nuclear Research |
| CKM | Cabibo-Kobayashi-Maskawa |
| CV | Central value |
| CVC | Conserved vector current |
| DAQ | Data acquisition |
| DOF | Degrees of freedom |
| DONUT | Direct Observation of NU Tau |
| EM | Electromagnetic |
| EMC | European Muon Collaboration |
| Fermilab or FNAL | Fermi National Accelerator Laboratory |
| FSI | Final state interactions |
| HPWF | Harvard-Penn-Wisconsin-Fermilab |
| IMB | Irvine-Michigan-Brookhaven |
| GWS | Glashow-Weiberg-Salam model |
| K2K | KEK to Kamioka |
| KamLAND | Kamioka Liquid Scintillator Antineutrino Detector |
| KATRIN | Karlsruhe Tritium Neutrino Experiment |
| LEP | Large Electron Positron accelerator |
| LSND | Liquid Scintillator Neutrino Detector |
| MC | Monte Carlo (Computer Simulated Data) |

| | |
|---|---|
| MINUIT | CERN function minimization and error analysis package |
| MiniBooNE | Mini Booster Neutrino Experiment |
| MINOS | Main Injector Neutrino Oscillation Search |
| NC | Neutral current |
| NCE | Neutrino-nucleon neutral current elastic |
| NCE (p+n) | Neutrino-nucleon neutral current elastic on both proton and neutron ($\nu + N \rightarrow \nu + N$) |
| NCE p | Neutrino-proton neutral current elastic ($\nu + p \rightarrow \nu + p$) |
| NCE n | Neutrino-neutron neutral current elastic $\nu + n \rightarrow \nu + n$) |
| NCFitter | Proton hypothesis reconstruction in MiniBooNE |
| NuMI | Neutrinos from the Main Injector |
| PMT | Photomultiplier Tube |
| $Q^2$ | Momentum transferred |
| QCD | Quantum chromodynamics |
| QED | Quantum electrodynamics |
| StancuFitter | Electron hypothesis reconstruction in MiniBooNE created by Ion Stancu |
| SM | Standard Model |
| h.c. | Hermitian conjugate |
| PE | Photo-electron |
| PDF | Probability density function |
| PDG | Particle Data Group |
| SciBooNE | SciBar Booster Neutrino Experiment |
| SNO | Sudbury Neutrino Observatory |
| T2K | Tokai to Kamioka |
| UV | Ultraviolet |
| WNC | Weak neutral current |

# Acknowledgments

I am very glad and fortunate that I had Ion Stancu as a supervisor. Also I am very proud of being his first Ph.D. student. Not only did I learn a lot about experimental physics, but also received lots of good general advices about how to work, manage my time, being punctual, polite, etc. It has been an incredible opportunity to start a research assistantship from my first semester and work on something I really enjoyed. I want to apologize for not being a perfect student and occasionally my bad English especially with articles, but it was a learning experience for me.

I want to thank all MiniBooNE people for being very helpful and friendly. A special thank you to Yong Liu, who was a postdoctoral fellow of Ion's at the time I was at Fermrilab. However, he is not just a colleague for me, he is also a great friend. As they call it in China, he is my older brother and always will be. I don't think I have met a nicer person in my life. He taught me everything about MiniBooNE, and in detail about the reconstruction and the particle identification, while seemingly spending much more time with me than on his own work. He is a great physicist and an extremely hard worker. I wish him and his family all great things in the world and hope to communicate more in the future.

I want to say thank you to all the people from Indiana University who were all part of the NC elastic/CCQE group in MiniBooNE. Rex Tayloe was practically my second supervisor. He is just a great person to work with, very experienced and understanding. Thank you so much for your guidance and, of course, for presenting the NC elastic results when I didn't have a chance to do it myself. I appreciate Chris Cox who was performing the first MiniBooNE NC elastic analysis. It was so much easier for me to work on my analysis after your work! Teppei Katori is my only Japanese friend so far, but really a good one! Not only he is a very good and knowledgeable physicist, but he also has a very interesting personality. I really enjoyed your company and I think it was very beneficial that we worked on similar measurements at some point. Chris Polly who was also a postdoctoral student at IU at the time helped me a lot in understanding the Monte Carlo simulation

and some systematic errors that we consider. I have to say that I was about to join Rex's group at IU as a postdoc before receiving an offer from Fermilab. It was very hard for me to turn them down, but I still hope to work on some projects together.

I am glad I had a chance to work with Sam Zeller who was always inspiring the cross-section people around her and convincing that their results really mean something. Our spokespersons, Janet Conrad, Bill Louis, Richard Van de Water, and Steve Brice are those, who made MiniBooNE a successful experiment. Among all graduate/postdoctoral students that I enjoy talking and working with are some international students, Zelimir Djurcic (Serbia), Alexis Aguilar-Arevalo (Mexico), Serge Ouedraogo (Burkina Faso), Jarek Novak (Poland), Bari Osmanov (Uzbekistan), and Kendall Mahn (USA, yes it is international to me).

I have been extremely lucky to find my Russian friends at Fermilab: Dmitriy and Andrey Sidorov, Alex Ferapontov, Kelly Ferapontova... oops I mean McMinn, Natalie Miklyukh, Marina Jouljik, Maxim Goncharov, Samvel Khalatian, Georgy Golovanov, and of course my MIPT buddy Grigory Safronov. We spent a lot of time together on weekends playing volleyball, watching football, celebrating occasions, just having a good time in general. Looking forward to continue doing that in future.

All my best friends in Russia, who went to MIPT with me and who I had a chance to see only once over the last 5 years. They are and always will be my best friends: Egor Rudi, Alexei Sokolov, Roman Kornienko, Roman Saptsov, and Sergey Kuznetsov, and of course their families that I also consider as my best friends.

I am very grateful to meet new friends at the University of Alabama, who were first to introduce me to the American culture, which I very much appreciate. Gregory Keefer aka Greggy, who was thought to never be successful by his classmates in Huntsville, but by hard work and determination became a Ph.D. before me (we had a little competition) and got a great position at Livermore National Laboratory. He is also a great friend and I wish him well. Tim Clausen aka Timmay, who is also in California now with Greg. I hope I visit you guys there sometime. Chris Grant aka Penny, I am going to be missing to hear all those countless stories that happened to you. Igor Ostrovskiy, thank you Igor for giving us a ride today to Panera :). I wish best of luck both in life and work to Yujing Sun and Ranjan Dharmapalan, my colleagues and an officemates for a long time.

I want to say thanks my family. If it was not for my sister Irina Perevalova, I would have never gotten to neither the University of Alabama, nor probably to MIPT. She is a very smart, kind and nice person, and I hope you get a Ph.D. soon too. I also wish my niece, Elena Perevalova, to graduate

from the high school with honors, attend a good school of her choice, reach all the goals in her life, and don't forget her uncle. I want to thank my mom, Nadezhda Perevalova, for... everything.

Last but not least, I want to thank Rakhno family, who I hope one day will formally become my family too. Igor and Olga Rakhno for being like my parents and, of course, for their daughter, Eugenia. Eugenia for being my heart and soul, and for being patient, even though it was hard not to see each other for long periods of time.

# Contents

# List of Tables

# List of Figures

# Part I

# Introduction

# Chapter 1

# Neutrinos and the Theory of Weak Interactions

In this chapter the history of the neutrino is discussed briefly, with some milestones from postulation and discovery to measuring neutrino properties. Also, a concept of the electro-weak theory is presented.

## 1.1 Brief History of Neutrinos

The first manifestations of the weak interactions were observed at the very end of the 19th century. In 1896, Henri Becquerell discovered radiation coming from uranium salts [1], then in 1898 Pierre and Marie Curie isolated radioactive radium [2]. In 1899–1902, three types of radiation were established, which differ by their charge: alpha (positive), beta (negative) [3] and gamma (neutral) [4, 5, 6, 7]. Moreover, in 1900 Becquerell showed that beta particles have a charge-to-mass ratio close to that of electrons [8], so they were identified as the latter.

Since then, the beta decay process has been studied intensively. The first evidence for the existense of the neutrino was obtained in 1920–1927, when Charles Drummond Ellis along with colleagues established clearly that the electron spectrum in beta decays is continuous [9, 10, 11, 12, 13, 14]. It was understood that a certain amount of nuclear energy is released in the decay, and thus in the two-body decay the outgoing electron energy should have been discrete. In order to save the energy conservation law Wolfgang Pauli proposed in 1930 the existence of a neutral particle that is

emitted along with the electron in the beta decay process [15].

In February 1932, James Chadwick discovered the neutron [16], which was a prime candidate for the particle emitted in the beta decay. However, in 1933 Francis Perrin showed that the neutrino mass has to be significantly lower than the electron mass [17]. Since neutrons are heavy particles, they can not correspond to the particle proposed by Pauli. Later that year, Enrico Fermi proposed the name for the new particle, *neutrino*, Italian for the "little neutral one". He published the first model of the beta decay in which the neutrino is produced [18].

In 1934, Hans Bethe and Rudolf Peierls calculated the neutrino interaction cross-section to be less than $10^{-44}$ cm$^2$, stating that it was therefore impossible to directly observe these interactions [19].

The series of the experiments by Frederick Reines and Clyde Cowan were the first step to directly observe neutrinos through the inverse beta decay:

$$\bar{\nu} + p \rightarrow n + e^+.$$

They used a new detection technology, a liquid scintillator counter, to detect the products of the decay [20]. The signal for this reaction would be the scintillation light from the primary positron, a delayed pair of gammas from the positron annihilation, and a 2.2 MeV gamma from the neutron capture on hydrogen. In their first experiment, the detector was placed near a plutonium-producing reactor at the Hanford Engineering Works near Richland, Washington. The experiment found an excess of events over the background which was consistent with the prediction of neutrino interactions [21]. However, the experiment had a signal-to-background ratio of only $\sim 0.2$.

In 1956, they performed a second experiment to confirm the existence of the neutrino. The detector was placed at the Savannah River Plant, South Carolina. It was separated into three regions to remove the appearance of signal events in all three tanks, which would signify cosmic ray muons. A neutrino signal was observed and was in $\sim 5\%$ agreement with the neutrino cross-section prediction, even though the latter had $\sim 25\%$ uncertainty [22]. The experiment had a signal-to-background ratio of 3/1. A second Savannah River experiment was held later in 1956–1959, with improved electronics; it also confirmed the neutrino signal [23].

In 1962, muon neutrinos were discovered by Leon Lederman, Mel Schwartz, Jack Steinberger and colleagues at Brookhaven National Laboratory (BNL) and it was confirmed that they were different from electron neutrinos [24].

In 1968, Ray Davis and colleagues collected the first radiochemical solar neutrino events by using

neutrino capture on chlorine in a detector in the Homestake Mine in North Dakota. The result lead to the observation of a deficit in the neutrinos produced by the Sun [25], as predicted by John Bahcall [26]. The problem became known as the *solar neutrino problem*.

In 1988, a deficit of atmospheric muon neutrinos was observed by the Kamiokande experiment [27] in Japan and the IMB experiment (Irvine, Michigan, Brookhaven) [28] in the Morton salt mine in Mentor, Ohio. This was the first clue to the neutrino oscillations.

In 1993–1998, the LEP (Large Electron Positron) accelerator experiments in Switzerland studied the width of the $Z^0$ boson. It was determined that there are only $2.984 \pm 0.008$ active and light (relative to the $Z^0$ boson mass) neutrino species that may couple to the $Z^0$ [29, 30, 31, 32].

In 1998, after analyzing more than 500 days of data, the Super-Kamiokande experiment reported finding atmospheric neutrino oscillations and, thus, indirect evidence for a non-zero value of the neutrino mass [33, 34].

In 2001, the DONUT (Direct Observation of NU Tau) experiment at the Fermi National Accelerator Laboratory (FNAL) observed $\nu_\tau$ charge current interactions [35], the third neutrino flavor.

In 2002, the SNO (Sudbury Neutrino Observatory) experiment near Sudbury, Ontario, Canada reported observation of neutral current and charged current scatterings from solar neutrinos, which provided a convincing evidence that neutrino oscillations are the solution of the solar neutrino problem [36].

In 2003, the KamLAND (Kamioka Liquid Scintillator Antineutrino Detector) experiment in Kamioka, Japan observed reactor antineutrino oscillations consistent with the solar neutrino problem and allowed a precision measurement of solar neutrino oscillation parameters [37].

In 2003, the K2K (KEK to Kamioka) long baseline neutrino oscillation experiment published the first measurement of atmospheric oscillation parameters using an accelerator-based neutrino beam created at KEK, a 12 GeV Proton Synchrotron facility in Japan [38]. Later, in 2006, the MINOS (Main Injector Neutrino Oscillation Search) experiment reported results on the atmospheric oscillation parameters measurement using an accelerator-based neutrino beam at FNAL. There are two MINOS detectors, the near one at FNAL site and the far one in the Soudan mine in Northern Minnesota. These results will be improved in a near future with more MINOS data and also with a new Tokai to Kamioka (T2K) experiment in Japan.

## 1.2 Neutrinos in the Standard Model

The Standard Model (SM) of particle physics is a theory explaining particles and interactions between them, including strong, electromagnetic (EM) and weak forces. The SM is a theory based on the local gauge group

$$SU(3) \times SU(2) \times U(1), \tag{1.1}$$

where color $SU(3)$ corresponds to quantum chromodynamics (QCD), and the weak isospin and weak hypercharge group $SU(2) \times U(1)$ to the electro-weak theory. The number of gauge bosons for an $SU(n)$ group is $n^2 - 1$, and there is only one boson for the $U(1)$ group. Thus there are 8+3+1=12 gauge bosons in the group in Eq.(1.1); these are 8 gluons, $W^+$, $W^-$, $Z^0$, and the photon.

The elementary particles of matter in the SM are fermions, which come in three generations of quarks and leptons, as shown in Table 1.1. $u$, $c$ and $t$ quarks have a charge $+2/3$ e, whereas $d$, $s$ and $b$ have a charge $-1/3$ e. They may participate in strong, EM, weak interactions. Charged leptons have a charge $-e$. They may participate in EM and weak interactions, whereas neutrinos may only interact weakly.

| Classification | Particles | | | Forces |
|---|---|---|---|---|
| | 1st Generation | 2nd Generation | 3nrd Generation | |
| Quarks | u (1.9 MeV) | c (1.32 GeV) | t (172.7 GeV) | Strong, EM, Weak |
| | d (4.4 MeV) | s (87 MeV) | b (4.24 GeV) | Strong, EM, Weak |
| Leptons | $e^-$ (511 keV) | $\mu^-$ (106 MeV) | $\tau^-$ (1.78 GeV) | EM, Weak |
| | $\nu_e$ ($<$ 2eV) | $\nu_\mu$ ($<$ 2eV) | $\nu_\tau$ ($<$ 2eV) | Weak |

Table 1.1: The Standard Model of elementary particles with their masses in the brackets, as taken from Ref.[39]. The last column describes the types of interactions the particles may participate in. The mass limits for the neutrinos come from the direct electron antineutrino mass measurements [40] and have been superseded by the neutrino oscillation measurements which imply small mass differences between different neutrino flavors (as we describe later in Section 1.3).

In the SM, neutrinos are neutral and massless particles. However, due to the phenomenon of neutrino flavor oscillations observed by various neutrino experiments [41], neutrinos must have masses. Currently, the best limits on the neutrino mass comes from the direct electron antineutrino

mass measurement from tritium beta decay in the Troitsk experiment [42] in Russia and the Mainz experiment [40] in Germany. In the tritium beta decay, ${}^3H \rightarrow {}^3He + e + \overline{\nu}_e$, electrons are emitted in the form of continuous energy spectrum with the end point energy of $\sim$ 18.57 keV. In these experiments the electron energy spectrum behavior around the end point is studied. If the electron antineutrino has a nonzero mass, then the endpoint energy would be lower by the amount of the antineutrino's rest mass. The current limit on electron antineutrino mass is given by

$$m(\bar{\nu}_e) < 2.2 \text{ eV} \qquad (95\% \text{ C.L.}).$$

In the near future, the KATRIN (Karlsruhe Tritium Neutrino) experiment will push the limit on the electron neutrino mass to 0.2 eV. The current measurements on $\Delta m^2_{21} = (7.59 \pm 0.20) \times 10^{-5}$ eV$^2$ and $|\Delta m^2_{32}| = (2.43 \pm 0.13) \times 10^{-3}$ eV$^2$ (square mass difference between neutrino masses) from neutrino oscillations combined with the above limit for the electron neutrino mass produce the same limits on the masses of the $\nu_\mu$ and $\nu_\tau$ as that for the electron neutrino, due to the small values of the $\Delta m^2$'s.

Finally, there is the Higgs boson, which is a consequence of the Higgs mechanism of spontaneous symmetry breaking, which describes the generation of particle masses in the SM. The Higgs is the only particle in the SM which has not been observed yet (as of 2009); it is expected to be seen at the LHC. All massive particles also experience gravitational interactions with each other, although it is very weak (about $10^{25}$ times weaker than weak interactions).

## 1.3 Neutrino Oscillations

Neutrino oscillations is a quantum mechanical phenomenon predicted by Bruno Pontecorvo [43], where a neutrino created with a specific lepton flavor (electron, muon or tau) can be measured to have a different flavor after traveling some distance in space. Suppose that there is a source of neutrinos of *flavor eigenstate* $\nu_l$ corresponding to the flavor of a charged lepton $l^-$ which is emitted together with the neutrino in a charge current (CC) weak interaction (discussed in Chapter 2). We further assume that neutrinos have three *mass eigenstates* of the Hamiltonian in free space, which are different from the flavor eigenstates. Each neutrino flavor eigenstate produced by the source is the coherent superposition of the mass eigenstates:

$$\nu_l = \sum_{m=1}^{3} U_{lm} \nu_m, \qquad l = e, \mu, \tau,$$

where $U_{lm}$ is a unitary matrix, called Maki-Nakagawa-Sakata matrix. It is usually presented in the following form:

$$\begin{aligned} U &= \begin{pmatrix} U_{e1} & U_{e2} & U_{e3} \\ U_{\mu 1} & U_{\mu 2} & U_{\mu 3} \\ U_{\tau 1} & U_{\tau 2} & U_{\tau 3} \end{pmatrix} \\ &= \begin{pmatrix} 1 & 0 & 0 \\ 0 & c_{23} & s_{23} \\ 0 & -s_{23} & c_{23} \end{pmatrix} \begin{pmatrix} c_{13} & 0 & s_{13}e^{-i\delta} \\ 0 & 1 & 0 \\ -s_{13}e^{i\delta} & 0 & c_{13} \end{pmatrix} \begin{pmatrix} c_{12} & s_{12} & 0 \\ -s_{12} & c_{12} & 0 \\ 0 & 0 & 1 \end{pmatrix} \begin{pmatrix} e^{i\alpha_1/2} & 0 & 0 \\ 0 & e^{i\alpha_2/2} & 0 \\ 0 & 0 & 1 \end{pmatrix} \end{aligned}$$

where $\theta_{ij}$ are three mixing angles, $c_{ij} = \cos\theta_{ij}$, $s_{ij} = \sin\theta_{ij}$, $\delta$ is a CP phase, and $\alpha_1$ and $\alpha_2$ are Majorana phases. The latter are non-zero only if neutrinos are Majorana particles [44], but for oscillations these factors can be ignored.

It has been shown [45] that, in a vacuum, the probability of neutrinos of flavor $\nu_l$ to be detected in state $\nu_{l'}$:

$$\begin{aligned} P(\nu_l \to \nu_{l'}) &= \delta_{ll'} - 4\sum_{i>j} Re(U^*_{li}U_{l'i}U_{lj}U^*_{l'j})\sin^2(\Delta m^2_{ij}L/4E) \\ &+ 2\sum_{i>j} Im(U^*_{li}U_{l'i}U_{lj}U^*_{l'j})\sin(\Delta m^2_{ij}L/2E), \end{aligned}$$

where $\delta_{ll'}$ is the Kronecker delta, $\Delta m^2_{ij} = m^2_i - m^2_j$ is the splitting between the squared masses of the mass eigenstates $\nu_i$ and $\nu_j$, $L$ is the distance from the creation point to the detection point, and $E$ is the neutrino energy.

So far we have used $\hbar = c = 1$. Using standard units for neutrino oscillation experiments,

$$\frac{\Delta m^2_{ij}L}{4E} = 1.27\frac{\Delta m^2_{ij}(\mathrm{eV}^2)L(m)}{E(MeV)},$$

then the oscillation probability becomes:

$$\begin{aligned} P(\nu_l \to \nu_{l'}) &= \delta_{ll'} - 4\sum_{i>j} Re(U^*_{li}U_{l'i}U_{lj}U^*_{l'j})\sin^2\left(1.27\Delta m^2_{ij}\frac{L}{E}\right) \\ &+ 2\sum_{i>j} Im(U^*_{li}U_{l'i}U_{lj}U^*_{l'j})\sin\left(2.54\Delta m^2_{ij}\frac{L}{E}\right). \end{aligned}$$

Under the assumption that the CP phase is $\delta = 0$, which makes all elements of the mixing matrix real, and that one of the mass square differences dominate, the two-neutrino oscillation formula can

be written as:

$$P(\nu_l \to \nu_{l'}) = \begin{cases} 1 - \sin^2 2\theta \sin^2 \left(1.27\Delta m^2 \frac{L}{E}\right) & \text{if } l = l' \\ \sin^2 2\theta \sin^2 \left(1.27\Delta m^2 \frac{L}{E}\right) & \text{if } l \neq l', \end{cases}$$

with the mixing matrix in this case,

$$U = \begin{pmatrix} \cos\theta & \sin\theta \\ -\sin\theta & \cos\theta \end{pmatrix}.$$

The current values of the oscillation parameters as given by the Particle Data Group (PDG) in 2008 [39] are shown in Table 1.2. These results represent a combined analysis of several neutrino oscillation experiments observing reactor, accelerator and solar neutrinos.

| Parameter | Value |
|---|---|
| $\Delta m^2_{21}$ | $(7.59 \pm 0.20) \times 10^{-5}$ eV$^2$ |
| $\lvert\Delta m^2_{32}\rvert$ | $(2.43 \pm 0.13) \times 10^{-3}$ eV$^2$ |
| $\sin^2 2\theta_{12}$ | $0.87 \pm 0.03$ |
| $\sin^2 2\theta_{23}$ | $> 0.92$ |
| $\sin^2 2\theta_{13}$ | $< 0.19$ |

Table 1.2: Current values for neutrino oscillation mixing parameters as reported by PDG in 2008 [39].

## 1.4 Plan of the Thesis

There are three parts of the thesis. Part I includes a review of the Standard Model of weak interactions in Chapter 2. A review of the neutrino-nucleon neutral current elastic cross-section model, the significance of such a measurement and current measurements from other experiments are given in Chapter 3. A detailed description of the MiniBooNE experiment is provided in Chapter 4.

Part II describes the analysis of neutrino-nucleon neutral current elastic (NCE) interactions in MiniBooNE and the physics results. In Chapter 5 the event reconstruction algorithm for proton events is described, which is used in the NCE analysis. In Chapter 6 the NCE cross-section analysis

and results are explained. In Chapter 7 the measurement of the axial vector mass using the MiniBooNE NCE data is presented. In Chapter 8 the measurement of the strange quark contribution to the nucleon spin using the MiniBooNE high energy NCE data is presented. In the concluding Chapter 9 the major results of the present work, consisting in the analysis of the neutrino-nucleon neutral current elastic scattering in MiniBooNE are summarized

The third part contains three appendices which include supplemental calculations and more detailed cross-section results.

# Chapter 2

# The Glashow-Weinberg-Salam Model of Electro-Weak Interactions

## 2.1 Introduction

In this chapter a review of Glashow-Weinberg-Salam (GWS) theory [46, 47, 48] of electro-weak interactions is presented. In the GWS model, the electro-weak force carriers are introduced, through which particles interact with each other. There are both charged and neutral electro-weak currents. In order to account for a small value of weak interaction cross-sections, it is necessary to have very massive weak force carriers. From the uncertainty principle, which relates the uncertainty in energy $\Delta E$ to the time taken by the measurement $\Delta t$: $\Delta E \Delta t \gtrapprox \hbar$, one can find a range of weak forces. Assuming the mass of weak force carriers of $\sim 100$ GeV, the range of the weak force is $\sim 10^{-17}$ m, which explains the rareness of weak interactions.

The GWS theory is based on constructing a Lagrangian which describes the propagation and electro-weak interaction of the particles. In the GWS formalism the Lagrangian remains invariant under so-called local *gauge* transformations, which will be defined later; the idea of gauge invariance is to generalize known Lagrangians which are invariant under global gauge transformations (those which do not depend on coordinates). For example, the Dirac Lagrangian, which describes free

fermion fields, is described by the following expression:

$$\mathcal{L}_{Dirac} = \bar{\Psi}(i\gamma^{\mu}\partial_{\mu} - m)\Psi,$$

where $\Psi$ and $\bar{\Psi}$ are the fermion and its Dirac conjugate fields, respectively, $\gamma^{\mu}$ are $4 \times 4$ gamma matrices, defined in Eq.(2.3), and $m$ is the fermion mass. The Dirac conjugate field is defined as $\bar{\Psi}(x) = \Psi^{\dagger}(x)\gamma^{0}$. A global gauge transformation in this case would be $\Psi \rightarrow e^{-i\omega}\Psi$, where $\omega$ is a constant. A local gauge transformation is if $\omega$ is a function of position, $\omega = \omega(x,t)$. $\mathcal{L}_{Dirac}$ in the form above is invariant only under global gauge transformations.

## 2.2 Gauge Fields

Let us first discuss the gauge fields of the GWS theory. In the GWS model, the Lagrangian should be invariant under $SU(2) \times U(1)$ gauge transformations,

$$\psi(x) \rightarrow \exp\left(i\alpha^{a}T^{a} + \frac{i}{2}\beta Y\right)\psi(x),$$

where $\alpha^{a}(x)$, $a = 1, 2, 3$ and $\beta(x)$ are arbitrary functions; $T^{a}$ and $Y$ are matrices acting on the fields and are generators of $SU(2)$ and $U(1)$, respectively, which can transform fields to other members of the group. The summation is understood over repeated indices in the same term.

The technique of the Lagrangian construction is to replace the partial derivative in the free field Lagrangian by a covariant derivative involving the boson fields. The covariant derivative in the Lagrangian in this case is given by

$$D_{\mu} = \partial_{\mu} - \frac{ig'}{2}\mathcal{A}_{\mu}Y - igb_{\mu}^{a}T^{a}, \tag{2.1}$$

where $g'$ and $g$ are the $U(1)$ and $SU(2)$ coupling constants, and $A_{\mu}$ and $b_{\mu}^{a}$ are matrices, acting on fields. The matrices $A_{\mu}$ and $b_{\mu}^{a}$ are the generators of $U(1)$ and $SU(2)$, respectively. With the gauge field tensors:

$$\begin{aligned} F_{\mu\nu}^{i} &= \partial_{\nu}b_{\mu}^{i} - \partial_{\mu}b_{\nu}^{i} + g\epsilon^{ijk}b_{\mu}^{j}b_{\nu}^{k}, \\ G_{\mu\nu} &= \partial_{\nu}\mathcal{A}_{\mu} - \partial_{\mu}\mathcal{A}_{\nu}, \end{aligned}$$

one can construct the gauge invariant Lagrangian describing the gauge fields:

$$\mathcal{L}_{gauge} = -\frac{1}{4}F^{l}_{\mu\nu}F^{l,\mu\nu} - \frac{1}{4}G_{\mu\nu}G^{\mu\nu}. \tag{2.2}$$

## 2.3 Lepton Fields with Massless Bosons

In the following we discuss leptons. In the GWS model, the form of lepton interactions of different flavors (electron, muon and tau) are equivalent to each other. Thus, one can discuss only the fields in one family, the electron family for instance ($e^-$ and $\nu_e$).

In field theory lepton fields, with spin 1/2, can be represented as a superposition of two fields with left and right handed *chirality*. The chirality is defined by the sign of the eigenstate of the $\gamma_5$ operator ("$-$" for left and "$+$" for right handed state, respectively). $\gamma_5$ is defined by the Dirac gamma matrices:

$$\begin{aligned}
\gamma_0 &= \begin{pmatrix} 1 & 0 & 0 & 0 \\ 0 & 1 & 0 & 0 \\ 0 & 0 & -1 & 0 \\ 0 & 0 & 0 & -1 \end{pmatrix}, \quad \gamma_1 = \begin{pmatrix} 0 & 0 & 0 & 1 \\ 0 & 0 & 1 & 0 \\ 0 & -1 & 0 & 0 \\ -1 & 0 & 0 & 0 \end{pmatrix}, \\
\gamma_2 &= \begin{pmatrix} 0 & 0 & 0 & -i \\ 0 & 0 & i & 0 \\ 0 & i & 0 & 0 \\ -i & 0 & 0 & 0 \end{pmatrix}, \quad \gamma_3 = \begin{pmatrix} 0 & 0 & 1 & 0 \\ 0 & 0 & 0 & -1 \\ -1 & 0 & 0 & 0 \\ 0 & 1 & 0 & 0 \end{pmatrix},
\end{aligned} \tag{2.3}$$

$$\gamma_5 = i\gamma_0\gamma_1\gamma_2\gamma_3 = \begin{pmatrix} 0 & 0 & 1 & 0 \\ 0 & 0 & 0 & 1 \\ 1 & 0 & 0 & 0 \\ 0 & 1 & 0 & 0 \end{pmatrix}.$$

One can always represent any field through its right and left components:

$$\psi = 1\psi = \frac{1+\gamma_5}{2}\psi + \frac{1-\gamma_5}{2}\psi = P_R\psi + P_L\psi$$

The projection operators $P_L = \dfrac{1-\gamma_5}{2}$ and $P_R = \dfrac{1+\gamma_5}{2}$ convert fields in the left and right eigenstate

fields, respectively. This is easy to see, using the gamma algebra $(\gamma_5)^2 = 1$, thus

$$\begin{aligned} \gamma_5 P_R \psi &= +P_R \psi \\ \gamma_5 P_L \psi &= -P_L \psi. \end{aligned}$$

It turns out that the weak interaction affects only left-handed lepton fields. Hence, we introduce the isospin doublet $L$ for the $SU(2)$ group:

$$L = P_L \begin{pmatrix} \nu \\ e \end{pmatrix} = \begin{pmatrix} \nu_L \\ e_L \end{pmatrix}, \tag{2.4}$$

where we have omitted the charge sign "–" for the electron and the lower index "e" for the neutrino for simplicity.

There may also exist right-handed components of the fields for the $U(1)$ group, singlets. In the GWS model there is only one singlet for the electron:

$$R = P_R e = e_R. \tag{2.5}$$

To specify the gauge structure completely, we need to define the action of $T^a$ and $Y$ on the fermion fields. The action of $T^a$ is given by

$$T^a L = \frac{\tau^a}{2} L \qquad T^a R = 0,$$

where $\tau^a$ are the Pauli matrices.

In order to incorporate quantum electrodynamics into the theory, one can represent a charge operator $Q$ through a linear combination of $T^a$ and $Y$. Thus we define:

$$Q = T^3 + \frac{1}{2} Y. \tag{2.6}$$

The eigenvalues of operators $Q$, $T^3$ and $Y$ for each of the lepton fields can be calculated from Eq.(2.6) and are shown in Table 2.1.

The most general gauge invariant Lagrangian describing leptons can be written as:

$$\mathcal{L}_{leptons} = \bar{R} i\gamma^\mu (\partial_\mu + \frac{ig'}{2} \mathcal{A}_\mu Y) R + \bar{L} i\gamma^\mu (\partial_\mu + \frac{ig'}{2} \mathcal{A}_\mu Y + \frac{ig}{2} \tau^a b^a_\mu) L. \tag{2.7}$$

| Lepton | $Q$ | $T^3$ | $Y$ |
|---|---|---|---|
| $\nu_L$ | $0$ | $\frac{1}{2}$ | $-1$ |
| $e_L$ | $-1$ | $-\frac{1}{2}$ | $-1$ |
| $e_R$ | $-1$ | $0$ | $-2$ |

Table 2.1: The eigenvalues of $Q$, $T^3$ and $Y$ operators for the lepton fields.

One may notice however, that the theory is not yet realistic, because in the total Lagrangian, which is the sum of the two Lagrangians in Eqs. (2.2) and (2.7), both bosons and fermions are massless.

## 2.4 The Higgs Mechanism

In order to generate masses for the gauge bosons and fermions, the Higgs mechanism is applied [49, 50] by introducing a complex scalar doublet:

$$\Phi = \begin{pmatrix} \Phi^+ \\ \Phi^0 \end{pmatrix} = \begin{pmatrix} \phi_1 + i\phi_2 \\ \phi_3 + i\phi_4 \end{pmatrix}. \tag{2.8}$$

The gauge invariant Lagrangian for the scalar field is given by

$$\mathcal{L}_{Higgs} = (D^\mu \Phi)^\dagger (D_\mu \Phi) - V(\Phi^\dagger \Phi), \tag{2.9}$$

with the covariant derivative taken from Eq.(2.1). Choosing the following form of the potential:

$$V(\Phi^\dagger \Phi) = -\mu^2 (\Phi^\dagger \Phi) + \lambda (\Phi^\dagger \Phi)^2,$$

with $\mu$ and $\lambda$ some real and positive numbers, then the potential has a locus of minima on a 4-dimensional space with $\phi_1$, $\phi_2$, $\phi_3$, and $\phi_4$ on axes. The minimum is on the 4-dimensional sphere:

$$\phi_1^2 + \phi_2^2 + \phi_3^2 + \phi_4^2 = \frac{\mu^2}{2\lambda}.$$

In GWS, the minimum is chosen at the point where $\phi_1 = \phi_2 = \phi_4 = 0$ and $\phi_3 = \dfrac{\mu^2}{2\lambda}$. The vacuum expectation value at the minimum is given by

$$\Phi_{vac} = \begin{pmatrix} 0 \\ \dfrac{\mu}{\sqrt{2\lambda}} \end{pmatrix} = \begin{pmatrix} 0 \\ \dfrac{\upsilon}{\sqrt{2}} \end{pmatrix} \qquad \text{with} \qquad \upsilon = \frac{\mu}{\sqrt{\lambda}}.$$

One can perturbatively expand $\Phi$ around the vacuum by introducing the four scalar fields $\xi_1$, $\xi_2$, $\xi_3$ and $\eta$:

$$\Phi = \exp\left(\frac{i\xi^a\tau^a}{2\upsilon}\right)\begin{pmatrix} 0 \\ \dfrac{\upsilon+\eta}{\sqrt{2}} \end{pmatrix}.$$

However, since the Lagrangian is invariant under gauge transformations, one can transform the complex scalar field:

$$\Phi \to \Phi' = \exp\left(\frac{-i\xi^a\tau^a}{2\upsilon}\right)\Phi = \begin{pmatrix} 0 \\ \dfrac{\upsilon+\eta}{\sqrt{2}} \end{pmatrix}. \tag{2.10}$$

Following Eq.(2.6), the Higgs field $\eta$ has the following quantum numbers $Q = 0$, $T^3 = 1/2$ and $Y = 1$.

Let us define the new gauge bosons:

$$W_\mu^\pm = \frac{1}{\sqrt{2}}\left(b_\mu^1 \mp i b_\mu^2\right), \quad Z_\mu = \frac{g b_\mu^3 - g'\mathcal{A}_\mu}{\sqrt{g^2+g'^2}}, \qquad \text{and} \quad A_\mu = \frac{g\mathcal{A}_\mu + g' b_\mu^3}{\sqrt{g^2+g'^2}}. \tag{2.11}$$

It is convenient to introduce a weak mixing angle $\theta_W$, which is also called a Weinberg angle to parametrize the mixing of the neutral gauge bosons:

$$\cos\theta_W = \frac{g}{\sqrt{g^2+g'^2}},$$

so that

$$\begin{pmatrix} Z_\mu \\ A_\mu \end{pmatrix} = \begin{pmatrix} \cos\theta_W & -\sin\theta_W \\ \sin\theta_W & \cos\theta_W \end{pmatrix}\begin{pmatrix} b_\mu^3 \\ \mathcal{A}_\mu \end{pmatrix}.$$

Putting Eqs. (2.10), (2.11) and (2.1) into (2.9) one can rewrite the Lagrangian as

$$\mathcal{L}_{Higgs} = \frac{1}{2}\partial^\mu\eta\partial_\mu\eta + \frac{g^2}{4}(\upsilon+\eta)^2 W^{+,\mu}W_\mu^- + \frac{g^2+g'^2}{8}(\upsilon+\eta)^2 Z^\mu Z_\mu + \frac{\mu^2}{2}(\upsilon+\eta)^2 - \frac{\lambda}{4}(\upsilon+\eta)^4.$$

The first term is the kinetic term for the Higgs field; the second term gives the mass term to $W^+$

and $W^-$ bosons as well as 3- and 4-point interactions of $W$'s with the Higgs; the third term gives a mass term to the $Z^0$ boson, as well as 3- and 4-point interactions of $Z^0$'s with the Higgs; the last two terms give a mass term to the Higgs and 3- and 4-point interactions between the Higgs fields. The masses of the $W^\pm$ and $Z^0$ bosons can be identified as follows

$$M_W = \frac{g\upsilon}{2}, \qquad M_Z = \frac{g\upsilon}{2\cos\theta_W}.$$

## 2.5 Fermion Masses

Although mass terms of the form $m\bar{\psi}\psi$ were excluded from the initial lepton Lagrangian in Eq.(2.7), the same Higgs field can also generate lepton masses. The interaction between the left-handed doublet, right-handed singlet and the Higgs doublet is gauge invariant. Thus, one can add such an interaction term, called a $Yukawa$ interaction:

$$\mathcal{L}^{leptons}_{Yukawa} = -G_e\left[\bar{R}\Phi^\dagger L + (\bar{L}\Phi)R\right] = -\frac{G_e}{\sqrt{2}}(\upsilon+\eta)\left[\bar{e}_R e_L + \bar{e}_L e_R\right] = -\frac{G_e}{\sqrt{2}}(\upsilon+\eta)\bar{e}e,$$

where $G_e$ is a Yukawa coupling constant. This Lagrangian generates the electron mass, as well as introduces a 3-point interaction with Higgs. The electron mass is identified as:

$$m_e = \frac{G_e\upsilon}{\sqrt{2}}.$$

Naturally, neutrinos remain massless, because there is no neutrino right-handed singlet.

## 2.6 Final Expression for the Lepton-Gauge Interaction

Plugging in the redefined vector bosons from Eq.(2.11) into (2.7) and expressing left and right field projections in Eqs. (2.4) and (2.5) in terms of actual fields, one can calculate the final expression for the Lagrangian for interaction of leptons with gauge fields [51]:

$$\begin{aligned}
\mathcal{L}_{lepton} &= -\frac{g}{2\sqrt{2}}\bar{\nu}\gamma^\mu(1-\gamma_5)eW^+_\mu - \frac{g}{2\sqrt{2}}\bar{e}\gamma^\mu(1-\gamma_5)\nu W^-_\mu \\
&+ g\sin\theta_W\bar{e}\gamma^\mu eA_\mu - \frac{g}{4\cos\theta_W}\bar{\nu}\gamma^\mu(1-\gamma_5)\nu Z_\mu \\
&+ \frac{g}{4\cos\theta_W}\bar{e}\gamma^\mu(1-4\sin^2\theta_W-\gamma_5)eZ_\mu.
\end{aligned}$$

The first line of the expression defines the interaction between electrons, neutrinos and $W$ bosons. The first term of the second line is the EM interaction of electrons and photons. The second term of the second line is the weak neutral current interaction between neutrinos and the $Z^0$ boson. Finally, the last line is the weak neutral current interaction between electrons and the $Z^0$ boson. From the EM interaction term we identify the coupling constant as the electric charge:

$$e = g \sin\theta_W = \frac{gg'}{\sqrt{g^2 + g'^2}}.$$

## 2.7 Incorporating Quarks

In principle, the quark sector is similar to the lepton sector. One could construct the same left-handed isospin doublets out of quarks and derive the Lagrangian in the same way it was done for leptons. The difference is that all quarks are massive, so one has to define right-handed singlets for each quark. Also, the charges for the quarks shown in Table 1.1 are different from the lepton sector.

As mentioned previously there are three generations of quarks. It has been experimentally observed that the quarks mass eigenstates are not the same as their flavor eigenstates. In other words, in free space where the quark is in the mass eigenstate, it may be represented as a superposition of the flavor eigenstates of the 3 quark generations. And vice versa, in the weak interaction the interacting quark may be represented as superposition of the mass eigenstates of the 3 quark generation. The matrix, which relates the mixing between quarks is called *Cabibo-Kobayashi-Maskawa* matrix (CKM) [52]:

$$V = \begin{pmatrix} V_{ud} & V_{us} & V_{ub} \\ V_{cd} & V_{cs} & V_{cb} \\ V_{td} & V_{ts} & V_{tb} \end{pmatrix}.$$

The matrix is unitary. Each element of the matrix is a relative amplitude of the charge current weak interaction involving given quarks. It is expected that diagonal elements would be close to unity. Currently, the best measurement of magnitudes of the CKM matrix elements is [39]:

$$\begin{pmatrix} |V_{ud}| & |V_{us}| & |V_{ub}| \\ |V_{cd}| & |V_{cs}| & |V_{cb}| \\ |V_{td}| & |V_{ts}| & |V_{tb}| \end{pmatrix} = \begin{pmatrix} 0.97419 \pm 0.00022 & 0.2257 \pm 0.0010 & 0.00359 \pm 0.00016 \\ 0.2256 \pm 0.0010 & 0.97334 \pm 0.00023 & 0.0415^{+0.0010}_{-0.0011} \\ 0.00874^{+0.00026}_{-0.00037} & 0.0407 \pm 0.0010 & 0.999133^{+0.000044}_{-0.000043} \end{pmatrix}.$$

Since in weak charge current interactions upper and lower weak isospin quarks come together

with the CKM matrix, one could chose which of the quarks effectively acquires the CKM matrix. It is chosen, that the lower isospin quarks acquire the CKM matrix. So, that quark flavor eigenstates (denoted with primes) with the lower ($T^3 = -1/2$) weak isospin can be represented through the corresponding quark mass eigenstates:

$$\begin{pmatrix} d' \\ s' \\ b' \end{pmatrix} = \begin{pmatrix} V_{ud} & V_{us} & V_{ub} \\ V_{cd} & V_{cs} & V_{cb} \\ V_{td} & V_{ts} & V_{tb}. \end{pmatrix} \begin{pmatrix} d \\ s \\ b \end{pmatrix}.$$

With these definitions we can construct the quark elements for the $SU(2) \times U(1)$ group. Just like in the case of leptons, all quark generations are equivalent to each other in terms of the form of interactions. Thus, without a loss of generality one can look on only one of them. For instance, the first generation of $u$ and $d$ quarks. There is a $SU(2)$ left-handed doublet:

$$\begin{pmatrix} u_L \\ d'_L \end{pmatrix} = P_L \begin{pmatrix} u \\ d' \end{pmatrix}$$

and two $U(1)$ right-handed singlets: $u_R = P_R u$ and $d'_R = P_R d'$. Using Eq.(2.6) one can calculate the weak hypercharge for quark fields. The eigenvalues of the $Q$, $T^3$ and $Y$ operators for quark fields are given in Table 2.2.

| Quark | $Q$ | $T^3$ | $Y$ |
|---|---|---|---|
| $u_L$ | $\frac{2}{3}$ | $\frac{1}{2}$ | $\frac{1}{3}$ |
| $d'_L$ | $-\frac{1}{3}$ | $-\frac{1}{2}$ | $\frac{1}{3}$ |
| $u_R$ | $\frac{2}{3}$ | $0$ | $\frac{4}{3}$ |
| $d'_R$ | $-\frac{1}{3}$ | $0$ | $-\frac{2}{3}$ |

Table 2.2: The eigenvalues of $Q$, $T^3$ and $Y$ operators for the quark fields.

The masses for the quarks are generated through the Yukawa interaction with the Higgs field.

The mass for the down quark is generated identically as in the procedure for the electron.

For the mass of the up quark one needs to take a complex conjugate of the Higgs field from Eq.(2.8):

$$\bar{\Phi} = i\tau_2\Phi^* = \begin{pmatrix} \bar{\phi}^0 \\ -\phi^- \end{pmatrix}.$$

Proceeding with the same symmetry braking mechanism, the gauge invariant Yukawa interaction Lagrangian for quarks is given:

$$\begin{aligned} \mathcal{L}_{Yukawa}^{quarks} &= -G_u\left[(\bar{L}_q\bar{\Phi})u_R + \bar{u}_R(\bar{\phi}^\dagger L_q)\right] - G_d\left[(\bar{L}_q\Phi)d'_R + \bar{d'}_R(\phi^\dagger L_q)\right] \\ &= -G_u\frac{(\upsilon+\eta)}{\sqrt{2}}\bar{u}u - G_d\frac{(\upsilon+\eta)}{\sqrt{2}}\bar{d'}d', \end{aligned}$$

which gives familiar mass terms for $u$ and $d$ quarks and their interactions with the Higgs boson.

The interaction of quarks with with gauge bosons differs from that of leptons by the values of the weak hypercharge. The resulting Lagrangian for the interaction is given by the following expression:

$$\begin{aligned} \mathcal{L}_{quarks} &= -\frac{g}{2\sqrt{2}}\bar{u}\gamma^\mu(1-\gamma_5)d'W_\mu^+ - \frac{g}{2\sqrt{2}}\bar{d'}\gamma^\mu(1-\gamma_5)uW_\mu^- \\ &- \frac{2}{3}g\sin\theta_W\bar{u}\gamma^\mu uA_\mu + \frac{1}{3}g\sin\theta_W\bar{d'}\gamma^\mu d'A_\mu \\ &- \frac{g}{4\cos\theta_W}\bar{u}\gamma^\mu\left[1-\frac{8}{3}\sin^2\theta_W-\gamma_5\right]uZ_\mu + \frac{g}{4\cos\theta_W}\bar{d'}\gamma^\mu\left[1-\frac{4}{3}\sin^2\theta_W-\gamma_5\right]d'Z_\mu. \end{aligned}$$

In summary, the GWS model gives a description of electro-weak interactions, involving leptons and quarks. It explains a small strength of weak interactions by assigning massive force carriers. It also reveals the origin of the particle's mass while predicting the existence of a scalar Higgs particle.

This thesis describes a measurement of neutrino-nucleon neutral current elastic scattering, shown schematically in Fig. 2.1, where the neutrino exchanges a $Z^0$ boson with one of the quarks in the nucleon. The interaction at the neutrino vertex is simple (as described in Section 2.6), whereas the one at the nucleon vertex is not, since the interacting quark is strongly bound inside the nucleus. Therefore, QCD effects complicate nucleon vertex; the nucleon currents can effectively be expressed through form factors, described in the next chapter.

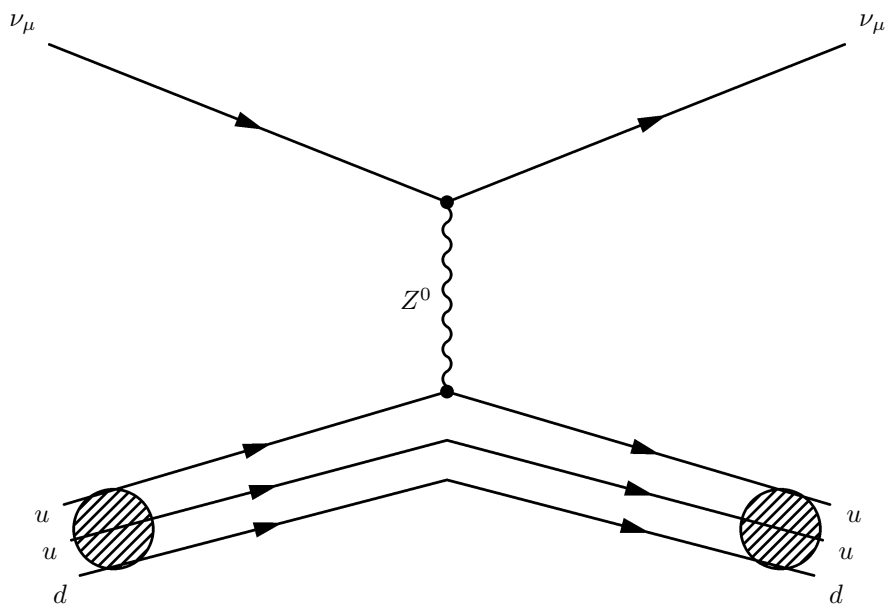


Figure 2.1: Feynman diagram for $\nu_\mu p \rightarrow \nu_\mu p$ neutral curent elastic scattering at the quark level.

# Chapter 3

# The Neutral Current Elastic Cross-Section

## 3.1 History of the Weak Neutral Currents

In 1949 the concept of the charged boson, the carrier of the weak force, has been proposed in order to describe weak interactions [53]. It was not until the 1960s that the modern Glashow-Weinberg-Salam theory [46, 47, 48] was developed which included both charged ($W^+$, $W^-$) and neutral ($Z^0$) bosons, hence implying the existence of the weak neutral currents (WNC).

The search for WNC processes began when the high-energy neutrino beams were initiated in the Alternating Gradient Synchotron facility at the Brookhaven National Laboratory (BNL) and in the Proton Synchrotron facility at CERN. However, the experiments did not find the signal. The CERN Heavy Liquid Bubble Chamber experiment even put a discouraging limit on the ratio of $NC/CC$ coupling to be less than 3% [54]. This limit was later revised upward, but, unfortunately, it discouraged further searches for WNC for a long period of time.

In 1973 two experimental groups became involved in the search for WNC. It is generally considered that WNC were first observed by the Gargamelle experiment at CERN and confirmed by HPWF experiment (Harvard-Penn-Wisconsin-Fermilab) at FNAL. Gargamelle was looking for neutrino-electron and antineutrino-electron neutral current elastic interactions:

$$\begin{aligned} \bar{\nu}_\mu + e^- &\rightarrow \bar{\nu}_\mu + e^- \\ \nu_\mu + e^- &\rightarrow \nu_\mu + e^-. \end{aligned}$$

The signal they were looking for was a high energy ($E > 300MeV$) and a very forward going electron, as the angle between the neutrino beam direction and the reconstructed electron direction is typically less than $5^o$. They did find one event that passed the selection cuts in the antineutrino mode [55], where the backgrounds are highly suppressed: both have CCQE backgrounds in which a muon is produced; however, the $\mu^+$ which is produced in the antineutrino CCQE has a different curvature than the $e^-$ in the magnetic field of the detector. The expected background was $0.003 \pm 0.002$ events, whereas the theoretical prediction ranged from 0.4 to 8.0 antineutrino-electron NCE events, depending on the value of $sin^2\theta_W$, which was obviously unknown at the time. The currently known $sin^2\theta_W$ value would have put the prediction right about the lower limit, namely at 0.4.

While this was an extremely interesting event, one would need more than just one event as proof of the existence of the WNC. Later Gargamelle observed candidates for the neutrino-nucleon neutral current deep-inelastic scattering:

$$\nu + N \rightarrow \nu + X,$$

where X is the hadronic final state [56]. The HPWF experiment also observed the same channel where they were looking for the muonless neutrino interactions [57].

Now that the WNC were discovered, it turned out that neutrino-proton and antineutrino-proton neutral current elastic scattering (NCE p),

$$\begin{aligned} \nu + p &\rightarrow \nu + p \\ \bar{\nu} + p &\rightarrow \bar{\nu} + p, \end{aligned}$$

is very useful for probing the structure of protons and neutrons (nucleons). In particular, it is sensitive to the presence of strange quarks inside the nucleons, as we shall discuss in Section 3.2. The first observation of NCE p scattering was in 1976 by the Columbia-Illinois-Rockefeller [58] and HPWF [59, 60, 61] experiments. However, the first relatively high statistics NCE p in both $\nu$ and $\bar{\nu}$ modes was obtained by the BNL E734 experiment in 1980s [62]. Using the BNL E734 NCE cross-section, the allowed region for the value of the strange quark contribution to the nucleon spin has been extracted to yield

$$\Delta s = -0.21 \pm 0.10.$$

The BNL E734 experiment will be discussed in some detail in Section 3.4.

The EMC (European Muon Collaboration) experiment result [63] and the appearance of the proton spin crisis (discussed in Section 3.4), which is still unsolved, has brought a lot of interest

among the nuclear physics community to the measurements of NCE. However, after BNL E734 there has been no specially designed experiments to measure the NCE channel. MiniBooNE and SciBooNE are among the recent ones that are able to measure the NCE channel with very high statistics, but their primary goal was not the NCE channel. MiniBooNE's primary goal is the $\nu_\mu \to \nu_e$ oscillation search at $\Delta m^2 \sim 1\ eV^2$, while SciBooNE was designed to measure CCQE and both NC and CC pion production cross-sections.

## 3.2 Neutral Current Elastic Scattering on Free Nucleons

We first describe the neutrino neutral current elastic scattering cross-section on free nucleons. This is represented by the formula:

$$\nu(q_1, \sigma_1) + N(p_1, \kappa_1) \to \nu(q_2, \sigma_2) + N(p_2, \kappa_2),$$

where the labels $p_i$, $q_i$ and $q$ refer to the energy-momentum and $\sigma_i$, $\kappa_i$ to the spin of the particles. The coresponding Feynman diagram is shown in Fig. 3.1.

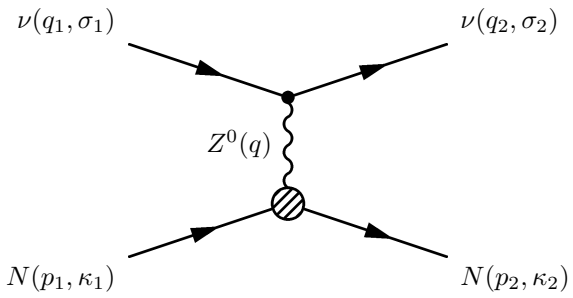


Figure 3.1: Feynman diagram for the neutrino-nucleon neutral curent elastic scattering.

Neglecting the neutrino mass, the differential cross-section in the laboratory frame can be expressed as:

$$\frac{d\sigma}{dQ^2} = \frac{\left\langle |M|^2 \right\rangle}{64\pi m_N^2 E_\nu^2},$$

where $Q^2 = -q^2$ is the four-momentum carried by $Z^0$, $q = p_2 - p_1 = q_1 - q_2$, $\left\langle |M|^2 \right\rangle$ is the matrix element squared averaged over the initial and final spin particles (since the particle polarizations are generally not measured), and $E_\nu$ is the neutrino energy.

The only particle one would observe in the detector is the nucleon. One can express $Q^2$ through

the kinematics of the outgoing nucleon, assuming that the initial nucleon at rest, simply through

$$Q^2 = 2m_N T_N,$$

where $T_N$ is the kinetic energy of the outgoing nucleon. This does not depend on the scattering angle of the nucleon, which is quite convenient, because some experiments may not be able to measure it.

Following the Feynman rules of the electro-weak theory which have been developed in Chapter 2 one can write the matrix element squared [44]:

$$M = -\left(\frac{ig}{4\cos\theta_W}\right)^2 \bar{\nu}(q_2)\gamma^\mu(1-\gamma_5)\nu(q_1) i \frac{(g_{\mu\nu} - q_\mu q_\nu/M_Z^2)}{q^2 - M_Z^2} \langle N(p_2)|J_Z^\nu|N(p_1)\rangle$$

For the scattering with a low momentum transfered ($q^2 \ll M_Z^2$), one can replace the propagator

$$-i\frac{(g_{\mu\nu} - q_\mu q_\nu/M_Z^2)}{q^2 - M_Z^2} \qquad \rightarrow \qquad -i\frac{g_{\mu\nu}}{M_Z^2}.$$

Furthermore, using the definition of the Fermi constant,

$$G_F = \frac{\sqrt{2}g^2}{8M_W^2} = \frac{\sqrt{2}g^2}{8M_Z^2\cos^2\theta_W}$$

one obtains the expression for the matrix element

$$M = \frac{i}{2\sqrt{2}} G_F \underbrace{\bar{\nu}(q_2)\gamma_\mu(1-\gamma_5)\nu(q_1)}_{\text{leptonic current}} \underbrace{\langle N(p_2)|J_Z^\mu|N(p_1)\rangle}_{\text{hadronic current}}.$$

The expression for the leptonic current is simple: it has the vector and axial vector parts in the so-called $V-A$ structure. On the other hand, the hadronic current is a complex object due to strong interactions inside the nucleon. The most general form for the hadronic weak neutral current is

$$\langle N(p_2)|J_Z^\mu|N(p_1)\rangle = \langle N(p_2)|\underbrace{F_1^Z(Q^2) + F_2^Z(Q^2)\frac{i\sigma^{\mu\nu}q_\nu}{2M_N}}_{J_{Z,V}^\mu} + \underbrace{F_A^Z(Q^2)\gamma^\mu\gamma_5}_{-J_{Z,A}^\mu}|N(p_1)\rangle,$$

where $F_1^Z(Q^2)$, $F_2^Z(Q^2)$ and $F_A^Z(Q^2)$ are Dirac, Pauli, and axial vector nucleon weak neutral current form factors, respectively; $\langle N(p_2)|J_{Z,V}^\mu|N(p_1)\rangle$ and $\langle N(p_2)|J_{Z,A}^\mu|N(p_1)\rangle$ represent the vector and axial vector parts of the hadronic neutral current.

The neutrino-nucleon neutral current elastic differential cross-section can be written [64] as

$$\frac{d\sigma}{dQ^2} = \frac{G_F^2 Q^2}{2\pi E_\nu^2}\left(A(Q^2) \pm B(Q^2)W + C(Q^2)W^2\right) \tag{3.1}$$

where the "+" sign corresponds to neutrinos and the "–" sign to antineutrinos, $W = 4E_\nu/M_N - Q^2/M_N^2$, $A(Q^2)$, $B(Q^2)$ and $C(Q^2)$ are form factors:

$$\begin{aligned} A(Q^2) &= \frac{1}{4}\left[(F_A^Z)^2(1+\tau) - ((F_1^Z)^2 - \tau(F_2^Z)^2)(1-\tau) + 4\tau F_1^Z F_2^Z\right], \\ B(Q^2) &= -\frac{1}{4}F_A^Z(F_1^Z + F_2^Z), \\ C(Q^2) &= \frac{M_N^2}{16Q^2}\left[(F_A^Z)^2 + (F_1^Z)^2 + \tau(F_2^Z)^2\right], \end{aligned} \tag{3.2}$$

where $\tau = Q^2/4M_N^2$. Each of the form factors itself may be different for protons and neutrons, as we shall discuss in Section 3.3.

In a real experiment, however, one usually has to deal with bound nucleons as the detector medium largely consists of nuclei with high atomic number. In this case, additional nuclear effects have to be taken into account, such as Fermi motion of the nucleons and Pauli blocking, which will be described in Section 4.5.

## 3.3 Nucleon Form Factors

The general expression of the weak neutral current through the weak charged current and electromagnetic current:

$$J^Z = \frac{1}{2}\tau_3 J - 2\sin^2\theta_W J^{EM}, \tag{3.3}$$

where $\theta_W$ is the Weinberg angle, $\sin^2\theta_W = 0.2325$ and $\tau_3 = \mathrm{diag}(1,-1)$. Using Eq.(3.3) and generalizing the charge current to have the isoscalar part (indicated by the index $s$), one can write down the expressions for the nucleon weak neutral current form factors:

$$\begin{aligned} F_i^Z &= (F_i - F_i^s)\frac{\tau_3}{2} - 2\sin^2\theta_W F_i^{EM}, \qquad i = 1,2. \\ F_A^Z &= (F_A - F_A^s)\frac{\tau_3}{2} \end{aligned} \tag{3.4}$$

The vector part of the hadronic weak current is similar to that of the electromagnetic current:

$$\langle N|J^{\mu}_{EM}|N\rangle = \langle N|\gamma^{\mu}F_1^{EM} + \frac{i\sigma^{\mu\nu}q_{\nu}}{2M_N}F_2^{EM}|N\rangle,$$

which describes the coupling of hadrons to photons. Of course, the electromagnetic current is conserved. Thus, the weak vector current is assumed to be conserved in analogy to the electromagnetic vector current. This assumption is called the *conserved vector current* (CVC) hypothesis [44]. It leads to the relation between the weak charged current vector form factors and those of the electromagnetic current for protons and neutrons [65]:

$$F_i = F_i^{EM,p} - F_i^{EM,n}, \qquad i = 1, 2. \tag{3.5}$$

Now, putting Eq.(3.5) into (3.4) allows one to express $F_1^Z$ and $F_2^Z$ through the electromagnetic form factors for protons and neutrons:

$$\begin{aligned} F_i^Z &= \left(\frac{1}{2} - \sin^2\theta_W\right)\left[F_i^{EM,p} - F_i^{EM,n}\right]\tau_3 - \sin^2\theta_W\left[F_i^{EM,p} + F_i^{EM,n}\right] - \frac{1}{2}F_i^s \quad , i = 1, 2. \\ F_A^Z &= \frac{\tau_3}{2}F_A - \frac{1}{2}F_A^s. \end{aligned} \tag{3.6}$$

Thus, under CVC, $F_1^Z$ and $F_2^Z$ can be measured using charged lepton scattering. The two important combinations of the Dirac and Pauli electromagnetic form factors are the so-called Sachs form factors [66]:

$$\begin{aligned} G_E &= F_1^{EM} - \tau F_2^{EM}, \\ G_M &= F_1^{EM} + F_2^{EM}, \end{aligned} \tag{3.7}$$

which express the nucleon's electric and magnetic form factors. In scattering theory, the three-dimensional Fourier transform of $G_E(Q^2)$ provides the electric-charge-density distribution within the nucleon, while that of $G_M(Q^2)$ gives the current-density distribution [67]. Naturally, $G_E^p(0)$ and $G_E^n(0)$ represent the proton and neutron electric charges, respectively; $G_M^p(0)$ and $G_M^n(0)$ are the anomalous magnetic moments for proton and neutron, respectively. Therefore,

$$\begin{aligned} G_E^p(0) &= 1 \\ G_E^n(0) &= 0 \\ G_M^p(0) &= 2.793 \\ G_M^n(0) &= -1.91. \end{aligned} \tag{3.8}$$

As for the $Q^2$ dependence, the experimental results are roughly consistent for these form factors to have a dipole form:

$$\frac{G_E(Q^2)}{G_E(0)} = \frac{G_M(Q^2)}{G_M(0)} = \frac{1}{\left(1+\frac{Q^2}{M_V^2}\right)^2}, \tag{3.9}$$

with the vector mass $M_V = 0.843$ GeV [65] being the same for both electric and magnetic form factors.

From Eqs. (3.7) and (3.9) one can derive the expressions for the Dirac and Pauli electromagnetic form factors:

$$\begin{aligned} F_1^{EM}(Q^2) &= \frac{G_E(0)+\frac{Q^2}{4M^2}G_M(0)}{(1+\frac{Q^2}{4M^2})\left(1+\frac{Q^2}{M_V^2}\right)^2} \\ F_2^{EM}(Q^2) &= \frac{G_M(0)-G_E(0)}{(1+\frac{Q^2}{4M^2})\left(1+\frac{Q^2}{M_V^2}\right)^2} \end{aligned} \tag{3.10}$$

The axial isovector form factor can be measured via weak charged current. It is also assumed to have a dipole form:

$$F_A = \frac{F_A(0)}{\left(1+\frac{Q^2}{M_A^2}\right)^2}. \tag{3.11}$$

$F_A(0) = g_A = 1.2671$ is measured precisely from neutron beta decay. The axial vector mass $M_A$ is still somewhat a puzzle. Before MiniBooNE, a value $M_A = 1.026 \pm 0.021$ GeV was set largely by deuterium-based bubble chamber experiments [68]. However, MiniBooNE [69] (carbon target), K2K [70, 71] (carbon and oxygen targets), and recently MINOS [72] (iron target) have determined it to have $\sim 20-30\%$ larger values, using the CCQE channel. MiniBooNE has performed a simultaneous fit of two parameters in the CCQE data: $M_A$ and $\kappa$, where the latter controls the lower bound on the nucleon energy inside the nucleus. In Ref.[69] it was measured that $M_A = (1.23 \pm 0.2)$ GeV and $\kappa = 1.019 \pm 0.011$. A more recent analysis finds $M_A = (1.35 \pm 0.17)$ GeV and $\kappa = 1.007 \pm 0.009$, where a more careful analysis with a constraint of the CC single pion production background has been performed, as reported in Ref.[67].

The isoscalar form factors $F_1^s$ and $F_2^s$ are the contributions of strange quarks to the electric charge and to the magnetic moment of the nucleon, whereas $F_A^s$ is the strange quark contribution to the nucleon spin. The expressions for these form factors are unknown, but in analogy to the isovector form factors they are usually represented in the dipole form with the same vector masses

$M_V$ and $M_A$ as for the nonstrange form factors [73]:

$$\begin{aligned} F_1^s(Q^2) &= \frac{F_1^s(0)}{(1+\tau)\left(1+\frac{Q^2}{M_V^2}\right)^2} \\ F_2^s(Q^2) &= \frac{F_2^s(0)}{(1+\tau)\left(1+\frac{Q^2}{M_V^2}\right)^2} \\ F_A^s(Q^2) &= \frac{F_A^s(0)}{\left(1+\frac{Q^2}{M_A^2}\right)^2}, \end{aligned} \tag{3.12}$$

where $F_1^s(0) = -\frac{1}{6}\langle r_s^2\rangle$, $F_2^s(0) = \mu_s$ and $F_A^s(0) = \Delta s$. Note that $\langle r_s^2\rangle$ is the strange radius, $\mu_s$ is the strange magnetic moment of the nucleon, and $\Delta s$ is the strange quark contribution to the nucleon spin.

$F_1^s$ and $F_2^s$ can be extracted from parity violating electron scattering experiments. Recent results from the HAPPEX-II experiment [74] show that these electric and magnetic strange form factors are consistent with 0. Finally, $\Delta s$ can be extracted through the neutrino-nucleon neutral current elastic scattering, which we are going to discuss in Section 3.4.

## 3.4 Measurement of the Nucleon Structure with Neutral Current Elastic Scattering

### 3.4.1 The Proton Spin Crisis

The main motivation for measuring $\Delta s$ is the so-called "proton spin crisis", which as of now is one of the biggest unsolved problems in nuclear physics. In the naive parton model, a proton consists of three valence quarks: two up quarks and one down quark ($uud$). With the total proton spin of 1/2, the simplest expectation would be that two valence quarks carry a spin of $+1/2$ and the other one caries a spin of $-1/2$. One may also add quark-antiquark pairs inside the nucleus (or a quark sea) to the nucleon model. Adding up and down quark sea would not change the nucleon structure, but adding a strange quark sea would do that, because the strange quark is a singlet in the weak isospin rotation, whereas the up and down quarks form a doublet [51]. The contribution from other heavier quarks may be neglected.

The polarized spin-dependent structure function of the proton $g_1^p$ was measured by the European Muon Collaboration (EMC) using deep inelastic muon-proton scattering $\mu^- p \to \mu^- X$. The Feynman

diagram for this process is shown in Fig. 3.2. The polarization asymmetry in the cross-section is expressed as [75]:

$$x\frac{d\sigma^{\uparrow\downarrow}}{dxdy} - x\frac{d\sigma^{\uparrow\uparrow}}{dxdy} = \frac{Y_P}{2}\frac{16\pi^2\alpha^2}{s}g_1^p(x,Q^2) + \mathcal{O}\left(\frac{M^2x^2}{Q^2}\right),$$

where the cross-section indices $\uparrow\downarrow$ and $\uparrow\uparrow$ are for muons polarized antiparallel and parallel to the spin of the target proton, the omitted term include the second polarized structure function $G_2^p$, $x = Q^2/(2p_2 \cdot q)$ is the Bjorken variable and $Y_P = (2-y)/y$, $y = Q^2/(xs)$ is the fractional energy transfer in the target rest frame, $s$ is the square invariant mass of the $\mu^-$p system, and $M$ is the nucleon mass.

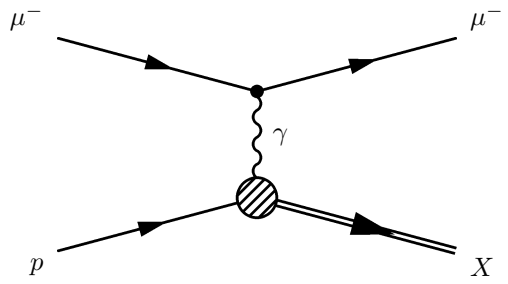


Figure 3.2: Feynman diagrams for deep inelastic scattering.

EMC measured $g_1^p(x)$ in the range $0.01 < x < 0.7$ and, with reasonable approximations, found the integral over $x$ to be [63]:

$$\int_0^1 g_1^p(x)dx = 0.126 \pm 0.010(stat) \pm 0.015(syst).$$

Before the EMC experiment was performed, Ellis and Jaffe derived the sum rule for $g_1^p(x)$ [76]:

$$\int_0^1 g^p(x)dx = 0.19,$$

which is clearly in contradiction with the EMC result.

In the simplest form of the parton model for large $Q^2$, the polarized proton structure function is given by

$$g_1^p(x) = \frac{1}{2}\sum_i e_i^2 \Delta q_i(x),$$

where $e_i$ is the charge of the quark $q_i$, $\Delta q_i(x) = q_i^+(x) + \bar{q}_i^+(x) - q_i^-(x) - \bar{q}_i^-(x)$ is the difference of the distributions of quarks and antiquarks with helicities parallel and antiparallel to the proton

spin. The quark contribution to the nucleon spin is defined as:

$$\Delta q_i = \int_0^1 q_i(x)dx, \qquad q_1 = u, q_2 = d, q_3 = s \ldots .$$

One can interpret the EMC result that quarks contribute to only a part of the total proton spin. After a more careful analysis of QCD corrections to $g_1(x)$ [77], recent results from the Hermes [78] and COMPASS [79] experiments yield:

$$\begin{aligned} Hermes &: \Sigma = 0.330 \pm 0.011(theory) \pm 0.025(exp) \pm 0.028(evol) \\ COMPASS &: \Sigma = 0.33 \pm 0.03(stat) \pm 0.05(syst) \end{aligned}$$

which represents the fraction of the proton spin carried by quarks and antiquarks,

$$\Sigma = \Delta u + \Delta d + \Delta s.$$

It is obviously very important to understand the spin structure of the proton and in particlular the strange quark contribution of that, because it is a very fundamental problem. On the other hand, a good understanding of the NCE scattering helps determining backgrounds for other measurements, such as dark matter searches. The sensitivity to measuring the weakly interacting massive particle (WIMP), which is a promising dark matter candidate, depends on the knowledge of the backgrounds. In this particular case, the NCE background represents a large component, which in turn depends highly on the $\Delta s$ value [80].

### 3.4.2 $\Delta s$ Measurement from Neutral Current Elastic Scattering

Neutrino-nucleon neutral current elastic scattering is a perfect tool for measuring $\Delta s$. It is the fundamental interaction of a proton with a simple object as neutrino, and it turns out that it is very sensitive to $\Delta s$.

Analyzing the expression for the NCE cross-section in Eq.(3.1), one can see that at low $Q^2$ the term $C(Q^2)$ dominates, and the cross-section is very sensitive to the axial form factor $F_A^Z$. In fact, to lowest order in $Q^2$,

$$\frac{d\sigma}{dQ^2} \sim \left[F_A^Z(0)\right]^2 + \left[F_1^Z(0)\right]^2 + \mathcal{O}\left(Q^2\right). \tag{3.13}$$

Recalling Eq.(3.6) and using $F_1^{EM,p}(0) = 1$, $F_1(0)^{EM,n} = 0$ and $F_1^s(0) = 0$ from Eqs. (3.10), (3.8) and (3.12),

one can rewrite the expression for $F_1^Z$ at $Q^2 = 0$:

$$\begin{aligned} F_1^{Z,p}(0) &= \frac{1}{2} - 2\sin^2\theta_W \\ F_1^{Z,n}(0) &= -\frac{1}{2}. \end{aligned} \tag{3.14}$$

Since $\sin^2\theta_W = 0.2325$, then $F_1^{Z,p}(0) \approx 0$. This leads to a higher NCE cross-section on neutron than that on proton.

Using Eqs. (3.6), (3.11) and (3.12) one can find the expression for the axial form factor at $Q^2 = 0$:

$$\begin{aligned} F_A^{Z,p} &= \frac{1}{2}g_A - \frac{1}{2}\Delta s \\ F_A^{Z,n} &= -\frac{1}{2}g_A - \frac{1}{2}\Delta s. \end{aligned} \tag{3.15}$$

Putting Eqs. (3.14) and (3.15) into (3.13) one finds the expression for the proton and neutron NCE cross-sections at low $Q^2$:

$$\begin{aligned} \frac{d\sigma_{\nu p}}{dQ^2} &\sim g_A^2 - 2g_A\Delta s + (\Delta s)^2 \\ \frac{d\sigma_{\nu n}}{dQ^2} &\sim 1 + g_A^2 + 2g_A\Delta s + (\Delta s)^2 . \end{aligned} \tag{3.16}$$

One can see that the negative $\Delta s$ makes the $\nu p$ cross-section higher and the $\nu n$ cross-section lower.

These features can be seen seen in Figs. 3.3 and 3.4. From Fig. 3.3 one can see that $F_A^Z(Q^2)$ dominates the low $Q^2$ region, especially for protons. From Fig. 3.4 one can see that indeed the cross-section for protons is higher than that for neutrons for $\Delta s = -0.5$, whereas it is lower for $\Delta s = 0.0$.

The best way to determine $\Delta s$ would be from the NCE proton to neutron ratio, namely

$$\frac{\sigma(\nu p \to \nu p)}{\sigma(\nu n \to \nu n)}$$

because with a negative value of $\Delta s$, the numerator increases while the denominator decreases, as can be seen in Fig. 3.5. Moreover, using the ratio helps removing the flux uncertainty, which is usually relatively large in neutrino experiments, as well as other systematic uncertainties. However, for some experiments it may be hard to distinguish protons from neutrons. One could also use a ratio of NCE proton to CCQE:

$$\frac{\sigma(\nu p \to \nu p)}{\sigma(\nu_l n \to l^- p)}$$

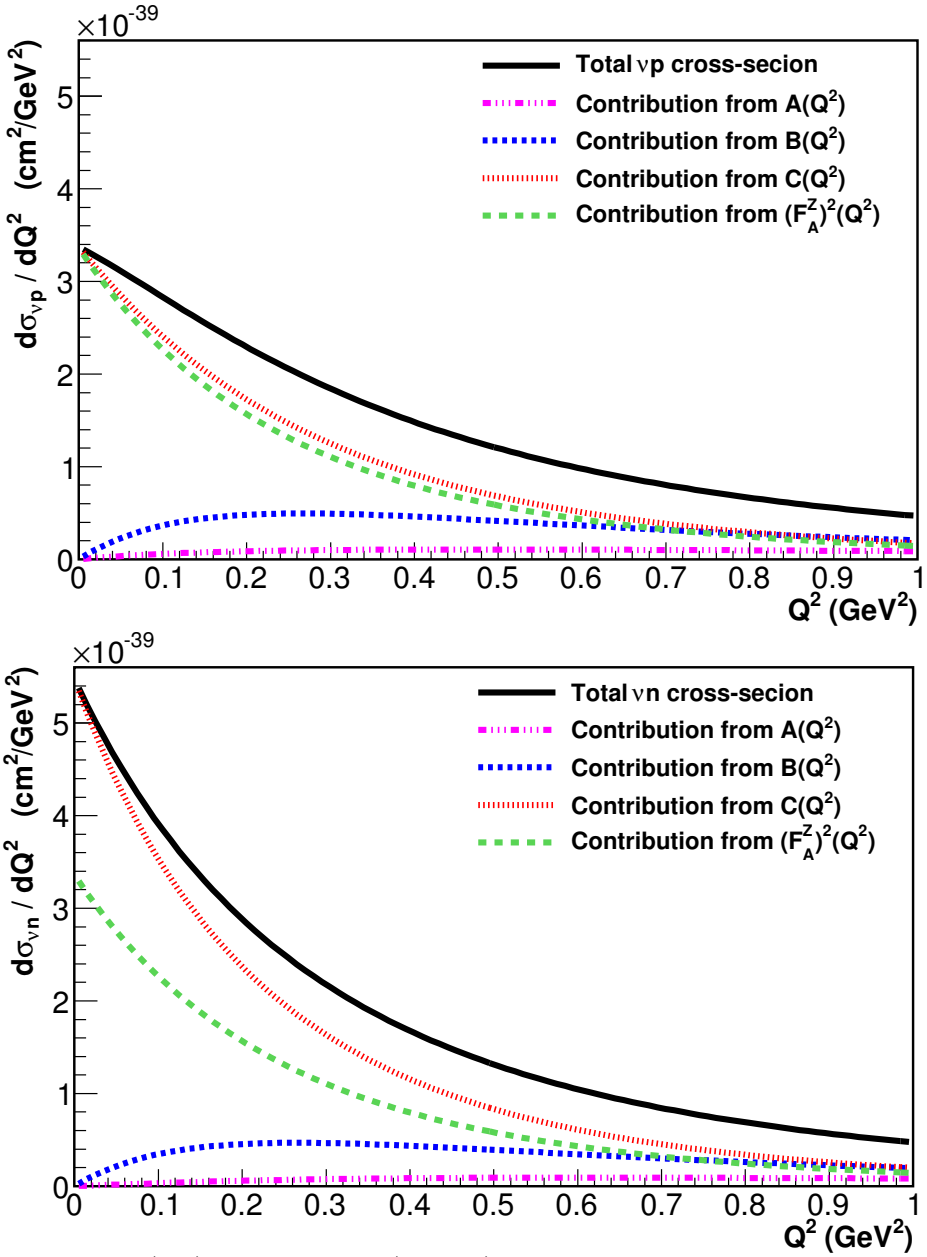


Figure 3.3: $\nu p \to \nu p$ (top) and $\nu n \to \nu n$ (bottom) differential cross-section for $E_\nu = 1$ GeV and $\Delta s = 0$. The contributions from $A(Q^2)$, $B(Q^2)$, $C(Q^2)$, defined in Eq.(3.2), and also from $(F_A^Z(Q^2))^2$ (part of $C(Q^2)$) are also shown.

In this case, the numerator is still sensitive to $\Delta s$ while the denominator is not, but once again this ratio eliminates a lot of systematic errors. In other words this measurement tells us how much muonless proton events we would see versus protons with a muon. One of the experiments proposed to use this ratio for a $\Delta s$ measurement is FINeSSE [81].

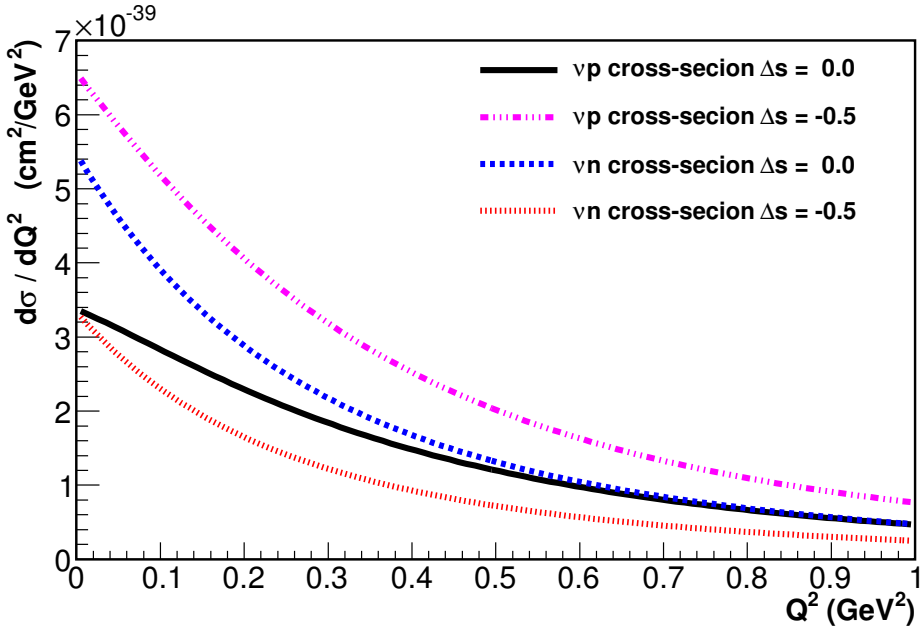


Figure 3.4: $\nu p \to \nu p$ and $\nu n \to \nu n$ for $E_\nu = 1$ GeV and different $\Delta s$ values.

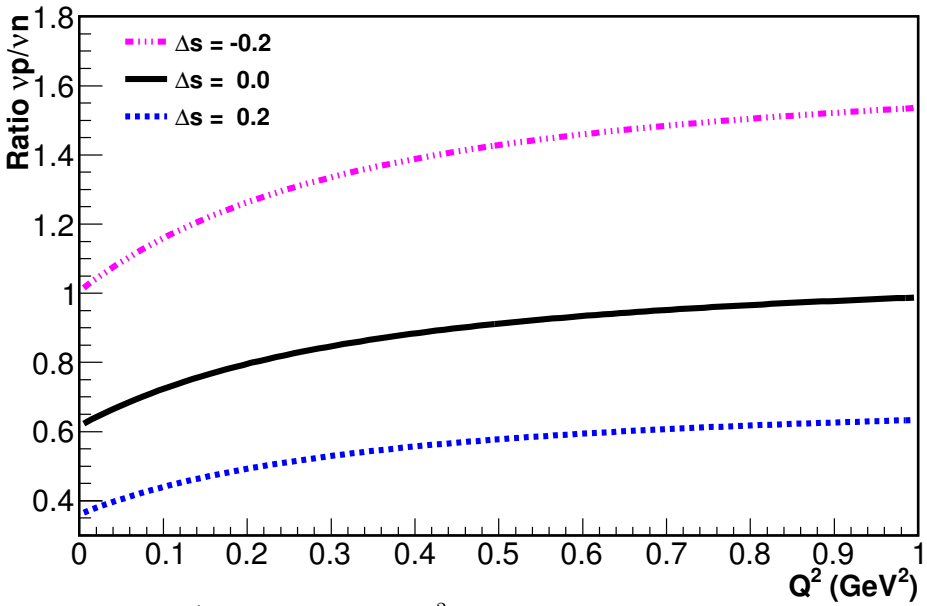


Figure 3.5: Ratio $p/n$ as a function of $Q^2$ for $E_\nu = 1$ GeV and two different $\Delta s$ values.

### 3.4.3 $\Delta s$ Measurement from the BNL E734 Experiment

Currently the best measurement for $\Delta s$ from neutrino NCE interactions comes from the BNL E734 experiment, which ran at Brookhaven in 1986. The measured the $\nu p \to \nu p$ and $\bar{\nu} p \to \bar{\nu} p$ flux-averaged differential cross-sections as a function of $Q^2$, which were used to obtain the allowed

regions of the $M_A$ and $\Delta s$ parameters [62].

BNL E734 used a 170 ton high-resolution target detector, which consisted of 112 modules, each of which contained a plane of 16 liquid-scintillator cells (4 m $\times$ 25 cm $\times$ 8 cm) and two crossed planes of drift tubes. There were also a shower counter (for longitudinal containment of electron and photon showers) and a muon spectrometer. The horn-focused neutrino beam was produced by a 28 GeV proton beam incident on a copper target, producing secondary mesons, yielding a beam of primarily $\nu_\mu$ (positive horn focus) and $\bar{\nu}_\mu$ (negative horn focus) with mean energies of 1.3 GeV and 1.2 GeV, respectively. The $\nu_\mu$ flux is shown in Fig. 3.6. Using the muon spectrometer was one of the advantages, because they could define the charge of the muon and this way measure the wrong-sign contamination (i.e., the presence of antineutrinos in the neutrino mode and vice versa), which are especially important for the antineutrino mode.

After all selection cuts, they obtained a total of 1,686 $\nu p$ candidates with a signal fraction of 56.4% (purity) and 1,821 $\bar{\nu} p$ candidates with a 42.6% purity. The measured NCE flux-averaged differential cross-sections are shown in Fig. 3.7. Using the cross-section data, the allowed region for $\eta$ and $M_A$ was obtained as shown in Fig. 3.8, where $\eta$ is a parameter is directly related to $\Delta s$, namely $\eta = -\Delta s / g_A$.

However, one should mention that the BNL E734 neutrino flux prediction was based on their CCQE measurement. In other words, using a *"known"* CCQE cross-section (with some errors) and by measuring the rate of CCQE events, the neutrino flux was calculated. In general, this could be a dangerous operation because it leads to a bias from the cross-section prediction. For example, BNL E734 used $M_A = 1.02$ GeV for the CCQE cross-section, which is consistent with value that they extracted from the NCE cross-section measurement. However, had they used another value for $M_A$ (such as $M_A = 1.35$ GeV, as discussed in Section 3.3), this would have led to a different neutrino flux and thus to possibly a different $M_A$ result from the NCE data, in fact probably close to the one in the CCQE input model. To eliminate this bias, current cross-section experiments use a full beam MC simulation with the meson production in the target measured independently in order to predict the neutrino flux at the detector.

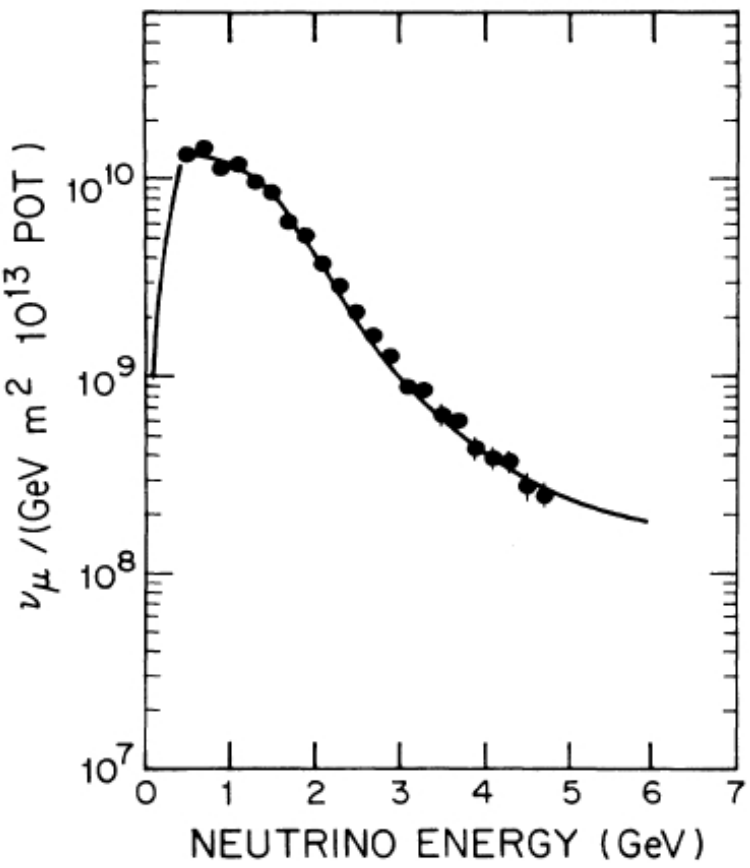


Figure 3.6: The BNL E734 $\nu_\mu$ flux as measured by CCQE interactions.

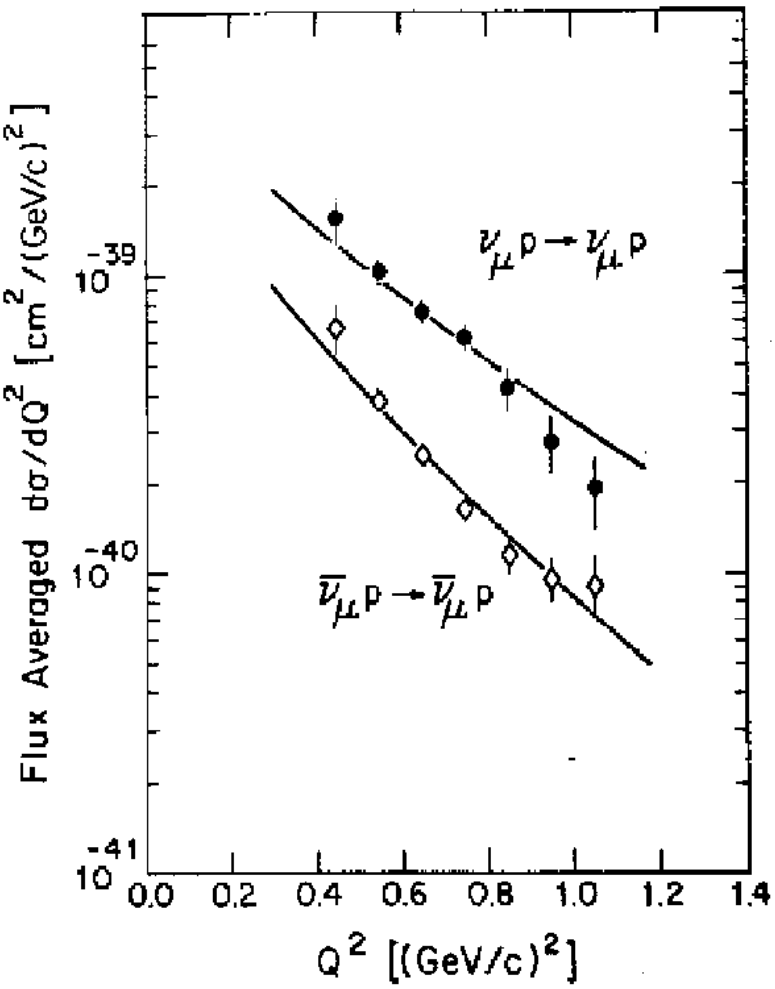


Figure 3.7: BNL E734 neutral current elastic flux-averaged differential cross-sections as a function of $Q^2$ for both neutrinos and antineutrinos, as labeled.

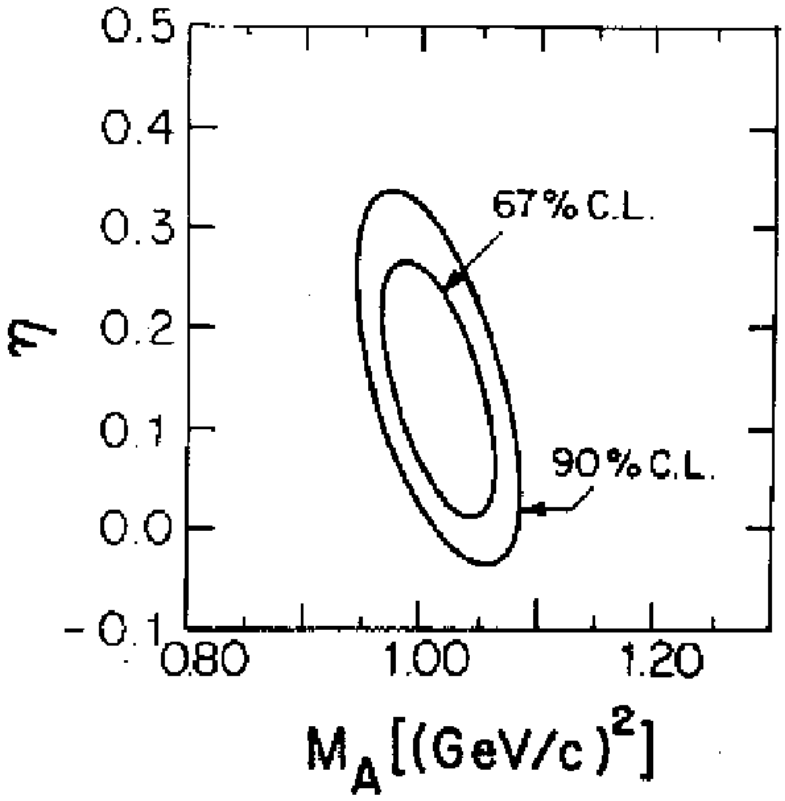


Figure 3.8: $M_A$ and $\eta = -\Delta s/g_A$ allowed regions from the $\chi^2$ fit of the MC prediction to the $\nu p$ and $\bar{\nu}p$ elastic cross-section data .

# Chapter 4

# The MiniBooNE Experiment

## 4.1 Overview

The Mini Booster Neutrino Experiment (MiniBooNE) at the Fermi National Accelerator Laboratory was motivated by the results of the Liquid Scintillator Neutrino Detector experiment (LSND) [82], which observed evidence for $\bar{\nu}_\mu \rightarrow \bar{\nu}_e$ oscillations with a $\Delta m^2$ in the range from 0.2 eV$^2$ to 10 eV$^2$ and a probability of $(2.6 \pm 1.0 \pm 0.5) \times 10^{-3}$. LSND used a 800 MeV proton beam incident on a water target, which produced a beam of $\bar{\nu}_\mu$ from $\mu^+$ decay at rest with a maximum energy of 52.8 MeV. MiniBooNE was designed to operate at neutrino energies $\sim 10$ times higher than LSND, with a different baseline ($L = 450$ m), but with $L/E$ about the same as LSND in order to have a convincing neutrino oscillation pattern at different neutrino energies. By construction, MiniBooNE has an option to run in both neutrino and antineutrino modes. The neutrino mode was chosen to be the main result due to higher statistics.

In April 2007 MiniBooNE presented the first neutrino oscillation results [83], where no two-neutrino oscillation evidence was found, as the data was consistent with background. Also, recently MiniBooNE reported the oscillation results running in the antineutrino mode, where also no two-neutrino oscillation evidence was found [84].

Operating with a high intensity neutrino beam of $\sim$ 800 MeV MiniBooNE can also address neutrino cross-section measurements. This thesis focuses on the neutrino-nucleon neutral current elastic scattering in MiniBooNE, and an analysis of this channel with the extraction of the axial vector mass ($M_A$) and the strange quark contribution to the nucleon spin ($\Delta s$).

## 4.2 Neutrino Beam and the Neutrino Flux at the MiniBooNE Detector

The Booster Neutrino Beamline (BNB) creates an almost pure and intense beam of $\nu_\mu$ ($\bar{\nu}_\mu$) with an average energy of $\sim$ 800 MeV. It is used by the MiniBooNE detector as a neutrino source for studying neutrino oscillations and interactions. The map of the MiniBooNE site at Fermilab is shown in Fig. 4.1. MiniBooNE uses protons coming from Fermilab Booster. The particle beam can be separated into three parts:

- primary proton beam,
- secondary meson beam,
- tertiary neutrino beam.

The primary protons from the Booster hit a beryllium target, producing a secondary beam of mesons, such as pions and kaons. These mesons go through a magnetic horn, which focuses particles with the same charge sign and defocuses particles with the opposite charge sign.

Mesons decay in flight in the *decay region*, producing a tertiary beam of leptons – neutrinos, muons and electrons. Charged leptons are then absorbed at the end of the decay region in the *absorber*, leaving only a beam of neutrinos.

Further downstream is the MiniBooNE detector, which registers neutrino interactions with its target medium, as shown in Fig. 4.2.

In this section we provide a brief summary of the BNB and the neutrino flux at the MiniBooNE detector prediction. The details can be found in Ref.[85].

### 4.2.1 Proton Beam

Protons with an energy of 8.89 GeV are extracted from the Fermilab Booster in 1.6 $\mu$s pulses with $\sim 4 \times 10^{12}$ protons in each beam pulse. The MiniBooNE data acquisition (DAQ) is synchronized with the Fermilab accelerator network timing signals. When the Booster extraction synchronization signal is true, the MiniBooNE beam trigger is also set to true. The DAQ starts recording data (or opens the time window) about 4.5 $\mu$s before it arrives at the detector. The DAQ beam time window is closed after 19.2 $\mu$s, when the beam trigger is set to false. This beam *macrostructure* in the DAQ window is shown on Fig. 4.3(a). The pulse rate is typically 4-5 Hz. One should mention that the

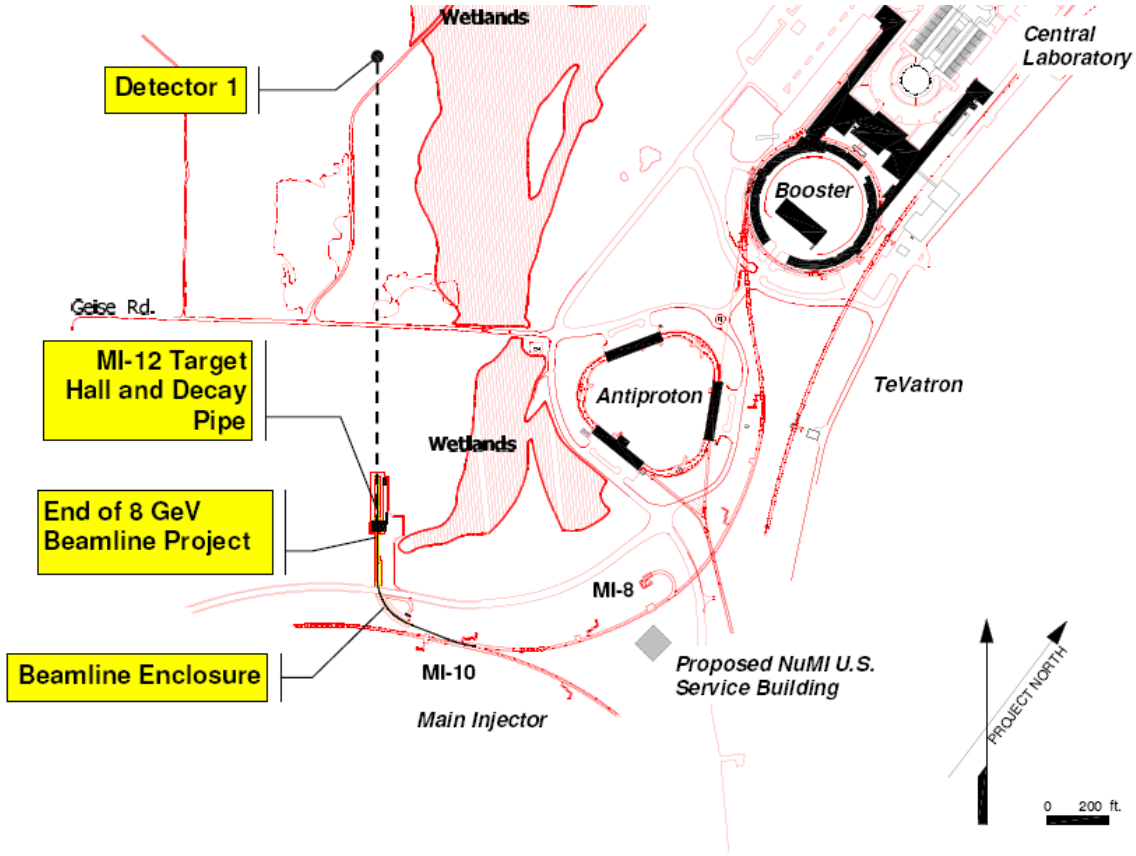


Figure 4.1: The Booster Neutrino Beamline.

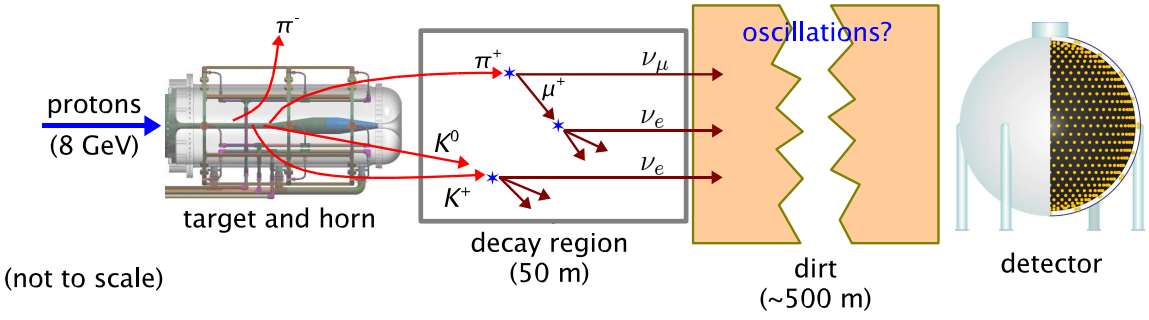


Figure 4.2: The MiniBooNE experimental setup.

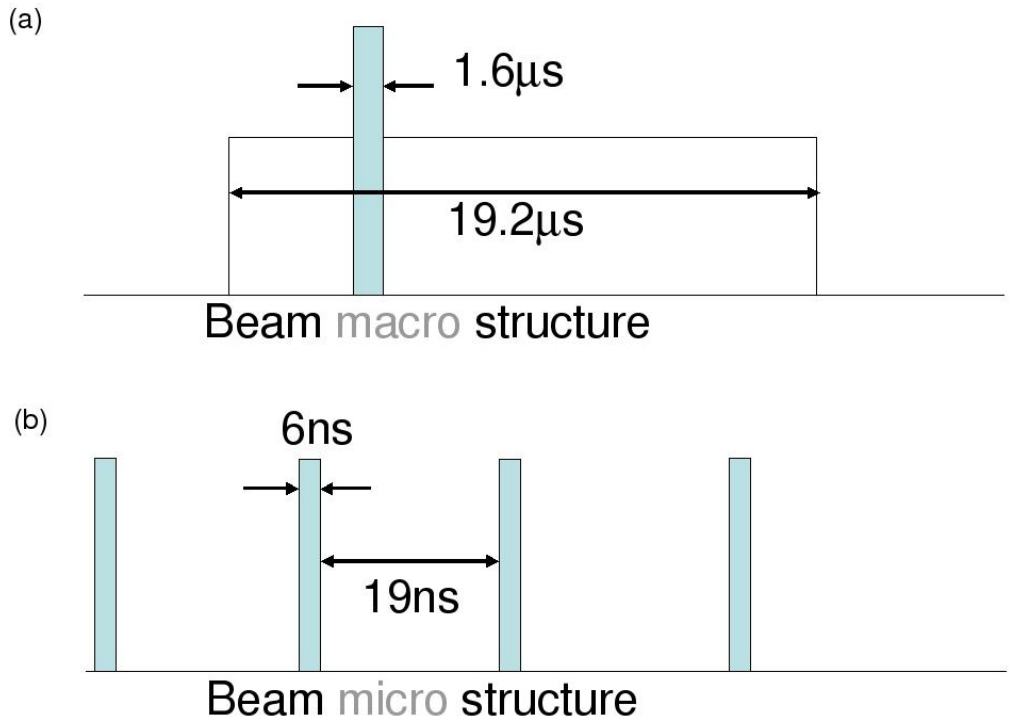


Figure 4.3: The proton beam pulse macro and micro structure.

beam pulse also has a *microstructure* of 81 bunches, shown in Fig. 4.3(b). Each bunch has a length of 6 ns and is spaced at 19 ns from the next one.

### 4.2.2 Secondary Meson Beam

Protons are incident on a target [86], which is comprised of 7 cylindrical beryllium slugs to produce a cylinder of 71.1 cm in length and 0.51 cm in radius. It provides 1.9 inelastic interaction lengths for the incoming protons.

Interacting with the Be target, protons produce a secondary beam of mesons and hadrons. This secondary beam goes through a magnetic horn. The horn is a toroidal electromagnet made of an aluminium alloy. It is designed to run at the frequency not more than 5 Hz. The electric current in the horn is $\sim$ 174 kA producing a magnetic field of about 1 T. Depending on the direction of the current, the horn focuses particles of one charge sign and defocuses particles with the opposite charge sign. In the process, it increases the value of the neutrino flux at the detector by a factor of about 6.

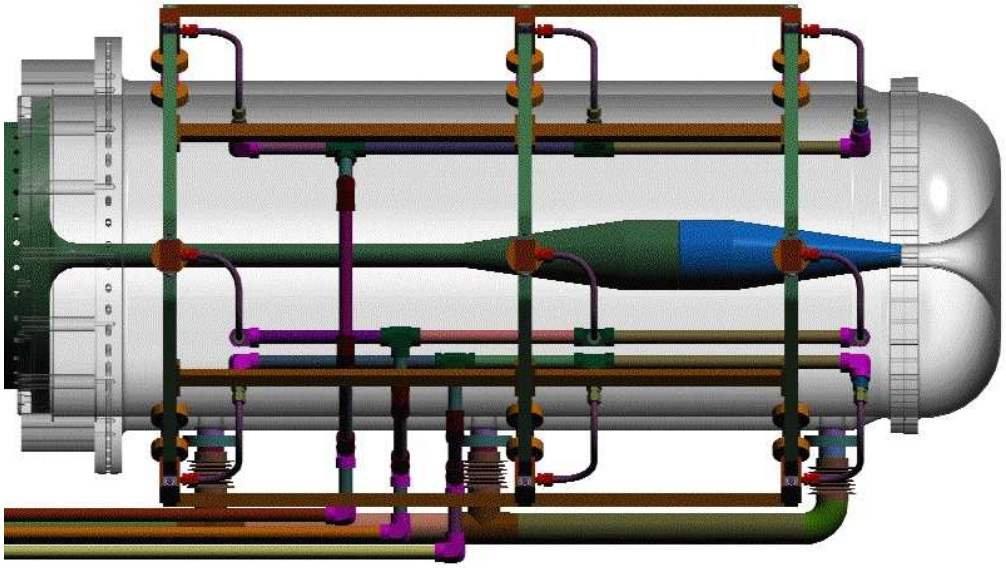

Figure 4.4: The MiniBooNE pulsed horn system. The outer conductor (gray) is transparent to show the inner conductor components running along the center (dark green and blue). The target assembly is inserted into the inner conductor from the left side. The plumbing associated with the water cooling system is also shown.

Particles produced by the p-Be interactions pass through a collimator with a radius of 30 cm, located downstream of the horn. This is to remove particles that are scattered with a large angle and would have otherwise missed the decay pipe, and to minimize the radiation elsewhere in the beamline.

### 4.2.3 Tertiary Neutrino Beam

After passing the horn, the secondary hadrons and mesons enter the *decay pipe*. It is an air-filled cylindrical decay region, which follows the collimator. The decay pipe is 3 feet in radius and extends to make the total length of the decay region of 49.87 meters, including the collimator region. At the end of the pipe, there is a beam stop which is made of steel and concrete. The beam stop is to absorb all remaining particles, except for the neutrinos.

In the decay region the neutrino beam is created. Neutrinos are created by several channels. Mesons ($\pi^{\pm}$, $K^{\pm}$ and $K^0$) decay relatively quickly ($\sim$ 10 ns) producing neutrinos and charged leptons. Muon decays into an electron and two neutrinos can also occur in the decay pipe. The branching fractions of decays of positively charged particles are shown in Table 4.1.

| Particle | Lifetime (ns) | Decay mode | Branching ratio (%) |
|---|---|---|---|
| $\pi^+$ | 26.03 | $\mu^+ + \nu_\mu$ | 99.9877 |
| | | $e^+ + \nu_e$ | 0.0123 |
| $K^+$ | 12.385 | $\mu^+ + \nu_\mu$ | 63.44 |
| | | $\pi^0 + e^+ + \nu_e$ | 4.98 |
| | | $\pi^0 + \mu^+ + \nu_\mu$ | 3.32 |
| $K^0_L$ | 51.6 | $\pi^- + e^+ + \nu_e$ | 20.333 |
| | | $\pi^+ + e^- + \overline{\nu}_e$ | 20.197 |
| | | $\pi^- + \mu^+ + \nu_\mu$ | 13.551 |
| | | $\pi^+ + \mu^- + \overline{\nu}_\mu$ | 13.469 |
| $\mu^+$ | 2197.03 | $e^+ + \nu_e + \overline{\nu}_\mu$ | 100.0 |

Table 4.1: Particle lifetimes and neutrino-producing decay modes with their branching ratios considered in the simulation.

### 4.2.4 Neutrino Flux at the Detector and Systematic Errors

The neutrino flux at the detector is calculated via a Geant4 [87] Monte Carlo (MC) beam simulation. The simulation includes a full beam geometry, specified by shape, location and material composition of the BNB components. The MC generates protons upstream of the target and propagates them through the target. In the target, p-Be interactions are simulated, creating particles of 7 types ($\pi^\pm$, $K^\pm$, $K^0$, p, n). The pion production cross-section used in the MC is based on measurements from the HARP [88] and E910 [89] experiments. For $K^+$ production, a fit to the results of several experiments are used [90, 91, 92, 93, 94] with a parametrization to extrapolate the incident proton energy to 8.89 GeV. The errors associated with the meson production are either estimated from the fit to the production data (kaons) or taken from the experiment (pions). Pions (which are responsible for the neutrinos dominating the total neutrino flux at the detector) have a production error of $\sim 5\%$.

Then the secondary particles are propagated through the rest of the BNB with a simulation of their subsequent decays with the proper branching ratios, giving the appropriate kinematics for the decay particles. Then, the decay particles are also propagated further. Whenever a neutrino is produced in the process, it is checked whether its track would go through the MiniBooNE detector. The histogram of neutrinos (antineutrinos) and their types for those that do go through the detector is filled. This simulation produces the neutrino flux, which is shown in Fig. 4.5 for the neutrino mode. The neutrino flux histograms are available in Ref.[95]. About 97% of the $\nu_\mu$ flux is from the $\pi^+$ decay and $\sim 3\%$ from $K^+$ decay.

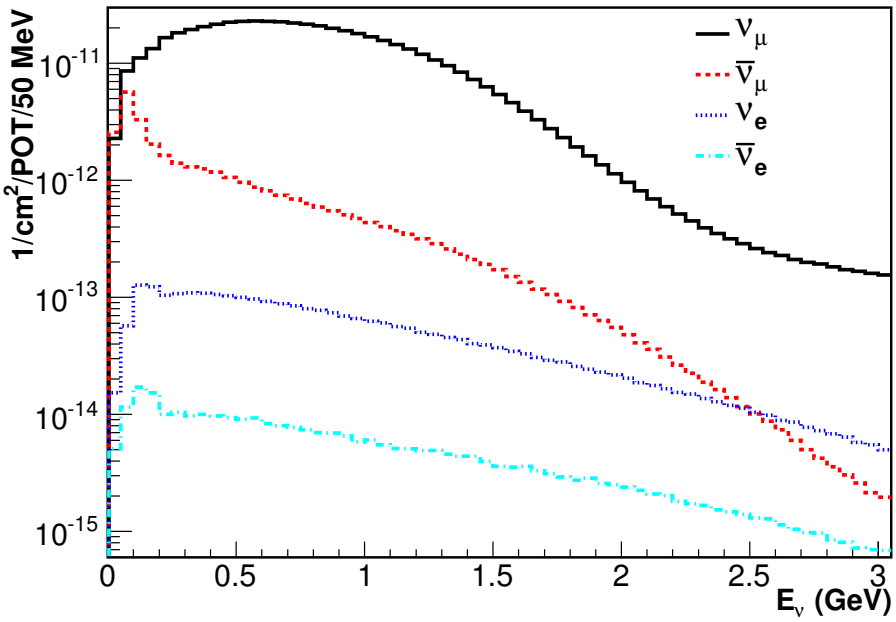


Figure 4.5: Neutrino flux at the MiniBooNE detector for different types of neutrino as a function of their energy in the neutrino mode.

There are additional systematic errors in the neutrino flux associated with uncertainties in the horn current, skin-effect, and the number of protons on target (POT). The latter ($\sim 2\%$) is relevant to the absolute neutrino cross-section measurements, but is cancelled in the neutrino cross-section ratio measurements.

## 4.3 The MiniBooNE Detector

### 4.3.1 Overview

In this section the MiniBooNE detector is described. The details can be found elsewhere [96]. The MiniBooNE detector is situated 541 m from the Be target and under 3 m of overburden to remove some of the cosmic muons activity. The schematic of the detector is shown in Fig. 4.6. It is a 12.2 m diameter spherical tank made of carbon steel, filled with mineral oil. The tank is divided into two optically isolated regions by a spherical shell of radius 5.75 m. The two regions, however, still share the oil circulation. A total of 1520 8-inch photomultiplier tubes (PMTs) are instrumented in the detector. There are 1280 PMTs attached to the spherical barrier from the inside in the *signal region*, facing toward the center of the tank, and distributed approximately uniformly. There are also 240

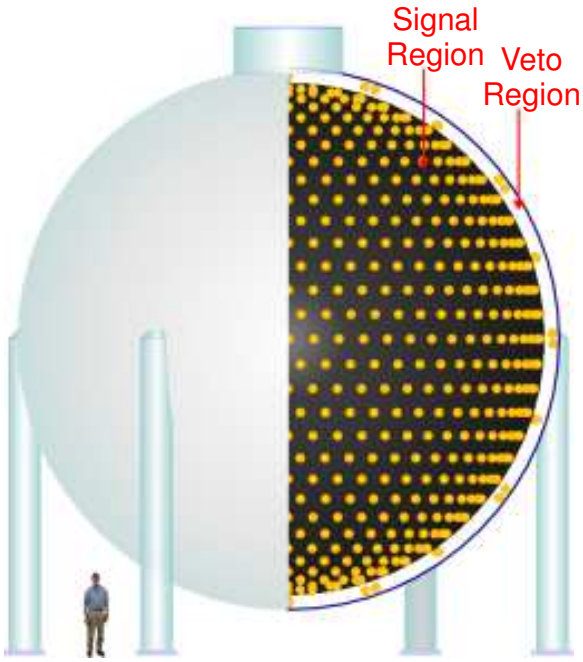


Figure 4.6: The MiniBooNE detector schematic.

PMTs in the *veto region*, which are used for external backgrounds detection. The veto PMTs are mounted back-to-back, facing perpendicular to the line from the tank center to the PMT in order to have as much veto view as possible. The scheme of the PMT arrangement in the detector is shown in Fig. 4.7.

The detector geometry is defined as follows: the $(0, 0, 0)$ point is at the center of the detector, the $Z$ axis is horizontal, in the direction of the beam, the $Y$ axis is vertical pointing up, and the $X$ axis is in the direction to satisfy the right-hand rule for $XYZ$ axes.

### 4.3.2 Photomultiplier Tubes

Of the total 1520 PMTs in the detector, 1198 are Hamamatsu R1408, shown in Fig. 4.8, taken from the LSND experiment, therefore referred to as *old PMTs*. The rest 322 PMTs are Hamamatsu R5912, purchased specifically for MiniBooNE, referred to as *new PMTs*. All new PMTs are used in the signal region. The new PMTs have a time resolution of $\sim 1.1$ ns and a single photo-electron charge resolution (1-PE) of 50%, whereas the old PMTs have a time resolution of $\sim 1.7$ ns and a 1-PE charge resolution of 140%.

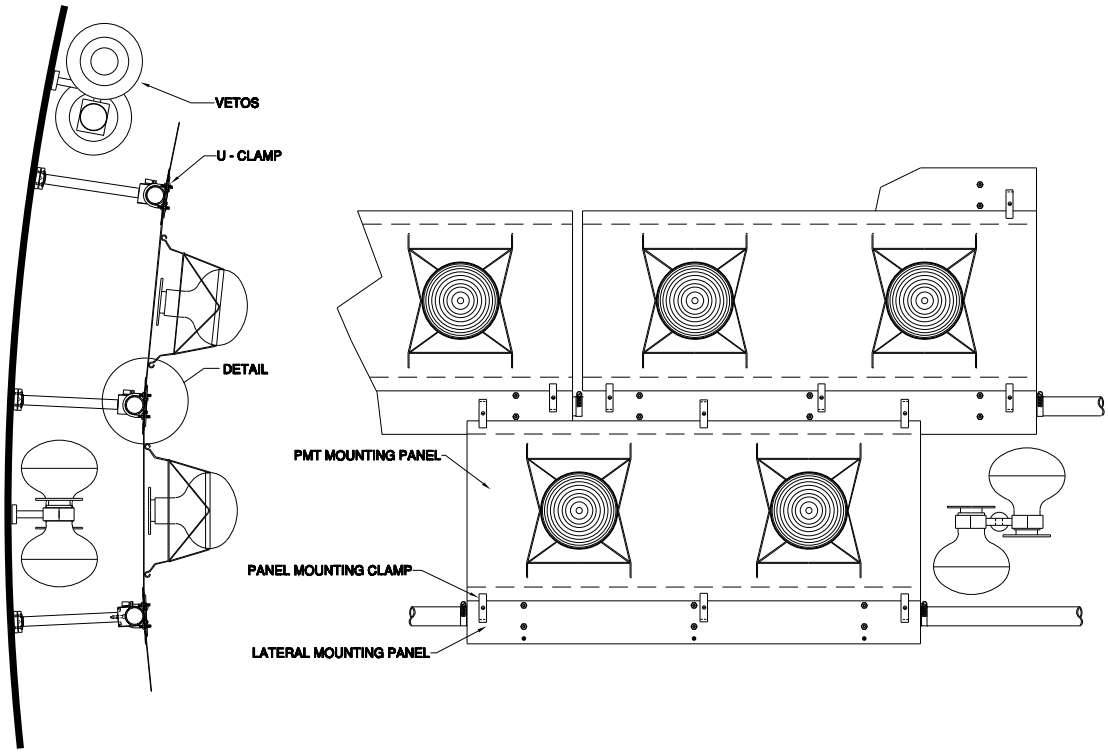


Figure 4.7: PMT configuration for both signal and veto regions. The signal regions PMTs are placed facing the tank center, whereas the veto PMTs are facing perpendicular to the line from the center of the tank.

Various tests of the PMTs have been performed. Each PMT was tested to determine its functionality by looking at their time and charge resolution, dark rate and operating voltage. Also, the angular acceptance for both new and old PMTs has been measured at Fermilab in a dark room in air. This is needed for the appropriate MC simulation and reconstruction. The tests and the PMT design are described in detail in Ref.[97]. The plot of the angular acceptance for the MiniBooNE PMTs is shown in Fig. 4.9. Since the PMT geometry is the same for both types of PMTs, all PMTs have approximately the same angular acceptance.

### 4.3.3 Mineral Oil

The MiniBooNE detector is filled with Marcol 7 mineral oil. The oil serves both as a target for the neutrino beam and as the light producing medium. It has an index of refraction of about 1.468, which is higher that that of water (1.33), providing a higher Cherenkov light fraction for charged

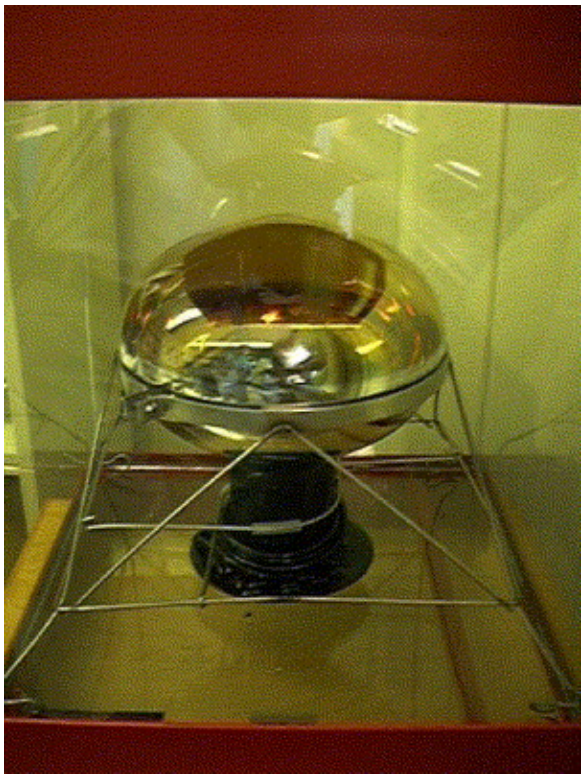

Figure 4.8: A typical phototube used in the MiniBooNE detector: an 8 inch Hamamatsu R1408 mounted on its wire frame.

particles and a lower Cherenkov threshold. More precisely, the index of refraction depends on the photon's wavelength ($\lambda$) and medium's temperature ($T$), as measured by H. Meyer using an Abbe refractometer [98]:

$$n(\lambda, T) = \left[ n_D + B \left( \frac{1}{\lambda^2 - \lambda_D^2} \right) \right] (1 - \beta(T - T_0)) \,,$$

where $n_D = 1.4684 \pm 0.0002$, $B = 4240 \pm 157$ nm$^2$, $\lambda_D = 589.3$ nm, $\beta = (3.66 \pm 0.04) \times 10^{-4}$ $^oC$, and $T_0 = 20$ $^oC$.

A lower Cherenkov threshold for heavy particles like protons allows to measure their direction and provides information for particle identification. The oil density is $0.845 \pm 0.001$ g/cm$^3$ and the extinction length $\sim 18$ m. The oil is kept in a nitrogen environment to get rid of oxygen, which can cause metal corrosion and other problems (like affecting the attenuation length of the medium).

Four different fluorophores (or fluors) were detected in detailed studies of the time fluorescence of the Marcol 7 mineral oil [99]. The light production and other properties of the mineral oil are described in more detail in Section 4.6.

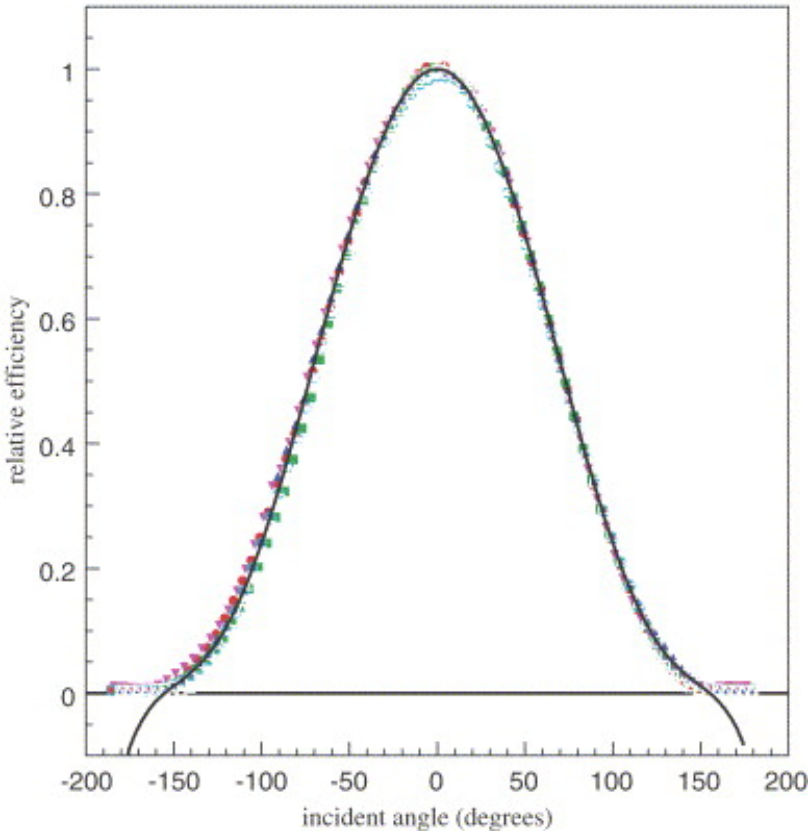


Figure 4.9: The relative PMT efficiency (angular acceptance) as a function of the incident photon angle for both new and old PMTs. The incident angle is the angle between the incident photon direction and the normal to the PMT. An even polynomial fit for both types is shown.

### 4.3.4 Data Acquisition System

The MiniBooNE electronics and data acquisition system (DAQ) digitize the analog signal from the PMTs, including time and charge, store this information for a substantial period of time and process it when one of the physics triggers (explained below) is set to true.

Both time and charge signals from each PMT are digitized by a 8-bit analog-to-digital converter (ADC), operating at 10 MHz (100 ns). Thus, we define 100 ns as a *clock tick*. A cartoon of a PMT readout is shown in Fig. 4.10. $V_{pmt}$ is the analog signal pulse from a PMT, which is integrated by an integrating capacitor with an output $V_q$. $V_q$ bleeds off with a time constant $\tau \approx 1.2$ $\mu$s. If $V_q > 0.2$ mV (a discriminator threshold, corresponding to $\sim 0.1$ PE), shown by a brown line in the figure, a separate voltage $V_t$ starts increasing linearly. This defines a PMT hit. It also generates a two time ticks holdoff, after which $V_t$ is reset to 0. This information is stored in a buffer within a 20.8 $\mu$s time interval, enough to cover the DAQ window. For each PMT hit four consecutive values

of $V_q$ and $V_t$ (each of them therefore called a *quad*) are stored in a buffer with the first quad taken before the discriminator was fired (in this case at the $t-1$ tick). These quads are later used to calculate the time of the PMT hit and the charge if the event is read out. The details on the time and charge calculation using this information are given in Ref.[100]. There might be several quads for the same PMT in the same DAQ window.

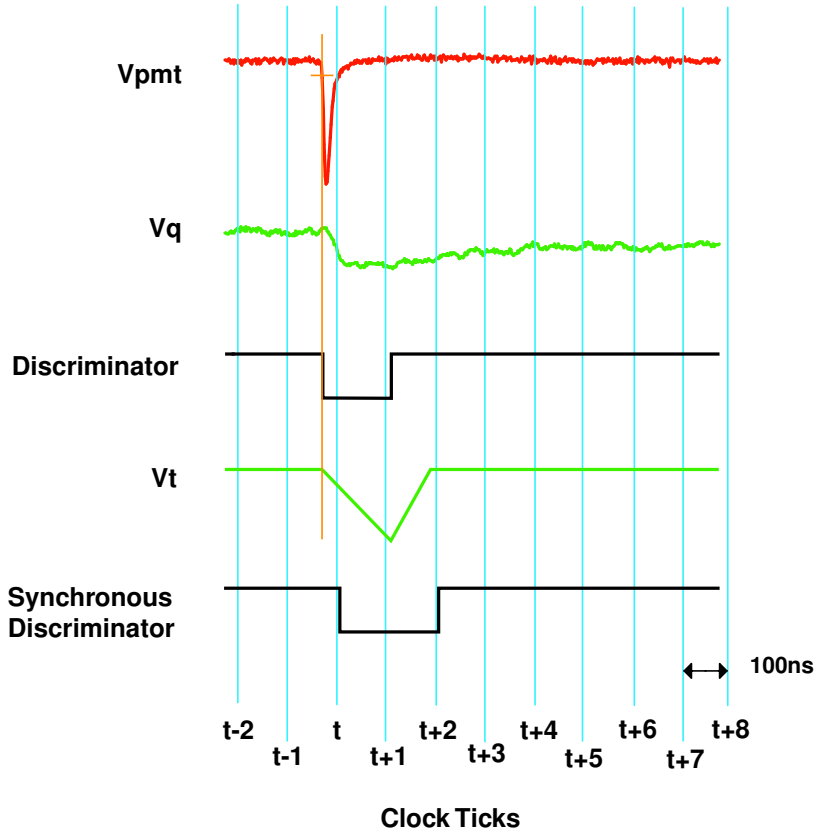


Figure 4.10: A cartoon of MiniBooNE electronic signals from a PMT.

### 4.3.5 Trigger System

The MiniBooNE trigger system uses both external information from the Fermilab ACNET system and the calibration system, as well as internal PMT hit multiplicity. There are 3 *external* triggers and 7 PMT hit *comparators* that are used for the *physics* triggers definition. If one of the physics triggers is true, the event is read out.

The following external trigger inputs are used:

| Comparator number | PMT Hits | Purpose |
|---|---|---|
| C1 | Tank hits≥10 | Activity Monitor |
| C2 | Tank hits≥24 | Michel electron |
| C3 | Tank hits≥200 | High-Energy Neutrino |
| C4 | Tank hits≥100 | Neutrino candidate |
| C5 | Tank hits≥60 | Supernova $\nu$ candidate |
| C6 | Veto hits≥6 | Cosmic Veto |
| C7 | Veto hits≥4 | Cosmic Activity |

Table 4.2: The MiniBooNE comparator settings. Tank hits represents the number of PMT hits in the signal region.

- *Beam trigger (E1)*: beam to MiniBooNE. Physically, this trigger is set to true when two Booster signals in ACNET are received: "1D" (ready for beam to MiniBooNE) and "1F" (beam extraction).

- *Strobe, NuMI, debuncher trigger (E2)*: this trigger is shared by the strobe, NuMI, and debuncher triggers. The strobe trigger sets E2 to true by a pulse generator with a frequency of 2.01 Hz. Its purpose is to study beam unrelated backgrounds. The debuncher trigger is set when the proton beam is to be delivered to the anti-proton source target. The NuMI trigger is set when the beam is delivered to the NuMI beamline (Neutrinos from the Main Injector). This trigger is to identify and study neutrino interactions from the NuMI beamline, which is an off-axis beamline for MiniBooNE (with an angle of $\sim 6.3^o$) [101]. The 3 types of $E2$ trigger differ by the time width of the trigger pulse, in order to identify which one is used.

- *Calibration trigger (E3)*: different time widths of the $E3$ trigger identify a type of the calibration event: laser, cube or tracker.

The comparators are signals that use PMT multiplicity information from either the signal or the veto regions. These signals are used as an input by the physics triggers. The MiniBooNE comparator settings are shown in Table 4.2.

The main physics trigger for the MiniBooNE data analysis is called the *Beam* trigger, which requires the external $E1$ trigger to be true and no conditions on the comparators is needed. The *strobe* trigger requires $E2$ to be in the strobe mode and also no C1–C7 conditions are used. The *NuMI* trigger is the same as the previous two, but requires $E2$ to be in the NuMI mode. Other physics triggers, such as *Supernova*, *Michel* (Michel electron), *BigNu* (energetic neutrino event candidate, which occurs outside of beam or laser windows), etc., may include comparators (details are in Ref.[96]). When the physics trigger conditions are met, all quads for each PMT in the DAQ window

are written to the DAQ computer disk-drive.

## 4.4 Detector Calibration

There are two types of calibrations used in MiniBooNE. The first one is using the calibration systems implemented in the detector, which includes a laser calibration system and cosmic muon calibration system. The second type is to reconstruct certain known physical quantities or distributions, such as the $\pi^0$ mass or the Michel electron energy distribution.

### 4.4.1 The Laser Calibration System

The MiniBooNE laser calibration system schematics is shown in Fig. 4.11. The light initiated via a pulsed diode laser is sent through optical fibers to four dispersing flasks, installed at different positions inside the detector. An additional fiber from the laser doesn't have a flask on its end. It emits light directly to the medium in a cone of $\sim 10^\circ$, illuminating PMTs in a small circle near the bottom of the detector to study light scattering in the detector. The list of flasks and the bare fiber positions in the detector are shown in Table 4.3. A dispersion flask is a 4-inch sphere filled with Ludox® colloidal silica. It diffuses light upon receiving the laser pulse signal. The diode laser emits light with a wavelength of $\sim$ 397 nm as a short pulse of $\sim$ 100 ps. A 440 nm laser is also used. There is a mechanical switchbox which selects the target flask. The switchbox and the laser driver are controlled by a computer. Normally, the laser operates at 3.33 Hz, asynchronous with the Booster proton beam to MiniBooNE. The laser system provides monitoring of individual PMT performance and a measurement of the oil attenuation length throughout the experiment lifetime. Low intensity laser runs were used to determine the 1-PE PMT charge response [102]. Time offsets have been derived from both low and high intensity laser runs, whereas the charge likelihoods have been obtained from laser runs which span a wide range of intensities [102, 103].

| Device | $X$ (cm) | $Y$ (cm) | $Z$ (cm) |
|---|---|---|---|
| Flask 1 | −0.3 | −4.1 | 1.5 |
| Flask 2 | 144.9 | 96.1 | −126.4 |
| Flask 3 | 1.7 | −0.8 | 83.7 |
| Flask 4 | −80.0 | 203.9 | −24.1 |
| Bare fiber | 82.0 | 540.0 | 65.0 |

Table 4.3: Positions of the laser light sources in the MiniBooNE detector.

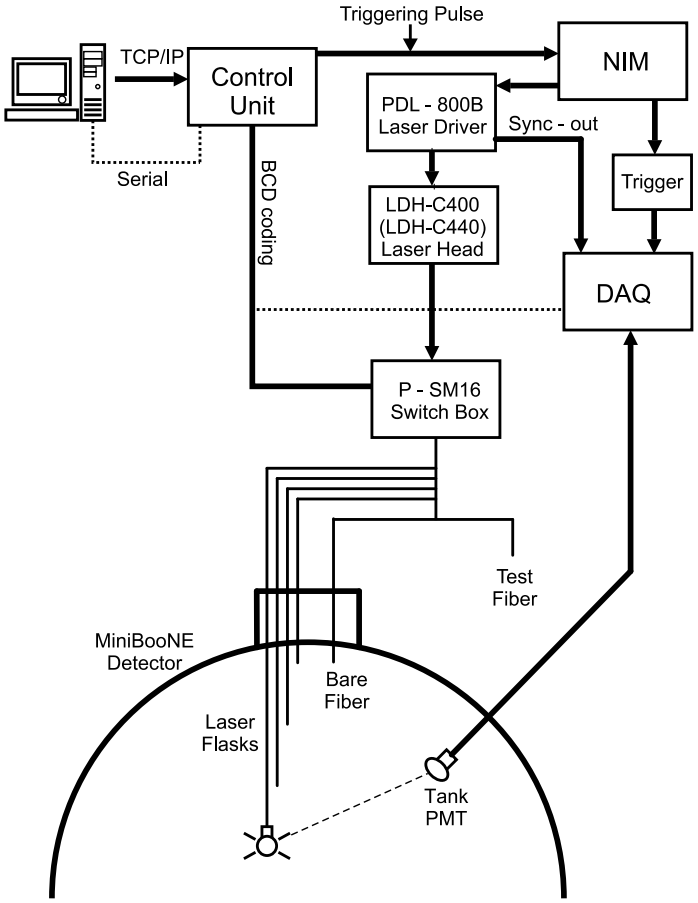


Figure 4.11: Schematics of the MiniBooNE laser calibration system.

### 4.4.2 The Cosmic Muon Calibration System

MiniBooNE also uses cosmic ray muons as a calibration source. It is a natural source, providing a free, constant and intense flow of muons created in the atmosphere. A two-plane scintillator *muon tracker* is placed above the tank to register the entrance point of muons. Six scintillator cubes with a side of 5 cm are placed at different positions inside the active region of the detector. The cubes are read by a single PMT and sealed in a aluminium box in order to isolate them from the rest of the detector. After passing through the tracker a muon enters the detector, where it loses energy by light emission. A muon may either stop inside or pass through the detector. If it stops it usually decays in the following manner: $\mu \rightarrow e + \overline{\nu}_e + \nu_\mu$; alternatively, there is $\sim 8\%$ chance of it being captured by a carbon atom. The emitted electron in the decay of a stopped muon is called a *Michel electron*, which has a continuous energy spectrum of a known shape [104] with an end point of half

the muon mass, $E_e^{max} = 52.8$ MeV. The characteristic decay time is 2.2 $\mu$s.

There is a small probability that a muon stops in one of the scintillator cubes, but a large muon flux ($\sim$ 1 muon per square centimeter per minute), provides enough statistics for this measurement. Here, the muon tracker registers the point of a muon entrance and Veto PMTs register the muon entrance in the detector. Inside the detector, the muon emitts Cherenkov and scintillation light, producing PMT hits in the signal tank region. The delayed light from a muon cube provides a tagging of the decay and gives the position of the muon track end point. Knowing the muon track length, one can calculate the muon energy, using stopping muon range tables [105]. The positions of the cubes are shown in Table 4.4. As one can see from the table, the system calibrates muons in the range of kinetic energy 100–800 MeV. The agreement for the energy calibration between the data and the MC is shown in Fig. 4.12.

| Cube depth (cm) | $X$ (cm) | $Y$ (cm) | $Z$ (cm) | $< T_\mu >$ (MeV) |
|---|---|---|---|---|
| 31.3 | $-60.8$ | 540.7 | 15.1 | $95.0 \pm 4.0$ |
| 60.3 | 15.6 | 511.7 | $-57.6$ | $155.0 \pm 5.0$ |
| 100.5 | 57.9 | 471.5 | $-13.5$ | $229.0 \pm 7.0$ |
| 200.8 | $-18.6$ | 371.2 | 59.2 | $407.0 \pm 9.0$ |
| 298.1 | 40.8 | 273.9 | 44.5 | $584.0 \pm 9.0$ |
| 401.9 | 40.8 | 170.1 | 44.5 | $771.0 \pm 9.0$ |

Table 4.4: Positions of cosmic muon calibration cubes. $< T_\mu >$ is the average kinetic energy of muons stopped in the cube.

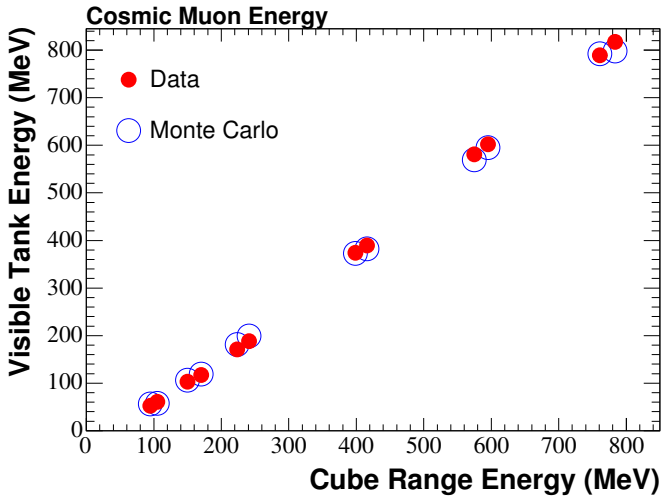


Figure 4.12: Muon energy calibration from the cosmic muon calibration system. The visible energy is from the *StancuFitter* electron hypothesis, since there was no muon hypothesis fitter at the time of the calibration measurement.

### 4.4.3 Michel Electron Calibration

As discussed previously, the Michel electrons provide yet another source of calibration. They provide an in-situ calibration for electrons at the end point of the Michel electron energy spectrum, namely $E_e \approx 52.8$ MeV.

In MiniBooNE a Michel electron candidate is an event with a number of main tank hits $< 200$ and veto hits $< 6$ following the primary muon event, which has number of main tank hits $> 200$ and veto hits $> 6$ with a typical decay time of 2.2 $\mu$s. The observed spectrum of Michel electron candidates and the best fit is shown in Fig. 4.13. The energy smearing in the fit accounts for the limited detector resolution. From the fit around the end point it was determined that the electron energy resolution at this energy is $\sim 14.8\%$.

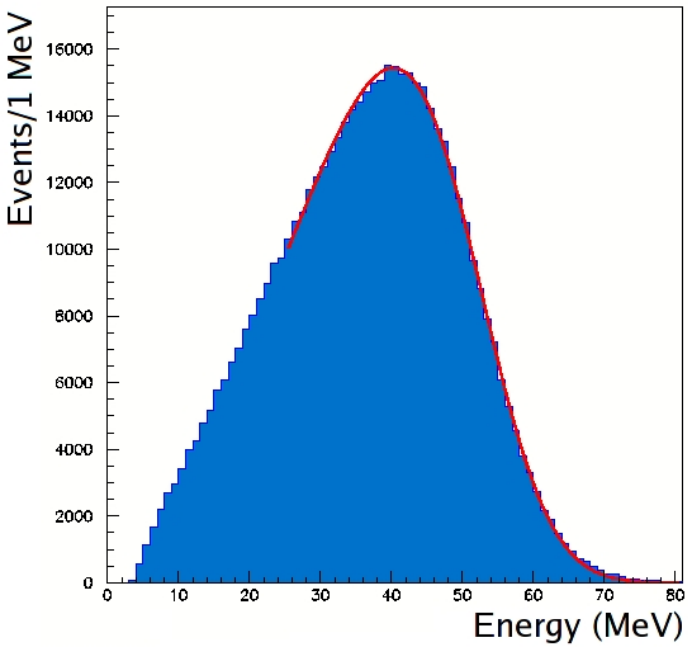


Figure 4.13: Michel electron energy spectrum calibration. Reconstructed spectrum for Michel electrons candidates (blue histogram) and the best fit (solid red curve), which is obtained by smearing the Michel electron kinetic energy spectrum with a Gaussian of width proportional to $\sqrt{E}$.

### 4.4.4 $\pi^0$ Mass Calibration

A sample of neutrino beam-induced neutral current $\pi^0$ events was used for another in-situ calibration, using the reconstructed $\pi^0$ mass ($M_{\gamma\gamma}$) distribution. The $\pi^0$ meson has a rest mass of about 135 MeV. When produced, $\pi^0$ decays essentially immediately with a characteristic time of $8.4 \times 10^{-17}$ s. The main decay mode (98.798%) is the production of two gammas: $\pi^0 \rightarrow \gamma + \gamma$. The second

largest decay mode (1.198%) is the decay into a gamma and an electron-positron pair: $\pi^0 \rightarrow \gamma + e^- + e^+$. A gamma after traveling typically $\sim 0.5$ m converts into an electron-positron pair. Both the electron and positron have the same direction as the gamma from which they were produced, due to the massless gamma. Propagating through the medium they produce an electromagnetic shower emitting Cherenkov and scintillation light. In a Cherenkov detector a gamma event with energy $E$ is essentially identical to an electron event with an energy $2E$.

Details of the NC $\pi^0$ sample selection and the reconstruction of such events including the event 4-vertex, directions of the 2 gammas, their conversion lengths, and energies are given in Ref.[100]. One can compare the reconstructed $M_{\gamma\gamma}$ distribution in different $\pi^0$ momentum bins, shown in Fig. 4.14. This method calibrates photons in the energy range from about 50 MeV to 350 MeV.

## 4.5 The MiniBooNE Cross-Section Model

As discussed in Section 4.2.4, MiniBooNE operates at neutrino energies of $\sim 1$ GeV. The charge current scattering cross-sections are shown in Fig. 4.15 and predictions of the NCE scattering cross-section on both protons and neutrons are shown in Fig. 4.16. This region is unique, as many types of scattering contribute to the total neutrino interaction cross-section. Neutrino cross-sections at high energies are well-known from neutrino DIS scattering experiments, with errors of the order about $1-2\%$. However, in the few-GeV region, the errors are relatively large, $\sim 10-20\%$. In this region there is a rollover in the cross-section shape, so this region is useful in cross-section prediction models testing. In this section the MiniBooNE cross-section prediction model is described.

### 4.5.1 NUANCE Neutrino Cross-Section Generator

In order to predict the rates of all possible neutrino interactions in the detector, the products of the interactions and their kinematics, MiniBooNE uses the *NUANCE v3* neutrino cross-section generator [107].

NUANCE is a FORTRAN-based MC program which simulates 99 distinct neutrino interactions, both charged and neutral current, in a very broad neutrino energy range, from 100 MeV to $10^3$ GeV. The full list of NUANCE channels is given in a Table 4.5. It was originally developed to simulate atmospheric neutrino interactions in the IMB detector, but later was generalized and is currently used by many neutrino experiments such as MiniBooNE, SciBooNE, Super-Kamiokande, K2K, SNO, MINOS, and KamLAND.

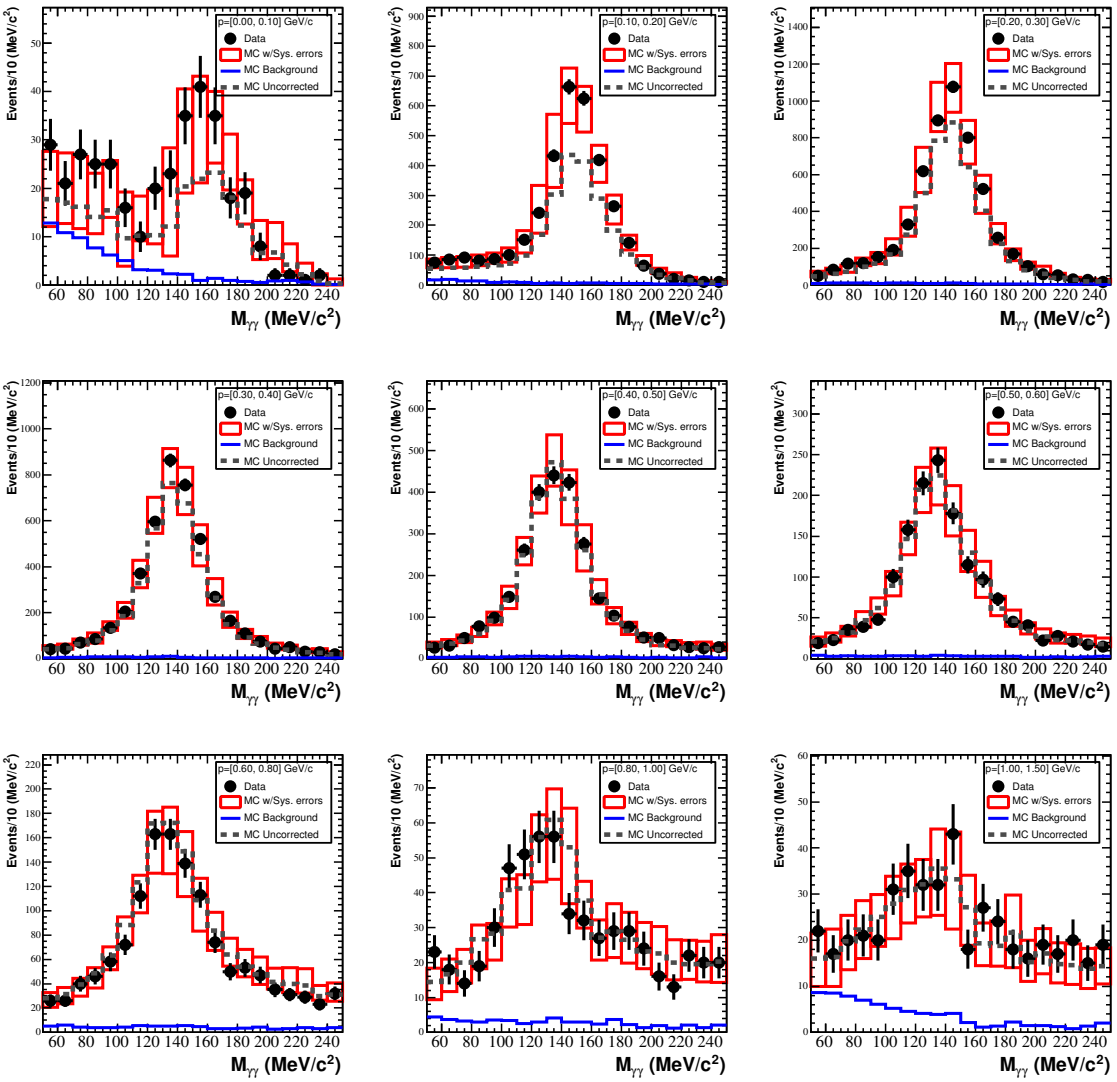


Figure 4.14: Reconstructed $M_{\gamma\gamma}$ distributions for the data (black points with statistical error bars), uncorrected MC (dashed histogram), and corrected MC with systematic errors (red boxes) in bins of reconstructed $\pi^0$ momentum, from 0 GeV/$c$ to 1.5 GeV/$c$. The blue histogram in each panel shows the MC estimated backgrounds for NC $\pi^0$ events, which are typically quite small.

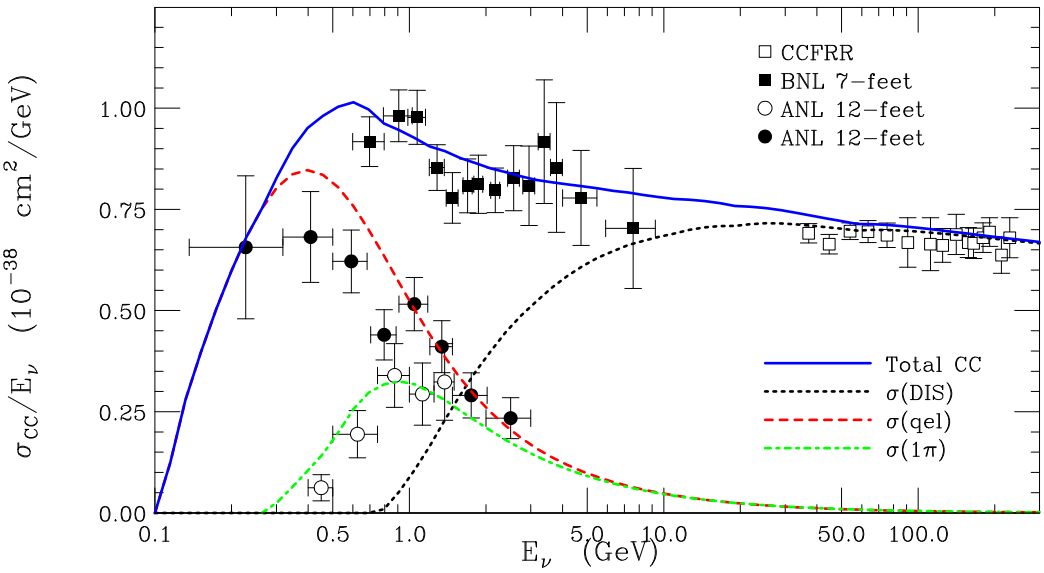


Figure 4.15: Charged current neutrino cross sections as a function of the neutrino energy. The data from different experiments (bars) and the theoretical prediction (curves). Figure from Ref.[106].

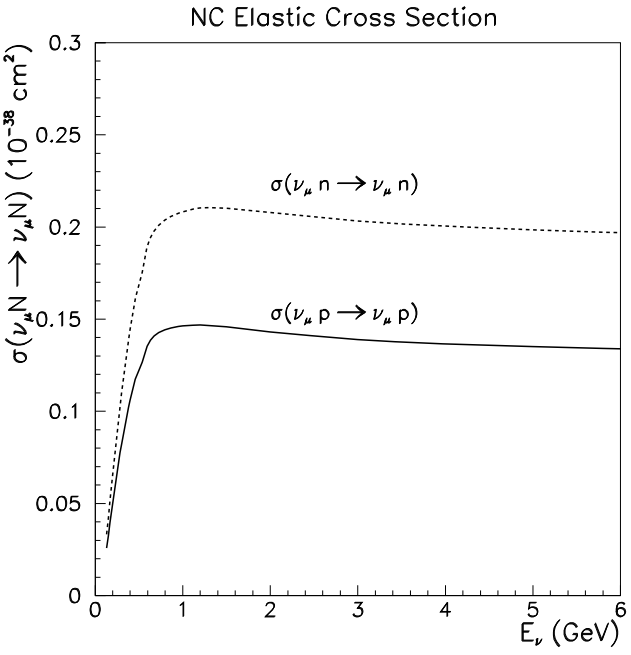


Figure 4.16: NC elastic scattering cross sections (per nucleon) as a function of the neutrino energy according to NUANCE.

| # | CC / NC | Reaction |
|---|---|---|
| Cabibbo–allowed quasi–elastic scattering from nucleons | | |
| 1 | CC | $\nu_\mu n \to \mu^- p$ ($\overline{\nu}_\mu p \to \mu^+ n$) |
| (Quasi–)elastic scattering from nucleons | | |
| 2 | NC | $\nu_\mu n \to \nu_\mu n$ ($\overline{\nu}_\mu n \to \overline{\nu}_\mu n$) $\nu_\mu p \to \nu_\mu p$ ($\overline{\nu}_\mu p \to \overline{\nu}_\mu p$) |
| Resonant single pion production | | |
| 3 | CC | $\nu_\mu p \to \mu^- p\pi^+$ |
| 4 | CC | $\nu_\mu n \to \mu^- p\pi^0$ |
| 5 | CC | $\nu_\mu n \to \mu^- n\pi^+$ |
| 6 | NC | $\nu_\mu p \to \nu_\mu p\pi^0$ |
| 7 | NC | $\nu_\mu p \to \nu_\mu n\pi^+$ |
| 8 | NC | $\nu_\mu n \to \nu_\mu n\pi^0$ |
| 9 | NC | $\nu_\mu n \to \nu_\mu p\pi^-$ |
| 10–16 | | Corresponding $\overline{\nu}_\mu$ processes |
| Multi–pion resonant processes | | |
| 17 | CC | $\nu_\mu p \to \mu^- \Delta^+ \pi^+$ |
| 18 | CC | $\nu_\mu p \to \mu^- \Delta^{++} \pi^0$ |
| 19 | CC | $\nu_\mu n \to \mu^- \Delta^+ \pi^0$ |
| 20 | CC | $\nu_\mu n \to \mu^- \Delta^0 \pi^+$ |
| 21 | CC | $\nu_\mu n \to \mu^- \Delta^{++} \pi^-$ |
| 22 | NC | $\nu_\mu p \to \nu_\mu \Delta^+ \pi^0$ |
| 23 | NC | $\nu_\mu p \to \nu_\mu \Delta^0 \pi^+$ |
| 24 | NC | $\nu_\mu p \to \nu_\mu \Delta^{++} \pi^-$ |
| 25 | NC | $\nu_\mu n \to \nu_\mu \Delta^+ \pi^-$ |
| 26 | NC | $\nu_\mu n \to \nu_\mu \Delta^0 \pi^0$ |
| 27 | NC | $\nu_\mu n \to \nu_\mu \Delta^- \pi^+$ |
| 28–38 | | Corresponding $\overline{\nu}_\mu$ processes |
| 39 | CC | $\nu_\mu p \to \mu^- p\rho^+(770)$ |
| 40 | CC | $\nu_\mu n \to \mu^- p\rho^0(770)$ |
| 41 | CC | $\nu_\mu n \to \mu^- n\rho^+(770)$ |
| 42 | NC | $\nu_\mu p \to \nu_\mu p\rho^0(770)$ |
| 43 | NC | $\nu_\mu p \to \nu_\mu n\rho^+(770)$ |
| 44 | NC | $\nu_\mu n \to \nu_\mu n\rho^0(770)$ |
| 45 | NC | $\nu_\mu n \to \nu_\mu p\rho^-(770)$ |
| 46–52 | | Corresponding $\overline{\nu}_\mu$ processes |
| 53 | CC | $\nu_\mu p \to \mu^- \Sigma^+ K^+$ |
| 54 | CC | $\nu_\mu n \to \mu^- \Sigma^0 K^+$ |
| 55 | CC | $\nu_\mu n \to \mu^- \Sigma^+ K^0$ |
| 56 | NC | $\nu_\mu p \to \nu_\mu \Sigma^0 K^+$ |
| 57 | NC | $\nu_\mu p \to \nu_\mu \Sigma^+ K^0$ |
| 58 | NC | $\nu_\mu n \to \nu_\mu \Sigma^0 K^0$ |
| 59 | NC | $\nu_\mu n \to \nu_\mu \Sigma^- K^+$ |
| 60–66 | | Corresponding $\overline{\nu}_\mu$ processes |
| 67 | CC | $\nu_\mu n \to \mu^- p\eta$ |
| 68 | NC | $\nu_\mu p \to \nu_\mu p\eta$ |
| 69 | NC | $\nu_\mu n \to \nu_\mu n\eta$ |
| 70–72 | | Corresponding $\overline{\nu}_\mu$ processes |
| 73 | CC | $\nu_\mu n \to \mu^- K^+ \Lambda$ |
| 74 | NC | $\nu_\mu p \to \nu_\mu K^+ \Lambda$ |
| 75 | NC | $\nu_\mu n \to \nu_\mu K^0 \Lambda$ |

Table 4.5: Processes available with NUANCE. The numbers in the leftmost column indicate the assigned reaction code in NUANCE.

The input variables for the code are: neutrino fluxes (described in Section 4.2.4), detector geometry, and the medium chemical composition ($CH_2$ for the mineral oil). NUANCE generates neutrino interactions inside the detector according to a probability for each of the processes based on their cross-section prediction. The output variables are: type of interaction (CCQE, NCE, CCPi+, etc.), its vertex, list of the final state particles produced in the interaction and their kinematics (direction and energy). If an interaction happened on a bound nucleon inside a nucleus, there is a special procedure to track the outgoing particles through the nucleus, as explained in Section 4.5.5.

| # | CC / NC | Reaction |
|---|---|---|
| 76–78 | | Corresponding $\overline{\nu}_\mu$ processes |
| 79 | CC | $\nu_\mu n \rightarrow \mu^- p \pi^+ \pi^-$ |
| 80 | CC | $\nu_\mu n \rightarrow \mu^- p \pi^0 \pi^0$ |
| 81 | NC | $\nu_\mu p \rightarrow \nu_\mu p \pi^+ \pi^-$ |
| 82 | NC | $\nu_\mu p \rightarrow \nu_\mu p \pi^0 \pi^0$ |
| 83 | NC | $\nu_\mu n \rightarrow \nu_\mu n \pi^+ \pi^-$ |
| 84 | NC | $\nu_\mu n \rightarrow \nu_\mu n \pi^0 \pi^0$ |
| 85–90 | | Corresponding $\overline{\nu}_\mu$ processes |
| Deep Inelastic Scattering | | |
| 91 | CC | $\nu_\mu N \rightarrow \mu X$ |
| 92 | NC | $\nu_\mu N \rightarrow \nu_\mu X$ |
| 93–94 | | Unused |
| 95 | CC | Cabibbo–supp. QE hyperon production: $\overline{\nu}_\mu p \rightarrow \mu^+ \Lambda$ $\overline{\nu}_\mu n \rightarrow \mu^+ \Sigma^-$ $\overline{\nu}_\mu p \rightarrow \mu^+ \Sigma^0$ |

| # | CC / NC | Reaction |
|---|---|---|
| Coherent / diffractive $\pi$ production | | |
| 96 | NC | $\nu_\mu A \rightarrow \nu_\mu A \pi^0$ $(\overline{\nu}_\mu A \rightarrow \overline{\nu}_\mu A \pi^0)$ |
| 97 | CC | $\nu_\mu A \rightarrow \mu^- A \pi^+$ $(\overline{\nu}_\mu A \rightarrow \mu^+ A \pi^-)$ |
| $\nu$–e elastic scattering | | |
| 98 | – | $\nu_\mu e \rightarrow \nu_\mu e$ $(\overline{\nu}_\mu e \rightarrow \overline{\nu}_\mu e)$ |
| $\nu$–e inverse $\mu$ decay | | |
| 99 | CC | $\nu_\mu e \rightarrow \mu^- \nu_e$ |

Table 4.5: Processes available with NUANCE. The numbers in the leftmost column indicate the assigned reaction code in NUANCE.(Continued from the previous page)

The relative fractions for the types of neutrino scattering in MiniBooNE according to NUANCE are shown in Fig. 4.17 before any cuts are applied. NCE correspond to $\sim$ 16% of all neutrino interactions in the MiniBooNE detector.

The important neutrino interaction channels for the NCE analysis consist of the signal (NCE, NUANCE channel 2) and backgrounds (CCQE, NUANCE channel 1, and NC pion production, NUANCE channels 6–9). These will be described in more details in Sections 4.5.2, 4.5.3 and 4.5.4.

The table of cross-section parameters and the assigned errors used in the MiniBooNE cross-section model is shown in Table 4.6.

### 4.5.2 Neutral Current Elastic Scattering

The target for neutrino interactions in the MiniBooNE detector has a chemical formula $CH_2$, which has six bound protons and neutrons in the carbon atom and two free protons. NUANCE uses the Llewellyn-Smith formalism [108] (described in Section 3.2) to model the scattering off free protons. For the neutrino scattering off bound nucleons, the Smith-Moniz formalism [109] is used. The vector nucleon form factors are taken in the form from the Ref.[110]. The nuclear effects for bound nucleons

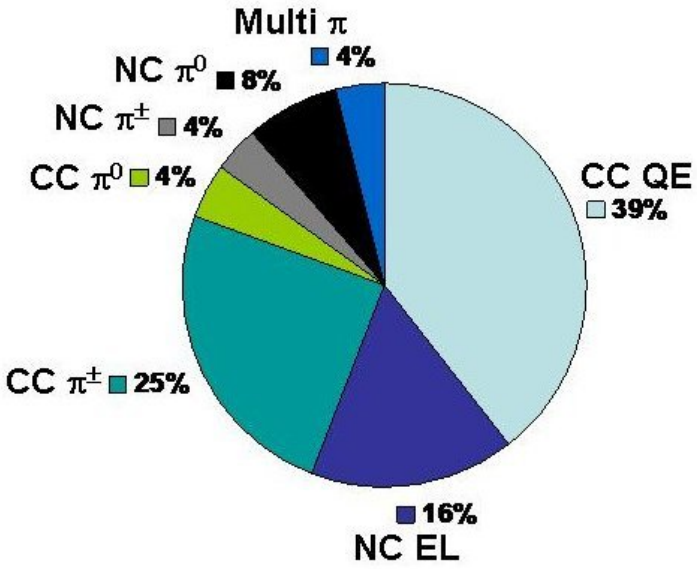


Figure 4.17: The neutrino events composition chart predicted by NUANCE for MiniBooNE.

| Parameter | Value | Uncertainty |
|---|---|---|
| $M_A$ for QE events on carbon | 1.2341 GeV | 0.077 GeV |
| Binding energy for carbon | 34.0 MeV | 9.0 MeV |
| Fermi momentum for carbon | 220.0 MeV | 30.0 MeV |
| $\Delta s$, the axial vector isoscalar term | 0.0 | 0.1 |
| $M_A$ for CC and NC single pion events | 1.1 GeV | 0.27 GeV |
| $M_A$ for CC and NC multiple pion events | 1.3 GeV | 0.52 GeV |
| Scale factor for NC coherent $\pi^0$ events | 1.302 | 0.14 |
| Scale factor for NC and CC $\Delta$ radiative events | 1.00 | 0.12 |
| Scale factor for deep inelastic scattering events | 1.00 | 0.25 |
| Pauli blocking scale factor, $\kappa$ | 1.0220 | 0.0205 |
| $M_A$ for CC single pion coherent events (not coherent NC $\pi^0$ ) | 1.030 GeV | 0.275 GeV |
| Scale factor for NC resonant $\pi^0$ events | 1.00 | 0.14 |
| $M_A$ for QE events on hydrogen | 1.13 GeV | 0.10 GeV |
| Vector mass $M_V$ | 850 MeV | 0 MeV |
| $\sin^2\theta_W$ | 0.2315 | 0 |

Table 4.6: Cross-section parameters and their 1-$\sigma$ uncertainties used in the MiniBooNE MC. Here the abbreviations are: QE – quasi-elastic, NC – neutral current, and CC – charge current. Uncertainties are used later to determine the contribution from the cross-section model uncertainties to the total error of the measurements.

are described in Section 4.5.5.

Due to final state interactions (FSI), described in Section 4.5.5, a NCE event may have more than one final state particle (excluding the neutrino). According to NUANCE, the probability of having only one outgoing nucleon after a NCE scattering on a nucleon inside carbon is $\sim 74\%$.

The value of $\Delta s = 0$ is chosen for the isoscalar form factor. An axial vector mass of $M_A = 1.23$ GeV for scattering off bound nucleons is taken from the MiniBooNE CCQE measurement [69]. For scattering off free protons $M_A = 1.13$ is used (approximately the average between the 1.03 GeV value obtained from deuterium-based CCQE measurements and the 1.23 GeV value measured by MiniBooNE CCQE as described in Section 3.3).

### 4.5.3 Charged Current Quasi-Elastic Scattering

The CCQE scattering is treated the same way as the NCE scattering. The difference is that CCQE in neutrino mode happens off neutrons only, $\nu_\mu + n \rightarrow \mu^- + p$. However, the only neutrons in mineral oil are those inside the carbon atom, and thus bound. Thus, for $\nu_\mu$ CCQE the Smith-Moniz formalism is used [109]. Although small, the contribution from the pseudoscalar form factor is included, where it is taken in the BBA-2003 form [110]. The same value of $M_A = 1.23$ GeV is used in the axial form factor. A Pauli blocking scaling parameter value of $\kappa = 1.022$ is taken from the same CCQE measurement [69]. $\kappa$ scales the lowest energy of the interacting nucleon that leads to a final nucleon just above the Fermi momentum, which modifies the shape of the CCQE cross-section at low values of $Q^2$ (see details in Ref.[67]).

### 4.5.4 Single Pion Production

Single pion production in neutrino-nucleon interactions happen primarily through the nucleon excitation into a resonant state ($\nu_\mu + N \rightarrow \nu_\mu + N^*$ for neutral current, or $\nu_\mu + N \rightarrow \mu^- + N^*$ for charged current) and a subsequent decay of the resonant state to a pion and a nucleon.

For resonant pion production the Rein and Sehgal model is used [111]. In the few GeV range, the interaction is dominated by the $\Delta(1232)$ resonance, although contributions from higher mass resonances are also included in the MC. The form factor forms used to describe the resonance production are assumed to be identical to those used in both NCE and CCQE scattering. However, the value of the axial vector mass is $M_A = 1.1$ GeV. Details are available elsewhere [112].

The neutral current single pion production channels:

$$\begin{aligned}
\nu_\mu + p &\rightarrow \nu_\mu + p + \pi^0, \\
\nu_\mu + p &\rightarrow \nu_\mu + n + \pi^+, \\
\nu_\mu + n &\rightarrow \nu_\mu + n + \pi^0, \\
\nu_\mu + n &\rightarrow \nu_\mu + p + \pi^-,
\end{aligned}$$

give a significant contribution to the NCE backgrounds. Pions may experience an absorption or a charge exchange in the nucleus through FSI:

$$\begin{aligned}
\pi + X &\rightarrow X', \\
\pi^\pm + X &\rightarrow \pi^0 + X'.
\end{aligned}$$

The final states of such neutrino interactions with a pion absorption include only nucleons, which is equivalent to the products of NCE interactions. The probability that an outgoing pion experiences absorption is $\sim 20\%$.

### 4.5.5 Nuclear Effects

There are three main nuclear effects for bound nucleons that affect the cross-section: Fermi motion, Pauli blocking, and FSI.

Each nucleon inside a nucleus is parametrized as a Fermi gas with an absolute temperature of 0 K. Its momentum density distribution is assumed to be uniform up to a Fermi momentum of $p_F = 220$ MeV for carbon. This defines the Fermi motion, which affects the cross-section.

In the Fermi gas model, scattering is only allowed if the momentum of the outgoing nucleon is greater than $p_F$. This effect is called Pauli blocking. It suppresses the cross-section, especially at low momentum transferred. Neglecting binding energy effects, the suppression can be calculated as $S = 1 - D/N$, where $N$ is the number of nucleons (N=6 for both protons and neutrons in carbon) in the nucleus and $D$ is given by [108]:

$$D = \begin{cases} \frac{A}{2}\left(1 - \frac{3}{4}\frac{|\vec{q}|}{p_F} + \frac{1}{16}\left(\frac{|\vec{q}|}{p_F}\right)^3\right), & \text{if } |\vec{q}| < 2p_F \\ 0, & \text{if } |\vec{q}| > 2p_F \end{cases},$$

where $\vec{q}$ is the 3-momentum transferred and $A$ is the atomic number ($A = 12$ for carbon).

Finally, there is an intranuclear final state interactions effect. Recoil hadrons produced in a neutrino interaction are subject to strong interactions with the surrounding nucleons in the carbon nucleus. FSI are interpreted in NUANCE, where the scattered hadrons are propagated through the nucleus, which is simulated based on models of nuclear density and Fermi momentum. At each step, the MC determines whether the hadron interacts with the target nucleus and if so, it generates an interaction and resulting new final state particles.

### 4.5.6 Dirt Backgrounds

Neutrino events that happen outside the detector, in the surrounding dirt or in the detector material (referred to as "dirt" background henceforth) are simulated the same way as in-tank events, but with a cross-section reweighed according to the density of the material relative to the density of the mineral oil.

For these events, the neutrino flux may be different than that which is passing through the detector because of the different neutrino angle range with respect to the beam direction. To calculate the flux, a sphere of radius 15 m with its center at the center of the detector was chosen as a target for neutrinos in the beam MC. This flux is only used for the dirt background events, but not for the in-tank events.

## 4.6 The MiniBooNE Detector Monte Carlo

The output final state particles produced by NUANCE are passed to a Geant3-based [113] MC detector simulation, which simulates particle propagation, light creation and transmission and the PMT response for the registered photons. Hadronic interactions are simulated by GCALOR package [114].

### 4.6.1 Light Production and Transmission

Optical photons with a wavelength in the range from 250 nm to 650 nm are created by charged particles traveling through the media via Cherenkov, scintillation and fluorescence light production. The photons are then propagated through the medium, where they may experience scattering, fluorescence, and absorption.

**Cherenkov light**

Energetic charged particles traveling with a speed of light greater than the speed of light in the medium produce Cherenkov radiation. Cherenkov photons are emitted with a characteristic angle, $\theta_{cer}$, with respect to the particle direction, depending on the particle velocity ($\beta = v/c$) and the index of refraction of the medium:

$$\cos\theta_{cer} = \frac{1}{\beta n}. \tag{4.1}$$

The number of Cherenkov photons with a wavelength $\lambda$ per particle path length $dx$ per wavelength $d\lambda$ is given by

$$\frac{d^2N_{cer}}{dxd\lambda} = \frac{2\pi\alpha z^2}{\lambda^2}\sin^2\theta_{cer},$$

where $\alpha = e^2/(\hbar c)$ and $ze$ is the particle charge.

One can express the particle's velocity through its kinetic energy, and thus Eq.(4.1) yields

$$\cos\theta_{cer} = \frac{1}{n}\left[\frac{(T+m)^2}{(T+m)^2 - m^2}\right]^{\frac{1}{2}}.$$

This function, for different particles that can be observed in the MiniBooNE detector, is shown in Fig. 4.18. From this figure one can see that protons have a much different Cherenkov profile, than muons and electrons.

The minimum kinetic energy for which charged particles can produce Cherenkov light (Cherenkov threshold) is calculated to yield:

$$T_{Ch} = m\left[\sqrt{\frac{n^2}{n^2-1}} - 1\right].$$

The Cherenkov threshold kinetic energy for protons is $T_{Ch} \approx 350$ MeV.

**Scintillation Light**

Charged particles moving through the medium ionize and excite the surrounding molecules. The atomic de-excitations of the latter produce isotropic and delayed (of the order of 1–50 ns) *scintillation* light. The scintillation light yield is only proportional to the total particle's ionization loss. Quenching effects reduce the light yield and thus Birk's law is used to convert the ionization energy

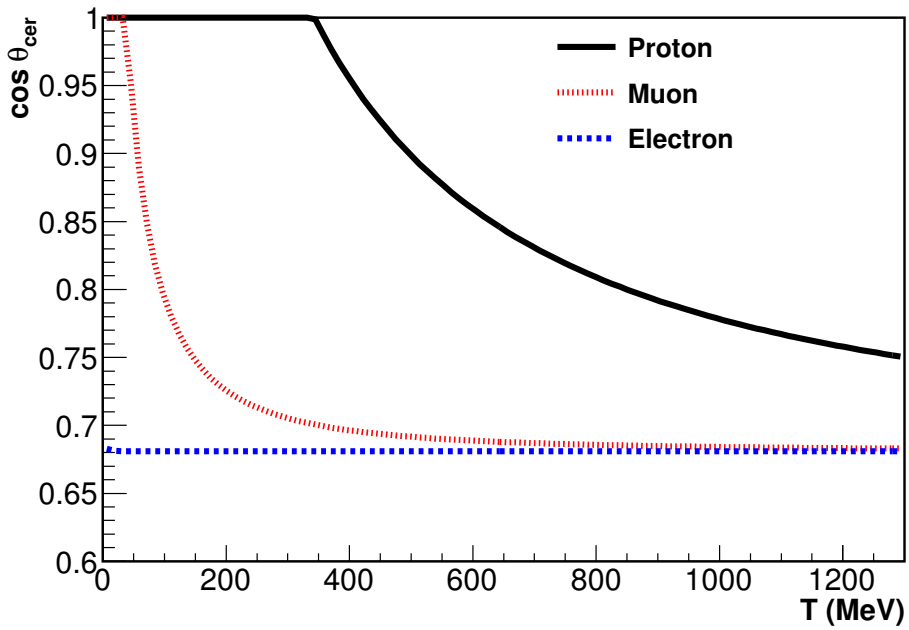


Figure 4.18: Cherenkov angle in mineral oil for different particles (as labeled) as a function of their kinetic energy.

loss per unit length per unit medium density ($dE/dx$) to scintillation light production:

$$\frac{dE_{sci}}{dx} = \frac{\frac{dE}{dx}}{1 + k_B \frac{dE}{dx} + k'_B \left(\frac{dE}{dx}\right)^2},$$

where the coefficients $k_B = 0.014$ g cm$^2$MeV$^{-1}$ and $k'_B = 0$ g cm$^2$MeV$^{-1}$ were obtained empirically.

**Light Transmission**

Photons have to travel typically several meters before reaching a PMT. The photon transport is affected mainly by three processes: fluorescence, scattering and absorption. Each process is described by its attenuation rate – probability of a photon interaction of a specific type per unit path length. The total attenuation rates and those individual for fluorescence and scattering for the Marcol 7 mineral oil have been measured using different experimental setups [99] and shown in Fig. 4.19.

- **Scattering**. Scattering is defined as a deflection of the photons off the medium molecules. Measurements of scattering in Marcol 7 mineral oil have been performed at Princeton [115]. There are two main types of scattering observed: Raleigh and Raman.

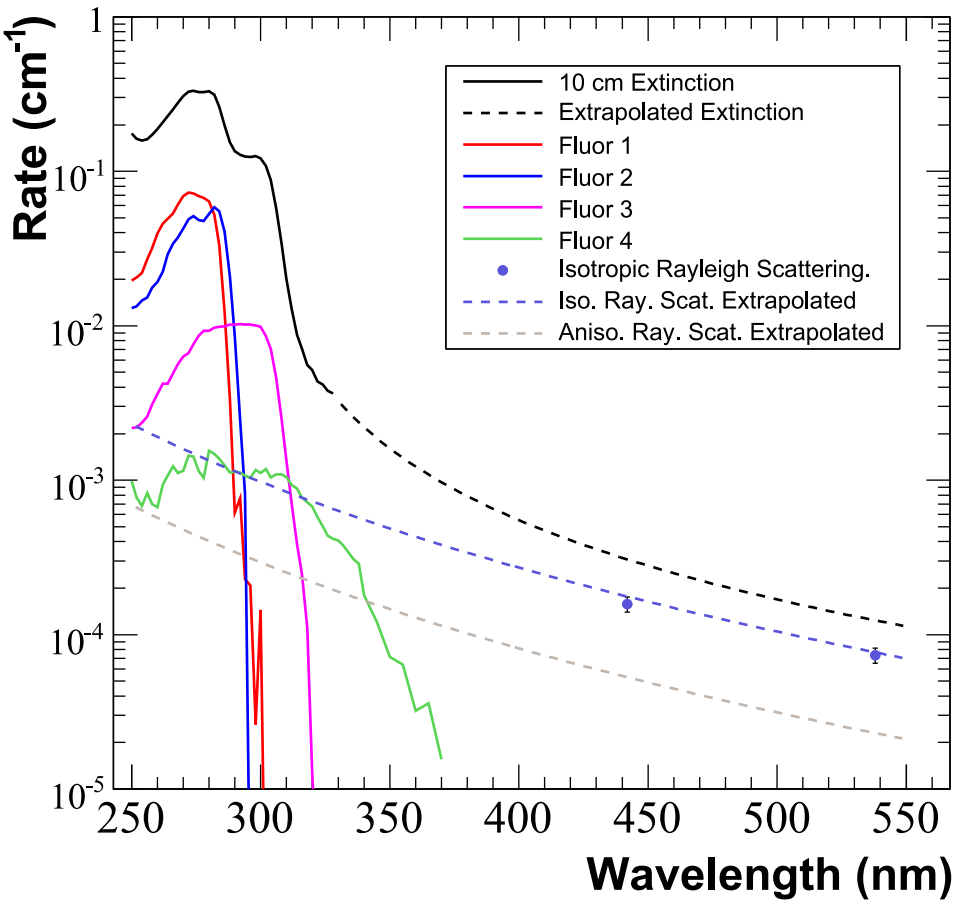


Figure 4.19: Extinction rate in the Marcol 7 mineral oil and some of the processes contributing to it, as labeled.

- **Fluorescence**. Fluorescence is a process in which a photon is absorbed by the mineral oil by a molecular excitation. The excited molecule eventually emits a photon which is delayed, has a longer wavelength than the original photon, and an isotropic direction. Fluorescence measurements have been performed by Dmitri Toptygin at John Hopkins University [116]. Four distinct fluors were identified, which differ by the emission and excitation energy spectra (shown in Fig. 4.20), and deexcitation time constants. It is assumed that the same fluors produce the scintillation light. The relative contributions from each of the fluors have been determined by comparing the data and MC for the Michel electron sample. From these studies it was found that one of the fluors with a decay constant $\tau = 34$ ns dominates the scintillation/fluorescence emission [100]. In the original MC contributions from the other three fluors are set to zero. However, an error on these contributions is assigned in the optical model MC variations.

  An important case of fluorescence is that of ultraviolet (UV) photons (with wavelength less than 250 nm). UV photons are not registered by PMTs as their quantum efficiency (shown in Fig. 4.21) drops to zero at wavelengths below 280 nm and above 650 nm. UV photons are therefore not propagated in the MC. However, since the reemitted photon spectrum is above 250 nm, thus it may be detected by a PMT. The attenuation length for UV photons is of the order of 1-10 cm. UV fluorescent photons are generated in the MC along the particle track, similar to scintillation photons.

- **Absorption**. Photon absorption is identified as the difference between the total extinction rate and that from fluorescence and scattering.

### 4.6.2 DAQ Simulation

The simulated event information with each photon arrival time at the PMT and the PMT number is passed to the DAQ simulation. This is a FORTRAN-based code which smears the PMT hit times and produces PMT charges according to the 1-PE charge response function measurements. Finally, it produces the output in the form of quads (as described in Section 4.3.4), just like it is in the real data.

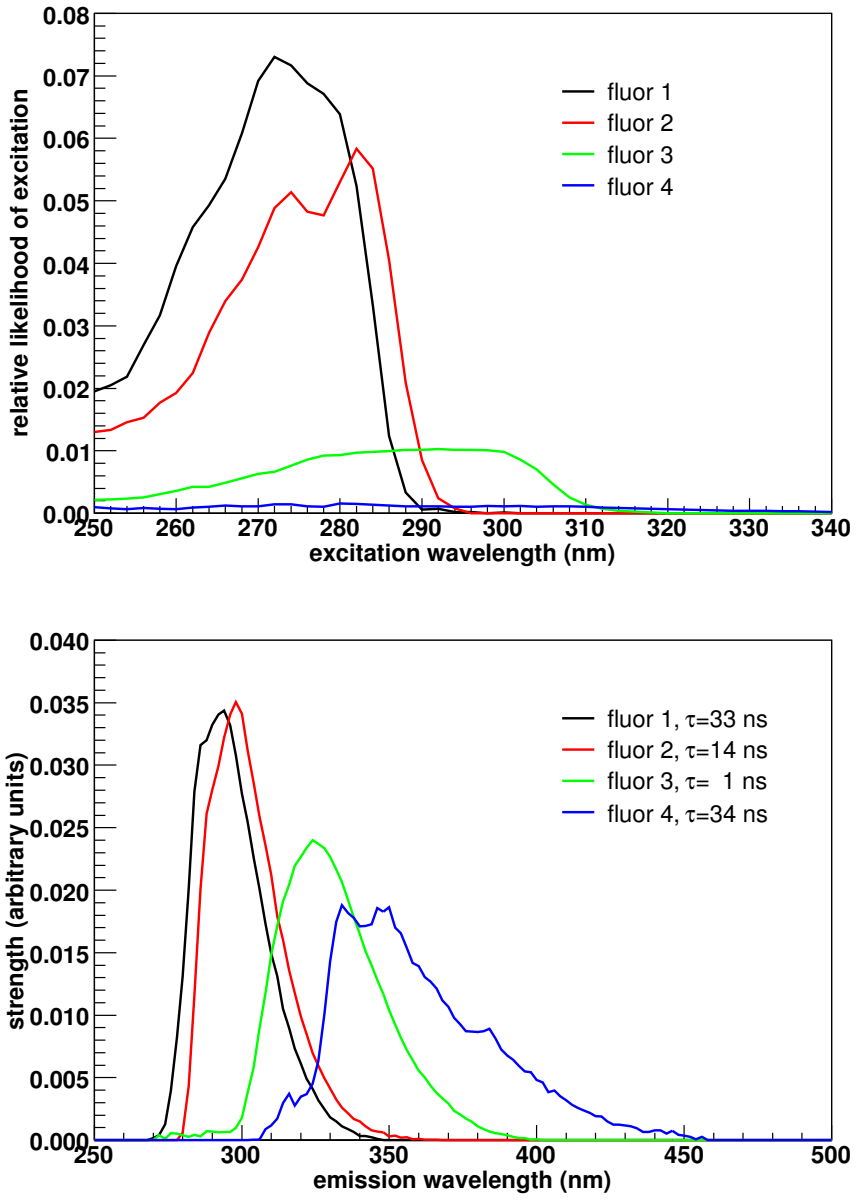


Figure 4.20: Fluorescence in the Marcol 7 mineral oil. Relative excitation probabilities for the four fluors in Marcol 7 (top plot). Relatively normalized corresponding photon emission probabilities (bottom plot).

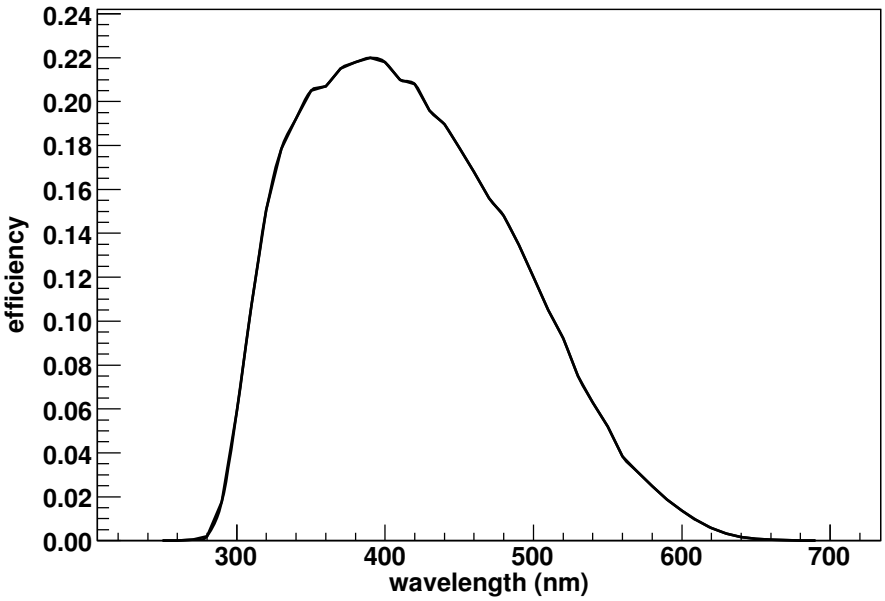


Figure 4.21: R5912 PMT quantum efficiency in the mineral oil. The curve has been obtained from Hamamatsu measurements.

# Part II

# Analysis

# Chapter 5

# Event Reconstruction

In this chapter we discuss the proton event reconstruction. Prior to these studies MiniBooNE had dedicated fitters for the following particles: electron (gamma), muon, and $\pi^0$. For the neutral current elastic events a special fitter had to be designed in order to have a reliable reconstruction performance of these events. The reconstruction problem, method used, tuning of the reconstruction fitter, as well as the performance of the proton fitter based on MC studies are described.

## 5.1 The Concept of Event Reconstruction

A NCE event in the MiniBooNE detector consists of an outgoing nucleon and a nuclear recoil. Ignoring nuclear recoil effects, we concentrate on the nucleon reconstruction. Since neutrons are neutral particles, they do not produce light in the detector by themselves. Thus, the only way one can observe them is through secondary interactions, where charged particles are produced – mostly protons, for example through an interaction with a proton, $n + p \rightarrow n + p$. Therefore, in order to reconstruct NCE events, we assume that those events consist of a single proton production. The proton hypothesis reconstruction package (or the proton fitter) in MiniBooNE will be called *NCFitter* henceforth.

Using the charge and time information from all PMTs in the detector the fitter calculates the following parameters which fully describe an event: event time ($t_0$), position ($x_0$, $y_0$, $z_0$), direction ($\theta_0$, $\phi_0$), and kinetic energy ($E$). Together they form a set of 7 independent reconstruction variables, which we denote as $\vec{\mathbf{X}} = (t_0, x_0, y_0, z_0, \theta_0, \phi_0, E)$. A full event geometry with respect to a given PMT is shown in Fig. 5.1. $\vec{R}$ is the vector from the center of the tank to the event vertex with $R = |\vec{R}|$

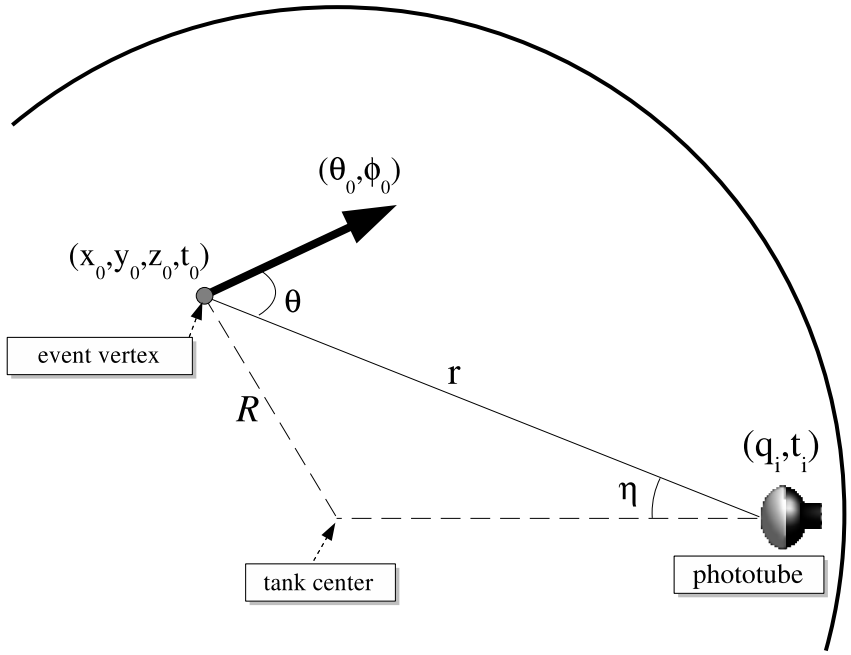


Figure 5.1: Reconstruction geometry.

and $\vec{U} = (U_X, U_Y, U_Z)$ is the event direction in terms of the direction cosines, which is equivalent to specifying the two angles ($\theta_0$, $\phi_0$).

As described in Section 4.6, protons are much different from other charged particles that can be seen in the MiniBooNE detector (muons, electrons and pions) in terms of light emission properties. They are much heavier than the latter and thus have a different Cherenkov angle. Protons in the detector produce scintillation light and, if energetic enough, may also produce Cherenkov light. In the MiniBooNE detector, below Cherenkov threshold, it is impossible to reconstruct the particle direction because of the isotropic scintillation light emission. However, above this threshold it may be possible to reconstruct the direction, for which one needs to know the proton Cherenkov angular emission profile in mineral oil.

As already mentioned, the MiniBooNE MC simulates the particle propagation. The optical properties of the medium have been calibrated. All reconstruction parameters are tuned for the best reconstruction performance of MC events, for which the generated $\vec{\mathbf{X}}$ is known. Thus, if the fitter reconstructs MC events reliably, it is expected that it should reconstruct data reliably as well.

## 5.2 Event Likelihood

MiniBooNE uses the method of charge and time likelihood maximization for the event reconstruction. Treating the PMT hits as independent, as well as the charge and time for each PMT that has been hit, the event likelihood is defined as

$$\mathcal{L}(\vec{\mathbf{X}}) \;=\; \prod_{i,\ q_i=0} f_q(0,\vec{\mathbf{X}}) \prod_{i,\ q_i>0} f_q(q_i,\vec{\mathbf{X}})\, f_t(t_i,\vec{\mathbf{X}})\ ,$$

where $i$ refers to the PMT number. The first product goes over the PMTs that have not been hit, while the second product goes over all PMTs that have been hit (i.e., record a non-zero charge $q_i$ at the registered time $t_i$); $f_q(q_i,\vec{\mathbf{X}})$ and $f_t(t_i,\vec{\mathbf{X}})$ are the charge and time probability distribution functions (PDFs), respectively.

It is convenient to work with the negative natural logarithm of $\mathcal{L}$, in which the task of maximizing $\mathcal{L}$ becomes minimizing $-\ln\mathcal{L}$. Upon performing this simple transformation the time and charge information from the PMTs are separated into two terms, as follows:

$$\begin{aligned} F_q(\vec{\mathbf{X}}) &= -\sum_i \ln f_q(q_i,\vec{\mathbf{X}}) \\ F_t(\vec{\mathbf{X}}) &= -\sum_{i,\ q_i>0} \ln f_t(t_i,\vec{\mathbf{X}}) \\ F(\vec{\mathbf{X}}) &= -\ln\mathcal{L}(\vec{\mathbf{X}}) = F_q(\vec{\mathbf{X}}) + F_t(\vec{\mathbf{X}}), \end{aligned} \tag{5.1}$$

where the sums run over either all PMTs (for the charge) or only over those that have been hit (for the time). $F_q$ and $F_t$ are called the charge and time likelihoods, while $F$ is the charge-time likelihood. In fact, these are negative log likelihoods, but we omit "negative log" to shorten the name.

The task of event reconstruction is to find among all possible values of event parameters the set $\vec{\mathbf{X}}_{min}$ which maximizes the event likelihood $\mathcal{L}(\vec{\mathbf{X}})$ (or equivalently, minimizes the charge-time likelihood, $F(\vec{\mathbf{X}}) = -\ln\mathcal{L}(\vec{\mathbf{X}})$).

## 5.3 Predicted Charge Model

The $\vec{\mathbf{X}}$ dependence for $f_q$ and $f_t$ is expressed through the predicted charge for each PMT, $\mu_i$, such that

$$\begin{aligned} f_q(q_i, \vec{\mathbf{X}}) &= f_q(q_i, \mu_i(\vec{\mathbf{X}})) \\ f_t(t_i, \vec{\mathbf{X}}) &= f_t(t_i, \mu_i(\vec{\mathbf{X}}), E). \end{aligned} \tag{5.2}$$

For the time likelihood we have also introduced an explicit energy dependence apart from the predicted charge, because the particle path length along which it emits light in general depends on the particle's energy. Thus, the predicted charge plays a central role in the reconstruction.

By definition, the predicted charge is the expected value of the charge at a given PMT, given the set of parameters $\vec{\mathbf{X}}$ for the event. To obtain the expected value, one has to generate the events with the same values of $\vec{\mathbf{X}}$ and propagate them through the detector MC. Then for any PMT $i$ the predicted charge is the average of the observed charge at that PMT:

$$\mu_i(\vec{\mathbf{X}}) = \left\langle q_i(\vec{\mathbf{X}}) \right\rangle, \tag{5.3}$$

or, equivalently, $\left\langle q_i(\vec{\mathbf{X}}) \right\rangle / \mu_i(\vec{\mathbf{X}}) = 1$.

### 5.3.1 Monte Carlo Proton Event Samples

In order to obtain the needed light emission profile for protons, samples of uniform and isotropic single protons with kinetic energies from 100 to 1300 MeV with a step size of 100 MeV, inside a sphere of 6.1 m (i.e.within the detector volume) have been generated. A total of $1.3 \times 10^6$ proton events has been simulated ($100,000$ events at each energy).

In the MiniBooNE detector MC one can extract the information about each individual photon that has been created. Furthermore, one has the possibility to turn off some physical effects. For example, one can turn off either the Cherenkov or the scintillation photons. By doing so we have divided the described initial sample of proton events into two samples: a Cherenkov light sample and a scintillation light sample. We proceed to study these samples separately, as they have different light emission properties: the Cherenkov light is prompt and directional, while the scintillation light is delayed and isotropic.

### 5.3.2 Simple Predicted Charge Model, Quantum Efficiency, and Attenuation Length

One needs to find a functional form of the predicted charge, $\mu(\vec{\mathbf{X}}) = f(\vec{\mathbf{X}})$. A priori, this function is unknown. Using the predicted charge definition in Eq.(5.3), with an unlimited computational power, one could create events in the entire allowed region for $\vec{\mathbf{X}}$ with the smallest grid in each of the 6 dimensions ($t_0$ for the event can be fixed). Also, for each of the points of the grid, a sufficient number of events would be generated to make statistical fluctuation of $\left\langle q_i(\vec{\mathbf{X}}) \right\rangle$ small. After doing this, the function $f_q$, defined in Eq.(5.2) would have been a 6-dimensional lookup table. However, the computational power of the computer cluster that was used does not allow for this level of computation in a reasonable time. For example, if one uses 100 points for a grid in each of the 6 dimensions ($X$, $Y$, $Z$, $\theta$, $\phi$, and energy), and only 100 events at each point of the grid, then, overall, one should generate $10^{14}$ events. Normally, we operate with $\sim 10^6$ events.

Thus, we have to make some reasonable assumptions on how the functions $f_q$ and $f_t$ should look like and determine their parameters. The idea behind measuring these parameters is that for any geometrical parameter describing the event (such as $R$, $r$, $\cos\eta$, $\vec{U}\cdot\vec{R}$, etc.) the amount of predicted charge, in average, must equal the amount of measured charge for any PMT. Here the The average goes over all events and all PMTs, since we consider all PMTs equivalent.

Assuming an isotropic light emission from the event vertex, the simplest model for the predicted charge at a given PMT at a distance r is represented by the following expression:

$$\mu = \epsilon\Phi\frac{\exp(-r/\lambda)}{r^2}f(\cos\eta), \tag{5.4}$$

where $\epsilon$ is the quantum efficiency, which relates to the probability of the photon detection by a PMT; $\Phi$ is the event flux, which is proportional to the total number of photons created in the event; $\exp(-r/\lambda)$ accounts for light attenuation with an effective attenuation length $\lambda$; $f(\cos\eta)$ is the PMT angular acceptance (as described below).

#### The PMT Angular Acceptance

$f(\cos\eta)$ defines the surface area, which is seen under the angle $\eta$ with respect to the normal of the PMT. For example, if the PMT were spherical of radius $R$, then $f(\cos\eta) = \pi R^2$. If the PMT were a flat disc, then $f(\cos\eta) = \pi R^2\cos\eta$.

However, any overall scaling factor in the right hand side of Eq.(5.4) can be absorbed in the

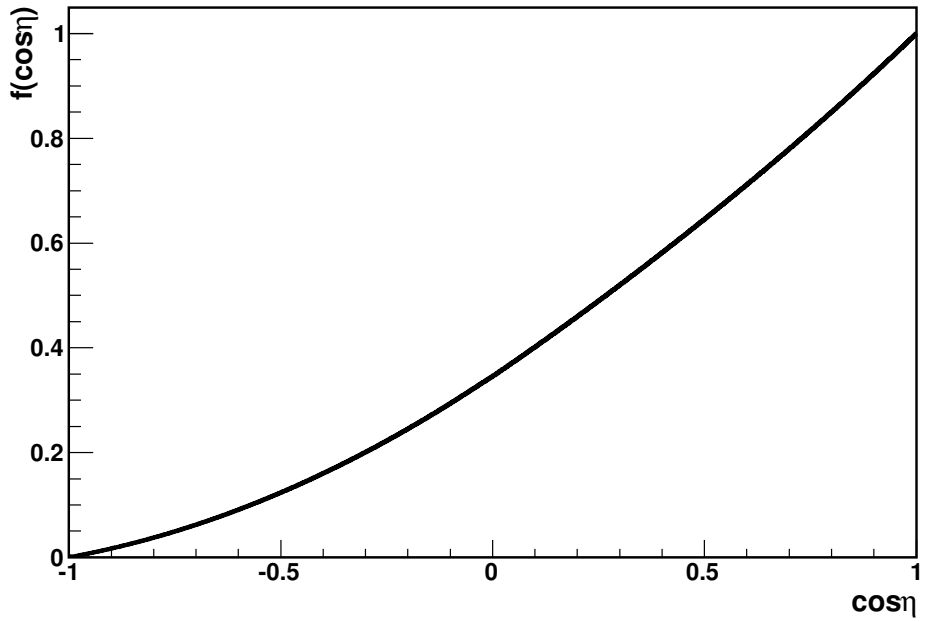


Figure 5.2: Angular acceptance as a function of $\cos\eta$.

definition of the flux $\Phi$. Hence, $\pi R^2$ goes into $\Phi$ and $f(\cos\eta)$ is just the angular response function (or angular acceptance), normalized such that $f(1) = 1$. The plot of the angular acceptance for the MiniBooNE PMTs as a function of $\cos\eta$ is shown in Fig. 5.2 as obtained from the measurements described in Section 4.3.2.

**Quantum Efficiency**

The reason for the quantum efficiency ($\epsilon$) in Eq.(5.4) is that MiniBooNE uses two types of PMTs, the new and the old ones. Otherwise, the overall absolute quantum efficiency could have been absorbed into the definition of $\Phi$. However, the two types of PMTs have different photon detection efficiencies which is taken into account by $\epsilon$.

In the formula for the predicted charge in Eq.(5.4), we may assume that the functions $\exp(-r/\lambda)/r^2$ and $f(\cos\eta)$ are independent from each other and the same for both new and old PMTs. Thus, they should average over the events to the same number for both types of PMTs, such that:

$$\begin{aligned} \left\langle \frac{\exp(-r/\lambda)}{r^2} \right\rangle &= \tfrac{1}{r_0^2} \\ \langle f(\cos\eta) \rangle &= f_0. \end{aligned}$$

Furthermore, assuming that the light flux is a constant, $\Phi_0$, for monoenergetic events (i.e., ignoring

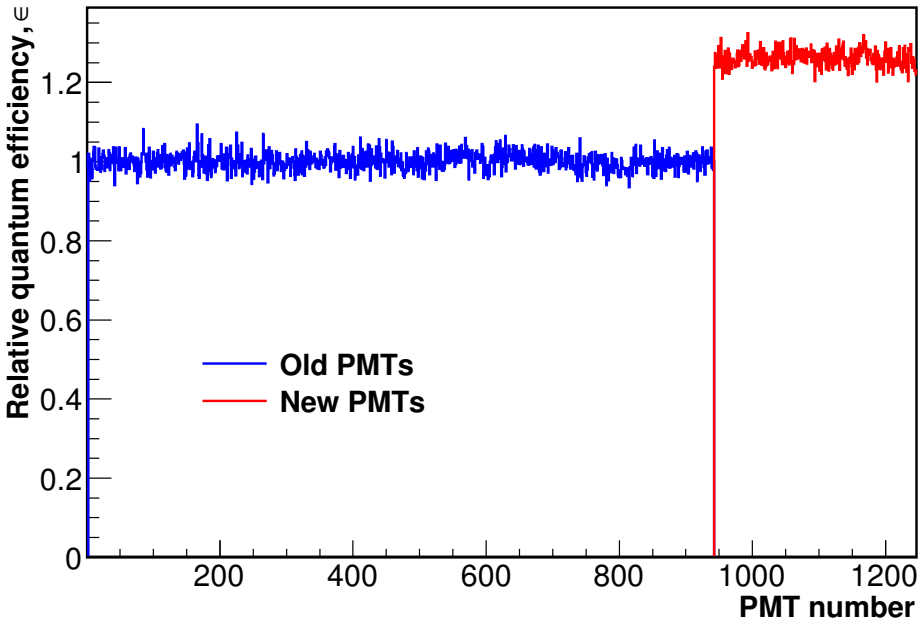


Figure 5.3: Normalized $\langle q \rangle$ distribution for old (blue) and new (red) PMTs.

the fluctuations in $\Phi$), then the expressions for the average of the predicted charges for the new and old PMTs are

$$\begin{aligned} \langle \mu^{old} \rangle &= \epsilon^{old} \Phi_0 \tfrac{1}{r_0^2} f_0 \\ \langle \mu^{new} \rangle &= \epsilon^{new} \Phi_0 \tfrac{1}{r_0^2} f_0 \end{aligned}$$

Using this, and equating the averaged predicted and measured charges, we find that

$$\epsilon^{new} = \epsilon^{old} \frac{\langle q^{new} \rangle}{\langle q^{old} \rangle}.$$

The normalization for $\epsilon$ was chosen such that $\epsilon^{old} = 1.00$. Normalized this way the $\langle q \rangle$ distributions for the new and old PMTs are shown in Fig. 5.3, as a function of the PMT number. From this plot the relative quantum efficiency for the new PMTs was determined to be: $\epsilon^{new} = 1.26$.

### Attenuation Length

In order to take into account for light attenuation effects, our simplest model given by Eq.(5.4) describes it simply by an exponential decay, $\exp(-r/\lambda)$, where $\lambda$ is the effective attenuation length. However, because of reflections and scattering effects, one may expect that this description would be too simplistic, which is indeed confirmed by the MiniBooNE MC and data. We find that a simple extention of our initial model, one in which we allow for the attenuation length to be a function of

the radial position of the event vertex, $\lambda \to \lambda(R)$, describes data relatively well.

For the purpose of measuring this effective attenuation length, all events inside a sphere of a radius 5.25 m were divided into 16 radial shells of the same volume, in which the attenuation length was to be determined independently. This way one has approximately the same statistics for each radial shell. This trick with radial shells will also be used later for measuring other light emission properties, which also may be dependent on the event radius $R$.

To determine the attenuation length, we define the histogram $\mu'$:

$$\mu' = \epsilon \frac{1}{r^2} f(\cos\eta),$$

where $\epsilon$ and $f(\cos\eta)$ have been described earlier. Now, if one plots $\langle q(r_j)\rangle / \langle \mu'(r_j)\rangle$, then from Eq.(5.4) and equating the predicted and measured charges, one obtains:

$$\langle \Phi \rangle \langle \exp(-r_j/\lambda)\rangle = \frac{\langle q(r_j)\rangle}{\langle \mu'(r_j)\rangle}, \tag{5.5}$$

from which $\lambda$ can be determined. As already mentioned, this operation was performed for each radial shell independently. In addition to that, it was done for Cherenkov and scintillation light samples independently, as the attenuation length may be different for them (they produce photons with different wavelength spectra). Figs. 5.4 and 5.5 show the fit of the histograms defined in Eq.(5.5) to the function $p_0 \exp(-r/p_1)$ for different radial shells. The first figure is for the scintillation and the latter is for Cherenkov light. As one can see, the fitted function is good enough in the first approximation for all radial shells. The parameter $p_1$ of the fitting function corresponds to the fitted value of $\lambda$.

The extracted values of the effective attenuation length in each radial shell were used for an additional fit to find the attenuation length as a function of $R$, $\lambda(R)$. Figs. 5.6 and 5.7 show the fits for the scintillation and Cherenkov light attenuation length radial dependence, respectively.

As one can see, the scintillation light attenuation has a dependence on $R$, which was used in the predicted charge model. For the first several inner shells for the Cherenkov light in Fig. 5.5 the histograms were not fit well and have large error bars; however, in the outer shells the fits are good and have smaller error bars. They do not show a convincing dependence on $R$, and thus the constant value of $\lambda_{cer} = 18.00$ m was chosen for the Cherenkov light model. For the scintillation

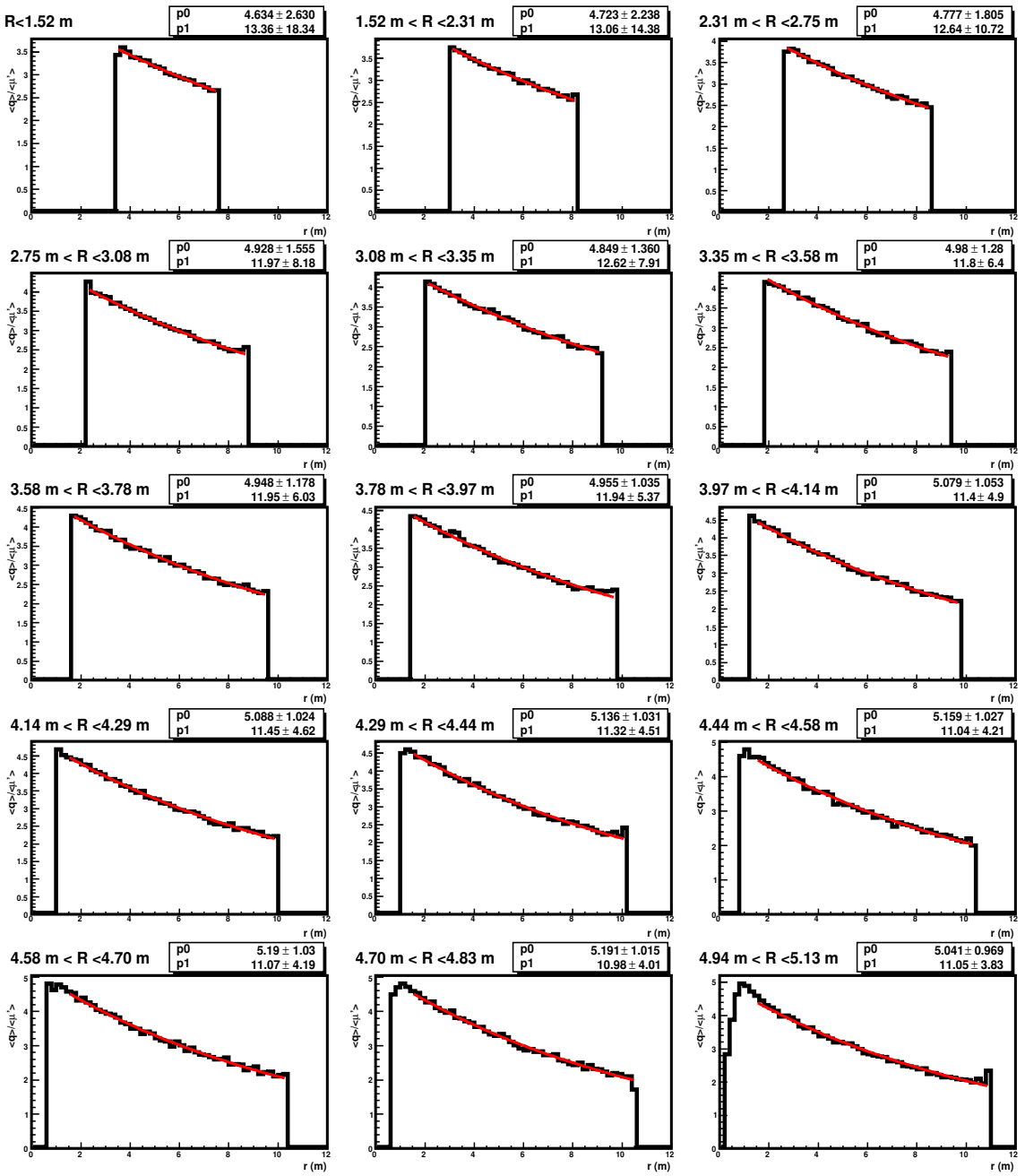


Figure 5.4: Average measured to predicted charge ratio as a function of the distance from vertex to PMT, $\langle q(r_j)\rangle/\langle\mu'(r_j)\rangle$, for the scintillation light for different event radial shells (black) and the fit to $p_0 \exp(-r/p_1)$ (red).

light we find the following functional form

$$\lambda_{sci}(R) = 16.32 - 2.22\exp(R/5.42), \tag{5.6}$$

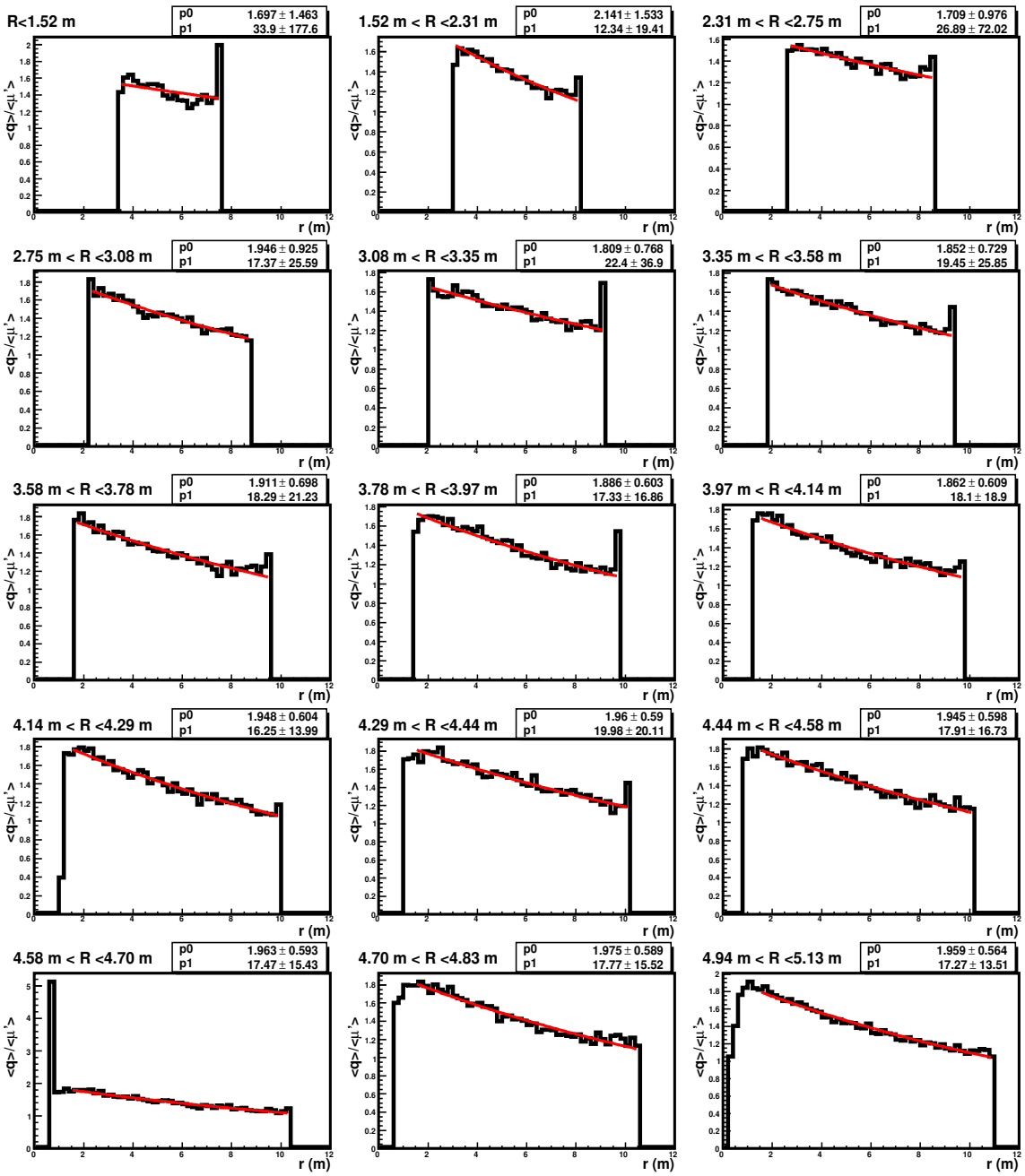


Figure 5.5: Average measured to predicted charge ratio as a function of the distance from vertex to PMT, $\langle q(r_j)\rangle/\langle\mu'(r_j)\rangle$ for Cherenkov light for different event radial shells (black) and the fit to $p_0 \exp(-r/p_1)$ (red).

where R and all numbers are in meters.

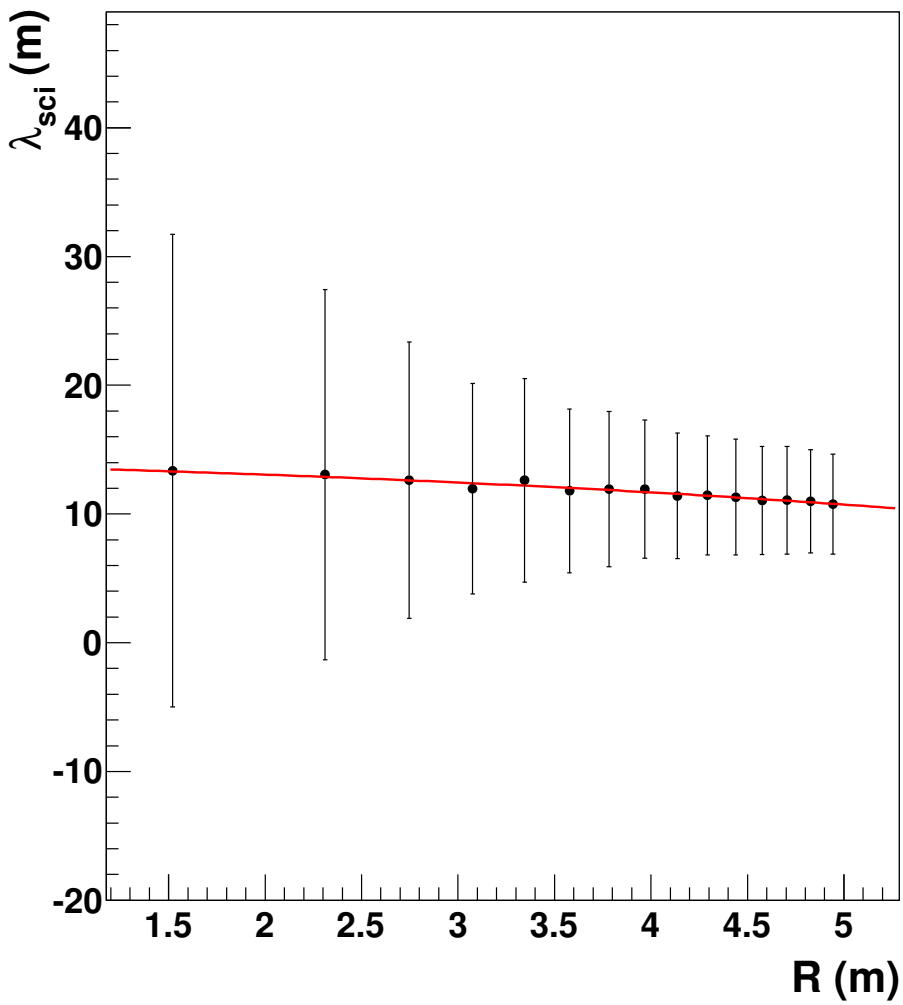


Figure 5.6: Effective attenuation length for scintillation light measured in different radial shells (black points) and a functional fit from Eq.(5.6) (red). The error bars are taken from the fits shown in Fig. 5.4.

### 5.3.3 Cherenkov and Scintillation Angular Emission Profile

As opposed to scintillation light which is emitted isotropically, Cherenkov photons are emitted at a particular angle with respect to the direction of the particle, $\theta_{cer}$, which depends on the particle's speed and the index of refraction of the medium, as given by Eq.(4.1).

If a particle stops immediately and produces all Cherenkov light at the event vertex, the only PMTs that would be hit are the ones with $\theta = \theta_{cer}$, where $\theta$ is the angle between the particle's direction and the line from the vertex to the PMT, as shown in Fig. 5.1. However, because of the fact that the event has a non-zero length and emits light all along the track, when assuming a point-like event in the reconstruction the light emission profile becomes effectively smeared about

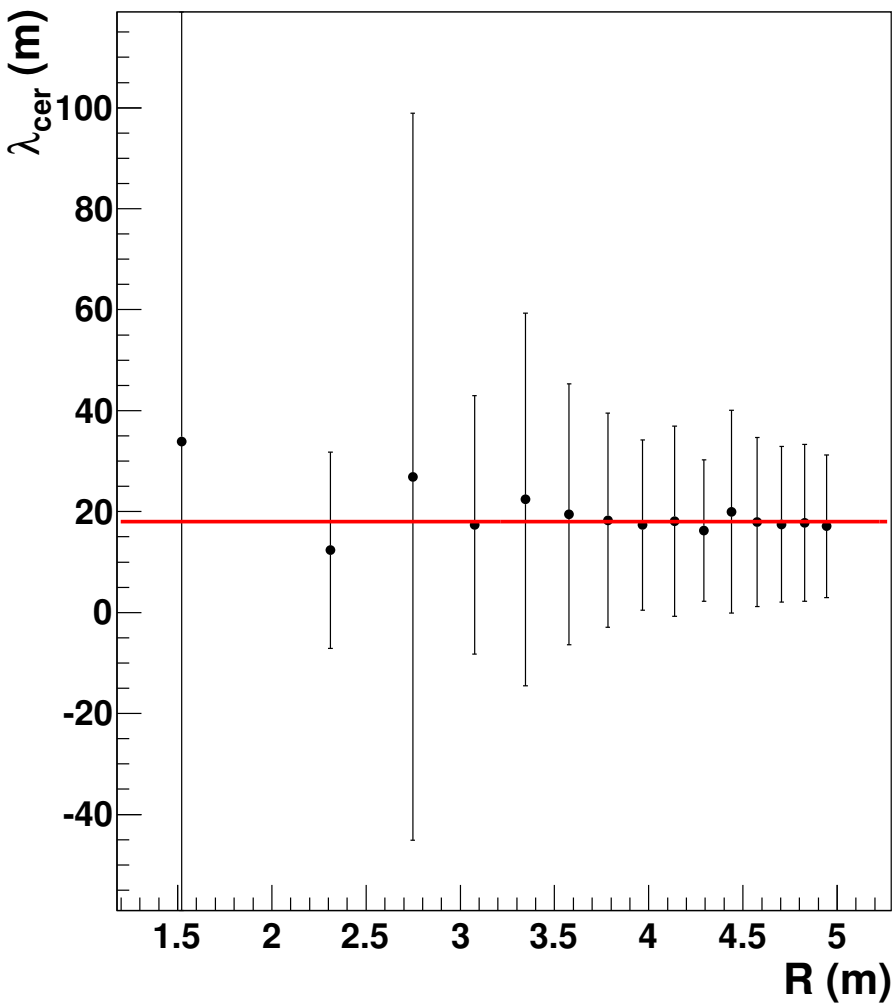


Figure 5.7: Effective attenuation length for Cherenkov light measured in different radial shells (black points) and a functional fit to a constant (red). The error bars are taken from the fits shown in Fig. 5.5.

$\theta = \theta_{cer}$.

When using a point-like event reconstruction there is a geometrical effect for the angular emission profile smearing, i.e., the smearing depends on the distance to the wall (or the radius of the event).

This is easy to understand from a simple 2-dimensional example, shown in Fig. 5.8. Let us consider a flat PMT surface and two otherwise identical events, going parallel to the wall, but at different distances from it. We also assume that the light was emitted at the same angle $\theta_{cer}$ along the particle track. The number of PMTs hit for both events are the same. If the length of the track is $L$ and the distance to the wall is $h$, then the possible values of the angle between the particle direction and the line from the center of the track to the PMT (effective angular emission profile

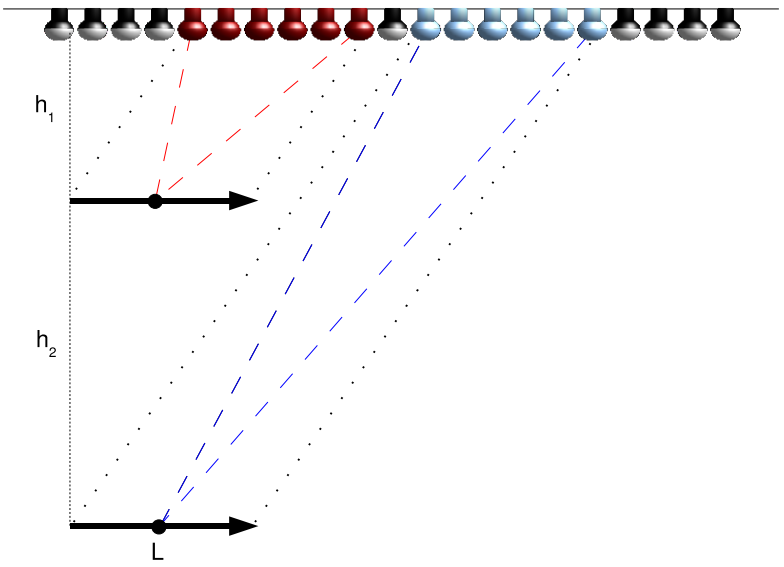


Figure 5.8: Explanation for the radial dependence of the angular emission profile. Two events with the same energy, but with different distance to the wall are shown. Blue PMTs are hit by the first event. Red PMTs are hit by the second event.

smearing) are in the following range:

$$\arctan\left(\frac{\tan\theta_{cer}}{1+\dfrac{L}{2h\tan\theta_{cer}}}\right) < \theta < \arctan\left(\frac{\tan\theta_{cer}}{1-\dfrac{L}{2h\tan\theta_{cer}}}\right).$$

Thus, the angular emission profile smearing in this case depends on $h$. The larger the value of $h$, the smaller the angular smearing.

The function $F_{cer}(E, \cos\theta, R)$ was added into the expression for the predicted charge, which simulates the angular emission profile. In this case, the equivalent of Eq.(5.4) for Cherenkov light yields

$$\mu_{cer} = \epsilon\Phi_{cer}\frac{\exp(-r/\lambda_{cer})}{r^2} f(\cos\eta) F_{cer}(E, \cos\theta, R). \tag{5.7}$$

In order to obtain the function $F_{cer}(E, \cos\theta, R)$, a similar procedure is followed as described in Section 5.3.2 for the attenuation length measurement. We use Cherenkov light samples for events

with different kinetic energies. Defining $\mu''_{cer}$:

$$\mu''_{cer} = \epsilon \frac{\exp(-r/\lambda_{cer})}{r^2} f(\cos\eta),$$

for each radial shell we plot the histograms of $q(\cos\theta)$ over $\mu''_{cer}(\cos\theta)$ and normalize the resulting histogram to have the overall integral equal to 1.0 with $\cos\theta$ going from $-1.0$ to 1.0. This way, the function $F_{cer}(E, \cos\theta, R)$ is normalized, thus

$$F_{cer}(E, \cos\theta, R) = N \frac{\langle q(\cos\theta)\rangle}{\langle \mu''_{cer}(\cos\theta)\rangle}, \qquad \int_{-1}^{1} F_{cer}(E, \cos\theta, R) d\cos\theta = 1.0, \qquad \forall E, R,$$

where $N$ is the normalization constant. $F_{cer}(E, \cos\theta, R)$ measured this way for $E = 700$ MeV are shown in Fig. 5.9. One may notice that the angular profile is wider (larger smearing) on the outside of the detector, compared to that on the inside. Also, the MC measured Cherenkov angular profile as a function of $R$ and $E$ is shown in Fig. 5.10. As one can see, $F_{cer}(cos\theta)$ becomes wider at higher values of $R$ in agreement with the radial dependence explanation presented above.

Also, the $\cos\theta$ value at the maximum of $F_{cer}(\cos\theta)$ decreases as the proton kinetic energy increases, which is consistent with the behavior of the proton Cherenkov angle in mineral oil as a function of the particle kinetic energy shown in Fig. 4.18.

The fit function $F_{cer}(cos\theta)$ shown in Fig. 5.9 is different in 3 different regions divided by $t_1$ and $t_2$, as follows:

$$F_{cer}(\cos\theta) = \begin{cases} B_1 \exp(\cos\theta/\sigma_1), & \text{if } \cos\theta < t_1 \\ \exp(-(\cos\theta - t_0)^2/\sigma), & \text{if } t_1 < \cos\theta < t_2 \\ B_2 \exp(-\cos\theta/\sigma_2), & \text{if } \cos\theta > t_2 \end{cases}, \tag{5.8}$$

where $t_0$, $t_1$, $t_2$, $\sigma$, $\sigma_1$, and $\sigma_2$ are free parameters. $B_1$ and $B_2$ can be calculated from the requirement of $F_{cer}(cos\theta)$ to be normalized to unit area as well as its derivative to be continuous.

For the scintillation light, in the first approximation the angular profile should be flat. However, due to the non-zero event track length, along which the scintillation light is emitted, in the point-like reconstruction there are also geometrical corrections to the angular profile. One should expect these corrections to be small at low energies and the angular profile to be close to flat. However, at higher energies, they may have a considerable contribution, since the event has a longer track length. The scintillation light angular profile was measured in the same manner as it was done for the Cherenkov

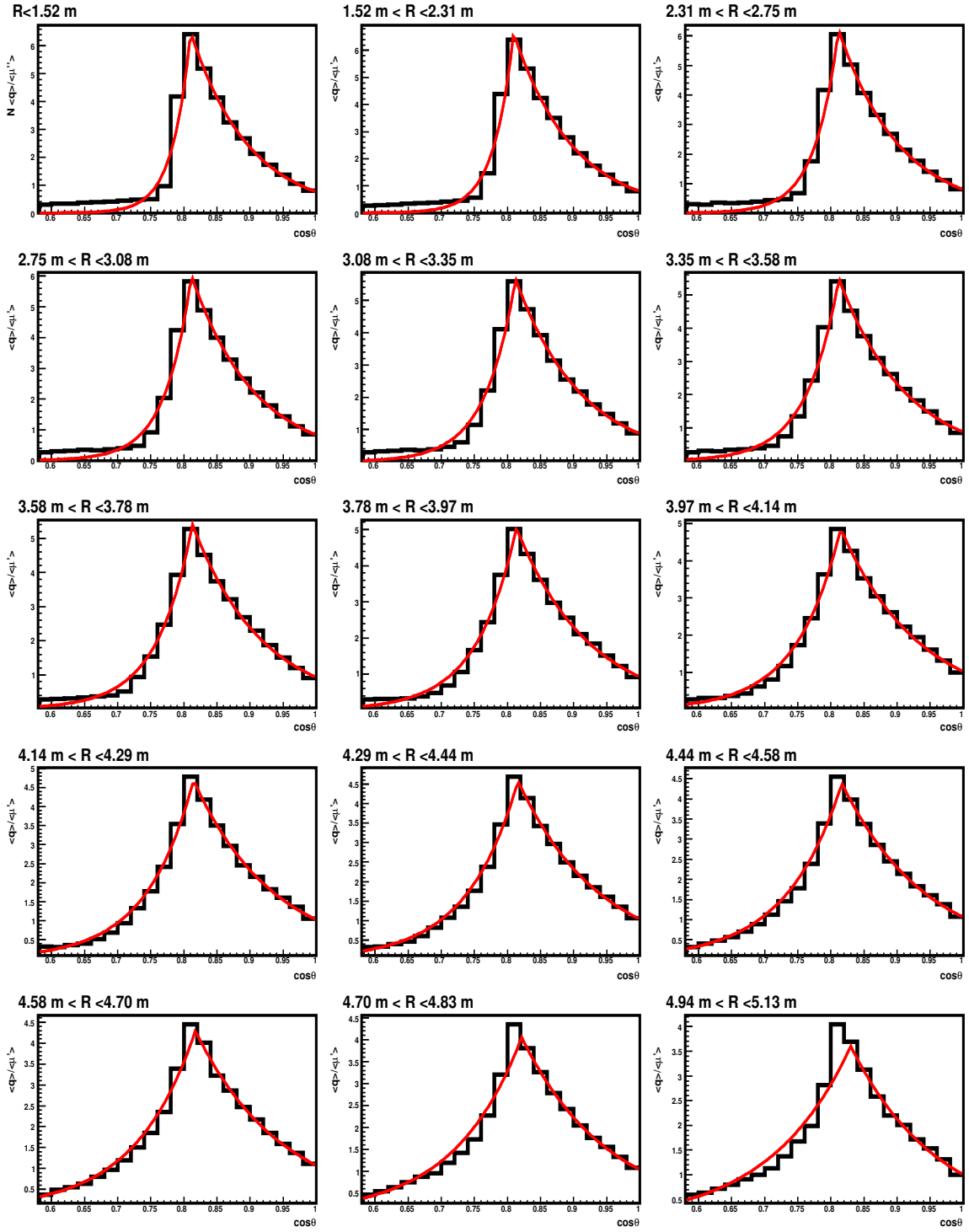


Figure 5.9: Cherenkov angular emission profile for 700 MeV protons inside different radial shells. The functional fit is described in Eq.(5.8).

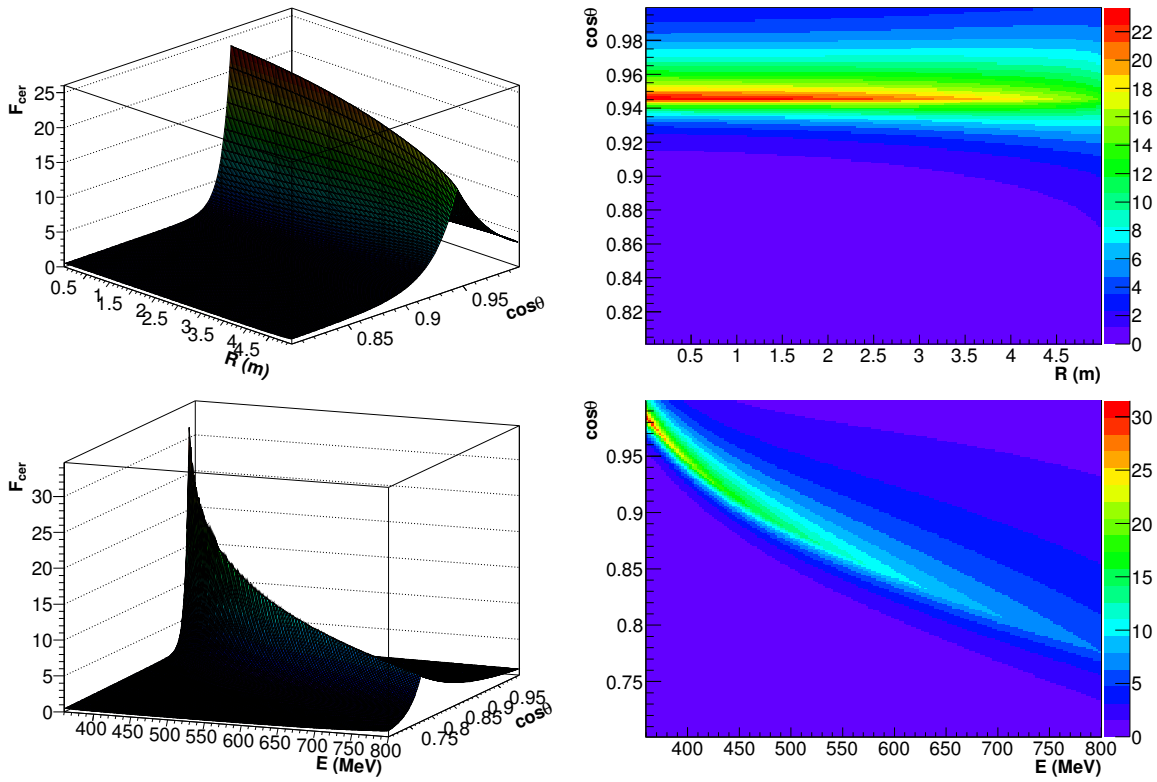


Figure 5.10: Cherenkov angular emission profile as a function of the event radius for protons with $E = 400$ MeV (top plots). Cherenkov angular emission profile as a function of the proton kinetic energy for events with $R = 2$ m (bottom plots)

angular profile, taking a predicted charge model in which

$$\mu_{sci} = \epsilon \Phi_{sci} \frac{\exp(-r/\lambda_{sci}(R))}{r^2} f(\cos\eta) F_{sci}(E, \cos\theta, R), \qquad \int_{-1}^{1} F_{sci}(E, \cos\theta, R) d\cos\theta = 1.0. \quad (5.9)$$

Figs. 5.11 and 5.12 show the scintillation light angular emission profile, $F_{sci}(E, \cos\theta, R)$ for different radial shells, for 200 MeV and 700 MeV protons, respectively. Also, the MC measured scintillation light angular emission profile functions for these energies are shown in Fig. 5.13. As one can notice, low energy protons have a fairly isotropic angular emission profile. However, for higher proton energies, the distributions are forward peaked, especially for the events that happen in the outer regions of the tank.

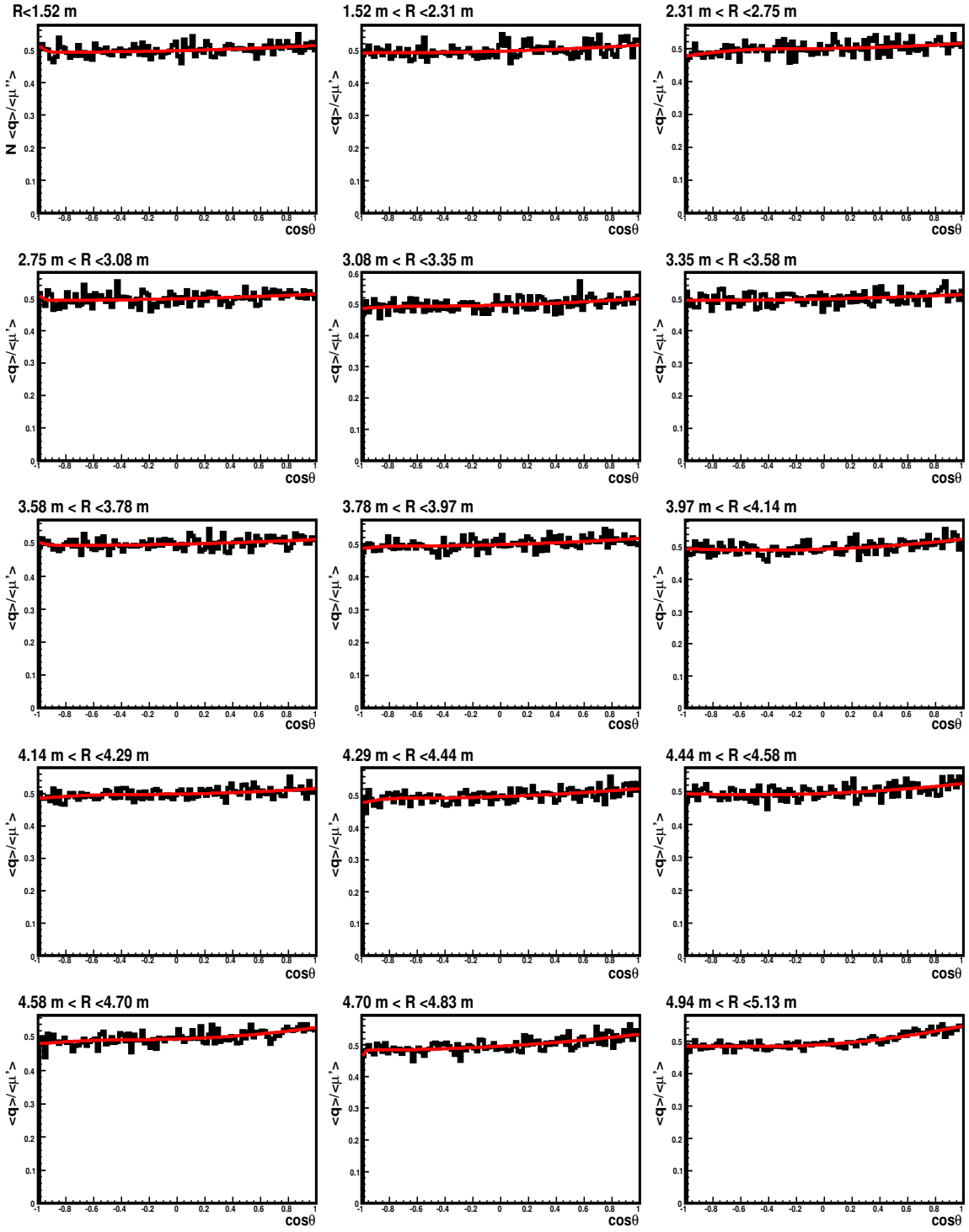


Figure 5.11: Scintillation light angular emission profile for 200 MeV protons inside different radial shells, as labeled.

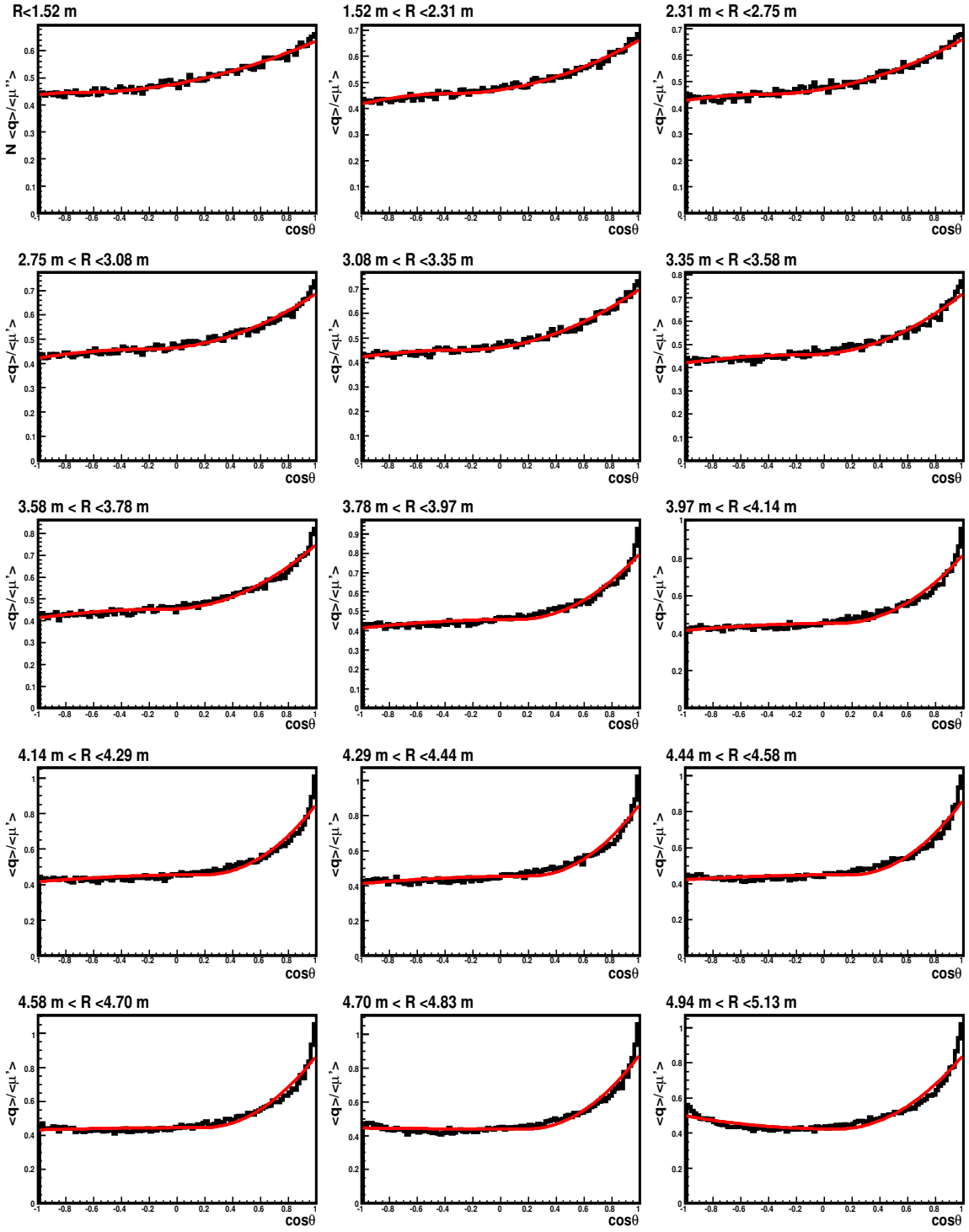


Figure 5.12: Scintillation light angular emission profile for 700 MeV protons inside different radial shells, as labeled.

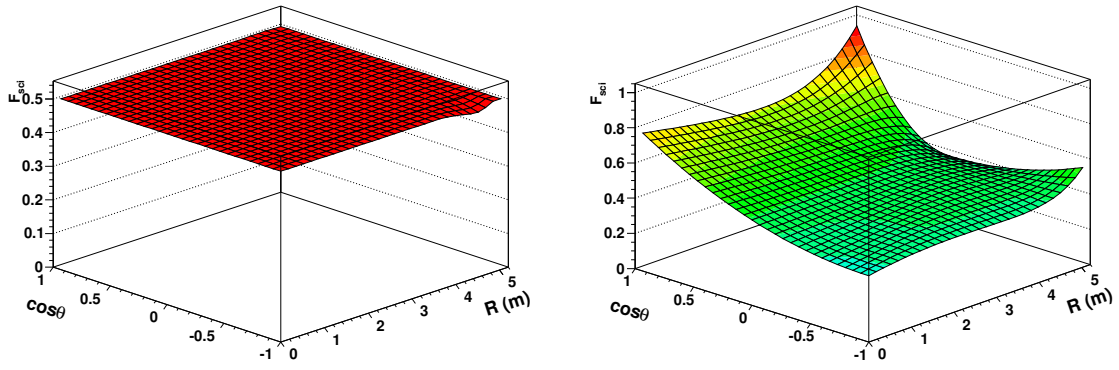


Figure 5.13: Scintillation light angular emission profile as a function of event radius for protons with $E = 200$ MeV (left) and $E = 700$ MeV (right).

### 5.3.4 Corrections for Outgoing Events

Using a predicted charge model for the scintillation light as in Eq.(5.9), one may still find discrepancies between the predicted and the measured charge in the outer regions of the detector. This can be seen in Fig. 5.4, where at the time we used a flat angular emission profile; the ratio of $\langle q(r)\rangle/\langle \mu'(r)\rangle$ is lower than expected for the outer-most shells for $r < 1$ m.

The explanation for this is that sometimes an energetic outgoing proton may leave the tank before it stops and gives up all its energy. Figure 5.14 explains the geometry of such an event. The corrections that we were looking at depend on the energy of the proton, event radius, and the angle $\alpha$ between the event direction and the line from the tank center to the event vertex.

One may expect such corrections to be more significant for the more energetic events, as well as for those events with larger values of $\cos\alpha$. Similarly to what was done in Section 5.3.3, the new predicted charge model for the scintillation light is:

$$\mu_{sci} = \epsilon\Phi_{sci}\frac{\exp(-r/\lambda_{sci}(R))}{r^2} f(\cos\eta)F_{sci}(E,\cos\theta,R)Corr(E,\cos\alpha), \tag{5.10}$$

where $Corr(E,\cos\alpha,R)$ is the correction function for outgoing events. Again, we define $\mu'''_{sci}$ as

$$\mu'''_{sci} = \epsilon\frac{\exp(-r/\lambda_{sci}(R))}{r^2} f(\cos\eta)F_{sci}(E,\cos\theta,R).$$

Then, taking the scintillation light samples of events with different kinetic energy $E$, dividing them

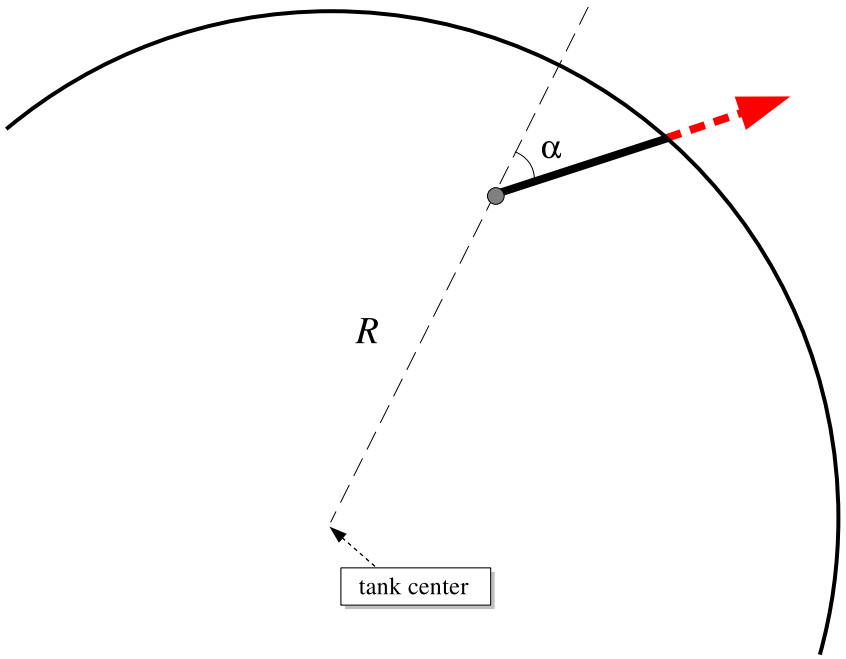


Figure 5.14: A long outgoing event geometry.

also into bins of $\cos\alpha$, and filling histograms of $q(r)$ and $\mu'''(r)$ we obtain the correction function:

$$Corr(E, \cos\alpha) = N \frac{\langle q(r) \rangle}{\langle \mu'''_{sci}(r) \rangle}. \tag{5.11}$$

Figure 5.15 shows these distributions for several values of $E$ and ranges in $\cos\alpha$, as well as the resulting functional fit.

One can see this effect when looking at the $\langle q(r) \rangle / \langle \mu'''_{sci}(r) \rangle$ for different energies and radial shells. As already mentioned, this quantity in principle should be as flat as possible as a function of any geometrical variable. As an example, Figs. 5.16 and 5.17 show these histograms for 700 MeV proton events before and after the correction function is applied, respectively. One may notice that for the outer region events, this distribution is improved for low values of $r$.

For the Cherenkov light, the same correction function was used to correct the predicted charge for the outgoing events, so that the new expression for the Cherenkov light predicted charge reads

$$\mu_{cer} = \epsilon \Phi_{cer} \frac{\exp(-r/\lambda_{cer})}{r^2} f(\cos\eta) F_{cer}(E, \cos\theta, R) Corr(E, \cos\alpha). \tag{5.12}$$

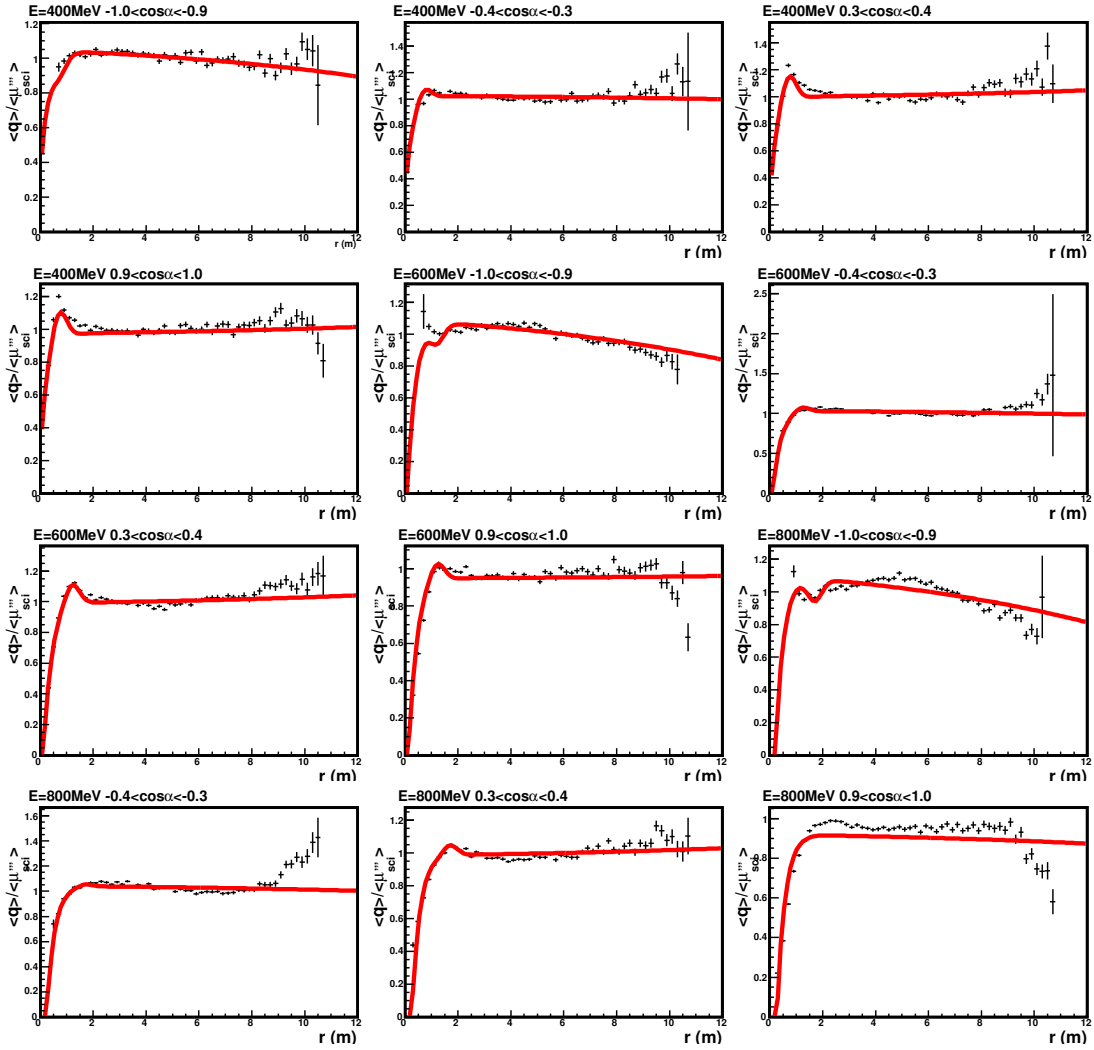


Figure 5.15: Correction function fit from $\langle q(r)\rangle/\langle \mu'''_{sci}(r)\rangle$ histograms for different energies and values of $\cos\alpha$.

### 5.3.5 Scintillation and Cherenkov Fluxes

The last quantity to determine in the expression for the predicted charges in Eqs. (5.10) and (5.12) are the scintillation and Cherenkov fluxes, $\Phi_{sci}$ and $\Phi_{cer}$, as a function of energy. Their physical meaning is that these quantities are proportional to the number of scintillation and Cherenkov photons emitted in the event, which in turn should be correlated with the particle's energy.

These fluxes were extracted by the charge likelihood minimization; the charge likelihood will be described in Section 5.4 and the minimization procedure in Section 5.6. In this case, for the proton events we varied the Cherenkov and scintillation fluxes for the expression of the predicted charge in Eqs. (5.10) and (5.12). A sample of proton events with a flat kinetic energy distribution was

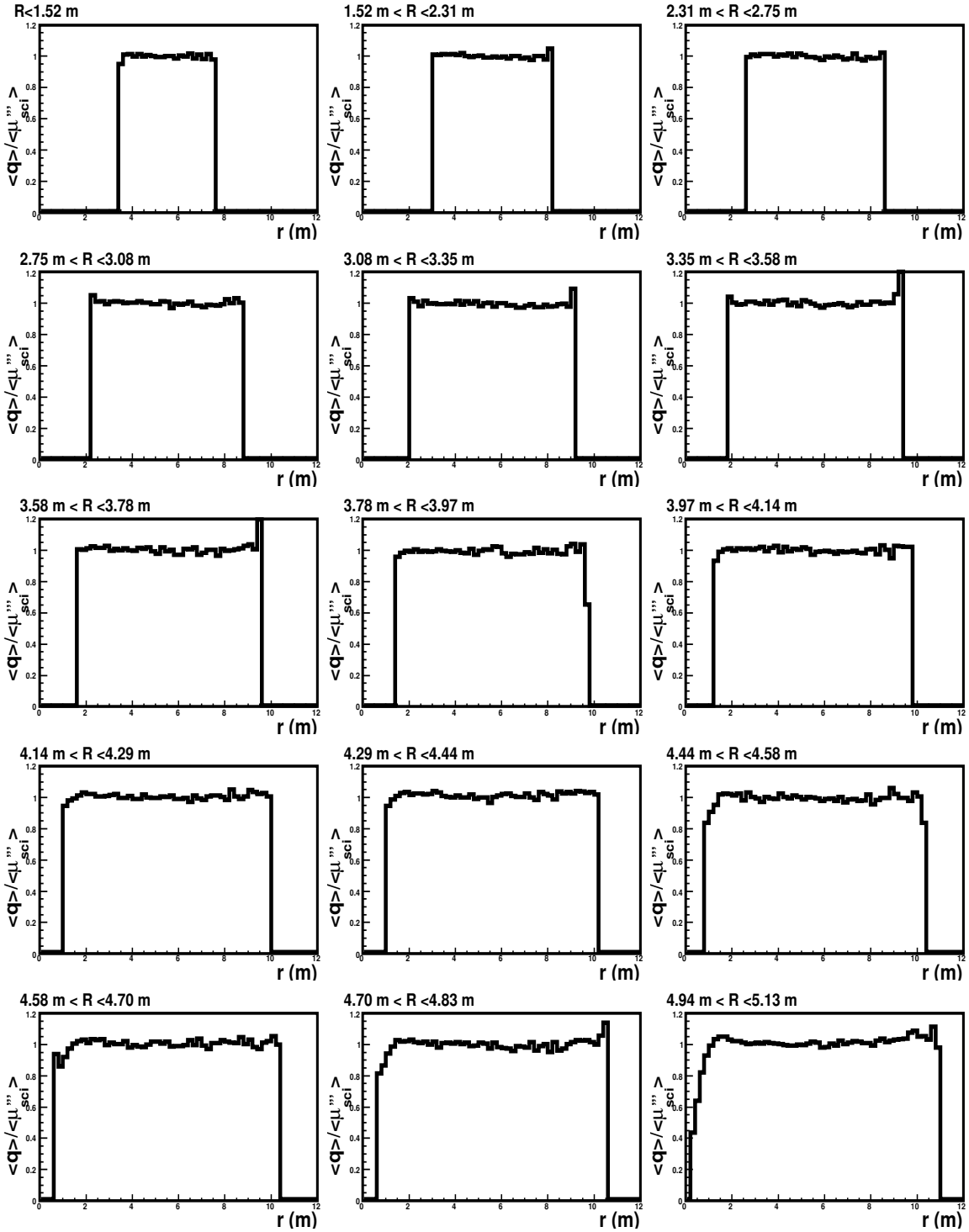


Figure 5.16: $\langle q(r)\rangle/\langle\mu'''_{sci}(r)\rangle$ for scintillation light for 700 MeV protons in different event radial shells before the correction function (5.11) is introduced (predicted charge model from Eq.(5.9)).

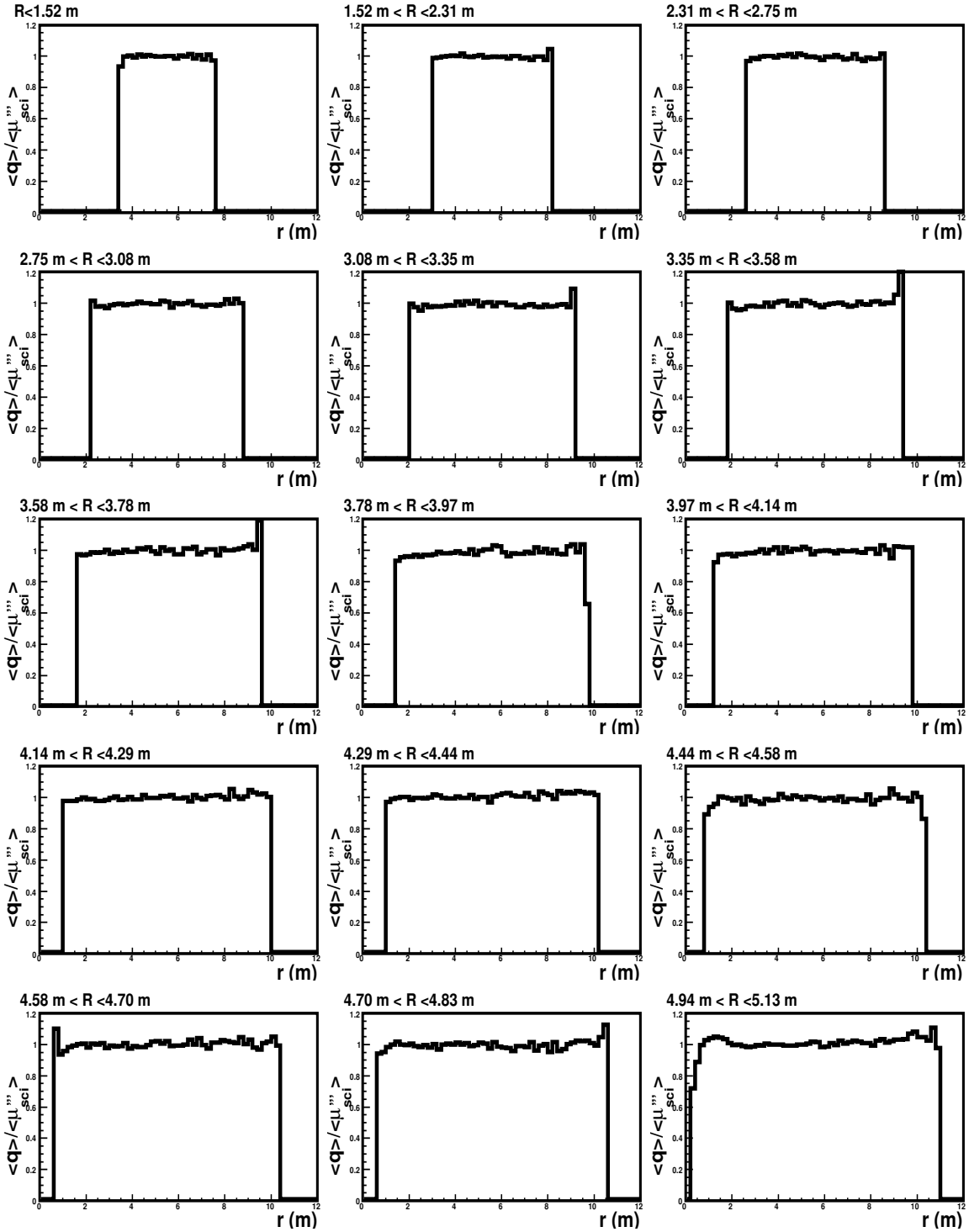


Figure 5.17: $\langle q(r)\rangle/\langle\mu_{sci}(r)\rangle$ for for the scintillation light of 700 MeV protons in different event radial shells after the correction function (5.11) is introduced(predicted charge model from Eq.(5.13)).

used in order to have more bins for the fluxes as a function of energy. The resulting fluxes from the minimization are shown in Figs. 5.18 and 5.19.

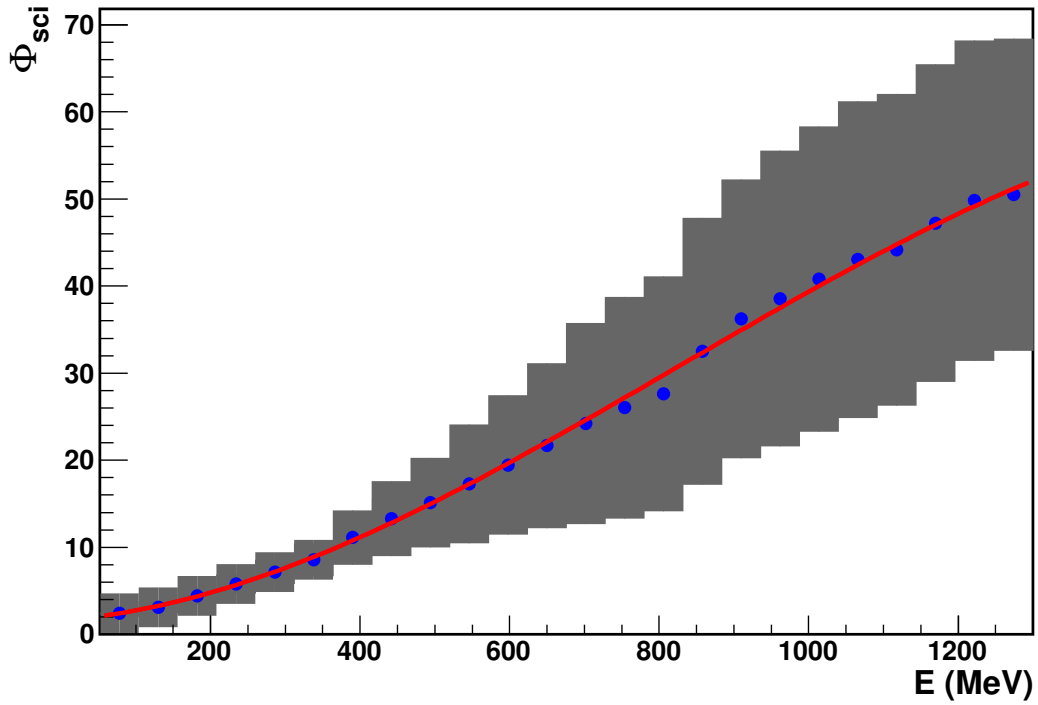


Figure 5.18: Scintillation flux as a function of energy. The error bars represent the RMS of the flux value.

### 5.3.6 The Final Expression for the Predicted Charge

In Section 5.3 the predicted charge model was developed and the methods of obtaining the functions on which these predicted charges may depend were described. Starting with a simple predicted charge model in Section 5.3.2, which included quantum efficiency, attenuation length, and PMT angular response, we have later added angular emission profile for both Cherenkov and scintillation light and corrections for the outgoing events. Finally, the Cherenkov and scintillation light fluxes have been determined in Section 5.3.5.

The final expressions for the Cherenkov and scintillation light predicted charges as a function of the event parameters $\vec{\mathbf{X}}$ are

$$\begin{aligned} \mu_{sci}(\vec{\mathbf{X}}) &= \epsilon\Phi_{sci}(E)\frac{\exp(-r/\lambda_{sci}(R))}{r^2}f(\cos\eta)F_{sci}(E,\cos\theta,R)Corr(E,\cos\alpha), \\ \mu_{cer}(\vec{\mathbf{X}}) &= \epsilon\Phi_{cer}(E)\frac{\exp(-r/\lambda_{cer})}{r^2}f(\cos\eta)F_{cer}(E,\cos\theta,R)Corr(E,\cos\alpha), \end{aligned} \tag{5.13}$$

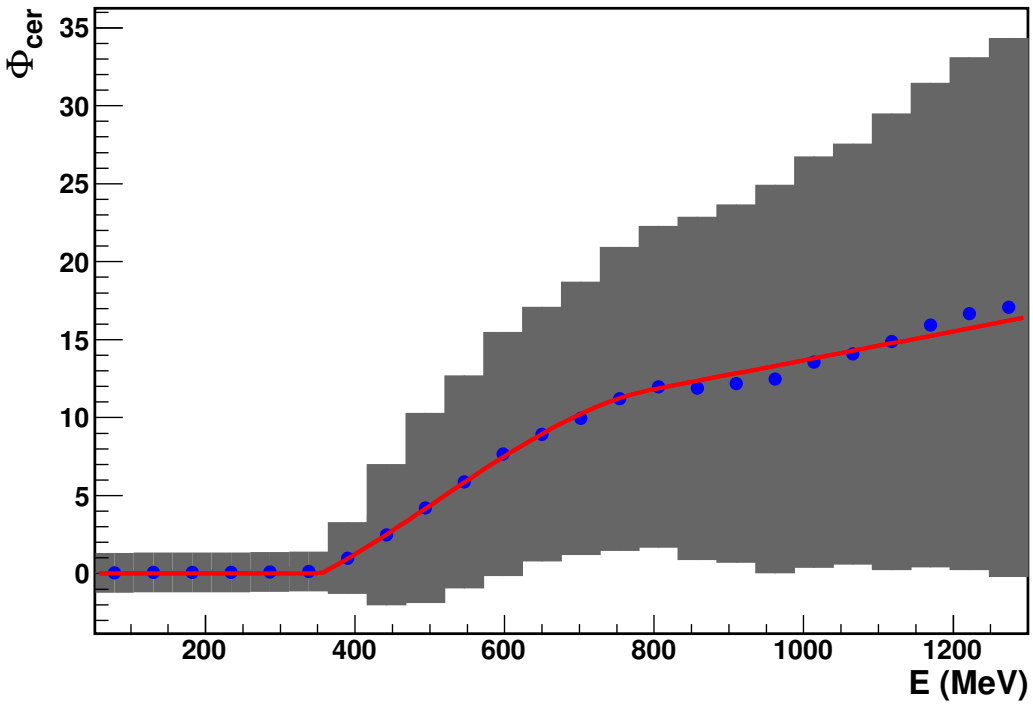


Figure 5.19: Cherenkov flux as a function of energy. The error bars represent the RMS of the flux value.

with the geometrical parameters defined in Figs. 5.1 and 5.14.

## 5.4 Charge Likelihood

In Section 5.3 the predicted charge model was developed. It includes models for both scintillation and Cherenkov light. In this section the charge likelihood function is described in some detail. The event likelihood $F_q$ introduced in Eq.(5.1) is a part of the total event likelihood $F$. The PMT charge likelihood $f_q(q_i;\mu_i)$ is either a probability (for $q = 0$) or a PDF (for $q > 0$) that the $i$-th PMT with a predicted charge $\mu_i$ measures a charge $q_i$. Then $F_q$ is interpreted as a PDF that an event of parameters $\vec{\mathbf{X}}$ produces the given charge pattern for all PMTs.

The charge likelihood $f_q(q > 0;\mu)$ used in this analysis is the standard used by all reconstruction algorithms as developed by Ion Stancu and Yong Liu and obtained from the MiniBooNE laser calibration data [102].

## 5.5 Time Likelihood

The event time likelihood function $F_t$ defined in Eq.(5.1) is the second part of the total event likelihood $F$. In that expression $f_t(t_i; \vec{\mathbf{X}})$ is a PDF that a particular $i$-th PMT would record a photon hit at time $t_i$.

In order to correct for the event time and the time of the photon propagation from the event vertex to the PMT, a corrected time is defined as:

$$t_{corr,i} = t_i - t_0 - \frac{r_i}{c_n}, \tag{5.14}$$

where $t_i$ is the recorded PMT hit time, $t_0$ is the event time, $r_i$ is the distance to the PMT and $c_n = 19.50$ cm/s is the effective speed of light in the mineral oil.

There are two possible sources of photons – from scintillation and from Cherenkov light. Cherenkov light is prompt, meaning that the photons are created directly by the charged particles and start propagating immediately. Thus, for the Cherenkov light the corrected time distribution is expected to be a Gaussian (the width would depend on the timing resolution of the PMT) centered around 0 ns. Scintillation light, on the other hand, is also created by the charged particle, but unlike the Cherenkov light, it has a characteristic time delay of roughly 35 ns. Once the corrected time distributions for both Cherenkov and scintillation light are obtained the total corrected time distribution is calculated as:

$$f_t(t_{corr}, \vec{\mathbf{X}}) = \frac{\mu_{sci}}{\mu_{sci} + \mu_{cer}} f_t^{sci}(t_{corr}, \mu_{sci}, E) + \frac{\mu_{cer}}{\mu_{sci} + \mu_{cer}} f_t^{cer}(t_{corr}, \mu_{cer}, E)$$

In order to obtain the corrected time distributions samples of Cherenkov and scintillation light photons from protons with different energies were used. The corrected time distributions for Cherenkov light from 400 MeV protons are shown in Figs. 5.20 and 5.21 for the old and the new PMTs, respectively. One may notice that most of the Cherenkov light is prompt, however, some PMTs with low values of $\mu_{cer}$ have some delayed photons. This is due to the UV fluorescence light induced by the Cherenkov photons. Just like scintillation light, this fluorescence is delayed with a typical decay time of $\sim 35$ ns. This is a small effect, and therefore, when fitting these corrected time distributions, a Gaussian distribution was used:

$$f_t^{cer}(t_{corr}, \mu_{cer}, E) = \frac{1}{\sqrt{2\pi}\sigma(E, \mu_{cer})} \exp\left[ -\frac{(t_{corr} - t_0(E, \mu_{cer}))^2}{2\sigma(E, \mu_{cer})^2} \right].$$

The fit parameters for the Cherenkov light corrected time distributions as a function of $\mu_{cer}$ are shown in Fig. 5.22. As one can see from the figure, MINUIT returns large errors on both $t_0$ and $\sigma$. Then, the best fit points as a function of $\mu_{cer}$ are used in another fit to obtain the analytical dependence $t_0(\mu_{cer})$ and $\sigma(\mu_{cer})$ for a particular energy $E$.

As already mentioned the scintillation light is delayed with a typical decay time of $\sim$ 35 ns. For fitting the corrected time distributions the following functional was used initially, which is an exponential function folded with a Gaussian:

$$f_t^{sci}(t_{corr}) \quad = \quad \frac{1}{2\tau} \exp\left(\frac{\sigma^2}{2\tau^2} - \frac{t_{corr}-t_0}{\tau}\right) \mathrm{Erfc}\left[\frac{\sigma}{\sqrt{2}\tau} - \frac{t_{corr}-t_0}{\sigma}\right]$$

where Erfc is the complementary error function [117], defined as

$$\mathrm{Erfc}(x) = 1 - \mathrm{Erf}(x), \qquad \mathrm{Erf}(x) = \frac{2}{\sqrt{\pi}} \int_0^x e^{-t^2} dt.$$

The time slewing $t_0$, time resolution $\sigma$, and decay time $\tau$ are also functions of $E$ and $\mu_{sci}$. They are to be obtained from fitting the corrected time distribution for different energies in bins of $\mu_{sci}$.

The fitting function was later modified to include two exponentials with different decay constants for a better fit. The expression for the scintillation corrected time function that was used for the final fit:

$$\begin{aligned} f_t^{sci}(t_{corr}, \mu_{sci}, E) \quad = \quad & (1-B) \quad \frac{1}{2\tau_1} \exp\left(\frac{\sigma^2}{2\tau_1^2} - \frac{t_{corr}-t_0}{\tau_1}\right) \mathrm{Erfc}\left[\frac{\sigma}{\sqrt{2}\tau_1} - \frac{t_{corr}-t_0}{\sigma}\right] \\ + \quad & B \quad \frac{1}{2\tau_2} \exp\left(\frac{\sigma^2}{2\tau_2^2} - \frac{t_{corr}-t_0}{\tau_2}\right) \mathrm{Erfc}\left[\frac{\sigma}{\sqrt{2}\tau_2} - \frac{t_{corr}-t_0}{\sigma}\right], \end{aligned} \tag{5.15}$$

where $t_0 = t_0(\mu_{sci}, E)$, $\sigma = \sigma(\mu_{sci}, E)$, $\tau_1 = \tau_1(\mu_{sci}, E)$, $\tau_2 = \tau_2(\mu_{sci}, E)$, $B = B(\mu_{sci}, E)$. The fitting procedure was done for the new and old PMTs independently.

The scintillation corrected time distributions for a sample of 400 MeV proton events (after excluding Cherenkov photons) for different ranges of $\mu_{sci}$ are shown in Figs. 5.23 and 5.24. Obtaining the functional dependencies for the corrected time parameters on $\mu_{sci}$ is slightly more complicated in this case, due to a more complex corrected time distribution, a larger number of parameters to vary, and correlations between them. A step-by-step fitting procedure is used, where some parameters are kept fixed and only a reduced set can vary freely. Then, the best fit parameters for each $\mu_{sci}$ range are used to find their functional dependence. For example, in Fig. 5.25, $t_0$ and $\sigma$ were released and

all were fixed to a given analytical form, as shown in the same figure. The procedure is repeated until the functional dependence on each parameter converges.

## 5.6 MINUIT Minimization

Now that the event likelihood $F(\vec{\mathbf{X}})$ in Eq.(5.1) is fully defined, a minimization procedure needs to be used in which the fitter finds a value $\vec{\mathbf{X}}_0$ which gives the minimum of $F(\vec{\mathbf{X}})$ among all possible values of $\vec{\mathbf{X}}$. For this purpose the standard minimization package MINUIT was used [118].

MINUIT is a tool to find the minimum value of a multi-parameter function and analyze the shape of the function around the minimum. The principal application is to compute the best-fit parameter values and uncertainties, including correlations between the parameters. It is especially suited to handle difficult problems, including those which may require guidance in order to find the correct solution. MINUIT requires the following inputs:

1. the user defined minimization function;
2. the total number of parameters to vary;
3. the lower and upper limit values for each parameter (optional);
4. the step size for each parameter (initial guess for a possible uncertainty);
5. the tolerance on the function value at the minimum;
6. maximum number of iterations (used in case MINUIT cannot converge to the minimum fast enough).

As discussed in Section 5.1, there are 7 parameters fitted in the proton hypothesis reconstruction, namely the position, time, energy and direction. It would be difficult for MINUIT to find the global minimum for the event likelihood for such a large space of $\vec{\mathbf{X}}$. Thus, a step-by-step minimization is used, gradually localizing $\vec{\mathbf{X}}$ to eventually find the global minimum. The tolerance and step size for each parameter were optimized to give the best reconstruction performance.

**Initial guess for the position and time**

The initial guess for the position of the event is the charge-averaged position:

$$\vec{R}_{initial} = \frac{1}{Q}\sum_i q_i \vec{r}_i,$$

where $Q$ is the total charge, $\vec{r}_i$ is the global position of the $i$-th PMT and $q_i$ is its charge. Once $\vec{R}_{initial}$ is calculated, the following formula is used for the initial guess of the event time:

$$T_{initial} = \frac{1}{N} \sum_{i,q_i>0} \left( t_i - \frac{|\vec{R}_{initial} - \vec{r}_i|}{c_n} \right),$$

where $t_i$ is the global time of the PMT hit and $N$ is the total number of PMTs that have been hit.

**First fit: event 4-vertex**

In the first minimization the event is assumed to have only scintillation light, for which the direction doesn't matter much. Thus, keeping Cherenkov light flux $\Phi_{cer}$ to be identically zero, the event likelihood is minimized by varying only 4 parameters – the position and time. For the energy of the event a function of total charge and the event radius is used,

$$E = E(Q, R). \tag{5.16}$$

To obtain this function, a 2-dimensional profile histogram for the $Q = Q(E, R)$ was filled, which gives the average total charge for events with energy $E$ and radius $R$. Then the function was converted to $E = E(Q, R)$, as shown in Fig. 5.26.

After this first minimization the output parameters are the event 4-vertex, $X_0$, $Y_0$, $Z_0$, $T_0$.

**Second fit: event 4-vertex and direction**

Next, we are ready to include the direction reconstruction into the fit. But first one needs to find the initial guess for the direction; again, the charge-averaged direction is used for this purpose:

$$\vec{U}_0 = \frac{1}{Q} \sum_i q_i \frac{\vec{r}_i - \vec{R}_0}{\left| \vec{r}_i - \vec{R}_0 \right|},$$

The input parameters for the vertex are those from the previous fit, namely $X_0$, $Y_0$, $Z_0$, $T_0$.

In this step, six parameters are varied: $x$, $y$, $z$, $t$, $\phi$ and $\theta$. The energy is kept as a function of $Q$ and $R$ as in Eq.(5.16) and Fig. 5.26. Also, at this stage we try several different starting directions – by rotating the initial direction guess. After each independent minimization the functional values at the minimum are compared to find the one that gives the lowest value. The idea of this procedure is to avoid MINUIT finding a local minimum and probing the likelihood function around it. Here

we are probing different locations, where better minima may be found.

After this minimization step the output parameters are the event 4-vertex and direction, $X_1$, $Y_1$, $Z_1$, $T_1$, $\Phi_1$, and $\Theta_1$.

**Third fit: the full fit**

The input parameters are taken from the previous fit: $X_1$, $Y_1$, $Z_1$, $T_1$, $\Phi_1$, $\Theta_1$ and the energy as $E_1 = E(Q, R_1)$. At this stage the energy parameter is added to the fitting. Thus, the full fit is performed with all 7 parameters varied: $x$, $y$, $z$, $t$, $\phi$ and $\theta$ and $E$. After this step the output parameters are the event 4-vertex and direction, and energy, $X_2$, $Y_2$, $Z_2$, $T_2$, $\Phi_2$, $\Theta_2$ and $E_2$.

**Final fit: improving the direction and energy**

At this stage the functional tolerance is decreased from $10^{-3}$ to $10^{-6}$ and only the direction and energy are varied to improve the values for these parameters. The position and time are being kept fixed with the values $X_2$, $Y_2$, $Z_2$, $T_2$, as found in the previous step. After the final fitting, the following output variables of NCFitter are returned:

- NCFitterT (reconstructed time),
- NCFitterX, NCFitterY, NCFitterZ (reconstructed event position),
- NCFitterUX, NCFitterUY, NCFitterUZ (reconstructed event direction),
- NCFitterE (reconstructed nucleon energy),
- NCFitterQLLK (event charge likelihood),
- NCFitterTLLK (event time likelihood).

We shall also refer to the reconstructed event radius as NCFitterR.

## 5.7 Event Reconstruction Performance

In this section the fitter performance for reconstructing proton events is described in terms of the main kinematic quantities, such as position, direction, time, and energy. For this study proton events with a flat kinetic energy spectrum from 100 MeV to 800 MeV were used.

The time resolution, which is the difference between the true and reconstructed event time, is shown in Fig. 5.27. As indicated in the plot, the uncertainty in the event time is about 1.5 ns.

The position resolution is an important quantity because, as will be described in Chapter 6, one of the most important backgrounds is the neutrino scattering that happens outside of the detector with particles created by the interaction penetrating inside the detector. These background events have a different spatial reconstructed distribution than the in-tank events. A good position reconstruction is useful in either removing these events by a fiducial volume cut or measuring these events. The position resolution is shown in Fig. 5.28. From the plot one can find that the typical uncertainty in the position reconstruction is $\sim 0.75$ m, which is a substantial improvement from $\sim 1.2$ m when using the MiniBooNE electron hypothesis fitter to reconstruct proton events. Also, one can see that there is no systematic shift in any coordinate for any value of the energy. The uncertainty in the position reconstruction stays roughly the same as a function of the proton energy.

The direction resolution, shown in Fig. 5.29, is very important for particle identification, which is needed for constraining the proton events. Furthermore, NCE events are kinematically more forward going than background events, which may also allow for additional constraints for the NCE events, as will be discussed in Chapter 8. In Fig. 5.29, $\phi$ is the angle between the true and reconstructed proton directions. Below Cherenkov threshold ($T < 350$ MeV) it is impossible to reconstruct the proton direction. As can be observed from the right plot, the mean value of $\phi$ is $90^o$, which means that the reconstructed direction for these events is random. However, once protons are energetic enough to produce Cherenkov light, the fitter picks up the Cherenkov cone and reconstructs their direction reliably enough. Thus, in the left plot the angular resolution is illustrated only for events above the Cherenkov threshold, 350 MeV $< E <$ 800 MeV.

A good energy reconstruction is most important when measuring differential cross-sections. The energy resolution for proton events in MiniBooNE is shown in Fig. 5.30. From the top left plot one can see that most of the events are well reconstructed. However, some protons may strongly reinteract inside the detector, producing other hadrons and losing energy. One can also observe such events with much lower reconstructed energy than the generated one. From the bottom plot one can see that the typical energy resolution for protons is $\sim 20\%$.

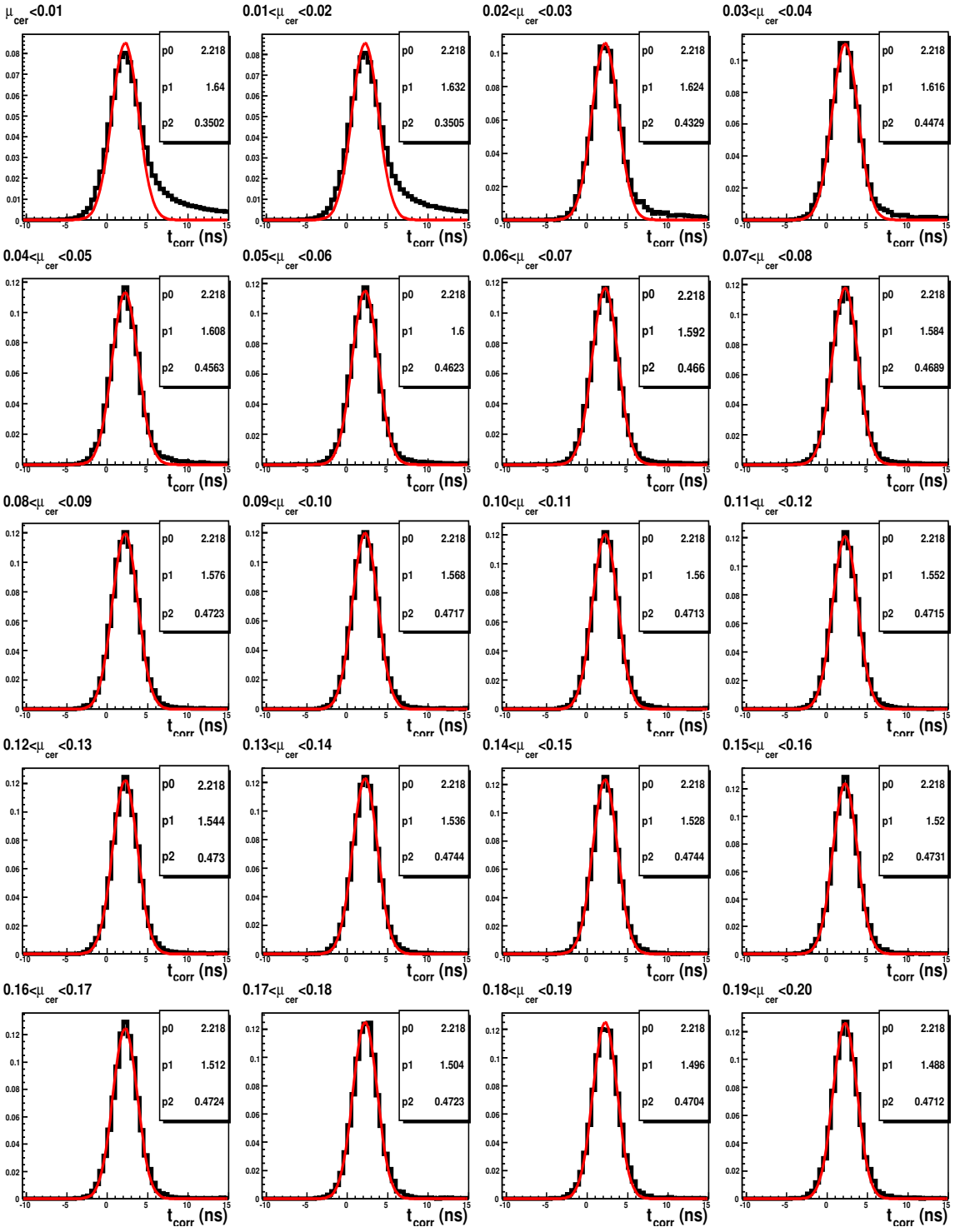


Figure 5.20: Cherenkov light corrected time distribution for old PMTs for different $\mu_{cer}$ ranges obtained from $E = 400$ MeV protons. The fit is to a Gaussian with $t_0$ and $\sigma$ being $p_0$ and $p_1$, respectively, and $p_2$ is a normalization factor.

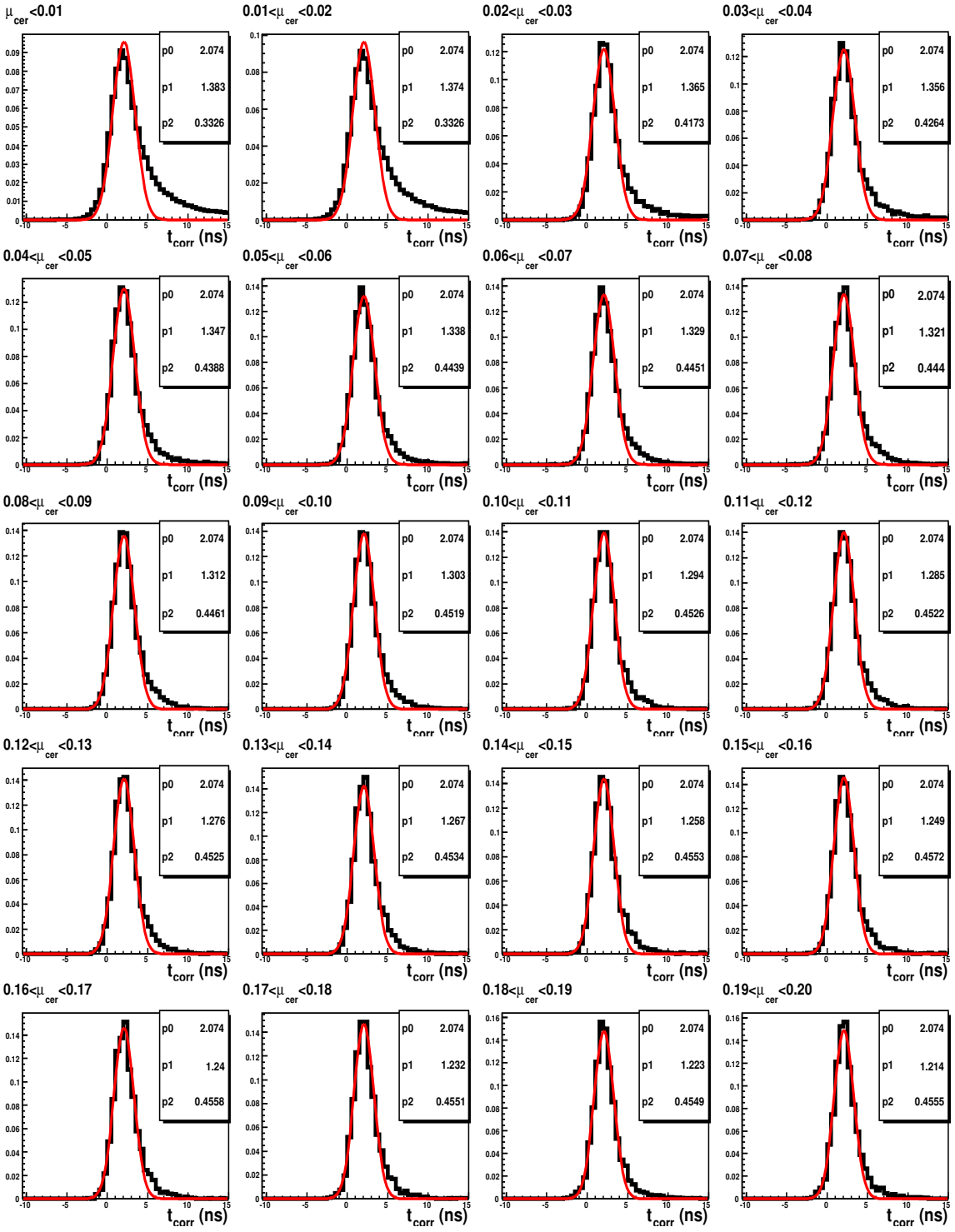


Figure 5.21: Cherenkov light corrected time distribution for new PMTs for different $\mu_{cer}$ ranges obtained from $E = 400$ MeV protons. The fit is to a Gaussian with $t_0$ and $\sigma$ being $p_0$ and $p_1$, respectively, and $p_2$ is a normalization factor.

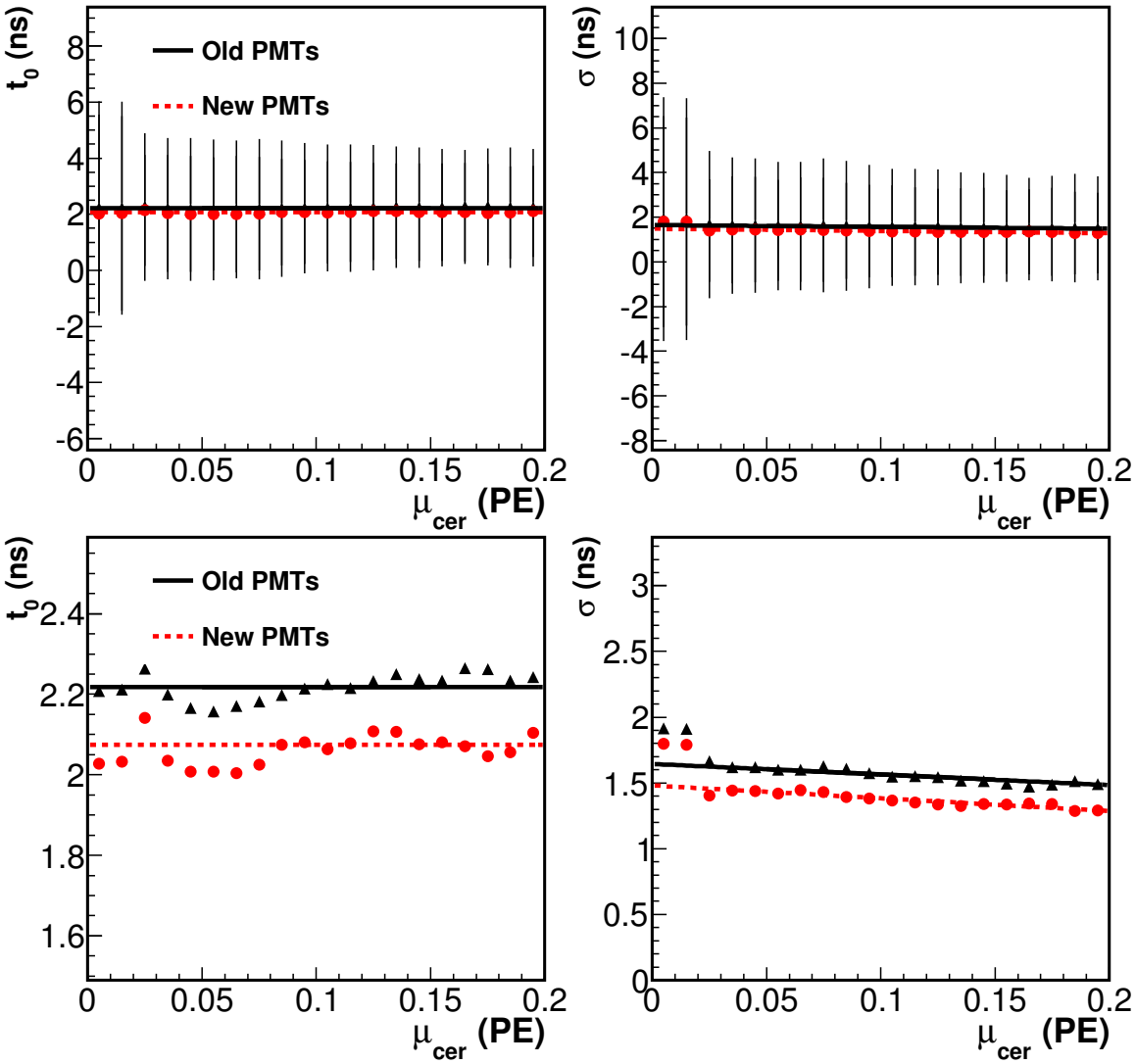


Figure 5.22: Cherenkov light corrected time parameters as a function of the predicted charge for the new (red dashed) and the old (black solid) PMTs, respectively. Top plot is with errors on the parameters as returned by MINUIT, whereas the bottom plot shows the best fit parameter values without errors.

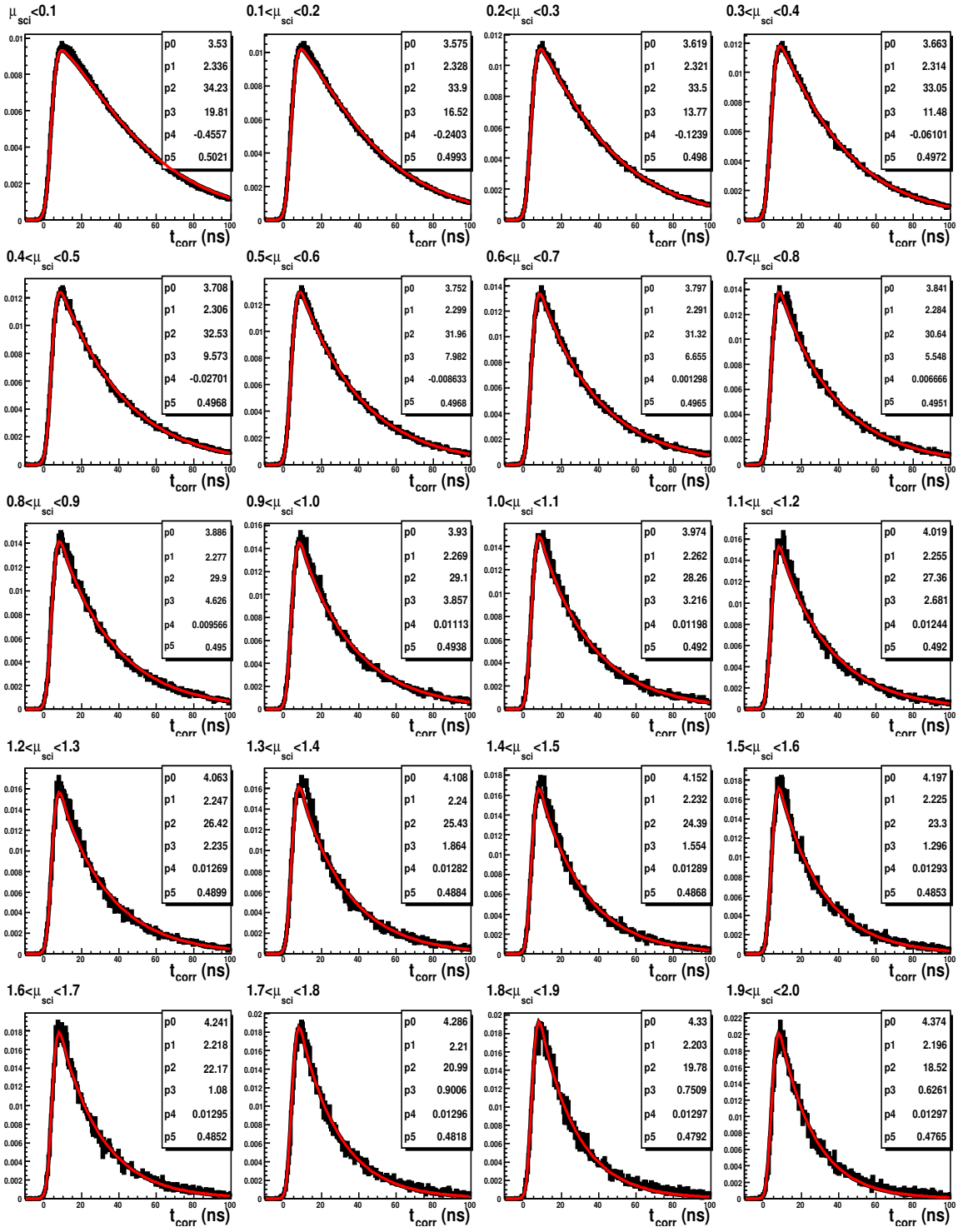


Figure 5.23: Scintillation light corrected time distribution for old PMTs for different $\mu_{sci}$ ranges obtained from $E = 400$ MeV protons. The fit is to the function in Eq.(5.15) with $t_0$, $\sigma$, $\tau_1$, $\tau_2$, $B$ being $p_0, \ldots, p_4$, respectively, while $p_5$ is a normalization factor.

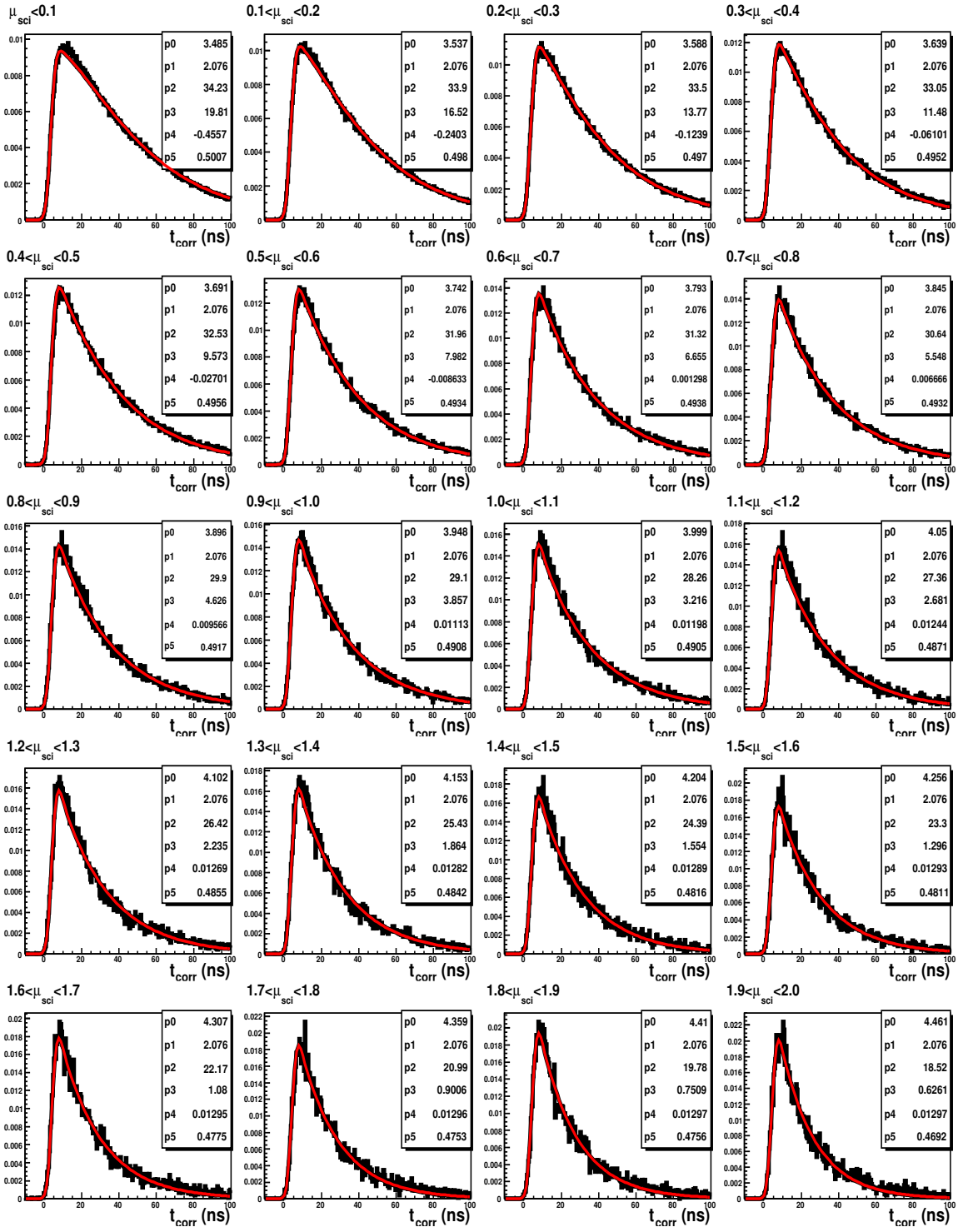


Figure 5.24: Scintillation light corrected time distribution for new PMTs for different $\mu_{sci}$ ranges obtained from $E = 400$ MeV protons. The fit is to the function in Eq.(5.15) with $t_0$, $\sigma$, $\tau_1$, $\tau_2$, $B$ being $p_0, \ldots, p_4$, respectively, while $p_5$ is a normalization factor.

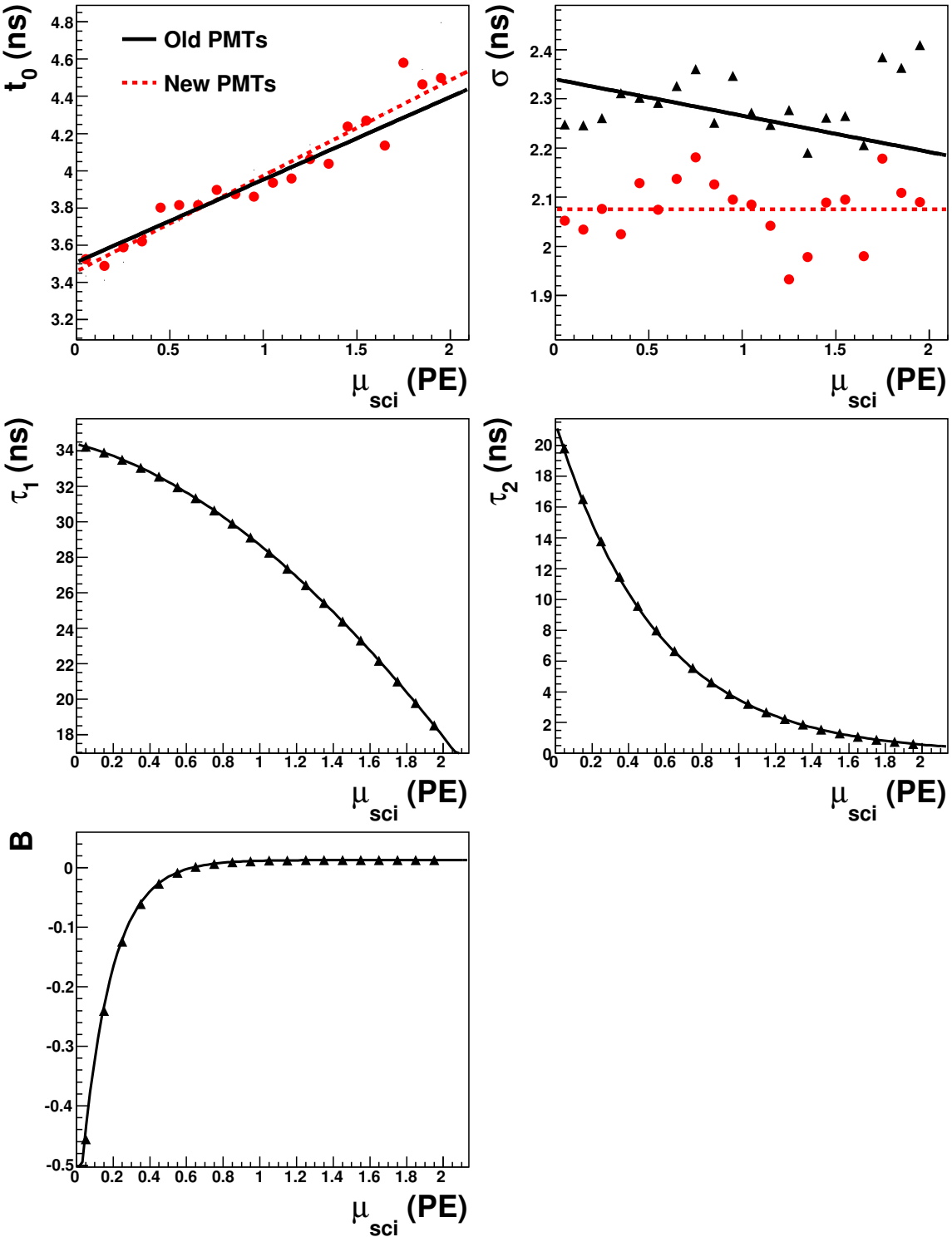


Figure 5.25: Scintillation light corrected time parameters as a function of the predicted charge. The top two distributions, $t_0$ and $\sigma$, are shown for the new (red dashed) and the old (black solid) PMTs, respectively. The errors for $t_0$ and $\sigma$ not shown here are on the order of 10 ns for both. $\tau_1$, $\tau_2$ and $B$ parameters are the same for the new and old PMTs and shown here without errors, after smoothing.

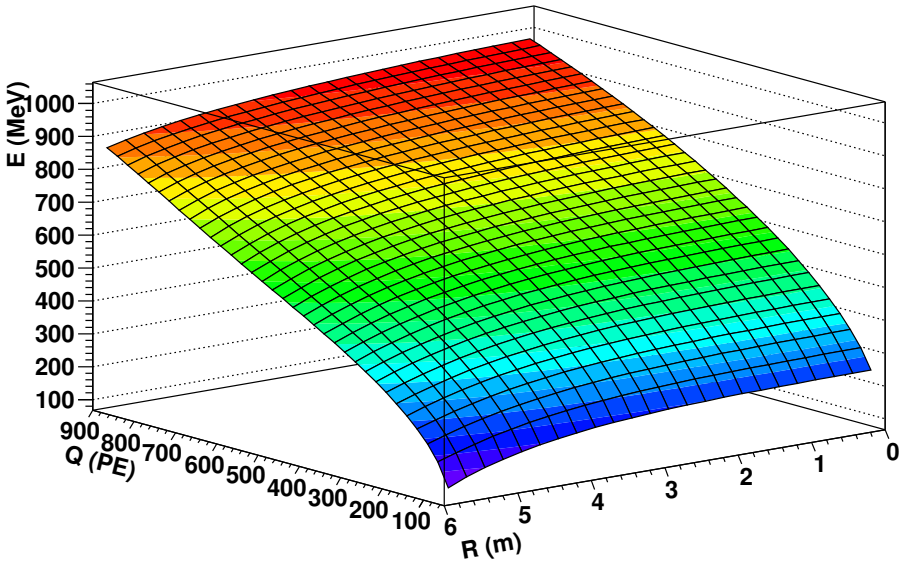


Figure 5.26: Energy as a function of the event radius and total charge.

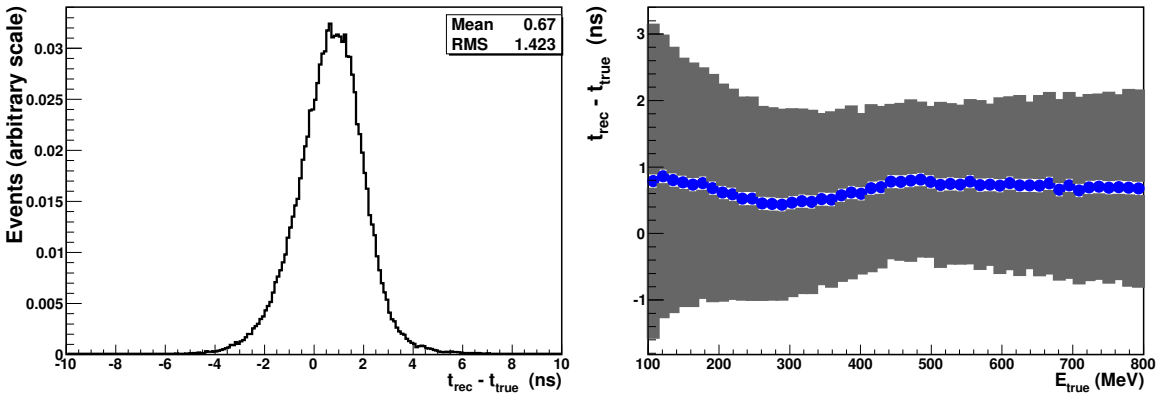


Figure 5.27: Time resolution, the difference between true and reconstructed event time for all proton events in the sample, relatively normalized (left). Time resolution as a function of the kinetic energy (right); the error bars correspond to the RMS in each bin.

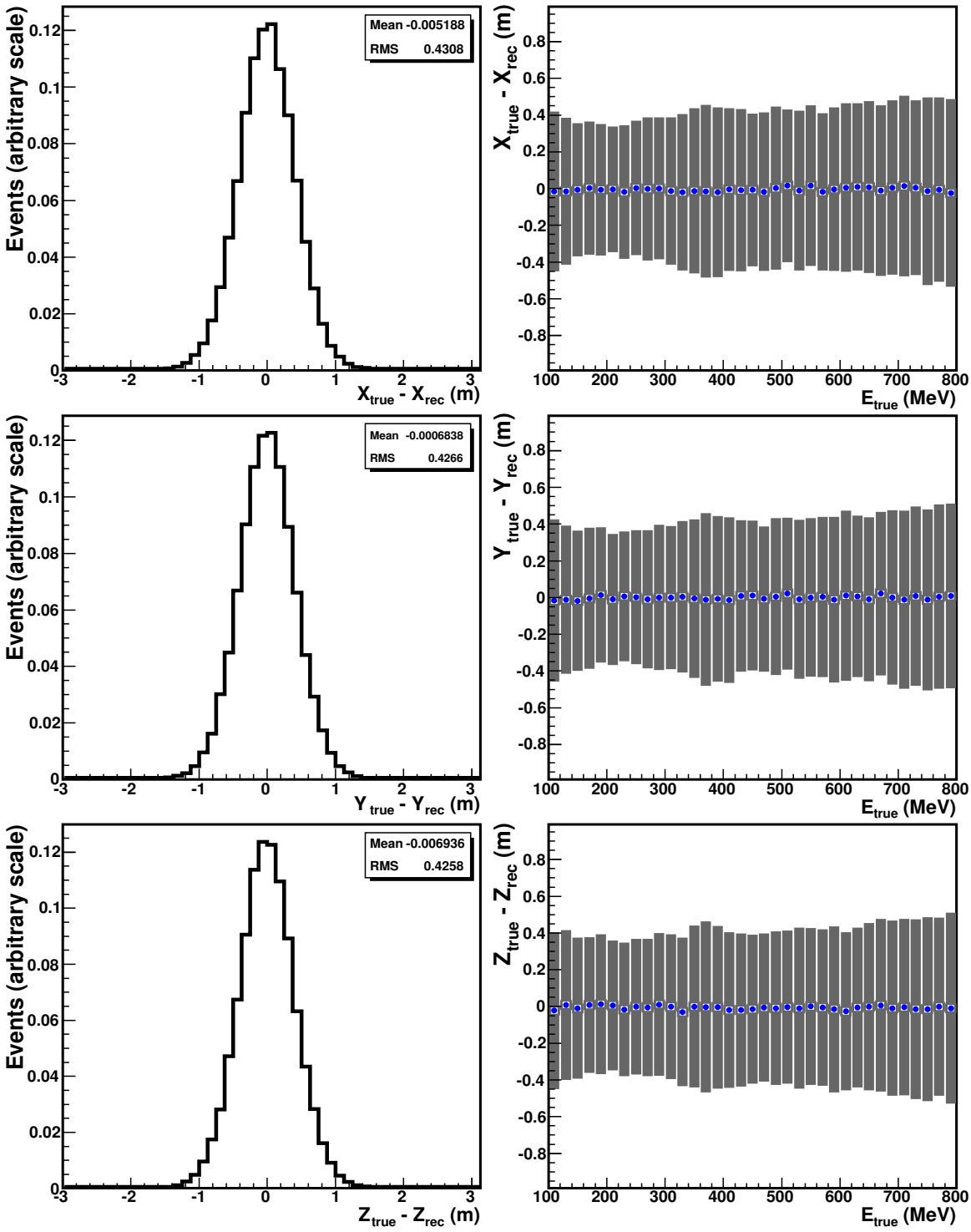


Figure 5.28: Position resolution for $X$, $Y$ and $Z$, respectively, for all proton events in the sample, relatively normalized (left column). Position resolution versus the proton kinetic energy (right column; error bars are RMS).

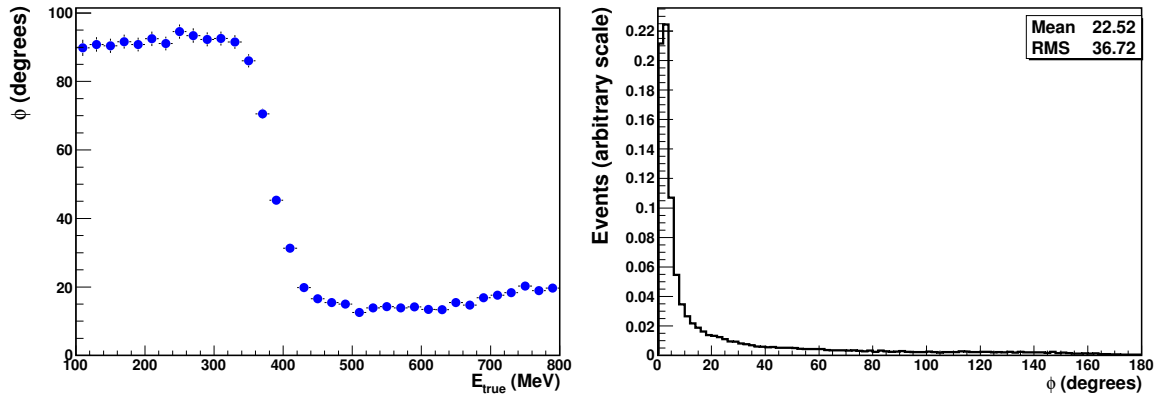


Figure 5.29: Direction resolution as a function of the kinetic energy (left). Direction resolution with $\phi$ as the angle between the true and reconstructed directions for proton events with 350 MeV< $E$ <800 MeV kinetic energy, relatively normalized (right).

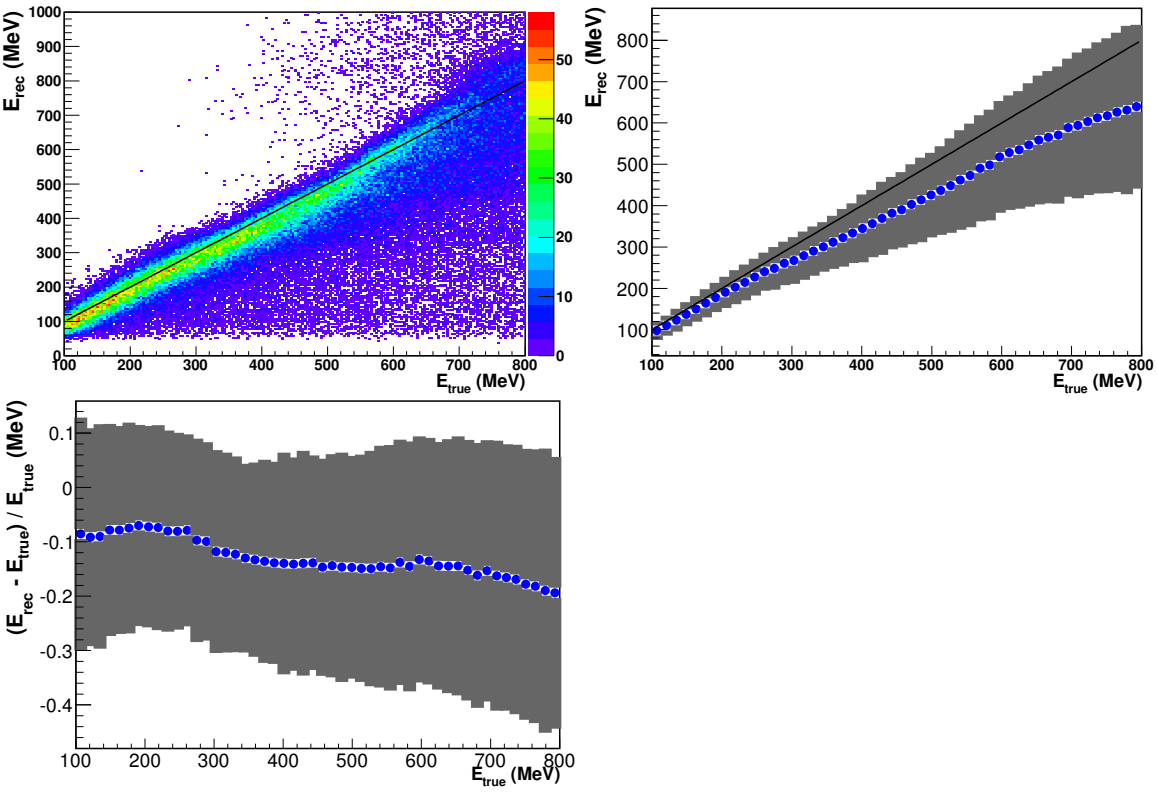


Figure 5.30: Reconstructed versus true proton kinetic energy (top left). The true vs reconstructed proton kinetic energy profile histogram with error bar as RMS (top right). The black lines on the top plots indicate the $E_true = E_{rec}$ line. The energy resolution, $(E_{rec} - E_{true})/E_{true}$, as a function of true proton kinetic energy (bottom).

# Chapter 6

# MiniBooNE NCE cross-section measurement

## 6.1 Introduction

NCE scattering is an interaction in which a neutrino exchanges a neutral boson with a nucleon, $\nu N \rightarrow \nu N$, and both particles remain in the same state. When it occurs, all one can see in the detector is usually one or multiple nucleons (the latter are due to final state interactions).

It is obviously important to distinguish nucleons from other energetic particles that may be produced in the detector through other channels, such as muons and pions. Recalling Fig. 4.17, where the neutrino event composition chart in MiniBooNE is shown, one can see that these particles are produced in CCQE and CCPi+ channels, the most dominant channels in MiniBooNE, thus initially the biggest NCE background. As explained in Section 4.4.3, most of muons produced by the $\nu_\mu$ beam ($\nu_\mu C \rightarrow \mu^- X$) stop and decay with a lifetime of $\tau \sim 2.2$ $\mu$s:

$$\mu^- \rightarrow e^- + \bar{\nu}_e + \nu_\mu.$$

The resulting electrons have a continuous spectrum [104] with a maximum energy of half the muon rest mass, $E_{max} = 52.8$ MeV. MiniBooNE is able to detect electrons with a minimum energy of 10 MeV (which produce $\sim 10$ tank PMT hits). Thus, these Michel electrons are usually observed in the MiniBooNE detector. However, there is also about 8% chance of a muon capture on either

carbon or hydrogen (the former dominates) [119, 120], in which case no electron is produced.

Charged pions (from the CCPi+ channel) 99.9877% of the time it decay into a muon and neutrino:

$$\pi^+ \rightarrow \mu^+ + \nu_\mu.$$

The muon produced in the process eventually decays as explained earlier.

The best way to eliminate backgrounds which have a muon (charged current interactions) or a charged pion in the final state is to apply a veto cut and apply a one subevent only cut (as described in Section 6.2). The veto cut limits the amount of PMTs which fire in the veto region and thus removes muons and pions either entering or escaping the tank. The one subevent cut removes events with subsequent decays in the tank.

When studying NCE one should look for 1-subevent events which have a low number of tank hits (or a low total charge), because nucleons do not produce as much light as muons, electrons or pions. Furthermore, they do not produce multiple subevents; The only possibility for the second subevent to occur in a NCE reaction is the production of 2.2 MeV gamma when the stopped neutron is captured by hydrogen in the reaction $n + p \rightarrow d + \gamma$. The neutron lifetime in oil is 186 $\mu s$, whereas the DAQ window is only 20 $\mu s$ long, which opens with typically 5 $\mu s$ before the beam window, thus leaving only 15 $\mu s$ to register the gamma. Therefore, only about 8% of the gammas can be recorded. Moreover, 2.2 MeV gamma produces approximately only 5 tank hits, whereas the standard setting for a subevent requires at least 10 tank hits within a very short time window. Thus, neutron identification through the 2.2 MeV capture gamma is essentially impossible in MiniBooNE.

The expected kinetic energy spectrum of nucleons for NCE events is shown in Fig. 6.1. Since multiple nucleons may be produced in the reaction due to FSI, the sum of kinetic energies of all nucleons in the reaction is plotted; for the same reason we define whether the event is NCE proton or neutron by the most energetic nucleon in the reaction.

## 6.2 Subevents

A *subevent* is a cluster of at least 10 tank PMT hits for which there is no more than 10 ns between any two consecutive hits. The subevents must happen in the same DAQ window to count as subevents

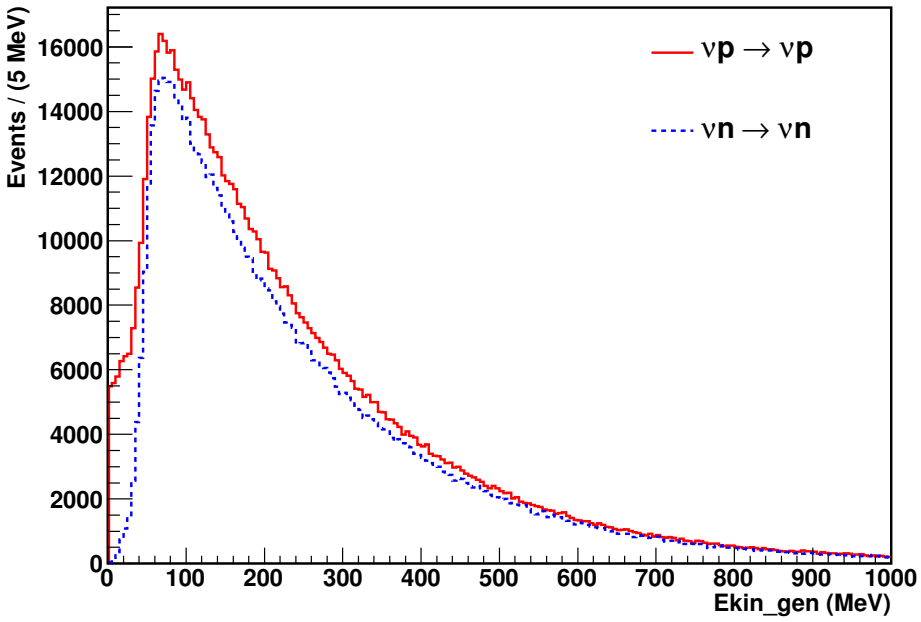


Figure 6.1: Nucleons true energy spectrum of nucleons from NCE scattering in MiniBooNE according to the MC simulation. The distributions are normalized to the same number of protons on target.

of the same event. For example, a CCQE event typically has two subevents:

$$\nu_\mu + n \xrightarrow{1} \mu^- + p$$
$$\mu^- \xrightarrow{2} e^- + \bar{\nu}_e + \nu_\mu$$

The first subevent is associated with a primary neutrino interaction where a muon and a proton are produced. The second subevent is associated with the decay electron. Since the muon lifetime is relatively short, compared to the DAQ time window, both subevents occur in the same DAQ window. A PMT hit time distribution for a typical CCQE candidate event is shown in Fig. 6.2.

Particles produced in CCPi+ event undergo a series of decays:

$$\nu_\mu + N \xrightarrow{1} \pi^+ + \mu^- + N$$
$$\mu^- \xrightarrow{2} e^- + \bar{\nu}_e + \nu_\mu$$
$$\pi^+ \xrightarrow{3} \nu_\mu + \mu^+$$
$$\mu^+ \xrightarrow{3} e^+ + \nu_e + \bar{\nu}_\mu$$

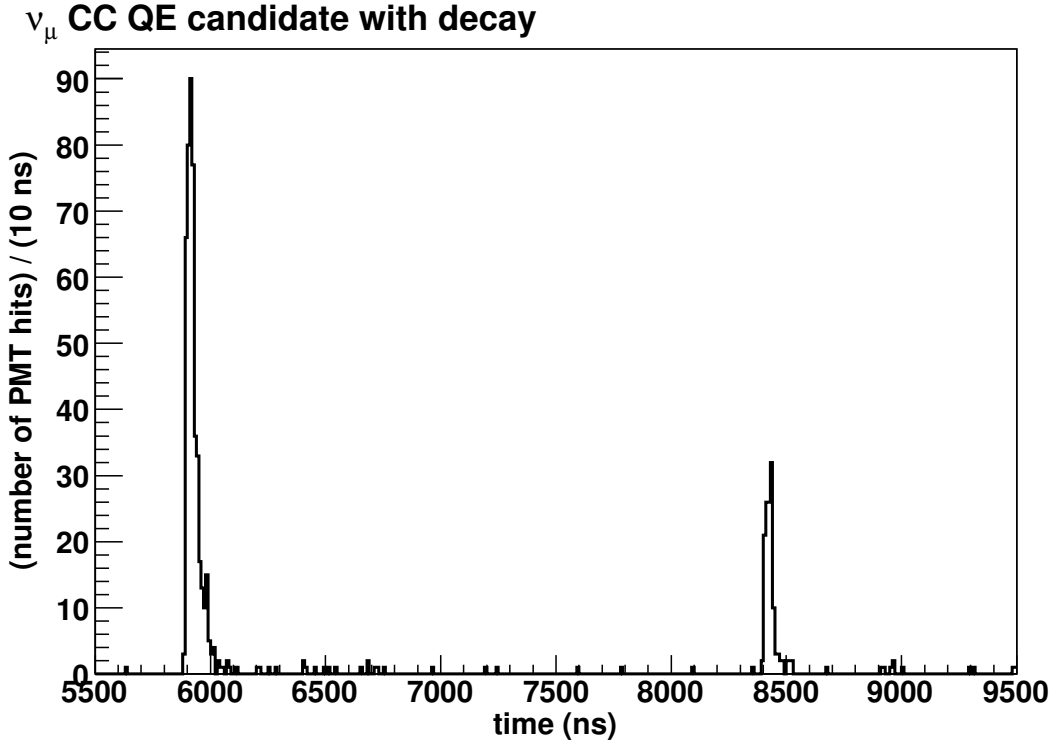


Figure 6.2: A portion of the beam spill containing a CCQE candidate event. The first cluster of PMT hits is from the muon in the primary neutrino interaction, whereas the second is due to the electron from the delayed decay of the muon.

Thus, a typical CCPi+ has 3 subevents. The first subevent is a primary neutrino interaction and the pion decay. The $\pi^+$ lifetime is $\sim 26$ ns, thus the pion decay happens within the primary subevent. The second and third subevents are from the $\mu^-$ and $\mu^+$ decays.

A typical NCE event has only 1 subevent, associated with a primary neutrino interaction.

## 6.3 Analysis Cuts

In this section the analysis cuts for the NCE candidate events selection in MiniBooNE are described, as well as their purpose and the efficiency. Table 6.1 shows all selection cuts that have been used in this NCE analysis, they are as follows:

- The first cut is on the number of veto PMT hits, $Veto\ PMTs < 6$, in order to remove cosmic ray muons, which usually have high levels of activity in the veto region. In Fig. 6.3 we show the number of veto PMT hits for cosmic ray muon candidates and laser (in-tank) events. Too

| Cuts | Purpose | Fraction of events (%) | | | | | | NCE eff. (%) | Total events |
|---|---|---|---|---|---|---|---|---|---|
| | | NCE | Dirt | Irr | CCQE | BU | Other | | |
| *No cuts* | | 0.2 | 0.4 | 0.1 | 0.5 | 98.4 | 0.4 | 100.0 | 161,500,000 |
| $Veto\ PMTs < 6$ | Remove cosmic rays | 0.3 | 0.4 | 0.1 | 0.5 | 98.2 | 0.4 | 95.3 | 130,180,000 |
| 1 *subevent* | No decaying particles | 7.1 | 5.1 | 1.1 | 2.4 | 80.8 | 3.5 | 80.8 | 2,092,960 |
| $4400 < Time < 6500$ | Event in beam time | 26.6 | 19.1 | 4.2 | 9.1 | 27.9 | 13.1 | 80.8 | 601,868 |
| $Tank\ PMTs > 24$ | Reconstructible events | 29.2 | 16.7 | 5.5 | 12.2 | 18.9 | 17.6 | 65.5 | 428,006 |
| $T < 650$ MeV | Ensure low energy | 38.7 | 20.1 | 7.4 | 1.9 | 26.7 | 5.2 | 59.5 | 293,832 |
| $\ln(\mathcal{L}_e/\mathcal{L}_p) < 0.42$ | Proton-like events | 56.6 | 21.4 | 11.0 | 2.5 | 1.6 | 6.9 | 59.1 | 178,995 |
| *CUTR* | Reduces dirt | 64.6 | 15.0 | 9.5 | 2.1 | 0.5 | 7.9 | 33.8 | 94,531 |

Table 6.1: NCE selection cuts. In this table the cuts that are applied are described, their purpose, different event channels fractions left after consecutive cuts, efficiency of NCE events and the total number of events for the MiniBooNE data after the cuts. Channels of events are shown here: *NCE*, *Dirt* are events outside of the detector, *CCQE*, *BU* are beam-unrelated backgrounds (data with a Strobe trigger), and *Other* backgrounds. *Total events* is the number of events after the consecutive cuts for $6.46 \times 10^{20}$ POT.

much activity in the veto region indicates that a cosmic muon is present. However, it is hard to see a change from Table 6.1 after applying this cut, because most of the events before any cuts do not have any activity. Also the cut removes some charge current backgrounds in case a muon passes through the tank and through the veto region, firing the veto PMTs, as well as neutrino events happen outside of the detector with created particles penetrating into the detector.

- The 1 *subevent* cut is to eliminate trigger events that do not have any activity and charge current backgrounds, where a muon is created, which generally stops and decays producing a Michel electron.

- The 4400 ns $< Time <$ 6500 ns cut (where $Time$ is NCFitterT, the reconstructed event time) is to ensure that the event is in the beam time window. Beam-unrelated backgrounds are mostly those Michel electrons from cosmic ray muons that happen just before the DAQ time window is open, thus making the decaying electron be the only subevent. One can see that this cut reduces the beam-unrelated backgrounds fraction from 81% to 28%.

- $Tank\ PMTs > 24$ is a cut on the total number of tank PMT hits. The purpose of the cut is to look only at reconstructable events. If the number of PMT hits is too small, it is impossible to reliably reconstruct the event vertex, energy and direction. Overall, we reconstruct 7 parameters of the event: the position (3 parameters), the time (1), direction (2) and the nucleon kinetic energy (1). The reconstructed time could be roughly obtained from the time of the PMT hits, while the event energy from the total visible charge. Thus, for each of the 5

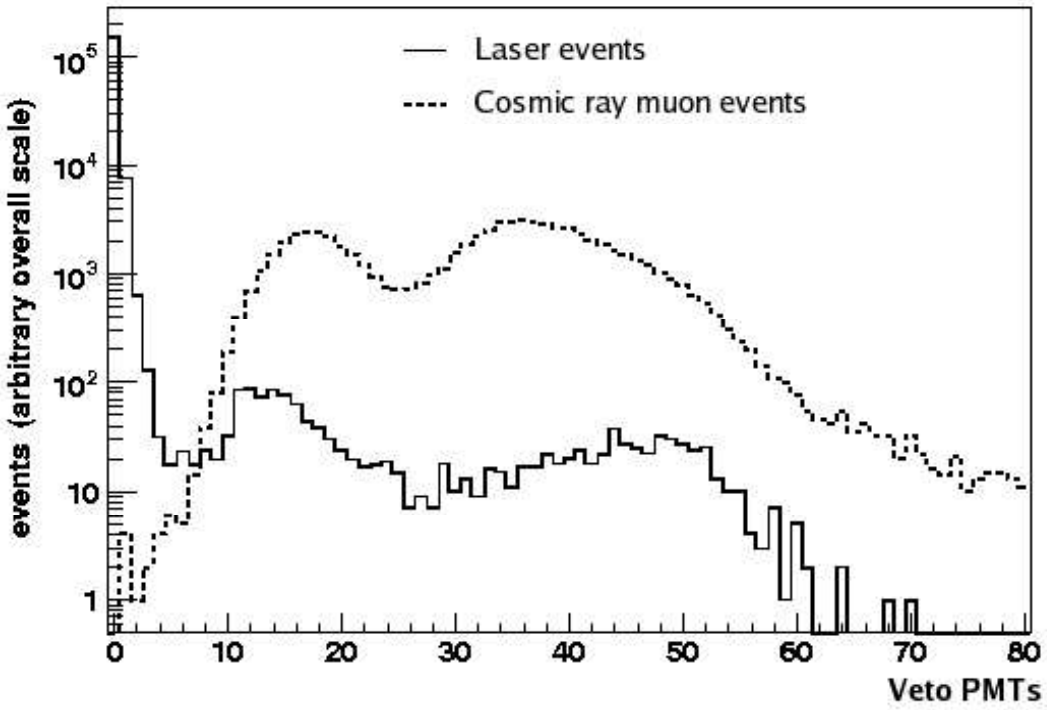


Figure 6.3: Distribution of veto PMT hits for laser flask events and cosmic ray muon candidate events.

parameters that are left we require at least 5 PMT hits.

- The $T < 650$ MeV cut (where $T$ is NCFitterE, the reconstructed nucleon kinetic energy) cut is to look only at low energy events. As discussed earlier, NCE events produce less light than other neutrino interactions, in which an electron, a muon, a $\pi^0$, or gammas are produced. The reconstructed energy spectra for different channels after the above cuts are applied are shown in Fig. 6.4. As one can see, the fraction of NCE events is small for energies above 650 MeV.

- The $\ln(\mathcal{L}_e/\mathcal{L}_p) < 0.42$ is a particle ID cut. As one can see from Table 6.1, the beam-unrelated backgrounds contributed a significant fraction to the sample so far. This is because the Michel electrons spectrum is also at low energy. The time likelihood difference between the proton and electron hypotheses is shown in Fig. 6.5, where the red histogram corresponds to the MC NCE and the blue histogram is the MiniBooNE beam off data (beam-unrelated backgrounds). Both histograms are normalized to unit area. As one can see from Fig. 6.5 and Table 6.1, the beam-unrelated backgrounds become negligible after this cut. We can also see why this

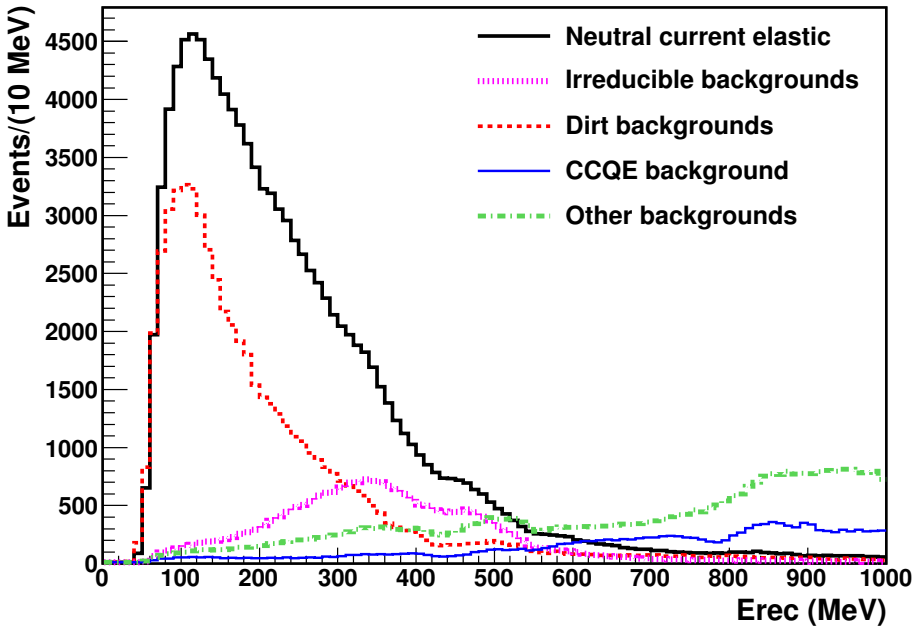


Figure 6.4: Reconstructed energy for different channels in the MC after the following cuts been applied: $Veto\ PMT < 6$, 1 *subevent*, 4400 ns $< Time <$ 6500 ns, $TankPMT > 24$.

cut is so efficient from Fig. 6.6, where the reconstructed corrected time of the PMT hits is shown for MC NCE and data with no beam under both electron and proton hypotheses. As one can see, the beam unrelated backgrounds have more prompt light than NCE events, thus the corresponding time likelihoods are much different for these hypotheses. In particular, from Fig. 6.7, one can see that electrons have a higher fraction of prompt light than protons.

- The last cut we apply is the fiducial volume cut:

$$CUTR = \begin{cases} NCFitterR < 4.2 \text{ m}, & \text{if } T \leq 200 \text{ MeV} \\ NCFitterR < 5.0 \text{ m}, & \text{if } T > 200 \text{ MeV}. \end{cases}$$

The cut serves two purposes: to consider only well-reconstructed events (the vertex should be far enough from the PMTs to be reconstructed reliably), and also to reduce the dirt background events. As one can see from Fig. 6.4, the dirt events are primarily at low reconstructed energies. Therefore, the cut on the reconstructed radius is tighter at low energies to reduce more of the dirt backgrounds.

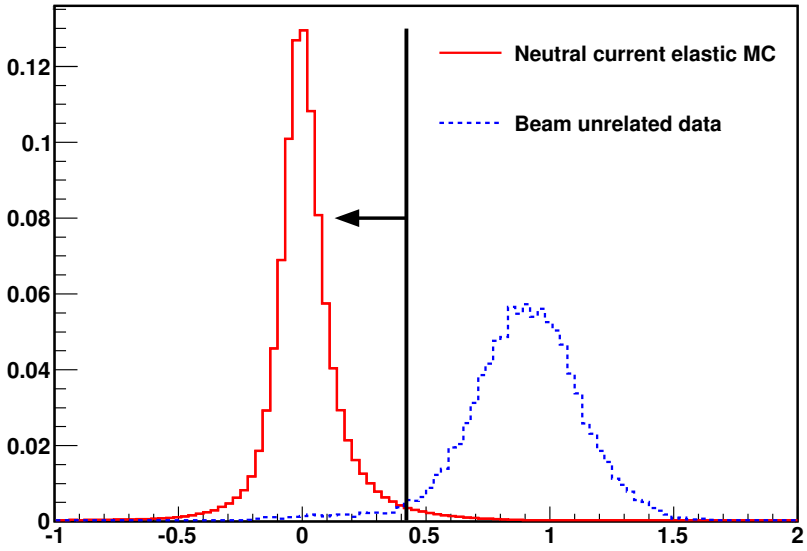


Figure 6.5: Time likelihood difference between proton and electron hypotheses for the MC NCE and the strobe (beam-off) data. Arrow indicates the part which is left for the analysis. Distributions are normalized to unit area.

## 6.4 Event Composition of the Neutral Current Elastic Candidate Sample

A total of 94,531 events pass the NCE cuts in the sample corresponding to $6.46 \times 10^{20}$ POT, which is the largest NCE event sample in the world up to date. The efficiency of the cuts is estimated to be 26% (a large part of the reduction is due to the fiducial volume cut). The predicted fraction of NCE events in the sample is 65%. The remaining 35% of events in the sample are backgrounds: 15% irreducible backgrounds, 10% dirt events, and 10% other backgrounds. The reconstructed nucleon kinetic energy spectrum for the selected NCE event sample is shown in Fig. 6.8, along with the predicted background contributions. The top plot is the reconstructed energy after the described NCE cuts are applied. The discontinuity at $T = 200$ MeV is due to the chosen fiducial volume cut $CUTR$. Since it is hard to visually observe the spectrum behavior at 200 MeV, we can alternatively apply a flat fiducial volume cut $R < 4.2$ m (bottom plot). The total error for the data shown in the plot was calculated considering all MiniBooNE systematic and statistical uncertainties, as described in Section 6.7.

Irreducible backgrounds are neutral current pion production channels containing no pion in the final state, as the pion is absorbed in the nucleus through a FSI process. In this case, the final state

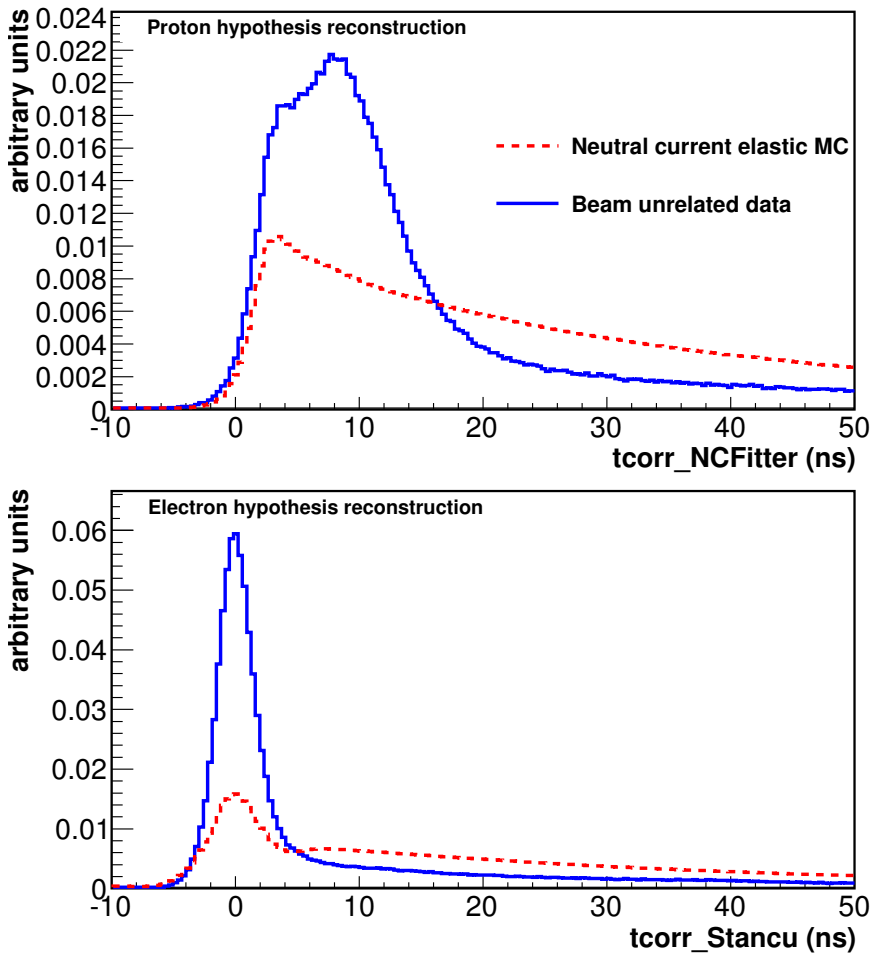


Figure 6.6: Reconstructed corrected time of the PMT hits with proton (top) and electron hypotheses (bottom). Strobe data (blue solid) and NCE MC (red dashed). Distributions are normalized to unit area.

particles for these events are just nucleons, identical to the final state particles produced in NCE events – hence these backgrounds are called "irreducible". Irreducible backgrounds are important at intermediate energies, for $T$ between 200 MeV and 500 MeV.

The dirt background is an important contribution to the NCE data sample at low energies, mostly below 200 MeV. Normally, this background is due to nucleons (mainly neutrons) which are produced in neutrino interactions outside of the detector, penetrating into the detector without firing enough veto PMTs. The dirt events are challenging to simulate in the MC because they occur in various media outside of the detector which have not been studied in detail (in the soil, detector support structures, etc.). Rather than rely on simulation, we directly constrain these backgrounds using the MiniBooNE data. The dirt events can be isolated from in-tank interactions using their

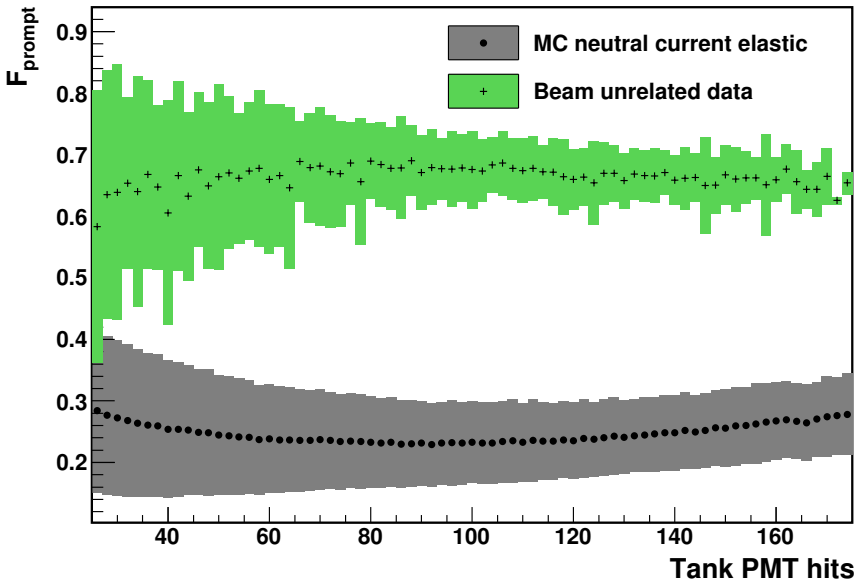


Figure 6.7: Prompt light fraction (tank PMT hits with the corrected time between -5 ns and 5 ns) for the beam unrelated data and the NCE MC reconstructed under an electron hypothesis. Corrected time is a time difference between the PMT hit time, reconstructed event time and the light propagation time from the reconstructed vertex to the PMT. The error bars are the RMS of the distributions.

distinct kinematics: the dirt events are preferentially reconstructed in the most upstream ($Z < 0$ m) and outer regions of the detector with relatively low energies (small $T$). The dirt energy spectrum is measured by fitting dirt-enriched samples in these variables ($Z$, $R$ and $T$) as explained in detail in Section 6.5.

Other backgrounds are mainly charge current channels, but also include neutral current pion channels, beam unrelated, and anti-neutrino NCE events. These backgrounds become relevant at high reconstructed energies, mainly above 400 MeV.

## 6.5 Dirt Background Measurement

The dirt energy spectrum is measured by fitting MC in-tank and dirt templates to the data in reconstructed $Z$, $R$, and energy distributions for the dirt-enriched event samples ($NCFitterZ$, $NCFitterR$, and $NCFitterE$, respectively, which are the output variables of the NCFitter). The $R$ and $Z$ distributions are obviously correlated. However, the samples used for the $Z$ and $R$ fits have a large fraction of events that are present in one sample and not present in the other.

To measure the dirt backgrounds in the NCE event sample, three additional samples of events

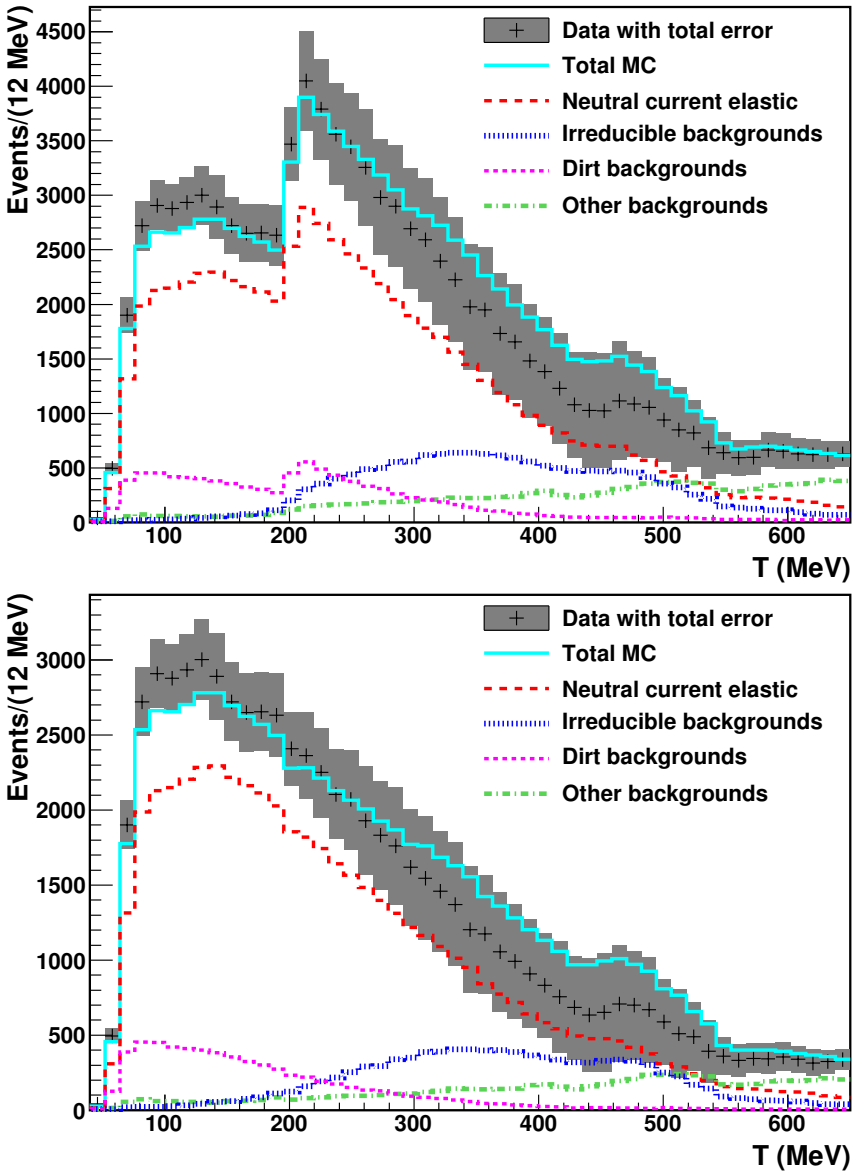


Figure 6.8: Reconstructed nucleon kinetic energy spectra for data and various MC contributions after the standard NCE cuts (top) and after an additional uniform fiducial volume cut of $R < 4.2$ m cut (bottom). Distributions are absolutely (POT) normalized.

with an increased dirt event fraction are used. For each of the variables (the reconstructed $Z$, $R$ and energy) different samples are used, based on cutting on the other of these variables: for example when measuring dirt events from the $Z$ distribution, an additional cut on $R$ is applied.

The selected samples for these fits are defined in Table 6.2. The following precuts are the same for each event sample:

$$\begin{aligned} \text{Precuts} &= 1 \text{ Subevent} + Veto\ PMTs < 6 + Tank\ PMTs > 24 \\ &+ 4400 \text{ ns} < \text{Time} < 6500 \text{ ns} + T < 650 \text{ MeV} \\ &+ \ln(\mathcal{L}_e/\mathcal{L}_p) < 0.42. \end{aligned}$$

As one can see from the same table, the dirt fraction for the dirt-enhanced samples is increased significantly.

| Sample name | Purpose of the sample | Cuts : *Precuts*+ | Dirt fraction, % |
|---|---|---|---|
| NCE | NCE sample (dirt-reduced) | *RCUT* | 13.4 |
| Dirt_Z | Fit dirt from $Z$ (dirt-enhanced) | 3.8 m $< R <$ 5.2 m | 27.8 |
| Dirt_R | Fit dirt from $R$ (dirt-enhanced) | $Z < 0$ m | 34.3 |
| Dirt_E | Fit dirt from energy (dirt-enhanced) | 3.8 m $< R <$ 5.2 m and $Z < 0$ m | 37.6 |

Table 6.2: Event sample cuts, their respective purposes and dirt events fractions. The dirt fractions are calculated from the initial MC simulation (before dirt fits) NCE is the signal sample defined in Section 6.3, whereas the other three samples are dirt-enriched samples for dirt fits.

### 6.5.1 Dirt Events Measurement from the Reconstructed $Z$ Distribution

To measure the dirt backgrounds from the $Z$ distribution, we use the "Dirt_Z" event sample from Table 6.2. The idea here is to use the shapes of the $Z$ distribution for the in-tank and dirt MC to fit the shape of the $Z$ distribution for the data. From the fit parameters one can extract how much dirt events we need to have in the MC to fit the data. Performing the fit at different energy bins allows measuring the dirt events spectrum, or the correction function that should be applied to the spectrum of the dirt events from MC. To get the shape of dirt events in the signal NCE sample, the same correction function should be applied to the spectrum of MC dirt events in the NCE sample.

The shapes of the $Z$ distributions for MC in-tank and dirt events in the "Dirt_Z" event sample are shown in Fig. 6.9. The plots are normalized to the same number of POT. Clearly, the dirt events tend to be on the negative side of the $Z$ distribution. Thus, one can use these distributions to fit the dirt contribution from the data.

The sum of the in-tank and the dirt templates gives a total MC $Z$ distribution for a chosen

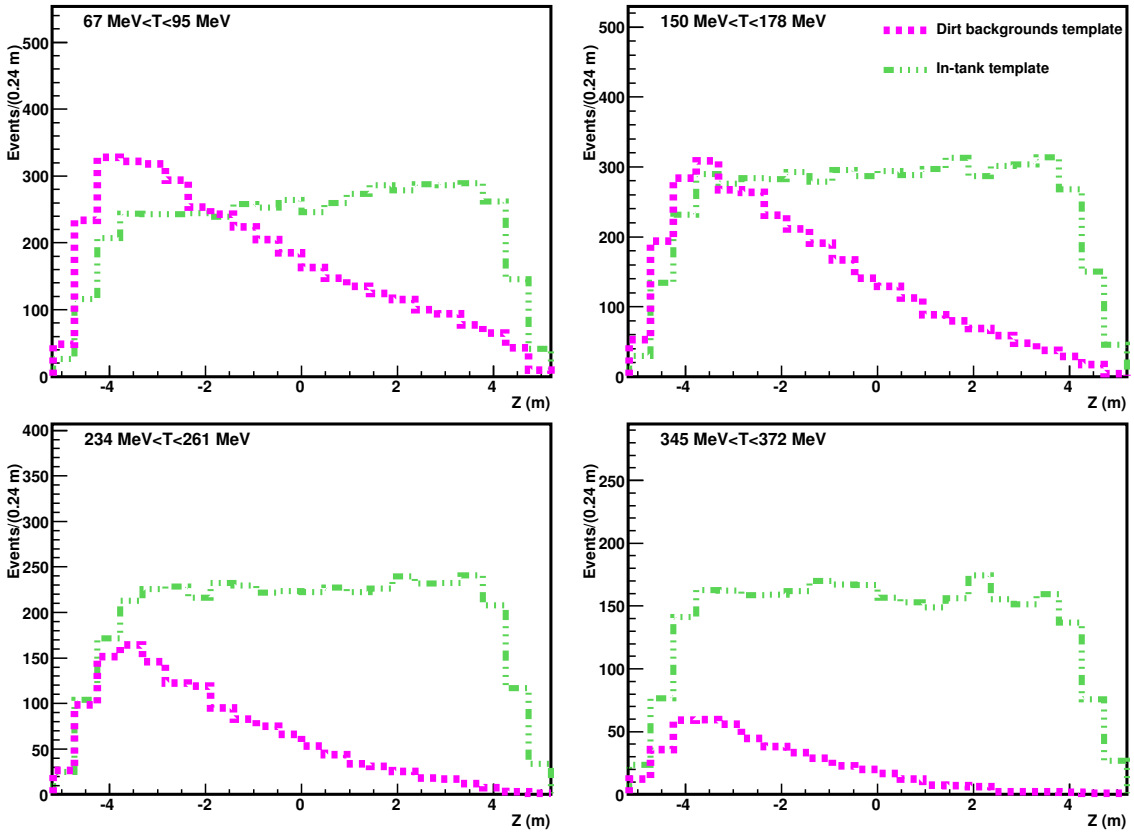


Figure 6.9: $Z$ distribution for the MC in-tank and dirt events in the "Dirt_Z" event sample before fitting (templates) for different reconstructed energy ranges.

energy bin. By varying the normalization of dirt and in-tank templates we find a minimum for the $\chi^2$ between the total MC and the MiniBooNE data in the $Z$ distribution for each energy bin. The results of the fit are shown in Fig. 6.10 for some energy bins; clearly, the MC after the fit describe the data better than the one before the fit.

The dirt energy correction function that we obtain in this fit is shown in Fig. 6.11, which is the dirt normalization value for the best fits. The error on the correction is returned from the fit by MINUIT.

### 6.5.2 Dirt Events Measurement from the Reconstructed $R$ Distribution

The same procedure used for the $Z$ distribution is applied for the fit using the $R$ distribution. However, for the $R$-fit the "Dirt_R" event sample is used.

The reconstructed $R$ distributions for the MC in-tank and dirt events with the "Dirt_R" cuts are shown in Fig. 6.12. The plots are normalized to the same number of POT. Dirt events tend to

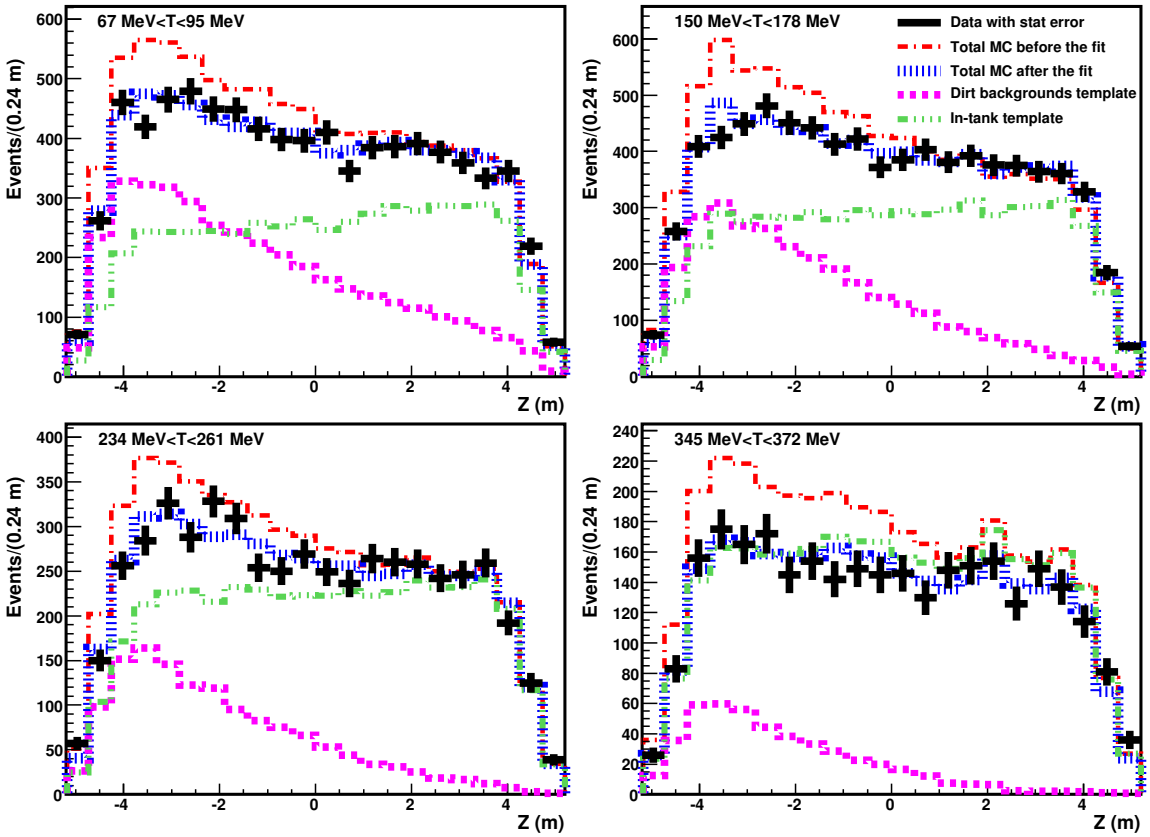


Figure 6.10: Fits to the data using MC templates for the in-tank and dirt events in the $Z$ distribution for different reconstructed energy bins.

be in the outer region of the tank, compared to the in-tank events; therefore, one can also use this distribution to fit the dirt from the data.

The results of the $R$-fit are shown in Fig. 6.13. Again, the MC after the fit describe the data better than the MC before the fit. The dirt energy correction function that we obtain from the $R$-fit is shown in Fig. 6.14.

### 6.5.3 Dirt Events Measurement from the Reconstructed Energy Distribution

For this method two event samples are used: the first is the signal (NCE), while the second is the dirt-enriched, signal-reduced sample with the "Dirt_E" cuts from Table 6.2. For both samples we have the MiniBooNE data available. Also there is a MC prediction for NCE, dirt and in-tank backgrounds histograms. These distributions for both samples are shown in Fig. 6.15.

Assuming that the fractions of signal and dirt events in both samples are stable relative to MC

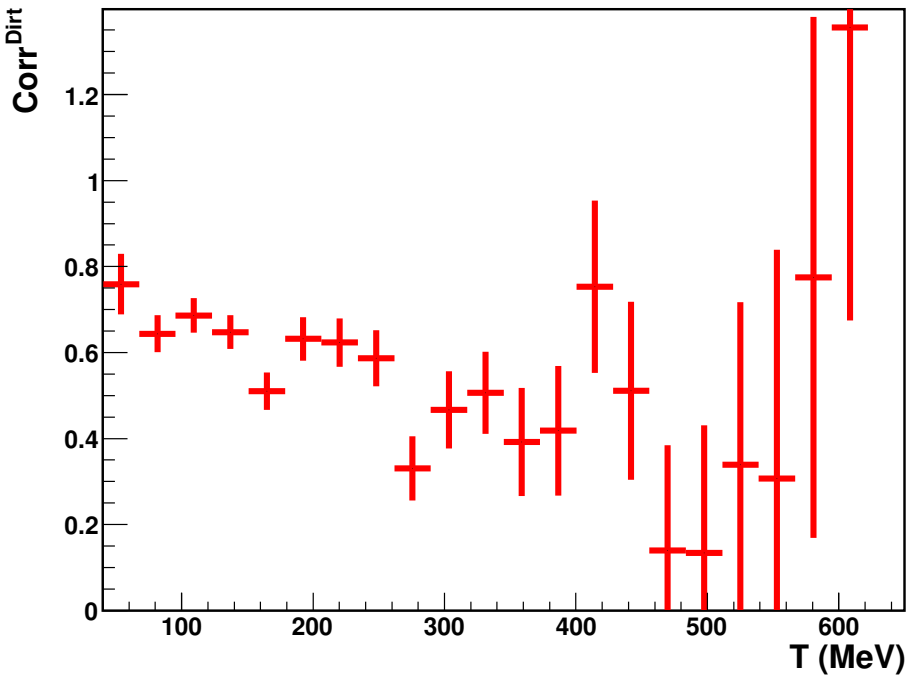


Figure 6.11: Dirt energy correction function from the fits of data in the $Z$ distribution. The error bars are the errors of $\chi^2$ fits, as returned by MINUIT.

variations, one can measure the spectrum of dirt events in the NCE sample from the data distribution for both of these samples. We define the following histograms:

$\nu$ – the reconstructed energy spectrum for the data,

$B$ – the reconstructed energy spectrum for the MC in-tank backgrounds,

$S$ – the reconstructed energy spectrum for the MC NCE,

$D$ – the reconstructed energy spectrum for the MC dirt,

which have upper indices describing the event sample:

$s$ – NCE event sample,

$d$ – "Dirt_E" event sample.

The new spectra of the dirt and signal events can be determined from fitting the data in both NCE and "Dirt_E" samples. In terms of the definitions that we have introduced, the condition that

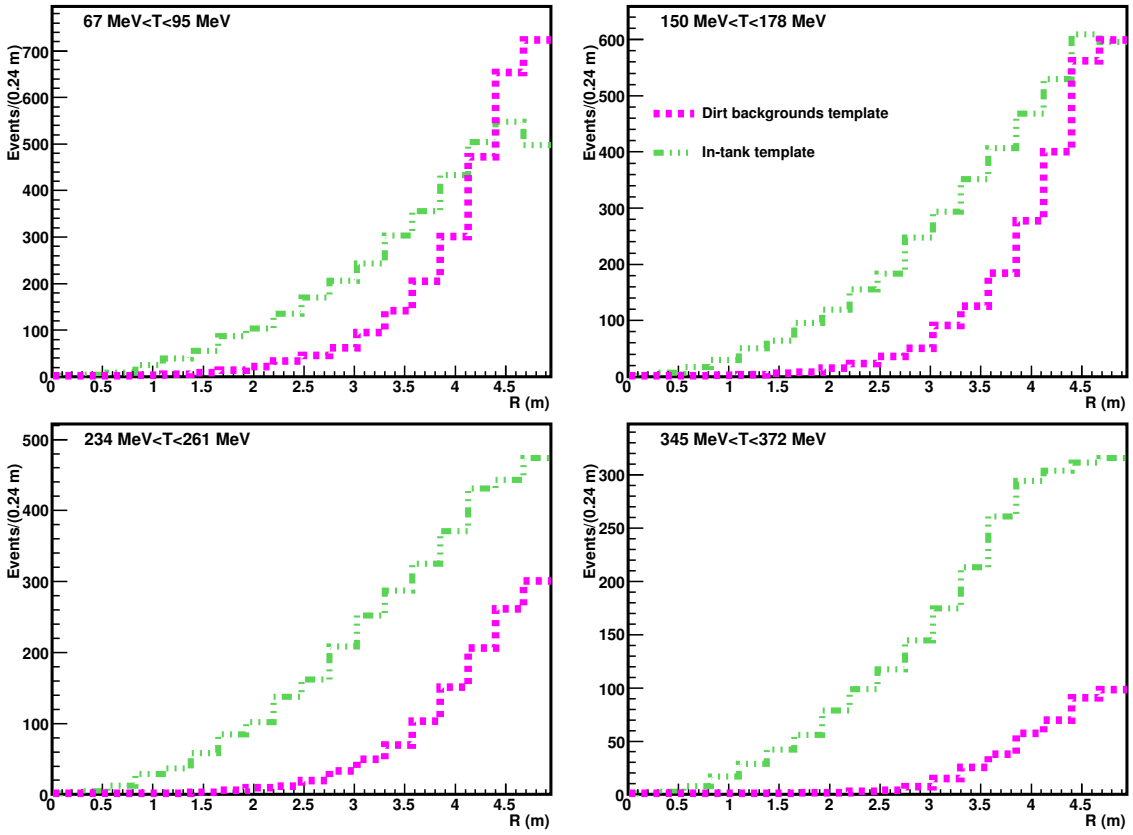


Figure 6.12: $R$ distribution for the MC in-tank and dirt events in the "Dirt_R" event sample before fitting (templates) for different reconstructed energy ranges.

these spectra coincide in both event samples can be written as

$$\begin{cases} B_i^s + S_i^s + D_i^s & = \nu_i^s \\ B_i^d + S_i^d + D_i^d & = \nu_i^d. \end{cases}$$

For each reconstructed energy bin $i$ there are 6 unknowns on the left hand side and 2 knowns on the right hand side (the data in both NCE and "Dirt_E" samples). Assuming a reliable in-tank backgrounds prediction, one can fix $B_i^s$ and $B_i^d$. Furthermore, we introduce the fractions of signal and dirt events in the two samples:

$$f_i = \frac{D_i^d}{D_i^s} \qquad \text{and} \qquad g_i = \frac{S_i^d}{S_i^s}.$$

Because these variables are ratios, one may expect them to be relatively stable to MC variations and independent of the dirt and NCE energy spectra. In this measurement we consider a dominating type

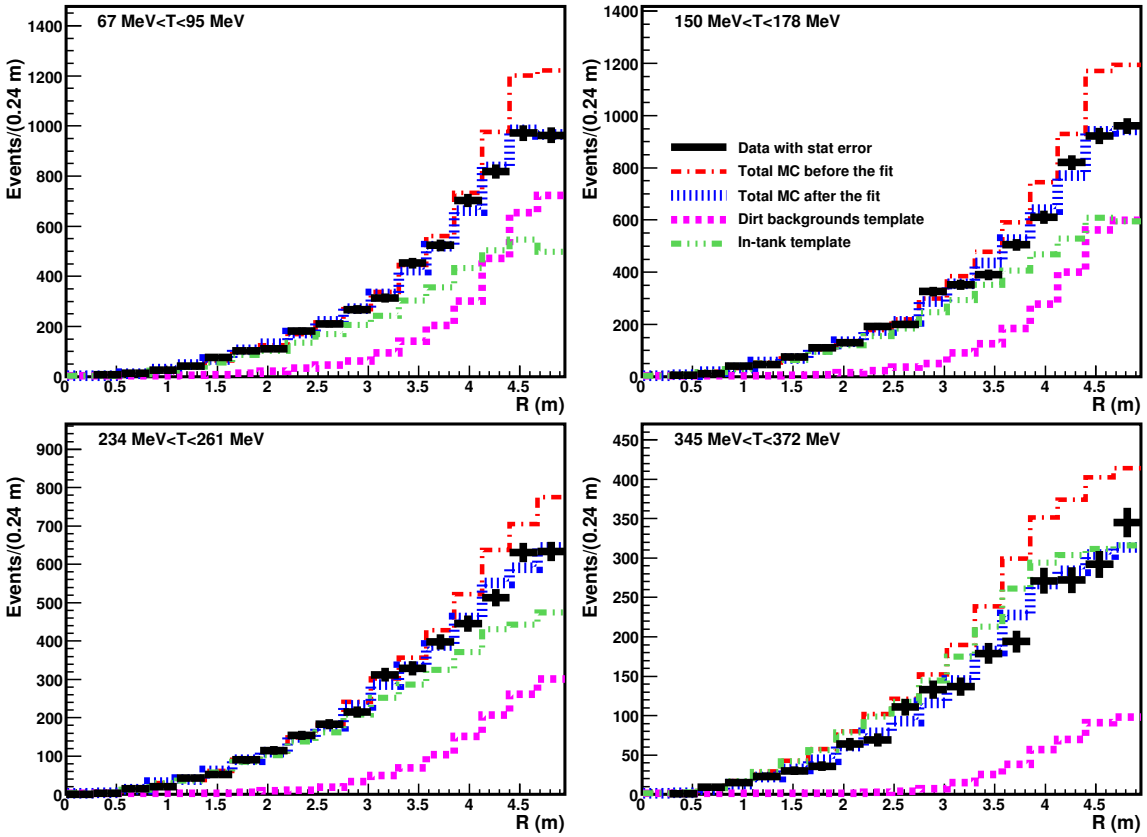


Figure 6.13: Fits to the data using MC templates for the in-tank and dirt events in the $R$ distribution for different reconstructed energy bins.

of the systematic uncertainty (optical model) to obtain the errors. The details of the systematic variations are described later in Section 6.7. Briefly, the MC with the best estimation of all its parameters is called the central value (CV). An optical model multisim is a set of MC variations with the optical model parameters (such as Cherenkov and scintillation strength, fractions of each fluors, etc.) varied about their mean values within an allowed region. The functions $f$ and $g$ determined from the MC are shown in Fig. 6.16. For dirt events there are no MC variations available, thus the function $f$ can be calculated only for the CV. The function $g$ can be also plotted for allowed variations of the MC. The plots of the function $g$ for optical model MC variations are also shown in the plot.

Finally, one can express $D_i^s$ (the dirt energy spectrum in the NCE sample) in terms of the above definitions:

$$D_i^s = \frac{g_i\left(\nu_i^s - B_i^s\right) - \left(\nu_i^d - B_i^d\right)}{g_i - f_i},$$

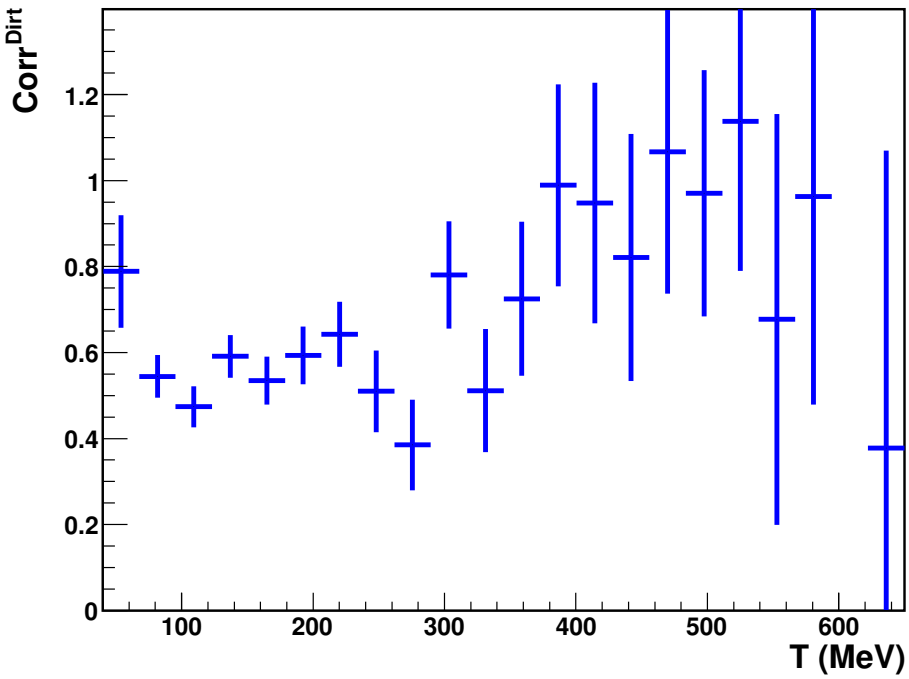


Figure 6.14: Dirt energy correction function from the fits of data in the $R$ distribution for different energy ranges. The error bars are the errors of $\chi^2$ fits, as returned by MINUIT.

which is the measured spectrum of dirt events in the NCE event sample. The result of this measurement in terms of the dirt energy correction function is shown in Fig. 6.17. As one can see, the result is consistent with the previous dirt measurements from the $Z$ and $R$ distributions.

### 6.5.4 Combined Dirt Energy Correction Fit

Finally, using all three methods, the combined dirt energy spectrum correction function fit is performed. It is done by fitting the correction functions shown in Figures 6.11, 6.14, and 6.17 together. As one can see the errors on the dirt correction functions are large for energies above 300 MeV or so. This is because dirt backgrounds are mostly at low energies, and there is not much dirt above 300 MeV, as can bee seen from Fig. 6.8. Thus, the chosen form of the fit function is linear below 300 MeV and a constant above, as shown in Fig. 6.18 (bottom plot), which is the main measurement result. Alternatively, one may choose the fit to a constant, which is shown in Fig. 6.18 (top plot), to obtain the approximate scaling factor for the dirt events.

All three measurements agree with each other in the form of the dirt backgrounds behavior, lending confidence to our overall ability to constrain dirt backgrounds in the analysis. The fitted

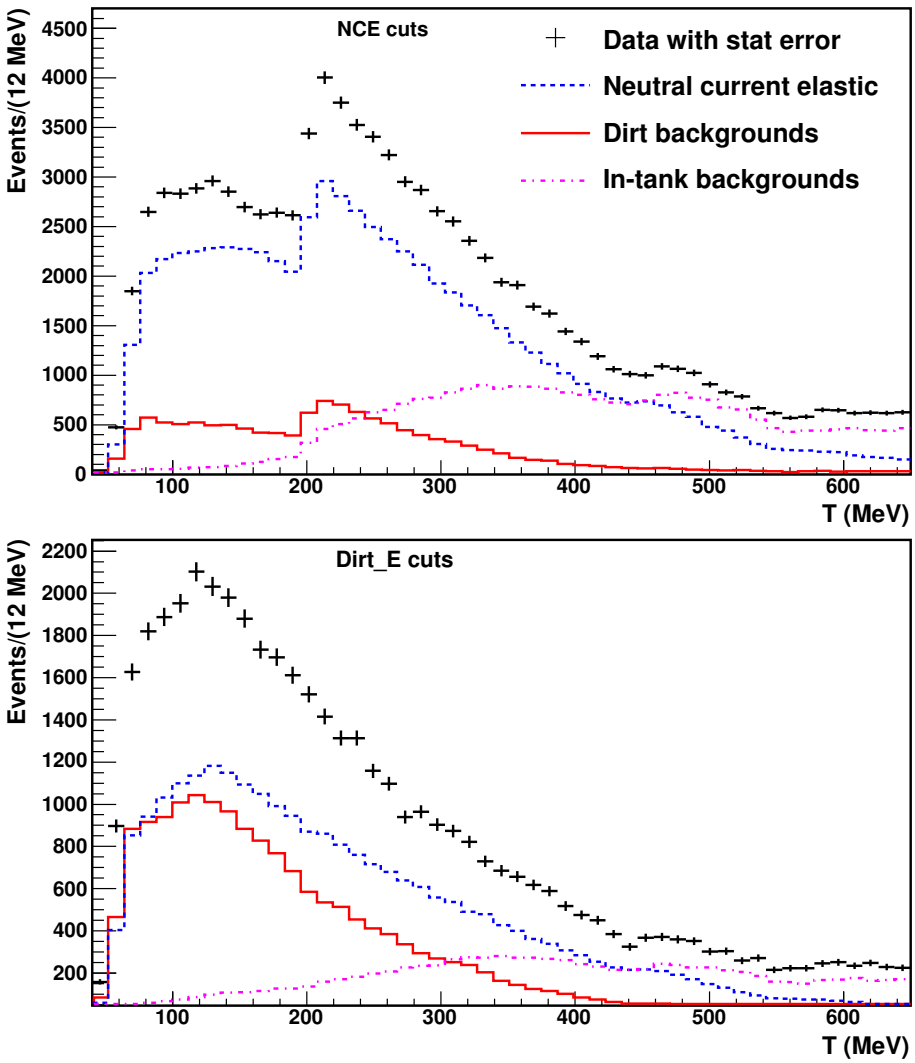


Figure 6.15: The reconstructed energy distribution of events with NCE cuts (top) and with the "Dirt_E" cuts (bottom) for the data, and the MC NCE, dirt, and in-tank backgrounds.

correction functions (below 300 MeV) are:

$$\begin{aligned} &0 - th\ order\ polynomial : 6.10 \times 10^{-1} \\ &1 - st\ order\ polynomial : 7.13 \times 10^{-1} - 6.27 \times 10^{-4} \times T \end{aligned} \tag{6.1}$$

Thus, the measured number of dirt events is determined to be $\sim 40\%$ lower than the original MC prediction.

To estimate the error on the dirt measurement, we calculate the average variation of the best-fit results from Figures 6.11, 6.14, and 6.17 about the fitted 1-st order polynomial from Fig. 6.18

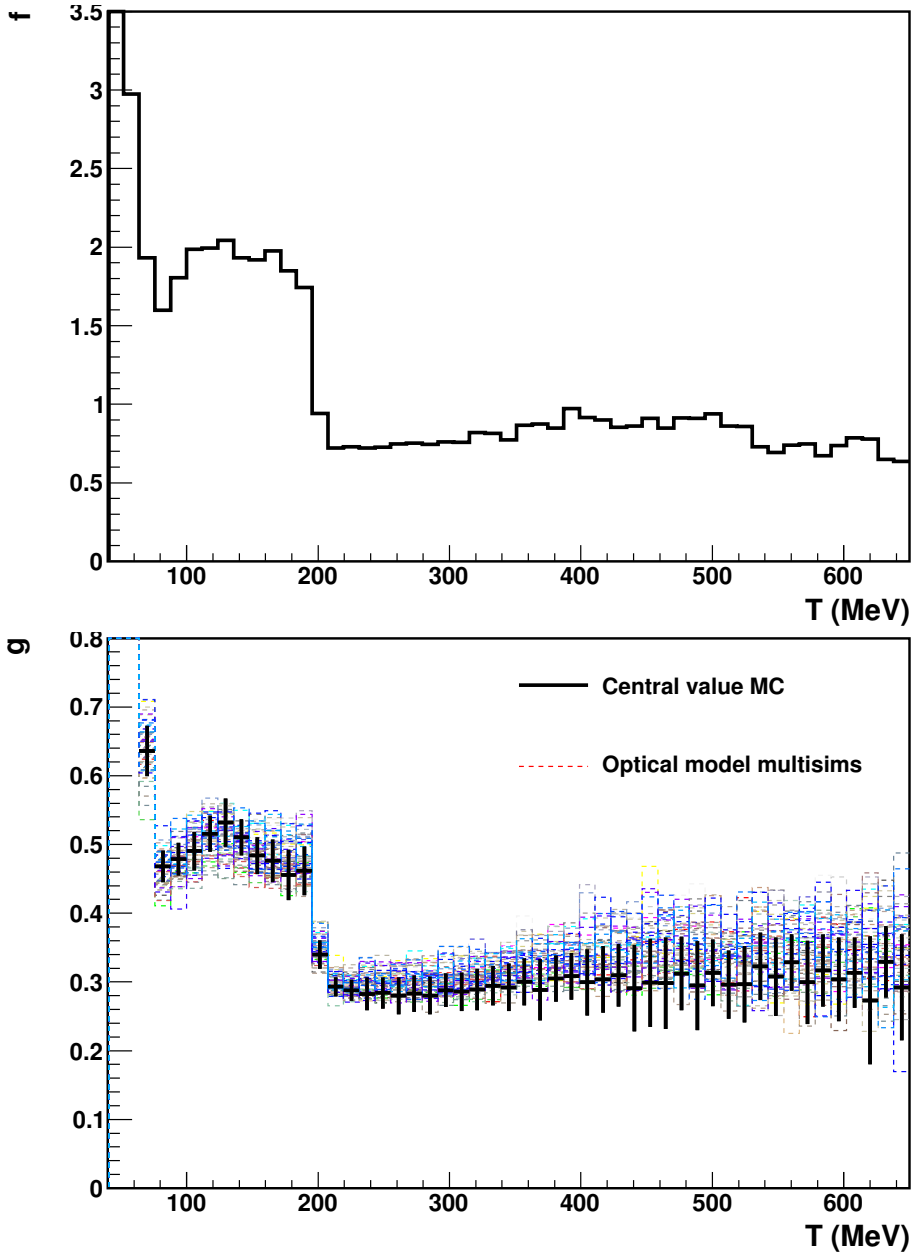


Figure 6.16: $f$ and $g$ as a functions of reconstructed energy. Function f is shown for CV only, whereas g is shown for the CV and optical model MC variations. The error bars for g are 1-$\sigma$ variations of the optical model MC variations about the CV for each bin.

(bottom). The fit to this mean variation is shown in Fig. 6.19. Thus, we estimate the error on the dirt measurement of $\sim 10\%$. The error is larger at energies above 250 MeV, but there is not much dirt backgrounds above that energy.

The new, measured reconstructed energy spectrum for the dirt events in the NCE sample is

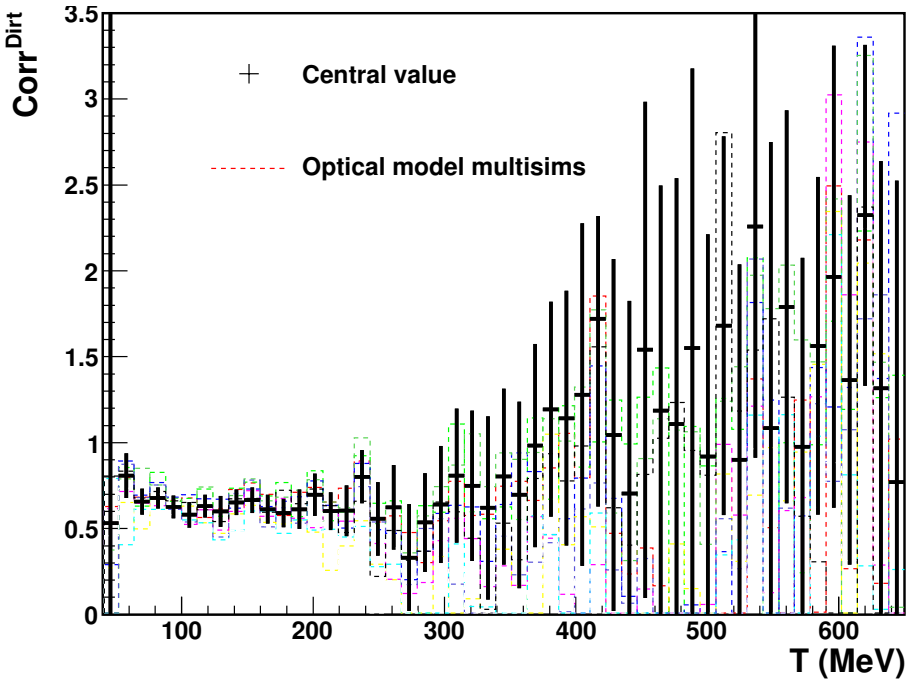


Figure 6.17: Dirt energy correction function from the dirt measurement using energy distribution for the CV (black solid) and optical model MC variations (colored dashed). The error bars are 1-$\sigma$ variations of the optical model MC variations about the CV for each bin.

calculated as a bin-by-bin correction of the initial MC dirt energy spectrum multiplied by the correction function (1-st order polynomial from Eq.(6.1)).

## 6.6 Correction for Limited Detector Resolution and Detector Efficiency Effects

After the dirt measurement described in the previous section, we have the reconstructed energy distribution for the data, as shown in Fig. 6.8. As one can see from the plot, the MC overpredicts the number of events at high reconstructed energy and underpredicts the number of events at low energy.

For analyzing NCE events one needs to account for backgrounds, which may be done by either subtracting the MC background prediction from the total reconstructed energy distribution or by applying the MC signal fraction [67]. We choose the latter as the main method. In this method, the extrapolated reconstructed energy spectrum for the *NCE data* is calculated using the data and the

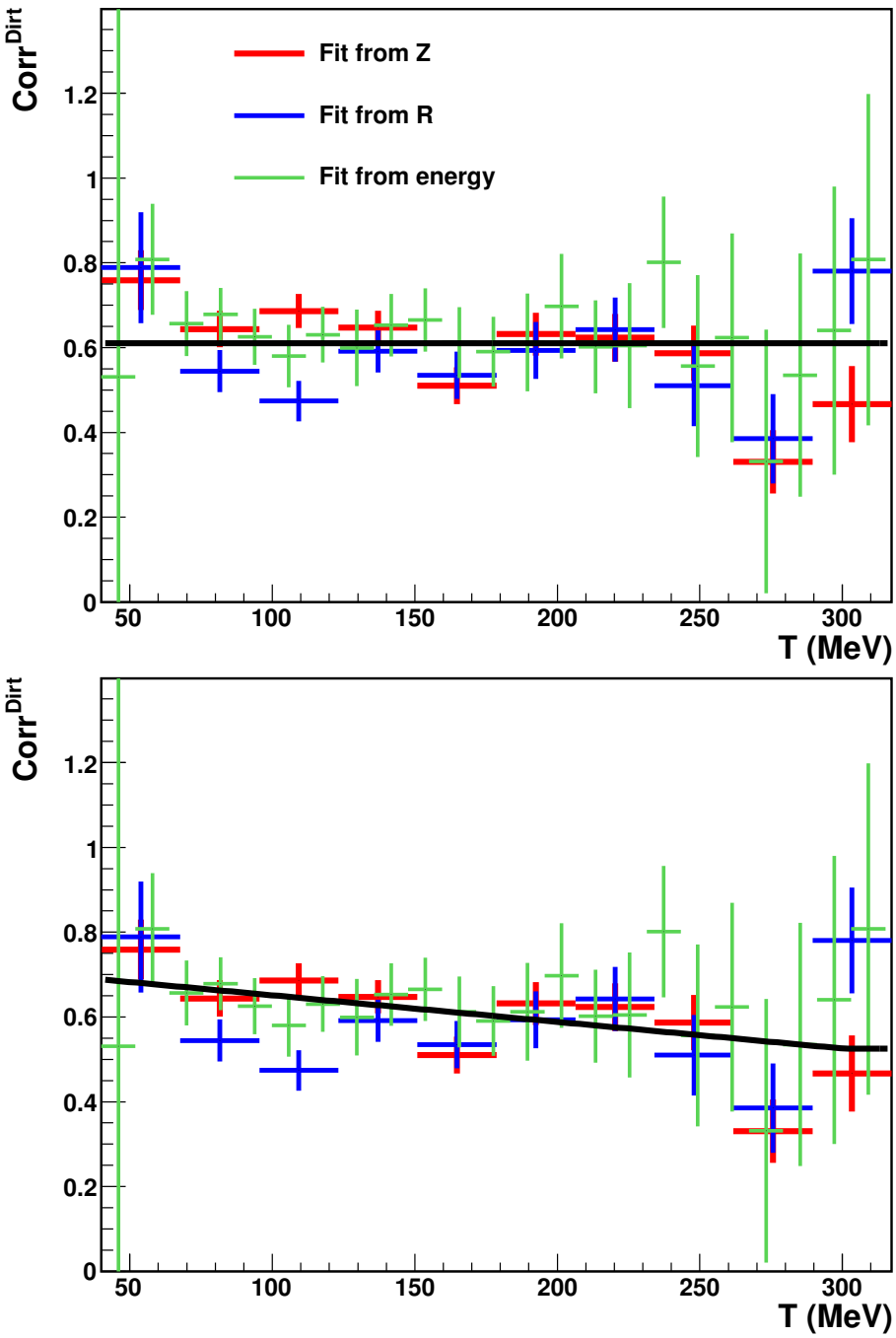


Figure 6.18: Dirt energy correction combined fit. 0-th order polynomial (top), 1-st order polynomial below 300 MeV and constant above 300 MeV (bottom).

MC in the following form:

$$S_j^{Data} = D_j \frac{S_j^{CV}}{S_j^{CV} + B_j^{CV}}, \tag{6.2}$$

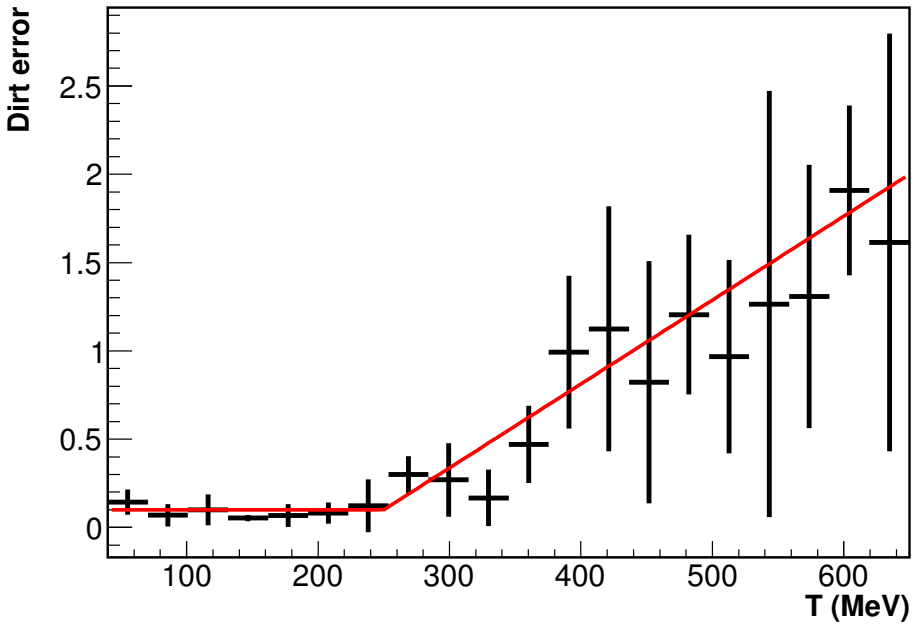


Figure 6.19: The deviation from the linear energy correction fit.

where $D_j$ = number of events in the $j$-th reconstructed energy bin for the data, $S^{CV}$ = the number of NCE events in the CV MC, $B^{CV}$ = all background events in the CV MC including in-tank, dirt, beam unrelated, and $\bar{\nu}$ NCE.

Next, the spectrum (6.2) is corrected for the limited detector resolution and the detector efficiency effects that distort the original spectrum. This is known as the unfolding problem [121], for which a direct matrix method is used and described in Appendix A in detail. This method is also equivalent to the method based on Bayes' theorem [122].

The unfolding matrix applied to (6.2) is calculated for NCE events in the MC using a correlation matrix of the true nucleon kinetic energy versus the reconstructed nucleon kinetic energy ($T$). The sum kinetic energies of all nucleons in the final state was taken for the true nucleon kinetic energy. This method gives a well-behaved but biased solution which depends on the original MC energy spectrum. The error due to the bias is estimated by iterating the unfolding procedure, where the new MC energy spectrum is replaced by the unfolded energy spectrum.

The MC migration matrix and the NCE efficiency that are used for the unfolding are shown in Fig. 6.20. Note that NCE proton and NCE neutron events may have different migration matrices and efficiencies (see Appendix B). We are using the combined NCE migration matrix and an averaged

NCE proton/neutron efficiency. The NCE unfolded energy spectrum is calculated the following way:

$$\sigma_i^{CV} = \sum_j U_{ij}^{CV} S_j^{Data},$$

where the unfolding matrix $U^{CV}$ is defined through the migration matrix and the efficiency; the index $i$ represents the true energy bins, while $j$ represents the reconstructed energy bins.

## 6.7 Error Analysis

### 6.7.1 Multisims and Unisims

The MC reconstructed energy spectrum depends on the flux and cross-section predictions, as well as detector uncertainties, which in turn depend on many other parameters (for example on the $M_A$ value in the cross-section, or the scintillation light strength in the optical model, etc.). For the systematic error estimation we use MC variations with some MC parameters floated around their best estimation within an estimated allowed region.

A set of MC variations is called a *unisim*, when only one such parameter is varied. To produce a unisim, a set of MC are created with the parameter value chosen randomly around its mean with a variance equal to its 1-$\sigma$ error. Sometimes however, it is easier to manipulate MC samples with variations of several parameters at once. In addition, some parameters may be correlated, and then the input error matrix is created with the variance of each parameter on the diagonal elements; the covariance between the two parameters is placed on the corresponding off-diagonal elements for the input error matrix. Then, a set of MC variations with the parameter values picked randomly using the input error matrix is called a *multisim*.

In the MiniBooNE NCE analysis 13 different multisims and unisims are used to estimate the systematic error, as follows

- **Optical Model Multisim**: uncertainty in the detector media model – parameters that describe scintillation and Cherenkov light parameters in the media, reflections, etc. This error is dominating in the NCE measurements.
- **Discriminator Threshold Unisim**: uncertainty in the value of the discriminator threshold value for each PMT.
- **qtcorr Unisim**: uncertainty in the model of charge-time simulation of the PMTs.

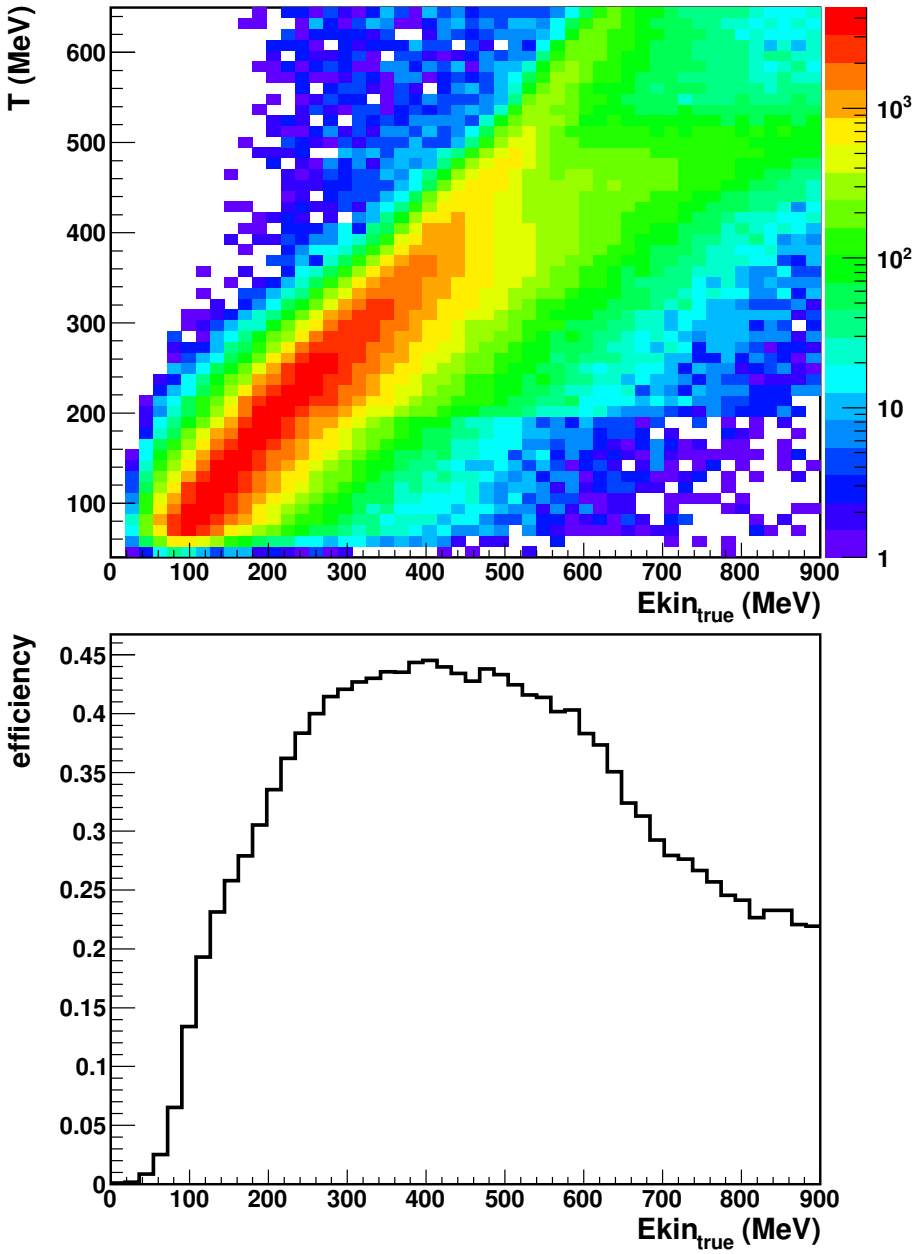


Figure 6.20: The migration matrix and the efficiency for the NCE events with NCE event selection cuts.

- **Dirt Unisim**: uncertainty in the dirt background. This is the 10% error on the dirt events spectrum measurement that we discussed earlier. Two MC variations have been created, one with 10% more dirt background, the other is with 10% less. Signal and in-tank background in the unisim are taken as in the CV.

- **POT Unisim**: uncertainty in the number of POT delivered from the Fermilab Booster. We

assign a 2% error to this number. For this unisim, two MC variations have been created, one has a 2% higher reconstructed spectrum than the CV, the other one is 2% lower.

- **Pi0Yield Multisim**: uncertainty in the $\pi^0$ production in the detector.
- **Hadronic Multisim**: uncertainty in the new hadronic model where a photonuclear effect has been introduced.
- **Cross-section Multisim:** uncertainty in the cross-section parameters, as shown in Table 4.6. For the NCE cross-section measurement, these parameters are allowed to vary only for background events. However, for the $M_A$ and $\Delta s$ measurements, other cross-section parameters (like the Pauli blocking scaling factor) are allowed to vary for NCE events as well.
- **Beam Unisim**: the error associated with some horn uncertainties and interactions in the target uncertainties that affect the neutrino flux: Even though it is technically a multisim, the parameters are uncorrelated.
  - skin depth
  - horn current
  - nuclear inelastic cross-section
  - nuclear quasi-elastic cross-section
  - pion inelastic cross-section
  - pion quasi-elastic cross-section
  - pion total cross-section
- **Meson Production Multisim**: errors assigned for the meson production in the target:
  - $K^0$ production in the target.
  - $K^+$ production in the target..
  - $\pi^-$ production in the target..
  - $\pi^+$ production in the target.

In addition to these, there is a statistical error and an unfolding error for the cross-section measurement, which is due to a bias in the unfolded energy spectrum, as described in Section 6.7.4.

### 6.7.2 Statistical Error Unisims

This is the error due to statistical fluctuations in the reconstructed energy distribution. The error on the reconstructed energy spectrum for data for each reconstructed energy bin is $\delta\nu_j = \sqrt{D_j}$. These unisims were generated with reconstructed spectra taking in each energy bin a value chosen randomly from a Gaussian with the mean value $D_j$ and variance $\sqrt{D_j}$

### 6.7.3 Error Calculation

For each $k$-th multisim the following formula is used to calculate the unfolded spectrum:

$$\sigma_i^k = \sum_j U_{ij}^k D_j \frac{S_j^k}{S_j^k + B_j^k}$$

where $i$ is the bin of the true energy, $j$ is the bin of the reconstructed energy, $U_{ij}^k$ is unfolding matrix for the k-th multisim, $D$ is the data, $S$ is the signal (NCE), $B$ is all backgrounds. Note that $\sigma^{CV}$ up to a normalization factor is the NCE differential cross-section.

The error on the NCE cross-section for each systematic uncertainty is calculated by taking the difference with respect to $\sigma^{CV}$ as follows

$$Error_i^\sigma = \sqrt{\frac{1}{N}\sum_{k=1}^{N}\left(\sigma_i^k - \sigma_i^{CV}\right)^2},$$

where $N$ is the total number of MC variations for each multisim.

### 6.7.4 Unfolding Error

The last systematic error that we consider is the error due to the bias of the unfolding procedure. Since we use only one iteration for the unfolding, the unfolded distribution depends on the CV that was used to produce the unfolding matrix. To eliminate the bias of the unfolding, one needs to make several iterations for the unfolded distribution to converge. However, it was found that the unfolding for the data doesn't converge because of significantly less statistics than in the MC. Therefore, we decided to estimate the error of the unfolding bias.

We assume that the bias goes away after $\sim$ 7 iterations, which is generally true as shown in Appendix A. For each MC variation in a multisim (unisim), we unfold the reconstructed energy spectrum with 7 iterations. Then, the bias of the unfolding is calculated for each MC variation in

the following way:

$$Bias_i^k = \sigma_i^{k,7\ iter} - \sigma_i^{k,1\ iter},$$

where $k$ is the k-th MC variation in the multisim (unisim) and i is the bin of the true energy. The bias for the entire multisim is calculated in the following way:

$$Multisim\_Bias_i^a = \sqrt{\frac{1}{N_a}\sum_{k=1}^{N_a}(Bias_i^k)^2},$$

where $a$ represents the multisim number and $N_a$ is the number of MC variations in the multisim. Assuming that the multisims are independent, one can calculate the total unfolding bias containing 14 systematic and statistical multisims (unisims):

$$Unfolding\_error_i = \sqrt{\frac{1}{14}\sum_{a=1}^{14}(Multisim\ Bias_i^a)^2}.$$

### 6.7.5 Total Error

Combining all the errors and adding them in quadratures, we obtain the total error. One can also estimate the contribution of each of the individual errors to the total error with one single number. One can do this by integrating an error over the range of the reconstructed or true energy and dividing by the total integral of the unfolded energy spectrum. Table 6.3 shows these individual and total errors.

As one can see, the cross-section measurement is dominated by the uncertainty in the optical model. After taking the signal fraction for data, the resulting reconstructed energy spectrum is shown in Fig. 6.21 (left plot) with a total error calculated from the MC variations about the CV. After applying the unfolding procedure and calculating all systematic and statistical uncertainties, the unfolded energy spectrum with the total error is shown in Fig. 6.21 (right plot). The latter represents the extrapolated true nucleon energy distribution for the NCE events in MiniBooNE.

## 6.8 The Neutral Current Elastic Differential Cross-Section

The right plot in Fig. 6.21 is pretty much the differential cross-section up to a normalization factor. Single differential cross-sections are usually expressed as a function of the momentum transfered squared, $Q^2$, rather than the nucleon energy. In NCE $Q^2$ is calculated by measuring the outgoing

| Type of error | Error | Value (%) |
|---|---|---|
| | Statistical | 3.1 |
| Cross-section | NC $\pi^0$ production yield | 0.1 |
| | Hadronic interactions | 0.2 |
| | Cross-section (shown in Table 4.6) | 3.4 |
| | Dirt background | 1.4 |
| Flux | POT | 1.7 |
| | Horn uncertainties | 4.7 |
| | $K_0$ production in the target | 0.1 |
| | $K^+$ production in the target | 0.5 |
| | $\pi^-$ production in the target | 0.3 |
| | $\pi^+$ production in the target | 4.1 |
| Detector | Discriminator threshold | 1.1 |
| | Optical model | 12.3 |
| | Charge-time PMT response | 2.0 |
| | Unfolding | 7.5 |
| | Total | 18.9 |

Table 6.3: Individual error contributions to the total integrated error of the NCE cross-section.

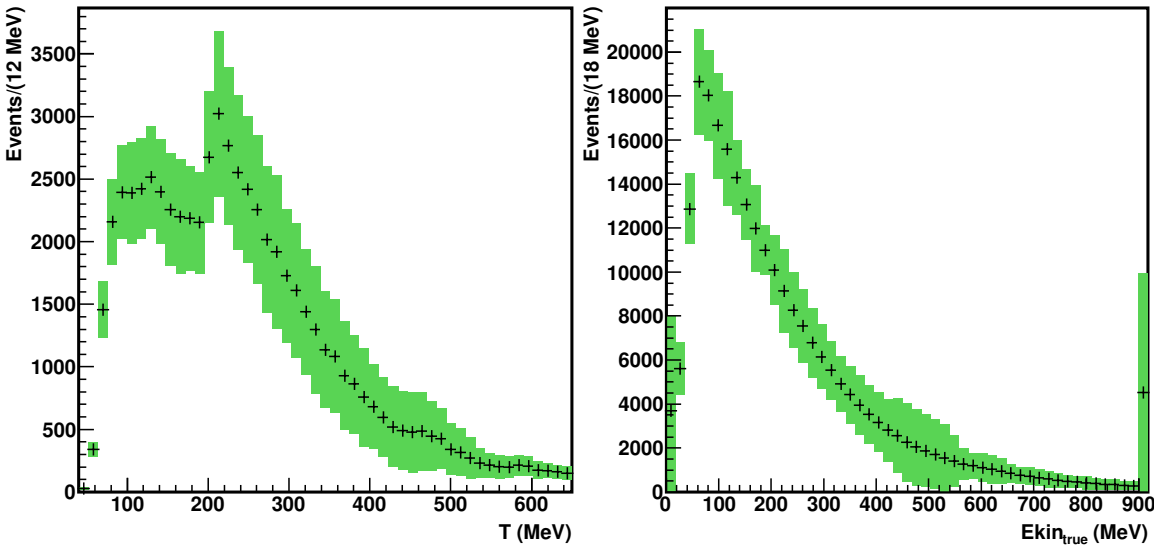


Figure 6.21: The reconstructed energy spectrum for the NCE data after taking the signal fraction with the total error (left plot). The unfolded energy spectrum with the total error (right plot).

nucleon kinetic energy using a simple relation, as $Q^2 = 2m_N T$, where $m_N$ is the nucleon mass and $T$ is the nucleon kinetic energy.

The full formula NCE differential cross-section is:

$$\frac{d\sigma_i^{NCE}}{dQ^2} = \frac{\sigma_i / \left(\frac{dQ^2}{dT_N}\Delta T_N\right)}{N_N N_{POT} \int \Phi_\nu dE_\nu}, \tag{6.3}$$

where $\sigma_i$ is the number of entries for the i-th bin of the unfolded nucleon kinetic energy distribution (right plot in Fig. 6.21); the factor $dQ^2/dT_N = 2m_N = 1.877$ GeV; $\Delta T_N$ is the bin width of the unfolded nucleon kinetic energy distribution (in this case $\Delta T_N = 0.018$ GeV); $N_N$ represents the number of nucleons in the detector, which is calculated as $N_N = N_A \rho_{oil}(4\pi R^3/3)$ where $N_A$ is Avogadro's number, $\rho_{oil} = 0.845 \pm 0.001$ g/cm$^3$, and $R = 610.6$ cm (the MiniBooNE detector radius); $N_{POT}$ represents the number of POT for the data (in our case $N_{POT} = 6.46165 \times 10^{20}$), and $\int \Phi_\nu dE_\nu$ is the total integrated neutrino flux for $\nu_\mu$ and $\nu_e$ (in MiniBooNE $\int \Phi_\nu dE_\nu = 5.22227 \times 10^{-10}$ cm$^{-2} \cdot$ POT$^{-1}$).

With this, the NCE flux-averaged differential cross-section is shown in Fig. 6.22 as a function of $Q^2$, The predicted distribution of irreducible backgrounds, which have been subtracted along with the rest of backgrounds, is also shown in the figure.

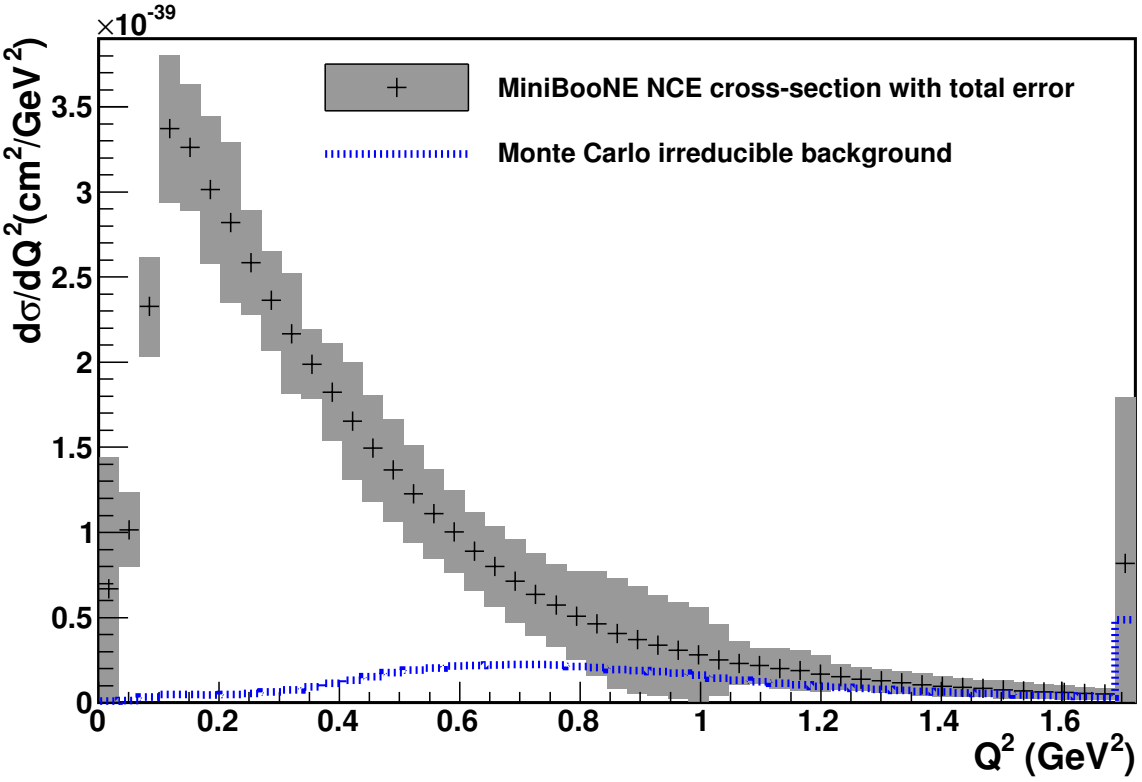


Figure 6.22: MiniBooNE $\nu N \to \nu N$ flux-averaged differential cross-section on $CH_2$ along with the predicted irreducible background, which has been subtracted out (technically signal fractioned out).

## 6.9 Analysis of the Cross-Section Result

The NCE scattering sample consists of three different processes: scattering off free protons in hydrogen, bound protons in carbon, and bound neutrons in carbon. Thus, the result shown in Fig. 6.22 is the flux-averaged NCE differential cross-section on $CH_2$, averaged over these processes. Therefore, the MiniBooNE $\nu N \to \nu N$ cross-section is expressed as:

$$\begin{aligned} \frac{d\sigma_{\nu N\to\nu N}}{dQ^2} &= \frac{1}{7}C_{\nu p,H}(Q^2)\frac{d\sigma_{\nu p\to\nu p,H}}{dQ^2} \\ &+ \frac{3}{7}C_{\nu p,C}(Q^2)\frac{d\sigma_{\nu p\to\nu p,C}}{dQ^2} \\ &+ \frac{3}{7}C_{\nu n,C}(Q^2)\frac{d\sigma_{\nu n\to\nu n,C}}{dQ^2}, \end{aligned} \tag{6.4}$$

where $d\sigma_{\nu p\to\nu p,H}/dQ^2$ is the NCE cross-section on free protons taken per free proton, $d\sigma_{\nu p\to\nu p,C}/dQ^2$ is the NCE cross-section on bound protons per bound proton, and $d\sigma_{\nu n\to\nu n,C}/dQ^2$ is the NCE cross-section on bound neutrons per bound neutron. The efficiency correction functions $C_{\nu p,H}$, $C_{\nu p,C}$, and $C_{\nu n,C}$ result from different efficiencies for each type of NCE scattering process, estimated from MC as functions of $Q^2$. They are defined as the ratios of the efficiency for a particular type of NCE event to the average efficiency for all NCE events in bins of $Q^2$. To calculate a cross-section which is to be directly compared with the MiniBooNE results (Fig. 6.22), one needs to apply these efficiency corrections to each predicted distribution (Fig. 6.23); however, note that in the bulk of the measured region they are roughly equivalent, $C_{\nu p,H} \approx C_{\nu p,C} \approx C_{\nu n,C} \approx 1$.

For a comparison of the cross-section result we show the result from a preliminary MiniBooNE NCE analysis (Chris Cox, Ph.D. thesis, Indiana University) [123] and the BNL E734 cross-section of NCE scattering on protons [62], as illustrated in Fig. 6.24.

The NCE cross-section is quite sensitive to the axial form factor at low $Q^2$, as derived in Eq.(3.13). One can test the $M_A$ and $\Delta s$ sensitivity at low $Q^2$ roughly by the NCE cross-section expressions from (3.16) into (6.4). By doing this, one can see that the MiniBooNE $\nu N \to \nu N$ NCE cross-section is not sensitive to $\Delta s$, as the linear term in $\Delta s$ nearly cancels, while the quadratic term in $\Delta s$ remains, but is small if $|\Delta s| \ll g_A$. However, these data are still useful for probing $M_A$, which we describe in Chapter 7.

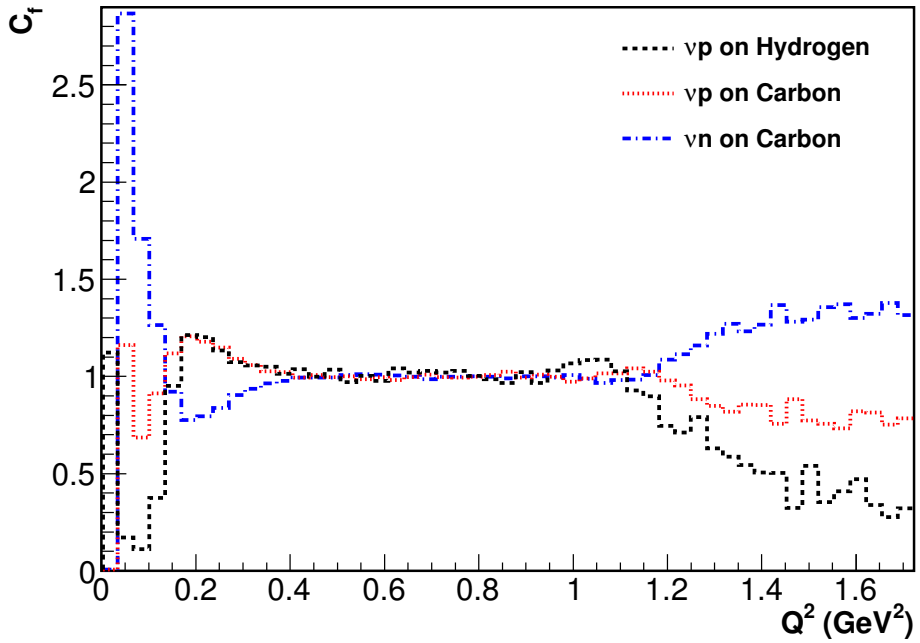


Figure 6.23: Efficiency corrections $C_{\nu p,H}$, $C_{\nu p,C}$, and $C_{\nu n,C}$ as functions of $Q^2$ for the different NCE processes in MiniBooNE.

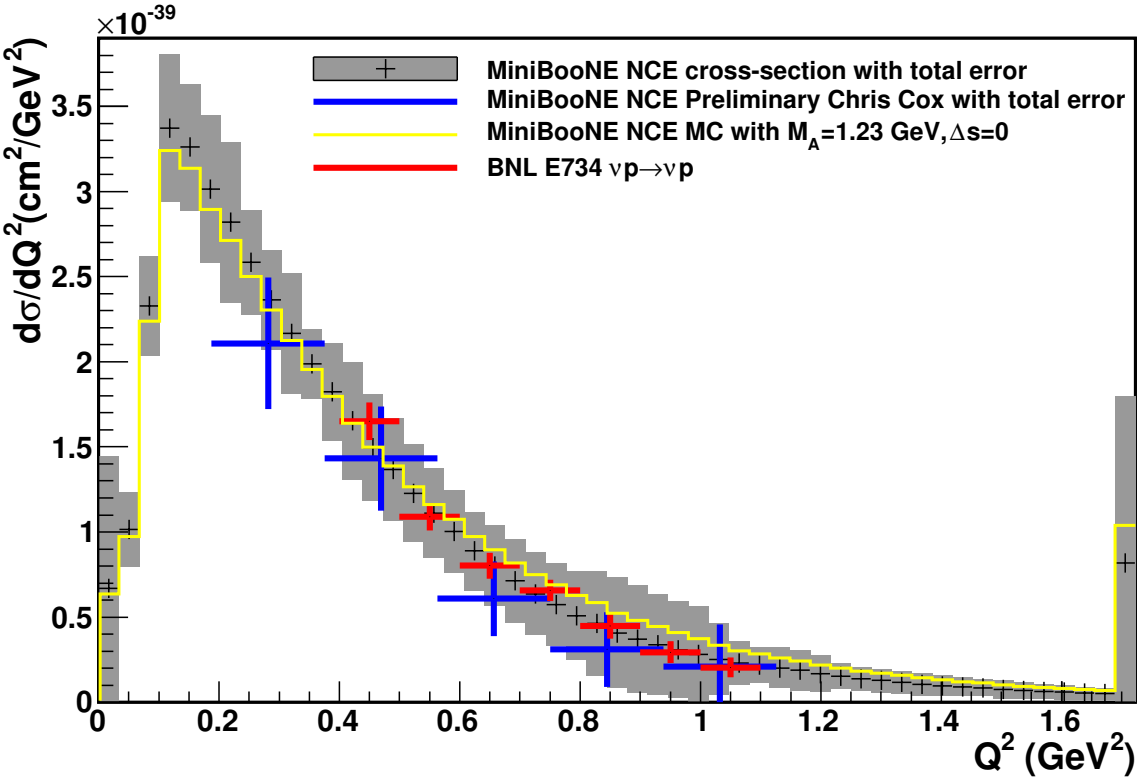


Figure 6.24: MiniBooNE $\nu N \to \nu N$ flux-averaged differential cross-section on $CH_2$ compared to the Chris Cox's MiniBooNE NCE preliminary result [123], the NCE MC cross-section prediction and the BNL E734 cross-section of NCE scattering on protons [62].

# Chapter 7

# Axial Vector Mass Measurement

## 7.1 NCE Reconstructed Energy Spectrum Dependence on the Cross-Section Parameters

In this section the $M_A$ fit of the observed cross-section is described. The procedure is similar to that described in [67] for the $M_A$ and $\kappa$ fits using the MiniBooNE CCQE channel. In principle, one needs to fit the observed data cross-section to the predicted cross-section for different $M_A$ values in $Q^2$ bins. Given the relationship between $Q^2$ and the nucleon kinetic energy in the NCE interaction is $Q^2 = 2m_N T_N$, all one really has to do is fit the cross-section in bins of nucleon kinetic energy. Moreover, in the MiniBooNE MC it is possible to generate the MC reconstructed energy spectrum that corresponds to any value of $M_A$. Hence, one does not need to use the unfolding procedure or subtract any backgrounds; simply use the total MC reconstructed energy spectrum after the NCE event cuts with a given value of $M_A$ for a $\chi^2$-test on the MiniBooNE data.

For this study the standard NCE selection cuts are used, described in Section 6.3, plus an additional $R < 4.2$ m cut to make a flat fiducial volume cut with a smooth reconstructed energy distribution (shown in the bottom plot of Fig. 6.8) which is analyzed.

First we look at the dependencies of the MC reconstructed energy spectrum on the cross-section parameters, which control the NCE cross-section, such as $M_A$, $\Delta s$, and $\kappa$. The 2-dimensional plot of the MC reconstructed energy spectrum depending on the value of $M_A$ is shown in Fig. 7.1. As one can see, there is an energy spectrum normalization dependence on the value of $M_A$, which can be also seen from Fig. 7.2, where we have integrated the spectrum over the energy bins. This last

plot also contains the total integral of the data spectrum from Fig. 6.8 (bottom plot) shown here as the dashed line. Thus, if one would chose to look at the total number of NCE events, the best $M_A$ value to describe data would be $\sim$ 1.13 GeV under assumption of $\Delta s = 0$ and $\kappa = 1.022$. However, the shape dependence of the energy spectrum on $M_A$ is quite weak, as can be seen in Fig. 7.3. Furthermore we also notice that none of the MC with different values of $M_A$ describe the reconstructed energy shape for the data well enough.

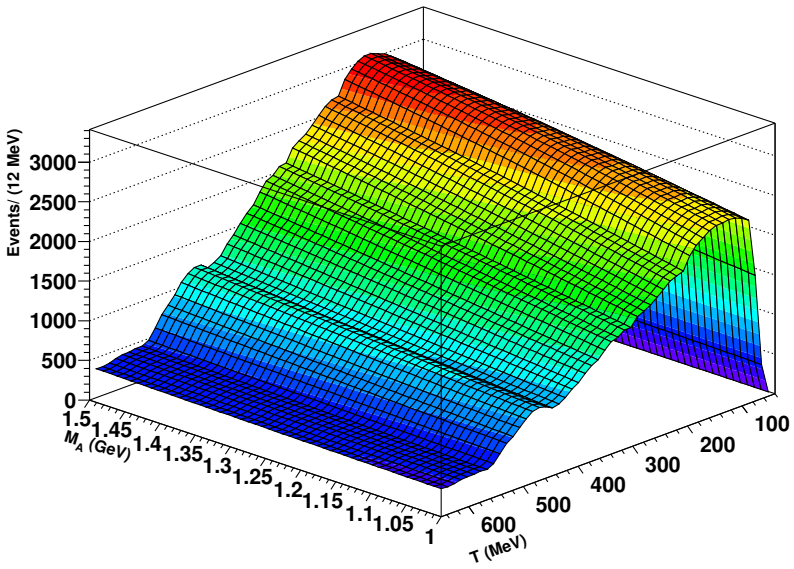


Figure 7.1: The MC reconstructed energy spectrum dependence on $M_A$ with $\Delta s = 0$ and $\kappa = 1.022$. Distributions are absolutely (POT) normalized.

The dependence of the MC reconstructed energy spectrum on $\Delta s$ is shown in Fig. 7.4. One can see that there is a normalization dependence of the reconstructed energy spectrum on $\Delta s$. Integrating the spectrum over all reconstructed energies, we obtain the result in Fig. 7.5, which fits to a second order polynomial very well. This is in agreement with the conclusion in Section 6.9, where the NCE cross-section having a quadratic term in $\Delta s$ is mentioned. From Fig. 7.6 one can see that there is almost no shape dependence of the reconstructed energy spectrum on $\Delta s$.

The dependence of the MC reconstructed energy spectrum on $\kappa$ is shown in Fig. 7.4 and is also very weak. The higher values of $\kappa$ make the Pauli blocking effect stronger, especially at low $Q^2$. However, because of the low cut efficiency at low $Q^2$ (bottom plot in Fig. 6.20), Pauli blocking does not have much effect on the reconstructed energy distribution, since events in the very low $Q^2$ region rarely pass the selection cuts. The integral over all values of $T$ is shown in Fig. 7.8. The shape dependence is shown in Fig. 7.9. Again, there is not much shape dependence (almost no dependence

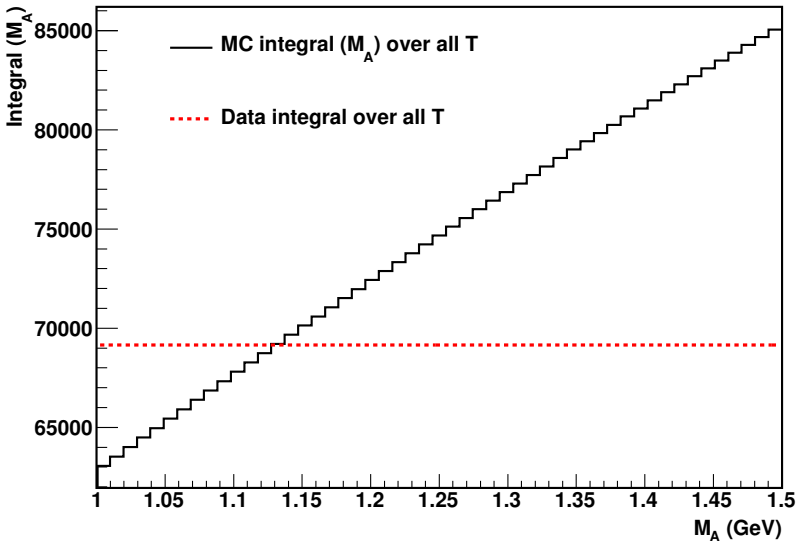


Figure 7.2: The total integral of the MC reconstructed energy spectrum from 40 MeV to 650 MeV depending on the value of $M_A$ with $\Delta s = 0$ and $\kappa = 1.022$. Also shown as a red dashed line is the total integral of the data reconstructed energy spectrum from Fig. 6.8 (bottom plot).

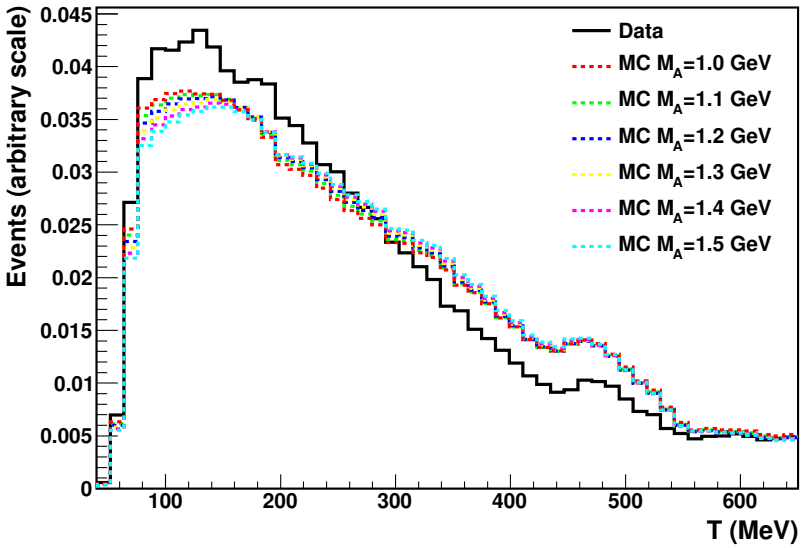


Figure 7.3: Relatively normalized (to a unit area) reconstructed energy spectra for the data and the MC with different $M_A$ values, and with $\Delta s = 0$ and $\kappa = 1.022$.

in the allowed physical region of $\kappa$ from 1.00 to 1.03).

Overall, one can see that varying any of the cross-section parameters that may affect the NCE cross-section would not fix the shape disagreement between the data and MC. Thus, the fit to the energy shape is meaningless for the MiniBooNE NCE, as opposed to $M_A$ and $\kappa$ fit for the MiniBooNE CCQE. For the $\chi^2$ test the absolute (POT) normalization is used, because there is only a very slight

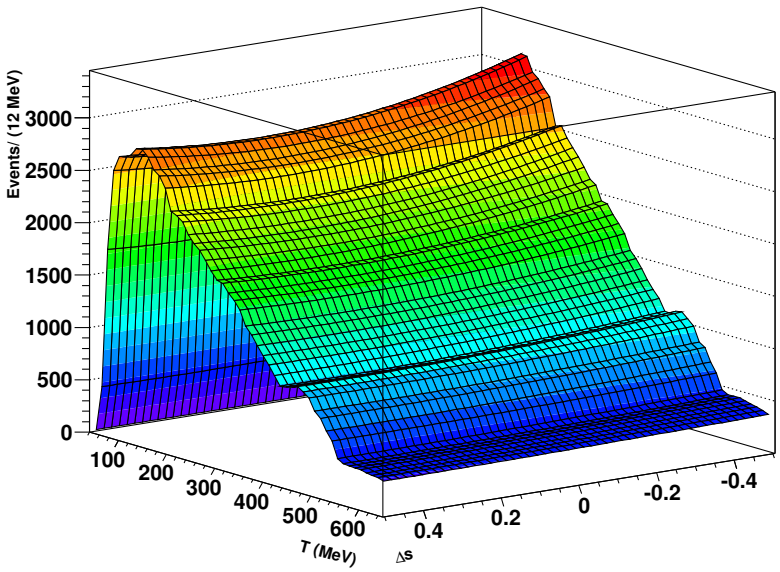


Figure 7.4: MC reconstructed energy spectrum dependence on $\Delta s$ with $M_A = 1.23$ and $\kappa = 1.022$. Distributions are absolutely (POT) normalized.

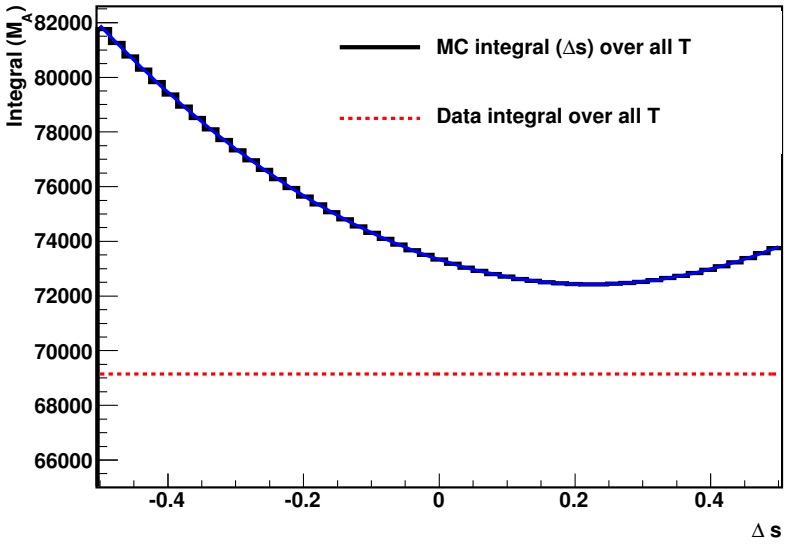


Figure 7.5: The total integral of the MC reconstructed energy spectrum from 40 MeV to 650 MeV depending on the value of $\Delta s$ with $M_A = 1.23$ GeV and $\kappa = 1.022$. The fit of the integral is to the second order polynomial: $Integral(\Delta s) = 7.3331 \times 10^4 - 8.0899 \times 10^3 \Delta s + 1.80614 \times 10^4 (\Delta s)^2$. Also shown as a red dashed line the total integral of the data reconstructed energy spectrum from Fig. 6.8 (bottom plot).

$M_A$ shape energy dependence, but a significant overall integral dependence.

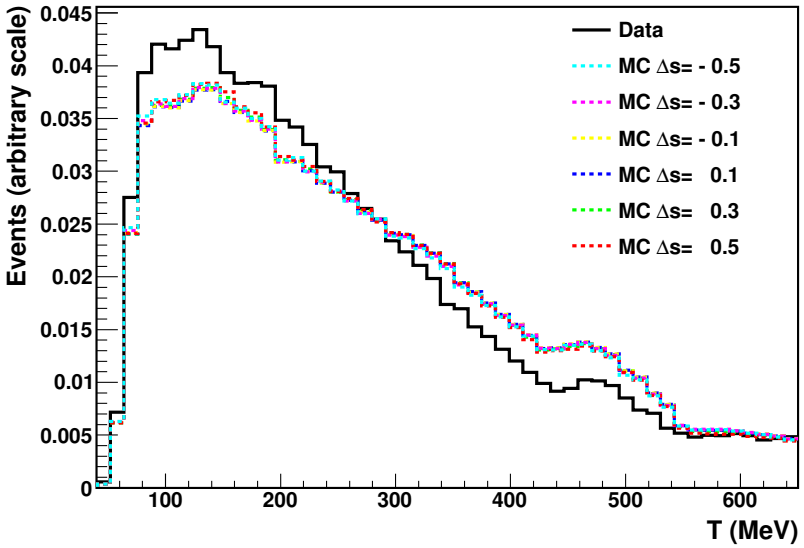


Figure 7.6: Relatively normalized (to a unit area) reconstructed energy spectra for the data and the MC with different $\Delta s$ values, and with $M_A = 1.23$ GeV and $\kappa = 1.022$.

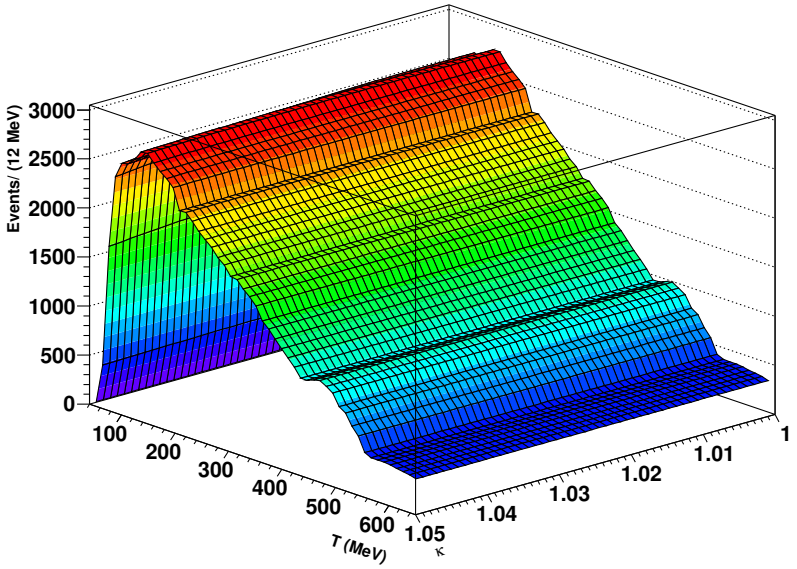


Figure 7.7: The MC reconstructed energy spectrum dependence on $\kappa$ with $M_A = 1.23$ and $\Delta s = 0$. Distributions are absolutely (POT) normalized.

## 7.2 Error Matrix

In order to account for the statistical and systematic uncertainties in the $M_A$ measurement from the reconstructed energy spectrum (or for any other variable), and also to consider bin-to-bin correlations we now construct the error matrix. For each MC uncertainty, a set of multisims (described in Section 6.7.1) is produced. Let $(T_i^l)_{i=1\ldots n}$ be the reconstructed energy spectrum for the $l$-th multisim

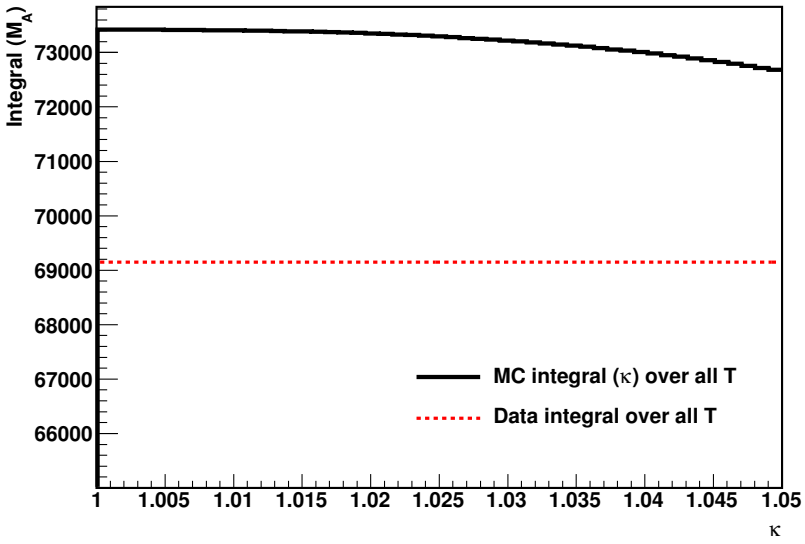


Figure 7.8: The total integral of the MC reconstructed energy spectrum from 40 MeV to 650 MeV depending on the value of $\kappa$ with $M_A = 1.23$ GeV and $\Delta s = 0$. Also shown as red dashed line the total integral of the data reconstructed energy spectrum from Fig. 6.8 (bottom plot).

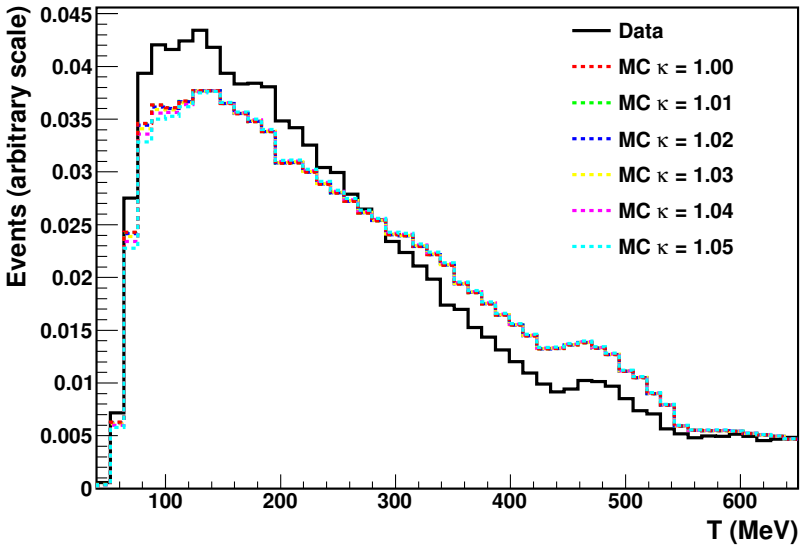


Figure 7.9: Relatively normalized (to a unit area) reconstructed energy spectra for the data and the MC with different $\kappa$ values, and with $M_A = 1.23$ GeV and $\Delta s = 0$.

or unisim; then the error matrix for the multisim is defined as

$$M_{ij} = \frac{1}{N_a} \sum_{l=1}^{N_a} (T_i^{CV} - T_j^l)(T_i^{CV} - T_j^l), \qquad i, j = 1...n$$

where $N_a$ is the total number of MC variations in the multisim. For each uncertainty that we take into account the number $N_a$ may be different, mostly depending on the computational limits. For

example, for the cross-section or any of the flux multisims $N_a = 200$ was used, for optical model $N_a = 65$, and for QTcorr as well as discriminator threshold unisims $N_a = 1$. The error matrix carries the information about bin-to-bin correlations in its off-diagonal elements.

This way we calculate the error matrix for each uncertainty that we consider and we add them up to the total error matrix, which is a sum of the error matrices of statistical and systematic uncertainties:

$$\begin{aligned} M^{tot} &= M^{stat} + M^{p0} + M^{hadr} + M^{xs} + M^{bu} + M^{k0} + M^{kp} + M^{km} \\ &+ M^{pm} + M^{pp} + M^{om} + M^{disc} + M^{qtcorr} + M^{dirt} + M^{pot}, \end{aligned} \tag{7.1}$$

where

- $M^{stat}$ (0.4%) data statistics
- $M^{p0}$ (0.5%) $\pi^0$ yield
- $M^{hadr}$ (0.5%) hadronic models
- $M^{xs}$ (5.0%) cross-section models
- $M^{bu}$ (4.7%) beam unisims
- $M^{k0}$ (0.5%) $K^o$ production Feynman scaling fit
- $M^{km}$ (0.5%) $K^-$ production Feynman scaling fit
- $M^{kp}$ (0.8%) $K^+$ production Feynman scaling fit
- $M^{pm}$ (0.7%) $\pi^-$ production Sanford-Wang fit
- $M^{pp}$ (4.0%) $\pi^+$ production spline fit
- $M^{om}$ (15.4%) optical model
- $M^{disc}$ (0.6%) discriminator threshold
- $M^{qtcorr}$ (2.1%) charge-time PMT response
- $M^{dirt}$ (1.0%) dirt events
- $M^{pot}$ (2.1%) POT

The numbers in brackets for the errors are the total normalization error:

$$Norm\ error = \frac{\sqrt{\sum_{ij} M_{ij}}}{N_{tot}},$$

where $N_{tot}$ = total integral for the CV MC. Comparing these numbers to those in the $M_A$ and $\kappa$ fits for CCQE in [67], we find a reasonable agreement. Since we now work with the reconstructed energy spectrum, there is no unfolding involved. Thus, there are no errors associated with this bias, as it was in the case in the NCE cross-section measurement in Section 6.8.

One matrix that needs to be investigated more closely is $M^{xs}$ (the cross-section models error matrix), because one has to be careful which parameters are fixed and which are allowed to vary for both signal (NCE) and backgrounds. Depending on what kind of fit is performed, different cross-section parameters are kept fixed for the NCE events. For background events all cross-section parameters from Table 4.6 are always allowed to vary. However, for NCE events in the simultaneous $M_A$ and $\kappa$ fit, the $M_A$ and $\kappa$ parameters are fixed to their mean values, with all other parameters varied. For NCE events in the simultaneous $M_A$ and $\Delta s$ fit, the $M_A$ and $\Delta s$ parameters are fixed to their mean values, with all other parameters varied.

## 7.3 Simultaneous $M_A$ and $\kappa$ Fit to the MiniBooNE Data

First we generate the reconstructed spectrum for MC corresponding to certain values of $M_A$ and $\kappa$ in a region going from 1.00 GeV to 1.5 GeV and 1.00 to 1.05, respectively. After properly calculating the error matrix, including the cross-section error matrix described in Section 7.2, we perform a $\chi^2$-fit of the MC with different values of $M_A$ and $\kappa$ to the MiniBooNE data. The $\chi^2$ is calculated in the following way:

$$\chi^2(M_A,\kappa) = \sum_{i=1}^{n}\sum_{j=1}^{n}\left[T_i^{MC}(M_A,\kappa) - T_i^{Data}\right]\left(M^{tot}\right)^{-1}_{ij}\left[T_j^{MC}(M_A,\kappa) - T_j^{Data}\right],$$

where $(M^{tot})^{-1}$ is the inverse error matrix from Eq.(7.1).

The results of the $\chi^2$-fit are shown in Fig. 7.10 for 49 degrees of freedom (DOF). The calculated allowed region of $M_A$ and $\kappa$ about the best fit point is shown in Fig. 7.11. The allowed region for $M_A$ and $\kappa$ corresponds to the points of ($M_A$,$\kappa$) with $\chi^2$ values less than $\chi^2_{min} + 2.3$ (2.3 is the $\chi^2$ value to have 68.3% cumulative probability for the $\chi^2$ distribution with 2 DOF [124]).

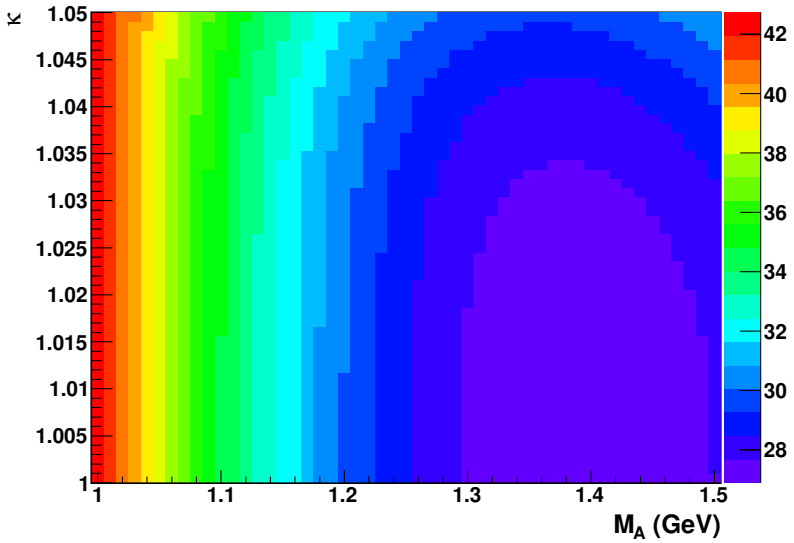


Figure 7.10: [
Results of the $M_A$ and $\kappa$ fit of the MC with $\Delta s = 0$ to the MiniBooNE NCE data with absolutely (POT) normalized distributions.] Results of the $M_A$ and $\kappa$ fit of the MC with $\Delta s = 0$ to the MiniBooNE NCE data with absolutely (POT) normalized distributions. The $\chi^2$ values are for 49 degrees of freedom (DOF). The $\chi^2$ surface has a minimum $\chi^2_{min} = 26.89$ at $M_A = 1.39$ GeV and $\kappa = 1.000$.

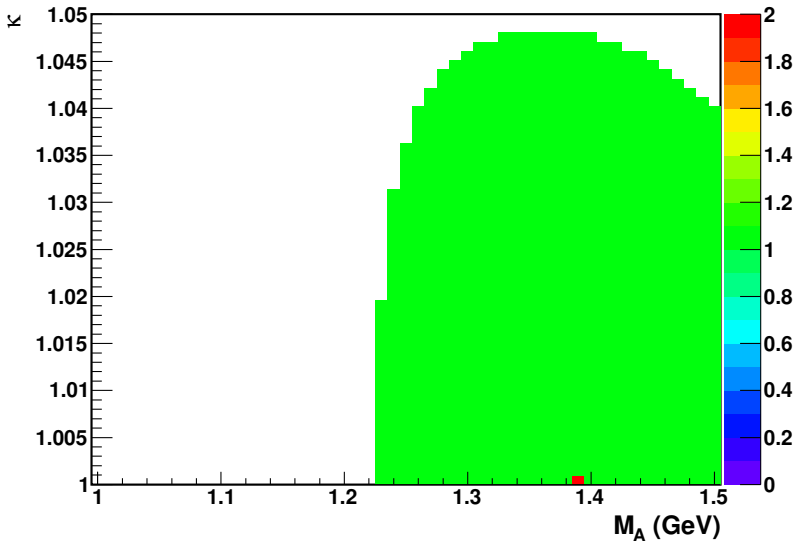


Figure 7.11: Allowed region of $M_A$ and $\kappa$, obtained from Fig. 7.10 by calculating the points in the ($M_A$,$\kappa$) region with $\chi^2$ values less than $\chi^2_{min} + 2.3$ (for 2 parameters varied independently). The red point represents the best fit point with $M_A = 1.39$ GeV and $\kappa = 1.000$.

We have also looked at some particular values of $M_A$ and $\kappa$ of special interest, as follows:

- $M_A = 1.02$ GeV and $\kappa = 1.000$: the world-average values of these parameters;

- $M_A = 1.23$ GeV and $\kappa = 1.022$: measured from MiniBooNE CCQE [69];
- $M_A = 1.35$ GeV and $\kappa = 1.007$: latest measurement from MiniBooNE CCQE with improved analysis [67].

The reconstructed energy spectra for data and MC with calculated $\chi^2$ are shown in Fig. 7.12. One can see that the world-average values of $M_A$ and $\kappa$ have a poor $\chi^2$, because the MC disagree with data at low energy. The MC with $M_A$ and $\kappa$ measured from the MiniBooNE CCQE data give a better $\chi^2$, having a reasonable agreement at low energies, but have a disagreement at high energies. One can conclude that the higher $M_A$ values that were measured in the MiniBooNE CCQE fit the MiniBooNE NCE data better than the world-averaged value of $M_A = 1.015$ GeV.

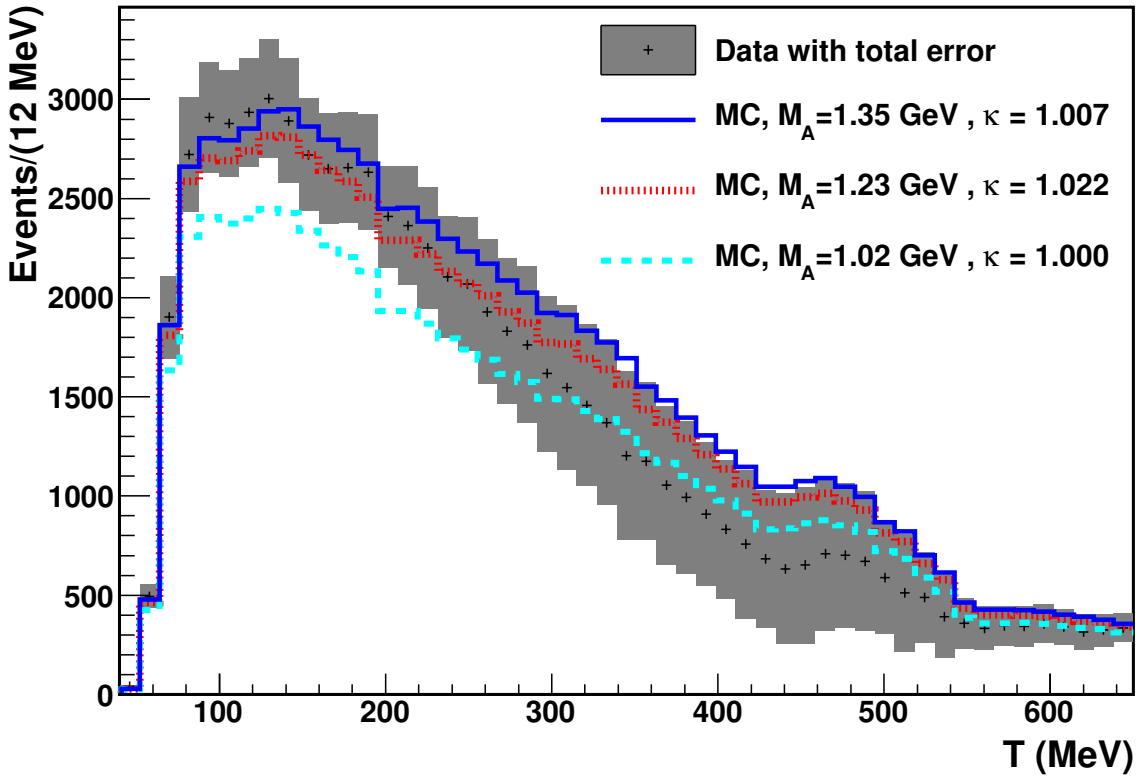


Figure 7.12: $\chi^2$-tests of the NCE reconstructed energy for $M_A$ values of 1.35, 1.23, and 1.02 GeV on the MiniBooNE NCE data. The $\chi^2$ values are 27.1, 29.2 and 41.3 for 49 DOF, respectively. The distributions are absolutely normalized.

## 7.4 Simultaneous $M_A$ and $\Delta s$ Fit to the MiniBooNE Data

Now keeping $\kappa = 1.022$ fixed, one can perform a simultaneous $M_A$ and $\Delta s$ fit. Again we first generate the reconstructed spectrum for MC corresponding to certain values of $M_A$ and $\Delta s$ in a region going from 1.00 GeV to 1.5 GeV and $-0.5$ to 0.5, respectively. After properly calculating the error matrix, including the cross-section error matrix described in Section 7.2, we perform a $\chi^2$-fit of the MC for different values of $M_A$ and $\Delta s$ to the MiniBooNE data.

The results of the $\chi^2$-fit are shown in Fig. 7.13 for 49 degrees of freedom (DOF). The calculated allowed region of $M_A$ and $\Delta s$ about the best fit point is shown in Fig. 7.14. As one can see in Fig. 7.13, there is a correlation between $M_A$ and $\Delta s$. This happens because there is a normalization variation as $\Delta s$ gets too far away from $\Delta s = 0.0$ value, which can be seen in Fig. 7.5. From the results of the BNL E734 experiment [62], which measured the value of $\Delta s = -0.21 \pm 0.1$, one can claim that the region of $\Delta s$ below $-0.3$ and above 0.0 are not likely. Thus, choosing this as a restricted $\Delta s$ value region, the $\chi^2$-fit result is shown in Fig. 7.15; here there is little dependence on $\Delta s$.

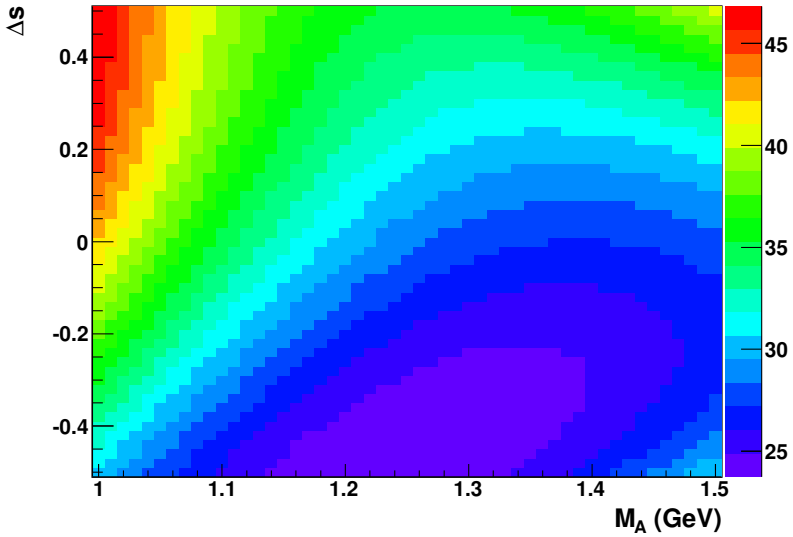


Figure 7.13: Results of the $M_A$ and $\Delta s$ fit of the MC with $\kappa = 1.022$ to the MiniBooNE NCE data with absolutely (POT) normalized distributions. The $\chi^2$ values are for 49 degrees of freedom (DOF). The $\chi^2$ surface has a minimum $\chi^2_{min} = 23.75$ at $M_A = 1.23$ GeV and $\Delta s = -0.5$.

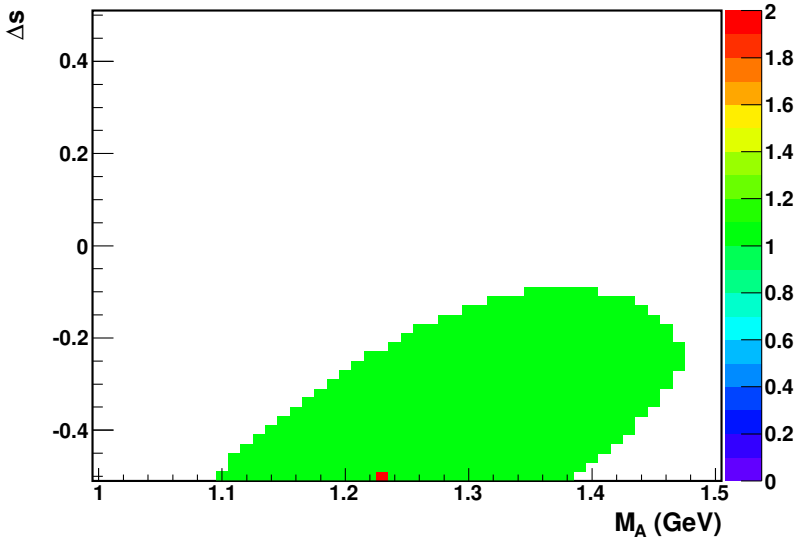


Figure 7.14: Allowed range of $M_A$ and $\Delta s$, obtained from Fig. 7.13. The red point represents the best fit point with $M_A = 1.23$ GeV and $\Delta s = -0.5$.

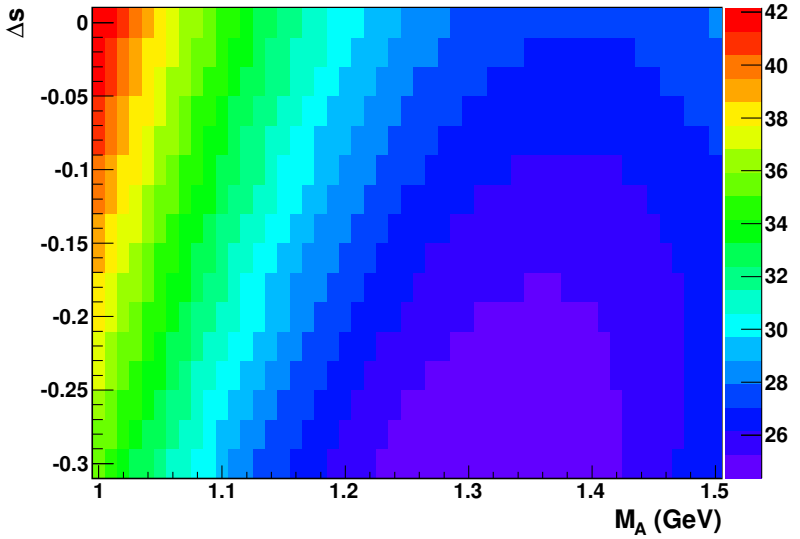


Figure 7.15: Results of the $M_A$ and $\Delta s$ fit of the MC with $\kappa = 1.022$ to the MiniBooNE NCE data with absolutely (POT) normalized distributions. The $\chi^2$ values are for 49 degrees of freedom (DOF). The region of $\Delta s$ is chosen from $-0.3$ to 0.0, different than that in Fig. 7.13.

## 7.5 $M_A$ Only Fit to the MiniBooNE Data

Now keeping $\kappa = 1.022$ and picking different values of $\Delta s$ one can perform $M_A$ only fits to the MiniBooNE data. Since there is a slight correlation between $M_A$ and $\Delta s$, we choose the $M_A$ fit to data with $\Delta s = 0$ to be the main result. However, as a comparison, we perform another $M_A$ fit for

$\Delta s = -0.2$ (the best fit from BNL E734).

For $\Delta s = 0$, the results of the $\chi^2$ fit of $M_A$ only is shown in Fig. 7.16. The allowed range of $M_A$ calculated from the $\chi^2$ surface corresponds to the $M_A$ points which have $\chi^2 < \chi^2_{min} + 1.0$, namely

$$M_A(\Delta s = 0) = (1.39 \pm 0.11) \text{ GeV}.$$

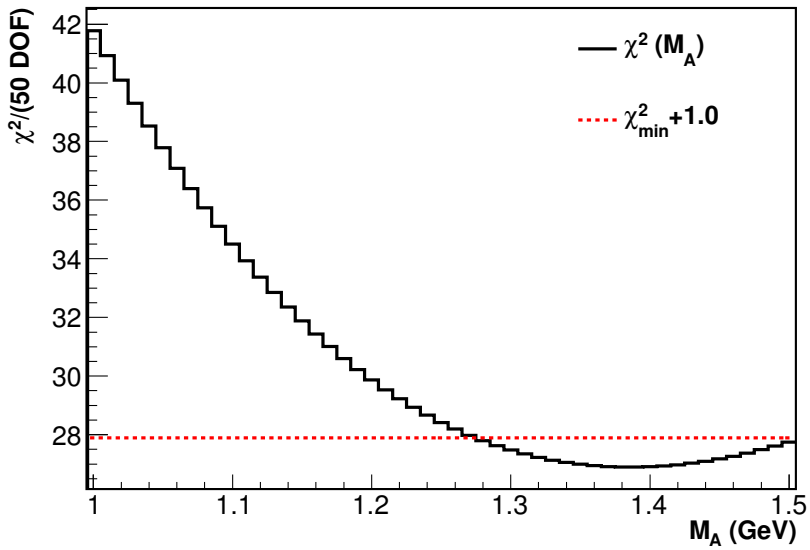


Figure 7.16: Results of the $M_A$ fit of the MC with $\kappa = 1.022$ and $\Delta s = 0$ to the MiniBooNE NCE data with absolutely (POT) normalized distributions. The $\chi^2$ values are for 50 degrees of freedom (DOF). The $\chi^2$ surface has a minimum $\chi^2_{min} = 26.89$ at $M_A = 1.39$ GeV. Also in the plot as red dashed line is the $\chi^2_{min} + 1.0$ value (1.0 is the $\chi^2$ value to have 68.3% cumulative probability for the $\chi^2$ distribution with 1 DOF [124]).

Similarly, taking $\Delta s = -0.2$, we identify $\chi^2_{min} = 24.90$ for 50 DOF and the allowed range of $M_A$ yields

$$M_A(\Delta s = -0.2) = (1.35 \pm 0.11) \text{ GeV}.$$

# Chapter 8

# High Energy Ratio of $\nu p \rightarrow \nu p$ over $\nu N \rightarrow \nu N$ and the $\Delta s$ fit.

## 8.1 Reconstruction of High Energy NCE Events

In this chapter we consider only events with a reconstructed energy above Cherenkov threshold (thus *high energy* events). First we explain why NCE proton and neutron events may be different at high energies.

As mentioned previously neutrons do not produce light by themselves, but rather through secondary interactions, where they interact strongly with matter, producing secondary charged particles, mostly protons. Since NCE neutron are detected through the secondary protons, it should be impossible to identify them from NCE proton events, which means there is no sensitivity to $\Delta s$ in the MiniBooNE data. Fortunately, there is a special class of NCE proton events which is possible to select, namely those NCE protons above Cherenkov threshold ($T > 350$ MeV) and with no FSI inside the nucleus.

In the case of NCE ($\nu N \rightarrow \nu N$), there is only one primary final state particle – either proton or neutron (not including the outgoing neutrino). After a neutrino interaction, the nucleon (if it is inside carbon) goes through the nuclear matter, where it may interact strongly with other nucleons. Our estimate of the FSI probability is 26% on carbon [125]. Obviously, there are no FSI in neutrino scattering on hydrogen. Overall, there is a 22% probability for a FSI in $CH_2$.

There are three important NCE-like channels to consider in this study: NCE proton, NCE

neutron, and the irreducible backgrounds.

**NCE proton.** Two cases of NCE proton may occur – with and without FSI.

- In the first case of NCE proton without FSI shown in Fig. 8.1 (top), the primary proton leaves the nucleus and no other particles are produced. It immediately starts producing both Cherenkov and scintillation light and usually stops before interacting with other nuclei.
- In the second case where a FSI has occurred, shown in Fig. 8.1 (bottom), there are at least two final state nucleons produced. The primary proton in this case loses energy in the FSI process, sharing it with secondary nucleons. All final state nucleons then interact with the detector media, producing scintillation light (and perhaps Cherenkov light as well).

  The biggest difference between these two cases is that there is one final state proton in the first case and multiple protons in the second case.

**NCE neutron.** NCE neutron events with and without FSI are shown in Fig. 8.2. Both cases are equivalent in terms of the properties of light produced in the reaction (up to nuclear recoil effects, which may be neglected here) because the neutron doesn't produce light and doesn't lose energy until it interacts with another nucleon. Thus it doesn't matter if the interaction happened inside the original nucleus or later, in the detector. In both cases there are multiple protons in the event.

**Irreducible backgrounds.** These are neutral current pion channels (NUANCE channels 6-9), but with the pion absorbed in the original nucleus. This is the case where the pion experiences absorption (see Section 4.5.4), producing one or more nucleons. An example of the irreducible event is shown in Fig. 8.3. In this case again, there are at least two final state nucleons, thus multiple protons are produced in the event.

Table 8.1 has a summary of the channels and the corresponding proton multiplicity. One can see that only NCE proton without FSI have a single outgoing proton, whereas all other channels have multiple protons. Therefore, from this description, one can consider only two classes of NCE-like events: *single proton* and *multiple protons*.

The idea why single and multiple protons events at high energy may look different in the detector is this: a high energy single proton produces more Cherenkov light than a multiple protons event. It

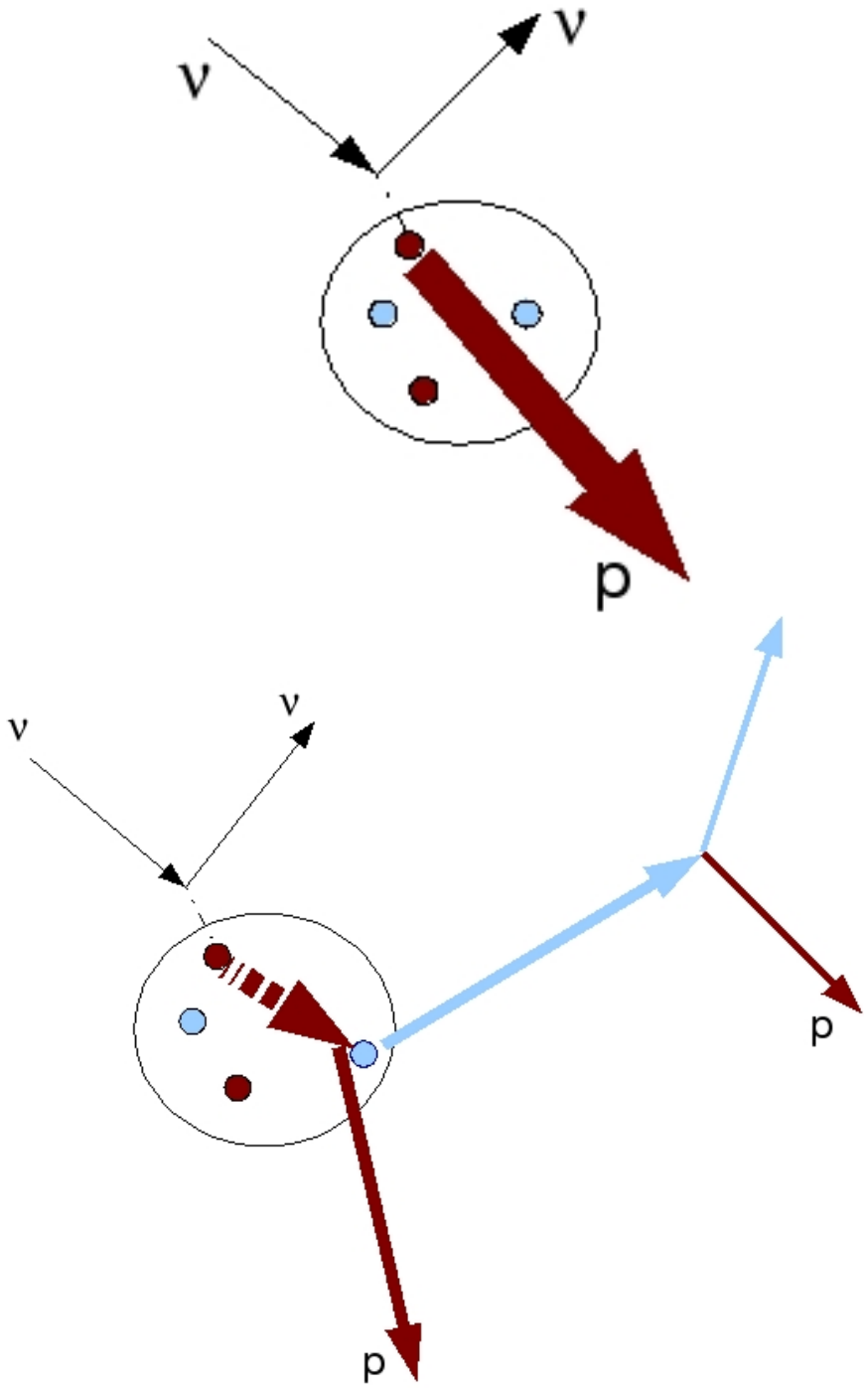


Figure 8.1: NCE proton without FSI (top) and with FSI (bottom).

has been discussed in Section 4.6 that Cherenkov and scintillation light have different properties – Cherenkov light is prompt and directional, whereas scintillation light is isotropic and delayed. The

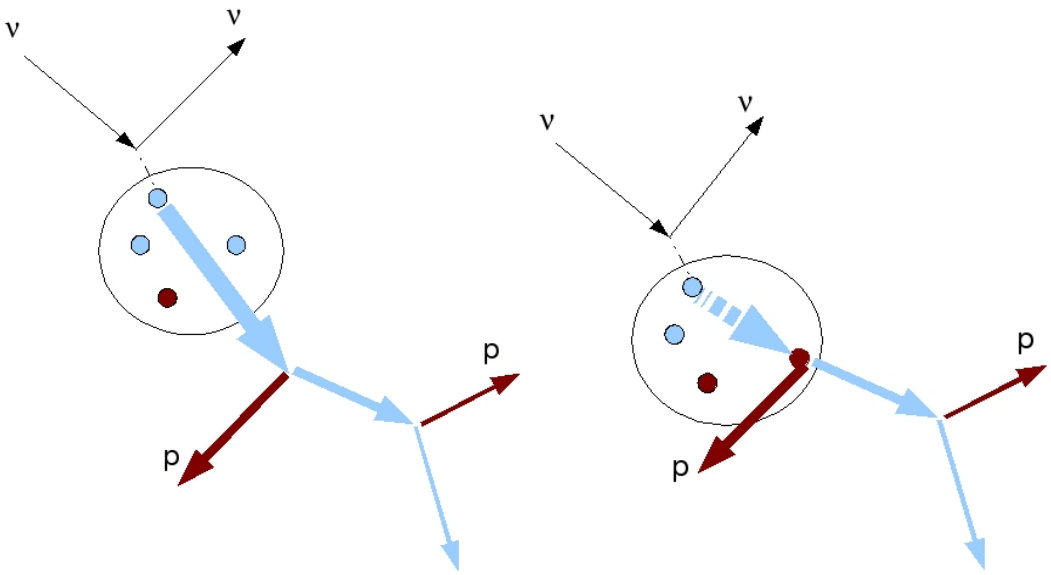


Figure 8.2: NCE neutron without FSI (left) and with FSI (right).

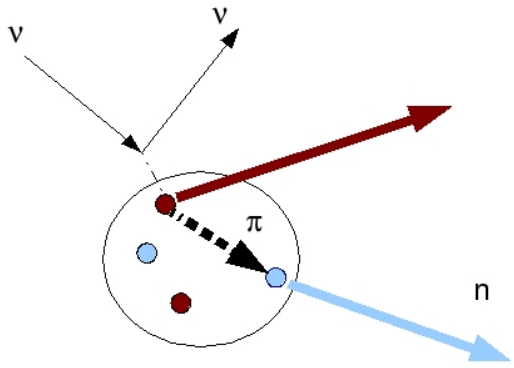


Figure 8.3: An irreducible background event example.

Cherenkov fraction depends on the proton energy: the higher the energy, the larger the Cherenkov fraction. A multiple protons event that in average emits the same amount of light as a higher energy single proton event should produce less Cherenkov light than the latter, because the nucleon in the single proton event is more energetic than either of the nucleons in the multiple protons event. For example, two protons of 200 MeV produce about the same amount of light as one 400 MeV proton (say, the same number of tank hits), but they would not produce Cherenkov light, as opposed to the single proton that would produce Cherenkov light.

To check this hypothesis, we selected MC events within a certain range of $Tank\ PMTs$ distribution, $150 < Tank\ PMTs < 155$, which roughly corresponds to 440 MeV single proton kinetic

| NCE-like channel | Charged particles produced |
|---|---|
| NCE proton without FSI | Single proton |
| NCE proton with FSI | Multiple protons |
| NCE neutron without FSI | Multiple protons |
| NCE neutron with FSI | Multiple protons |
| Irreducible backgrounds | Multiple protons |

Table 8.1: Summary of the NCE-like channels and the corresponding proton multiplicity.

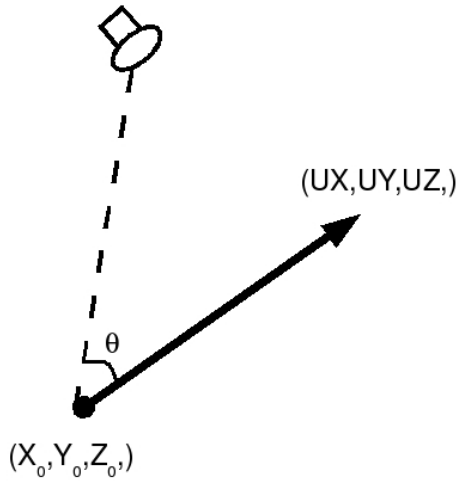


Figure 8.4: $\theta$ is the angle between the reconstructed event direction and the line from the event vertex to the PMT. $(X_0, Y_0, Z_0)$ is the reconstructed vertex, $(UX, UY, UZ)$ is the reconstructed direction.

energy. After the event reconstruction we filled two distributions for each PMT hit: the reconstructed corrected time (defined in Eq.(5.14)) and $cos\theta$ (defined in Fig. 8.4) for NCE events. These distributions for different NCE-like channels are shown in Fig. 8.5. The corrected time distribution shows that the single proton events (NCE proton without FSI) have in average more prompt light than the multiple proton events (NCE proton with FSI and NCE neutron). The $\cos\theta$ distribution shows that the single proton events are more directional than multiple proton events. Furthermore, NCE proton with FSI and NCE neutron events are virtually identical in both of these variables. This means that single proton events have in average more Cherenkov light than multiple proton events and thus can be distinguished to a certain degree.

## 8.2 Most Energetic Nucleon in NCE-like Events

We also studied how often the multiple proton events have a dominant proton and the energy of the dominant proton, because these events are hard to distinguish from single proton events. We looked

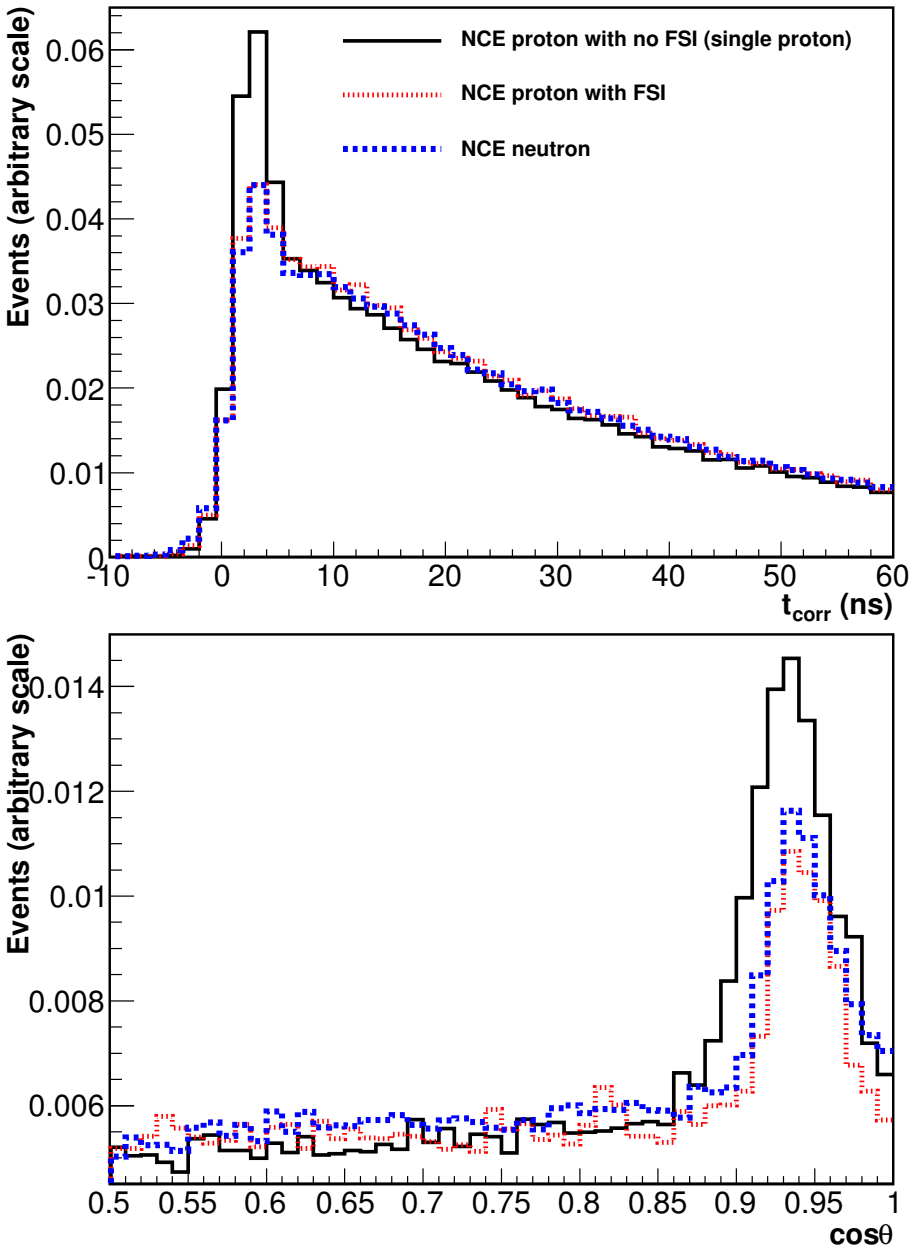


Figure 8.5: Corrected time distribution (top) and $cos\theta$ (bottom) for different NCE-like channels (as labeled).

at high energy NCE proton events only and divided the events into two samples:

- NCE proton without FSI (single proton)
- NCE proton with FSI (multiple protons).

We compared the generated energy of the most energetic nucleon (which we denote as $T_{gen}^{MEN}$) for both samples for events with about the same visible energy at high energies. If $T_{gen}^{MEN}$ in the multiple proton sample is much smaller than the total generated kinetic energy, then this event should produce significantly less Cherenkov light than events in the single proton sample.

The distributions of $T_{gen}^{MEN}$ versus the reconstructed energy ($T$) for the single and multiple proton samples are shown in Fig. 8.6. One can see from this plot that single proton events are well reconstructed as the generated and reconstructed energies are close to each other. However, in a multiple protons sample one can see that there are two regions – one is along the $T_{gen}^{MEN} = T$ line and the other is below it. Events with FSI which are found along this line represent the case where one of the nucleons dominates, and the fitter reconstructs the dominating proton well. The events that are found below the $T_{gen}^{MEN} = T$ line is where there is no dominating proton. One can also see that most of the events in the last category have $T_{gen}^{MEN}$ below the Cherenkov threshold for protons (one can also see that from Fig. 8.7 where the $T_{gen}^{MEN}$ distribution is shown for all events). Also, by looking at the difference between $T_{gen}^{MEN}$ and the reconstructed energy, as shown in Fig. 8.8, we can find that events with FSI have 2 peaks, which represent the 2 regions (along and below $T_{gen}^{MEN} = T$ line in Fig. 8.6). The second peak is rather small – about 30% of the FSI sample. Thus, about 30% of the multiple proton events have a dominating proton in the final state.

The conclusion is that the NCE-like with FSI events (multiple protons), in average, produce indeed less Cherenkov light than the NCE proton events without FSI (single proton) and thus these two can be distinguished. The difference in the corrected time distributions and $cos\theta$ that was shown in Fig. 8.5 is just a reflection of this fact.

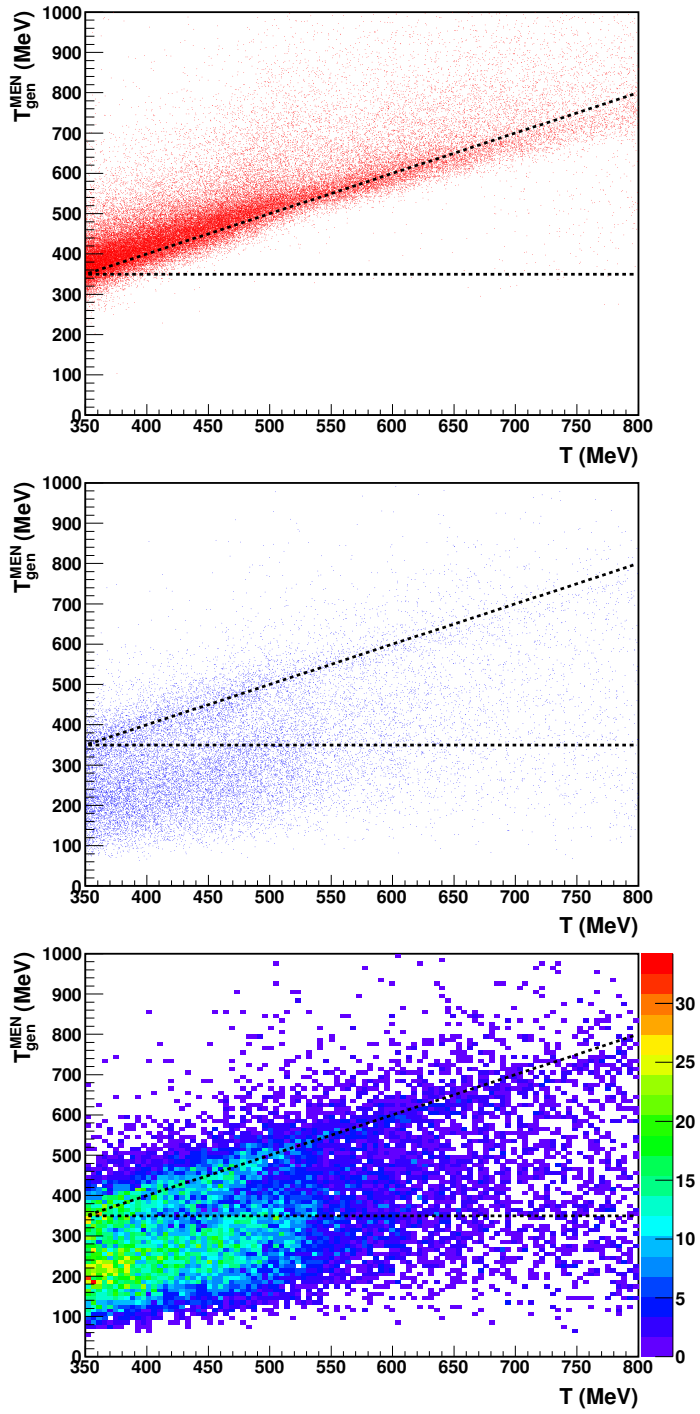


Figure 8.6: The energy of the most energetic nucleon vs reconstructed energy of the event. NCE proton without FSI scattered plot (top), NCE proton with FSI (middle and bottom plots) as a scattered plot (middle) and as a box option with color scale varying with contents (bottom). The two lines are $T^{MEN}_{gen} = T$ (true energy equals to the reconstructed energy) and $T^{MEN}_{gen} = 350$ MeV (Cherenkov threshold).

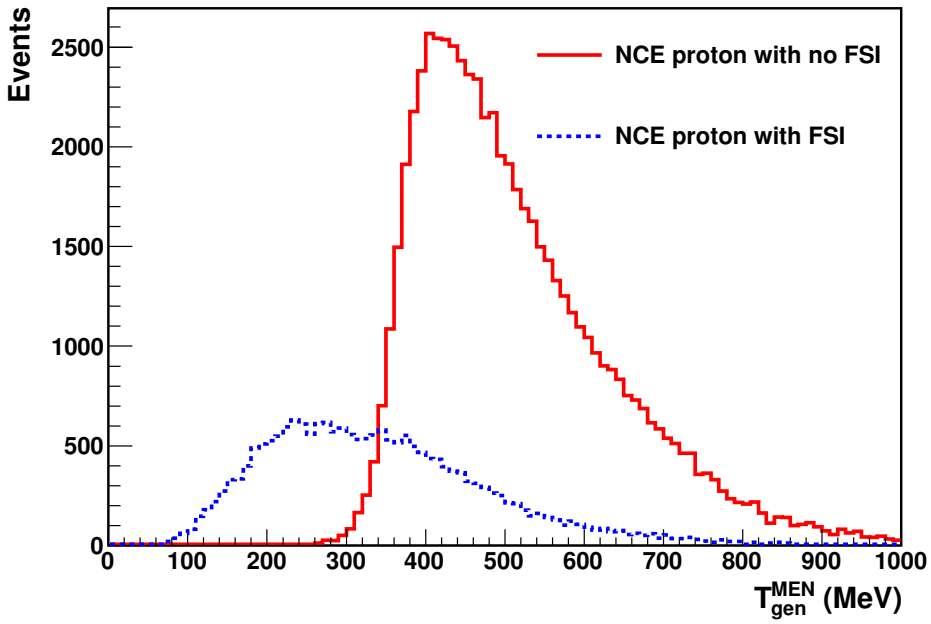


Figure 8.7: The energy of the most energetic nucleon for NCE protons with and without FSI.

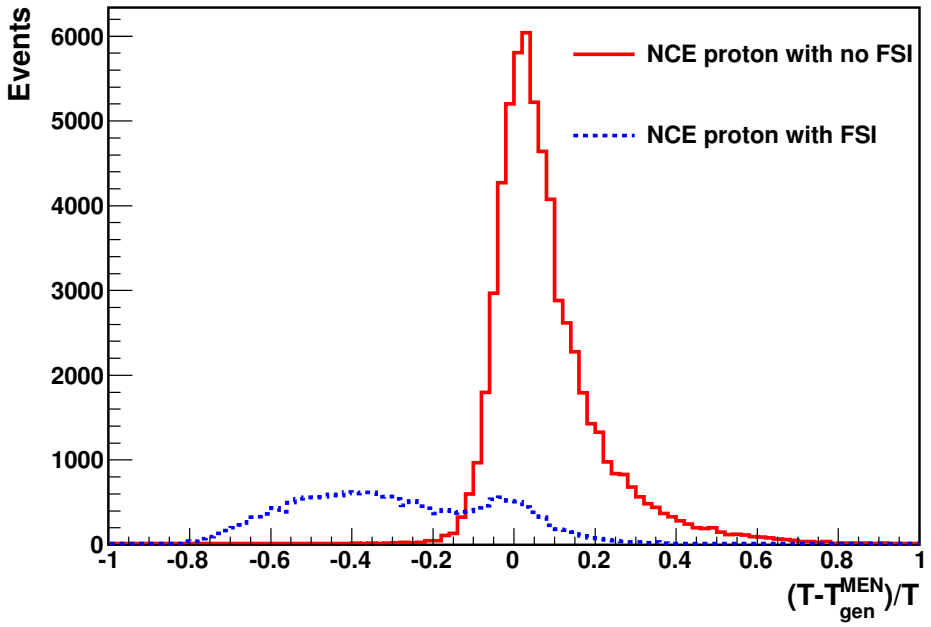


Figure 8.8: Difference between the reconstructed energy and $T_{gen}^{MEN}$ for NCE protons with and without FSI.

## 8.3 High energy $\nu N \to \nu N$ and $\nu p \to \nu p$ Samples

### 8.3.1 The $\nu N \to \nu N$ Sample

We start with the standard NCE cuts (as defined in Section 6.3) but concentrate only on high energies; i.e., instead of $T < 650$ MeV we use 350 MeV $< T <$ 800 MeV:

$$\begin{aligned} \text{Precuts} &= 1 \text{ Subevent} + Veto\ PMTs < 6 + Tank\ PMTs > 24 \\ &+ 4400 \text{ ns} < \text{Time} < 6500 \text{ ns} + 350 \text{ MeV} < T < 800 \text{ MeV} \\ &+ \ln(\mathcal{L}_e/\mathcal{L}_p) < 0.42. \end{aligned}$$

The reconstructed energy distribution after the Precuts is shown in Fig. 8.9. This is the same distribution as the one shown in Fig. 6.8 (top plot), but at higher energies (also the histograms have a different bin width). First of all, one can see that there is a lot of "other backgrounds", especially at high energies, which have lots of charge-current interactions with the muon producing most of the light.

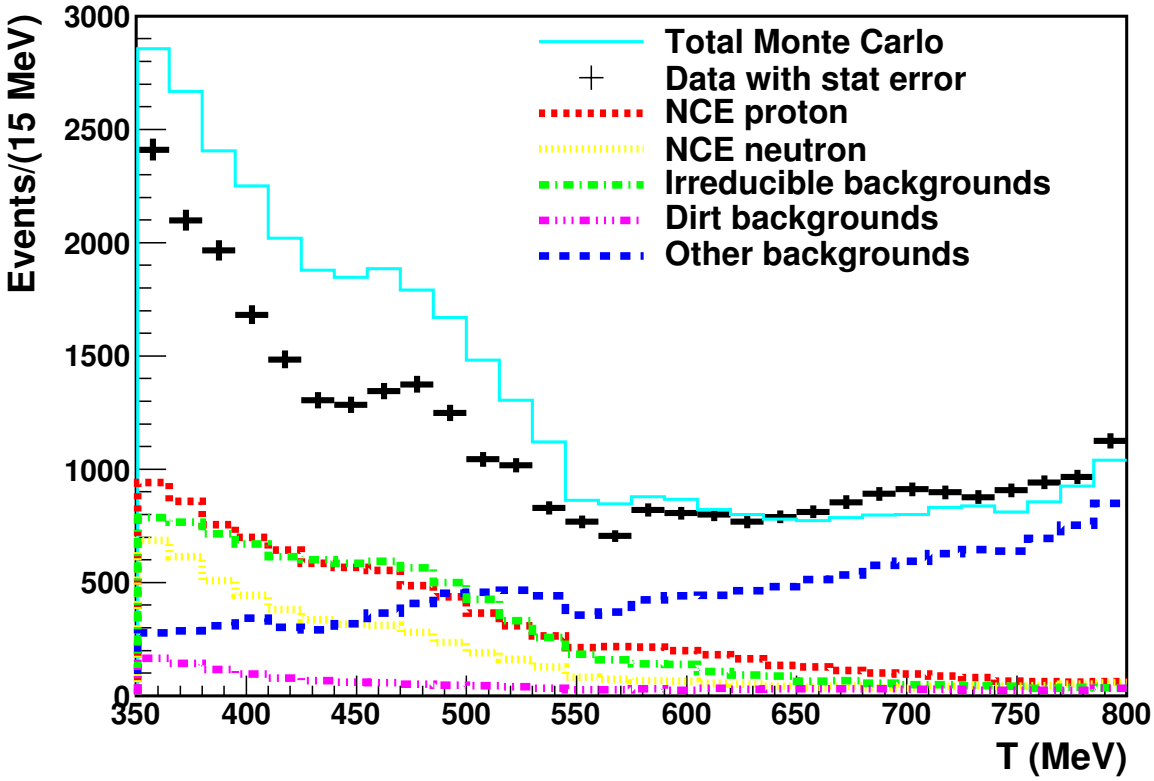


Figure 8.9: Reconstructed energy after Precuts are applied.

We have studied the MC composition of (what we call) "other backgrounds". The NUANCE channels (as defined in Table 4.5) for these background events are shown in Fig. 8.10. The top plot

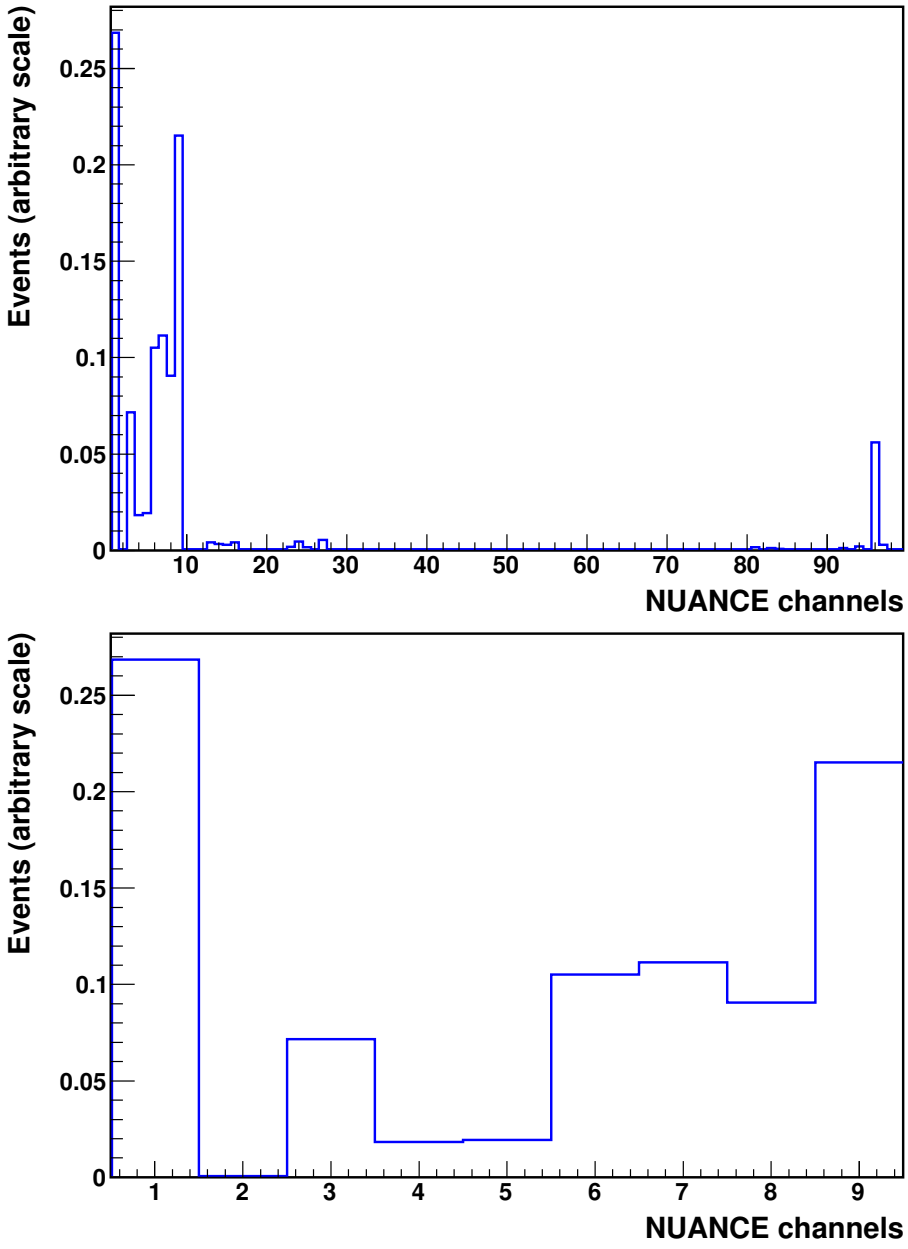


Figure 8.10: NUANCE channels for "other backgrounds". All channels from 1 to 100 (top plot) and only channels from 1 to 10 (bottom plot).

shows all channels. One can clearly see that channels from 1 to 9 dominate; therefore, the bottom plot shows a closer look at only channels from 1 to 9. The "Other backgrounds" consist of about 40% charge current events (mostly CCQE), where a muon is emitted. The rest are neutral current

channels, of which there are those where a charged pion is produced (for example channels 7 and 9) which for the most part have very similar properties to a muon, because they have a similar mass. If one adds those channels together one would have about 70% of the "other backgrounds" events have a muon-like particle produced in the interaction.

If a muon is emitted in the interaction, it generally produces much more light than any other particle created in the event. We expect to be able to distinguish between muons and protons, because their Cerenkov light profile are much different, as they have different masses. It was found that the $\log(\mathcal{L}_p/\mathcal{L}_\mu)$ variable (which is a log likelihood ratio between the proton and the muon hypotheses) gives a good separation between NCE and "other backgrounds", as shown in Fig. 8.11, where an energy dependent cut is applied. This cut is used in the $\nu N \rightarrow \nu N$ event sample. The events that are below the cut line (proton-like) are left for the analysis. Let us call this cut the "Proton/Other" cut. Also, one can project the values of $\log(\mathcal{L}_p/\mathcal{L}_\mu)$ on the "Proton/Other" cut by subtracting the value of the "Proton/Other" cut line at the reconstructed energy. Then, the projection is shown in Fig. 8.12. As one can clearly see, the cut eliminates a big chunk of the "other backgrounds", leaving most of the NCE events.

After the NCE Precuts and the Proton/Other cut, we are left with the $\nu N \rightarrow \nu N$, or NCE (proton+neutron), event sample. The reconstructed energy spectrum for the sample is shown in Fig. 8.13. Comparing this energy spectrum to the one before the Proton/Other cut (in Fig. 8.9), one can see that the "other backgrounds" are highly reduced, while leaving most of NCE events. The $\nu N \rightarrow \nu N$ data sample has 24,004 events with the following predicted channel fractions: 45% NCE, 26% irreducible backgrounds, 3% dirt backgrounds, and 25% other backgrounds.

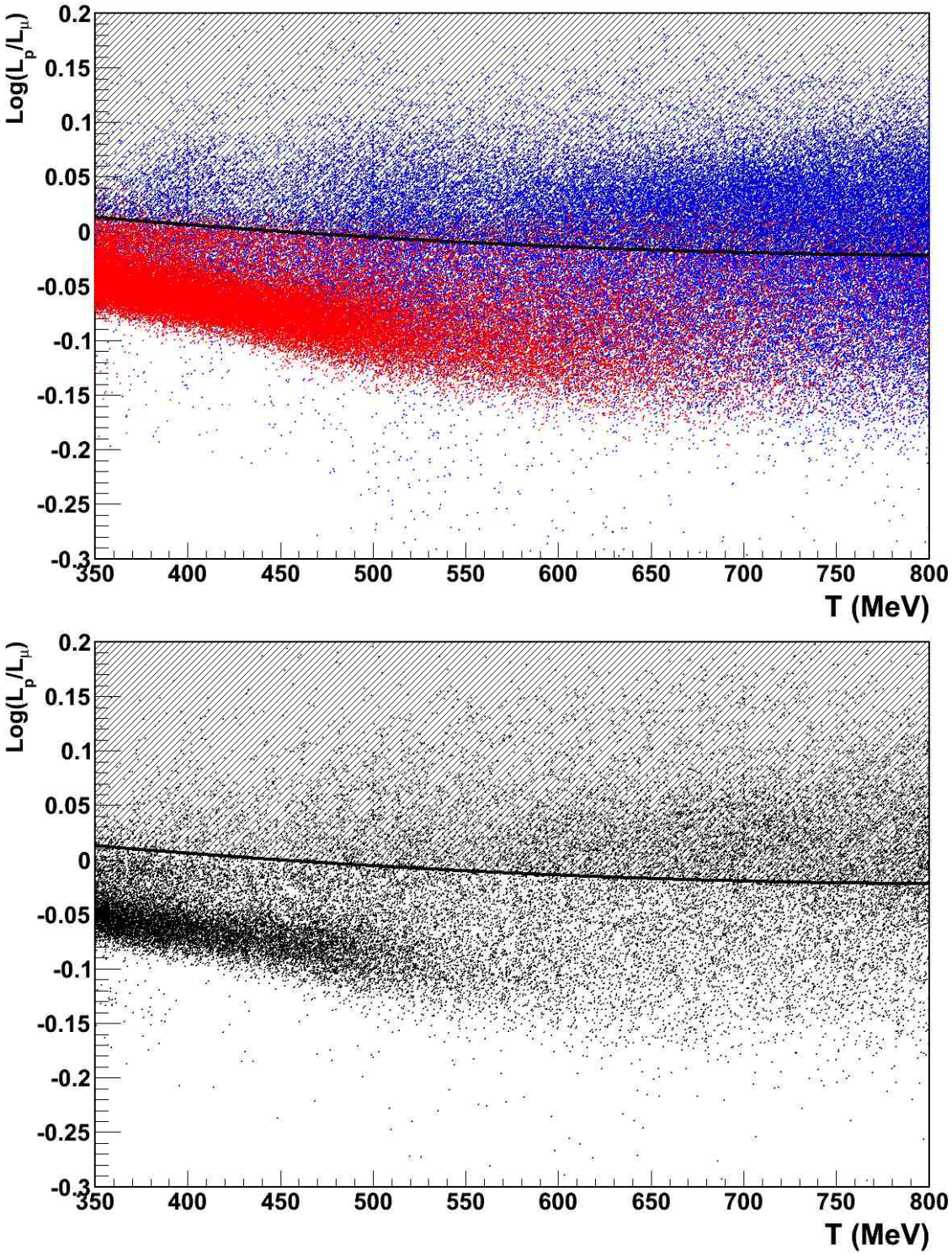


Figure 8.11: Proton/Other cut based on the $\log(\mathcal{L}_p/\mathcal{L}_\mu)$ variable, which is the log-likelihood ratio of proton and muon event hypotheses for the MC (top plot) and data (bottom plot). The top plot have the NCE (red) and "other backgrounds" (blue) events. The dashed region is cut out. This cut reduces the muon-like backgrounds, which are a big fraction of "other backgrounds".

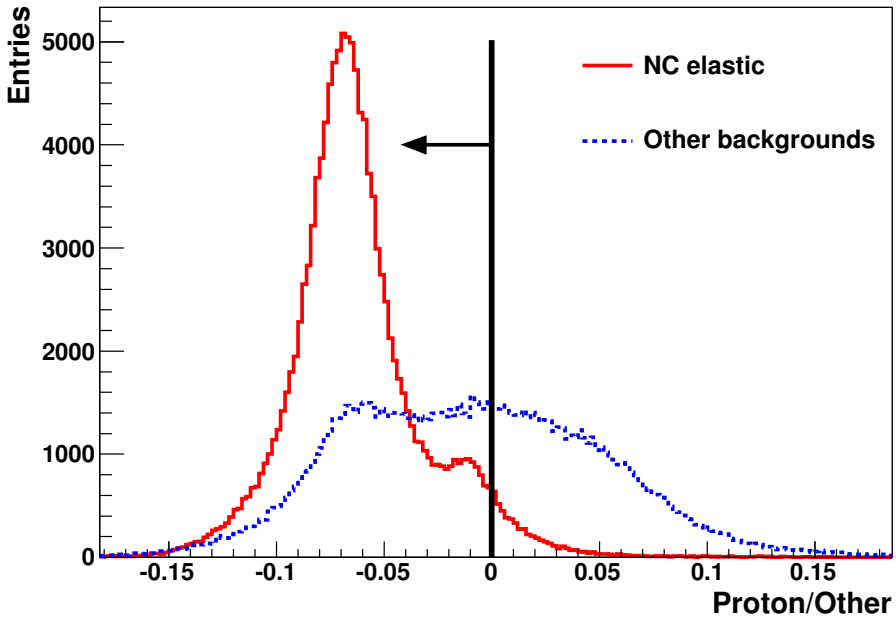


Figure 8.12: The projection of the $\log(\mathcal{L}_p/\mathcal{L}_\mu)$ variable on the cut for all energies for the NCE and "other backgrounds" events. The arrow indicates the part which is left for the analysis after the cut.

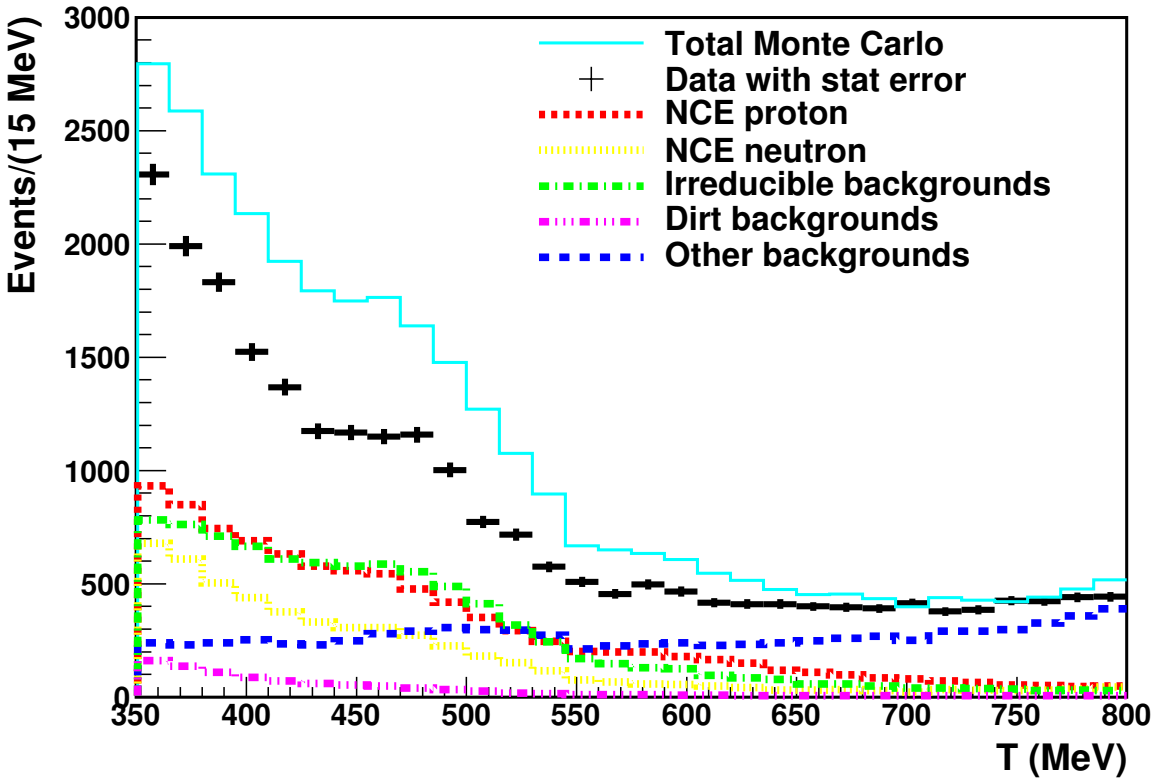


Figure 8.13: Reconstructed energy after Precuts and Proton/Other cut are applied. Data with statistical error and different MC channels as labeled.

### 8.3.2 The $\nu p \rightarrow \nu p$ Sample

Following the previous event selection it was found that the fraction of prompt PMT hits (with a corrected time from 0 ns to 5 ns) in the $cos\theta > 0$ region (where $\theta$ is defined in Fig. 8.4) is the best particle identification variable to distinguish single proton from multiple proton events. It is expected that single proton events have a higher Cerenkov light fraction and have a better direction reconstruction than multiple proton events, as shown in Fig. 8.14. Again, an additional energy dependent cut was chosen based on this variable to select single proton events which is also shown in this plot. We call this the "Proton/Neutron" cut. The area above the line is left for the $\nu p \rightarrow \nu p$ sample. Also, one can project the values of the variable on the "Proton/Neutron" line, as shown in Fig. 8.15. One can see that the cut increases the single proton events fraction while reducing the multiple proton events in the sample.

After the "Proton/Neutron" cut, we investigate the distribution of $\theta_p$, the angle between the reconstructed direction of the proton and the Z-axis, i.e., that of the beam direction. One expects NCE proton events to be in the more forward direction than the rest of events. The $\theta_p$ distribution is shown in Fig. 8.16. The appearance of the forward going events in this plot convincingly shows that we are indeed reliably reconstructing the proton direction in MiniBooNE in both data and MC.

Both data and MC have a distinct peak in the forward direction relative to the beam direction. According to the MC, this peak is dominated by NCE proton events. The rest of the events, especially the "Other backgrounds" are less forward going. Thus, for the $\nu p \rightarrow \nu p$ event selection, an additional cut on the $\theta_p$ is applied in order to reduce the backgrounds, namely $\theta_p < 60^o$.

After the last cut we obtain the final $\nu p \rightarrow \nu p$, or NCE proton-enriched event sample. The energy spectrum for this sample is shown in Fig. 8.17. One can see from the plot that the NCE proton channel dominates almost throughout the entire energy range 350 MeV $< T <$ 800 MeV, especially the lower $T$ region. The $\nu p \rightarrow \nu p$ data sample has 7,616 events with the following predicted channel fractions: 55% NCE p, 10% NCE n, 14% irreducible backgrounds, 1% dirt backgrounds, and 19% other backgrounds.

We now have two samples of events, obtained with different cuts, which we are going to use for the ratio measurement:

$$\begin{aligned} \nu p \rightarrow \nu p &= \text{Precuts} + \text{Proton/Other} + \text{Proton/Neutron} + \theta_p < 60^o, \\ \nu N \rightarrow \nu N &= \text{Precuts} + \text{Proton/Other}. \end{aligned}$$

## 8.4 Ratio of $\nu p \to \nu p$ over $\nu N \to \nu N$ and its sensitivity to $\Delta s$

Now that we have the proton-enriched $\nu p \to \nu p$ and the inclusive $\nu N \to \nu N$ event samples, one can form the ratio

$$ratio = \frac{\nu p \to \nu p}{\nu N \to \nu N}, \tag{8.1}$$

which we calculate bin by bin. This ratio should be sensitive to $\Delta s$ because the numerator consists of mostly NCE scattering on protons, which in turn depends on $\Delta s$ (see Eq.(3.16)). The denominator is nearly independent on $\Delta s$, as discussed in Section 6.9 and shown in Section 7.4. Thus, this ratio should have larger values for negative $\Delta s$ values as for positive $\Delta s$ values. Furthermore, we expect a lot of systematic errors to cancel in the ratio. For example, the flux errors should cancel for the most part since it is the same neutrino flux for both the numerator and the denominator. The POT error cancels out completely.

All systematic and statistical uncertainties have been obtained in the same manner as described in Section 7.2. The total error matrix has been obtained in order to perform fits to data.

The ratio of $\nu p \to \nu p$ to $\nu N \to \nu N$ for the data and MC with $\Delta s = 0$ along with the MC with values of $\Delta s = -0.5$, 0, and 0.5 are shown in Fig. 8.18. The data histogram has the diagonal elements of the total error matrix for the error bars. As one can see, the $\nu p \to \nu p / \nu N \to \nu N$ ratio is sensitive to $\Delta s$, however the errors are quite large. Again it is the uncertainty in the optical model that dominates the errors in this measurement accounting for $\sim 16.2$ out of the total $\sim 19.7\%$ error.

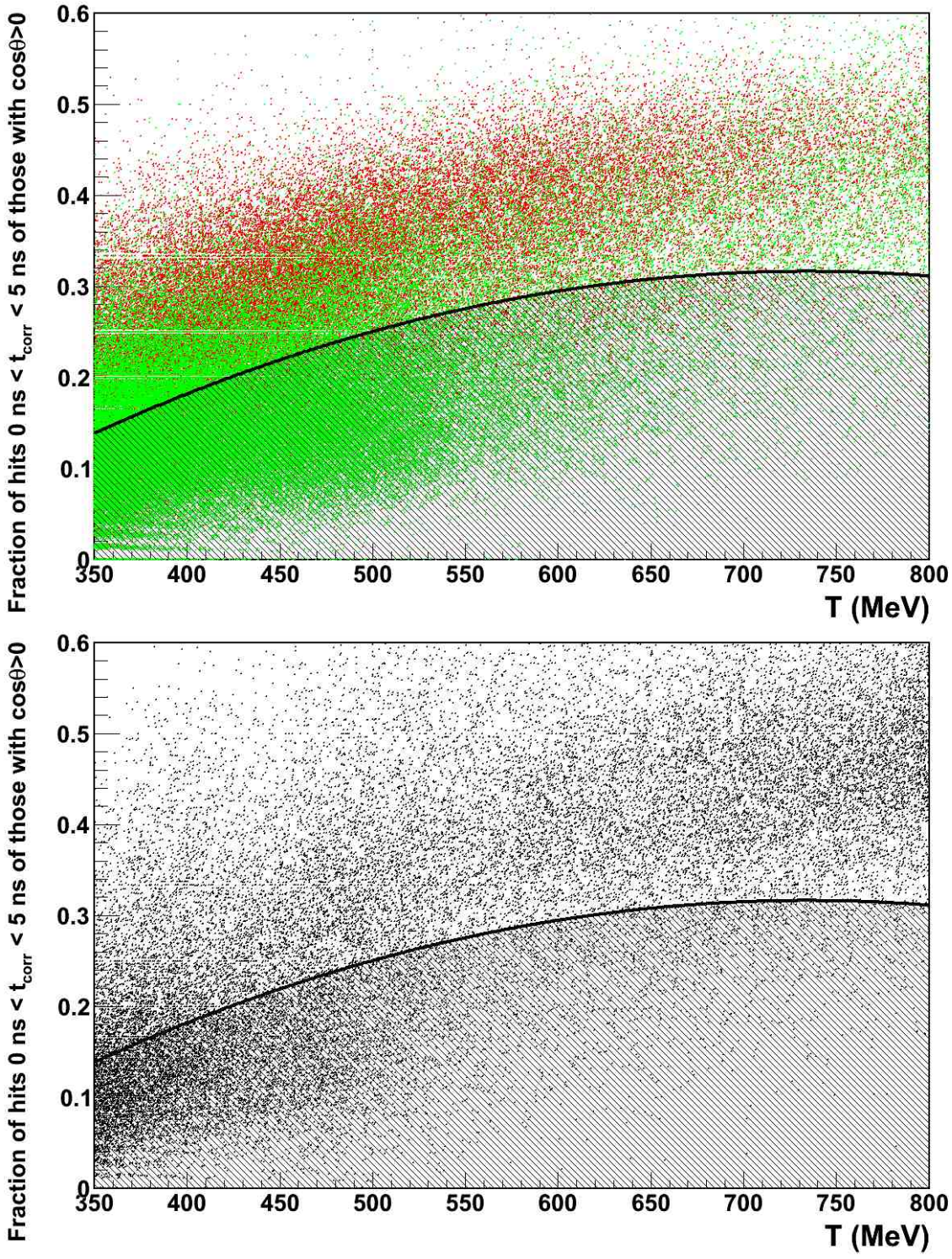


Figure 8.14: Proton/Neutron cut based on "the fraction of prompt hits among those with $cos\theta > 0$" variable for the MC (top plot) and the data (bottom plot). The top plot have single proton (red), multiple protons (blue) events. The dashed region is cut out. This cut is to reduce the multiple proton events in the sample.

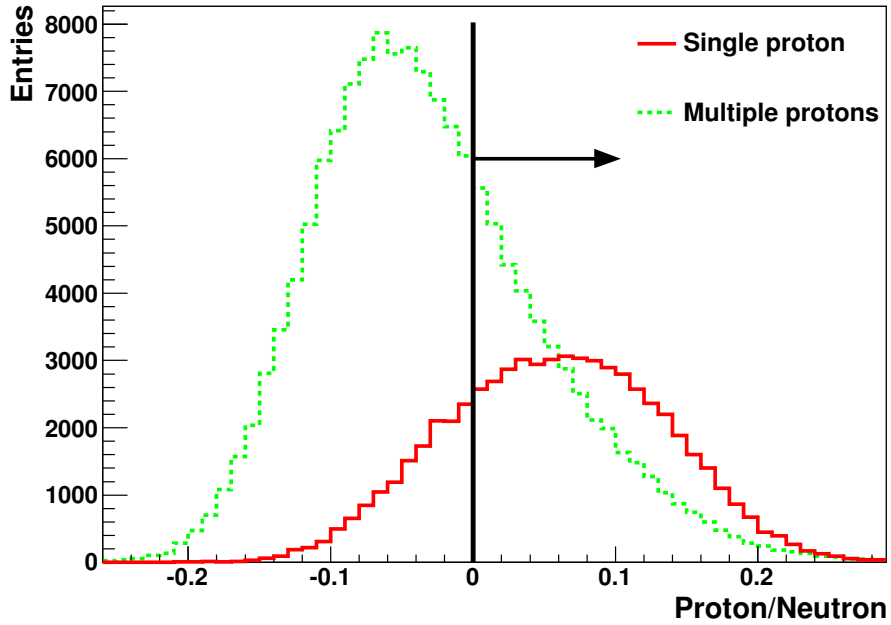


Figure 8.15: The projection of the "fraction of prompt hits of those with $cos\theta > 0$" variable on the "Proton/Neutron" cut line for all energies for the single proton and multiple protons events. The arrow indicates the part which is left after the cut for the analysis.

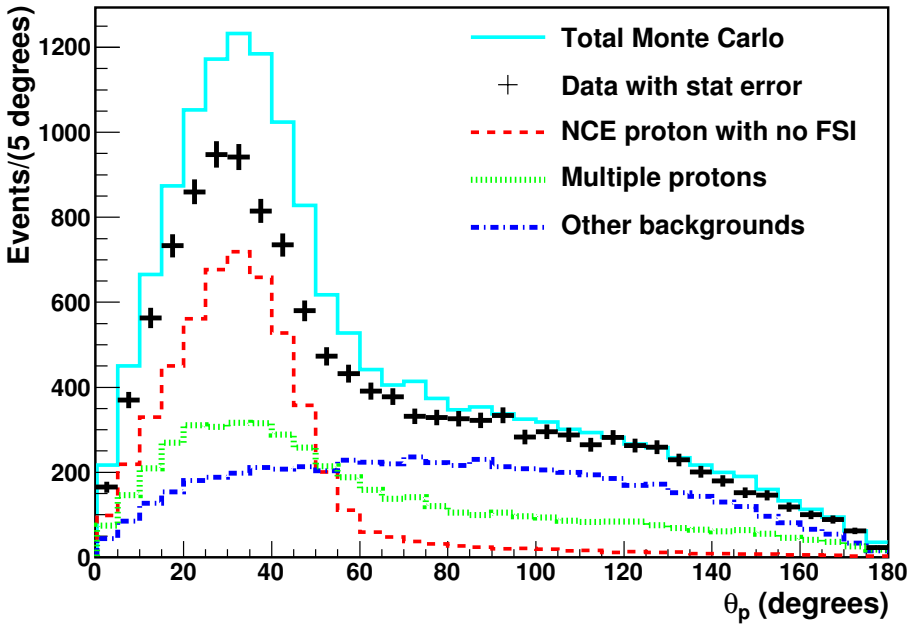


Figure 8.16: The angle between the reconstructed proton direction and the incident neutrino (beam) direction.

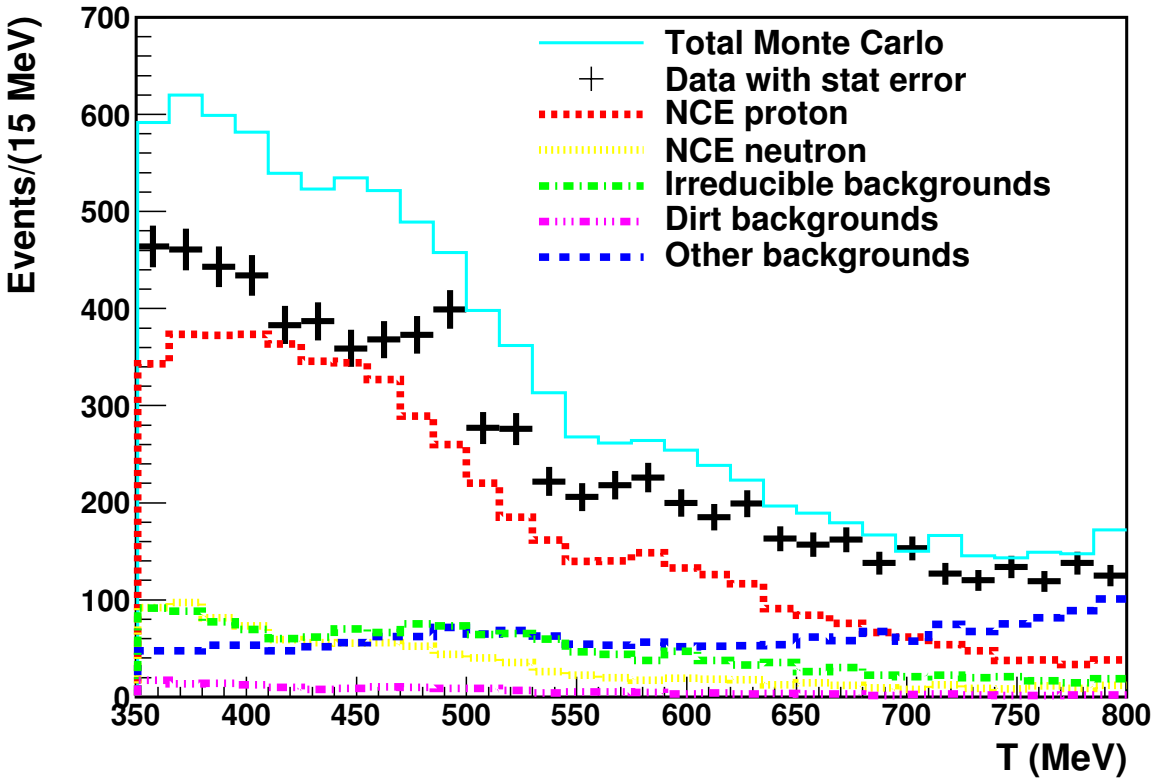


Figure 8.17: Reconstructed energy after Precuts and Proton/Other, Proton/Neutron and $\theta_p < 60^o$ cuts are applied. Data with the statistical error and different MC channels as labeled.

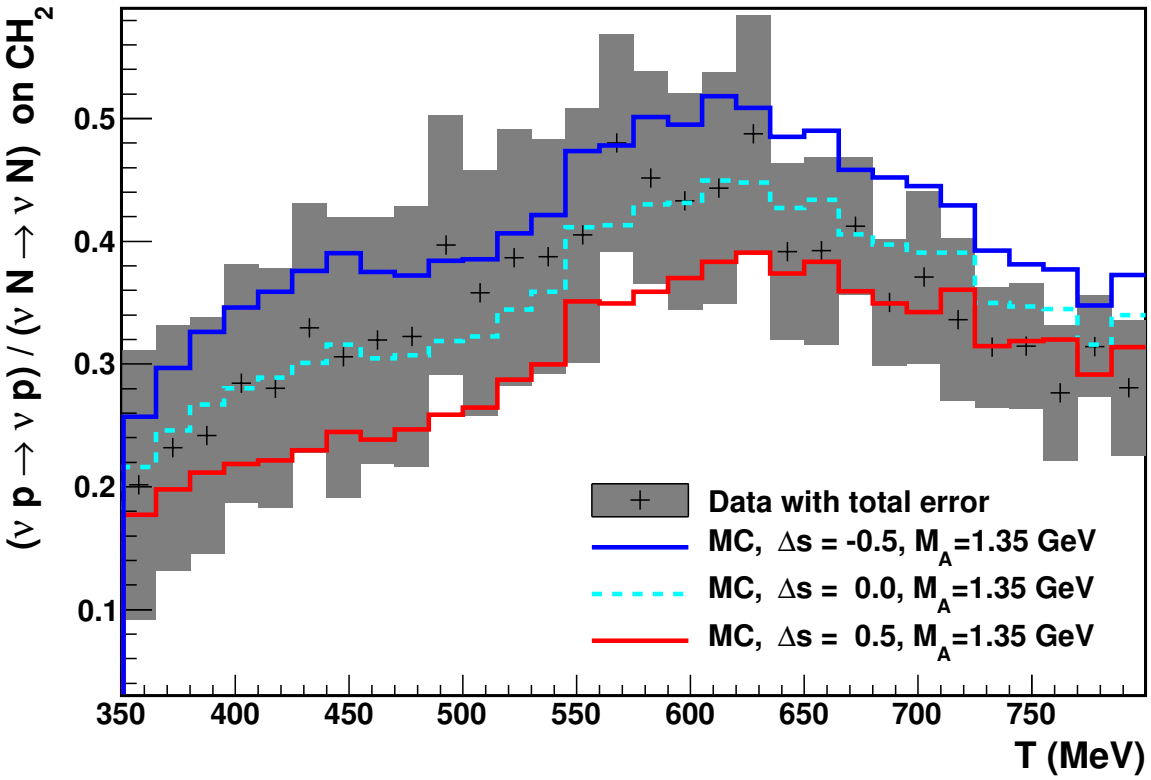


Figure 8.18: The ratio of $\nu p \to \nu p / \nu N \to \nu N$ as a function of the reconstructed energy for the data and MC with $\Delta s$ values as labeled.

## 8.5 The $\Delta s$ Measurement

### 8.5.1 Simultaneous $M_A$ and $\Delta s$ Fit to the Ratio of $\nu p \to \nu p$ over $\nu N \to \nu N$

Next we generate the ratio in Eq.(8.1) for MC with values of $M_A$ going from 1.0 GeV to 1.5 GeV and $\Delta s$ from $-0.5$ to 0.5. Then we perform a simultaneous $M_A$ and $\Delta$ $\chi^2$-fit to the data ratio.

The $\chi^2$ surface obtained in the procedure, where the total error matrix is used, is shown in Fig. 8.19. One can see that there is a slight correlation between $M_A$ and $\Delta s$, but this is probably because of considering $M_A$ values which are over a wide range. Once the $M_A$ region is restricted to a most likely region as shown in Fig. 8.20, the ratio depends mostly on $\Delta s$ only.

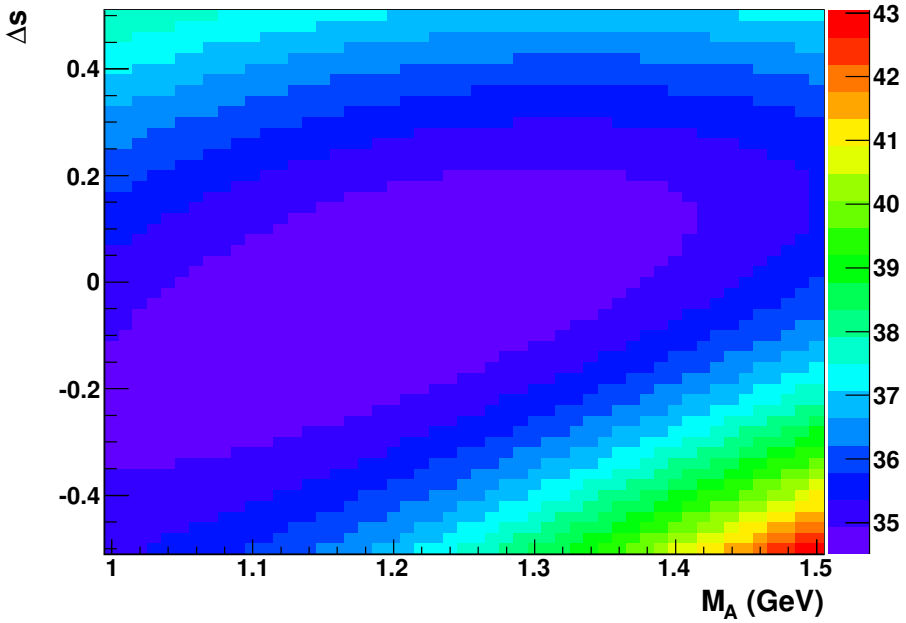


Figure 8.19: $\chi^2$ as a function of $M_A$ and $\Delta s$ for 28 DOF. The $\chi^2_{min} = 34.51$ is at $M_A = 1.21$ GeV and $\Delta s = 0.00$.

### 8.5.2 $\Delta s$-only Fit to the Ratio of $\nu p \to \nu p$ over $\nu N \to \nu N$

Since there is a slight dependence of the $\chi^2$ on $M_A$, we perform an $\Delta s$-only fit to the data ratio of $\nu p \to \nu p$ over $\nu N \to \nu N$ with $M_A = 1.35$ GeV (measured recently from the MiniBooNE CCQE [67]) and then an alternative fit with $M_A = 1.23$ GeV (which represents an older CCQE result [69]).

The $\chi^2$ surface of the $\Delta s$ fit with $M_A = 1.35$ GeV is shown in Fig. 8.21. From this figure, the fitted value of $\Delta s$ yields

$$\Delta s = 0.08 \pm 0.26. \tag{8.2}$$

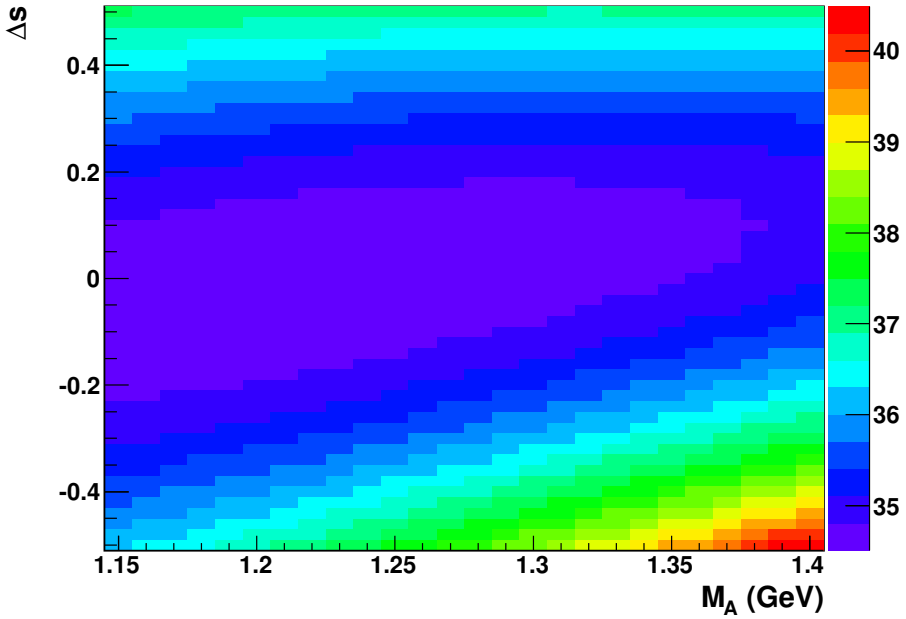


Figure 8.20: $\chi^2$ as a function of $M_A$ and $\Delta s$ for 28 DOF with the reduced $M_A$ region, than in Fig. 8.19.

Alternatively using $M_A = 1.23$ GeV yields $\Delta s = 0.00 \pm 0.30$ with $\chi^2_{min}/DOF = 34.5/29$.

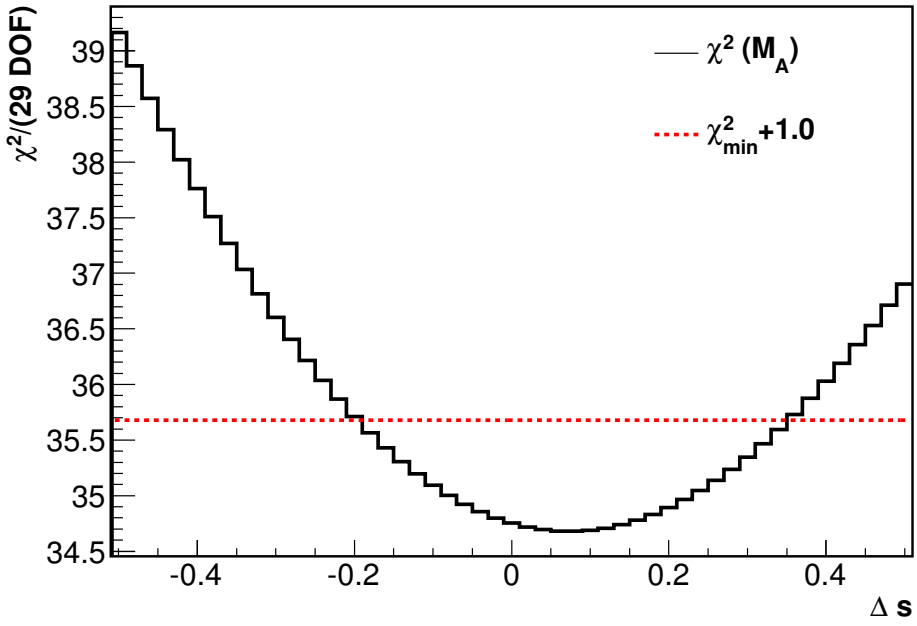


Figure 8.21: $\chi^2$ surface as a function of $\Delta s$ for 29 DOF with the reduced $M_A = 1.35$ GeV. $\chi^2_{min} = 34.6795$ at $\Delta s = 0.08$.

## 8.6 Conclusion

In this chapter we have performed a measurement of the strange quark contribution to the nucleon spin ($\Delta s$) using the MiniBooNE NCE data.

In Section 8.1 we have discussed the method of obtaining a sample of NCE proton that do not experience FSI inside the nucleus. It is possible to obtain such sample of events at high energies (above Cherenkov threshold) for protons. These events have single proton in the final state and produce a higher Cherenkov light fraction than NCE neutrons and irreducible backgrounds, which have multiple protons in the final state. In Section 8.3 the $\nu p \to \nu p$ and $\nu N \to \nu N$ samples have been constructed. These two samples of events were used in the measurement of the ratio in Eq.(8.1), which is sensitive to $\Delta s$.

The total error matrix including statistical and systematic uncertainties was calculated, where the uncertainty in the optical model of the medium is the dominating source of error, while other systematic errors are greatly reduced by using the ratio.

Using the total error matrix a simultaneous $\chi^2$-fit of $\Delta s$ and $M_A$ to the MiniBooNE data ratio of $\nu p \to \nu p$ to $\nu N \to \nu N$ was performed. It showed that there is a slight $\chi^2$ dependence on $M_A$: with $M_A = 1.35$ GeV, we obtain a value of $\Delta s = 0.08 \pm 0.26$, which is consistent with the BNL E734 result [62].

One needs to comment on the implications of Figures 6.8, 8.16, and 8.18 on the $\Delta s$ result. From Fig. 6.8 one can see that the MiniBooNE MC overpredicts the total number of events passing the NCE selection cuts at high reconstructed energy, (above 250 MeV) by as much as 50%. Then the high energy NCE proton-enriched sample was obtained for events with high reconstructed energy, between 350 MeV and 800 MeV. For these events, looking at the $\theta_p$ distribution in Fig. 8.16 it seems the entire disagreement between the data and MC at these energies comes from the forward going events (NCE protons). Clearly there is a deficit of protons in the data, which in principle implies that this might be due to positive values of $\Delta s$. However, Fig. 8.18 and the result in Eq.(8.2) shows that the allowed $\Delta s$ region is consistent with zero. This may indicate that there is also a deficit of NCE neutrons.

This is the first attempt at a $\Delta s$ measurement using this ratio. The systematic errors are quite large, mostly due to large uncertainties in the optical model of the mineral oil. MiniBooNE has sensitivity to $\Delta s$ for proton energies above Cherenkov threshold for protons, where the contribution from irreducible backgrounds is significant. In order to have a good sensitivity for $\Delta s$, future

experiments need to have good proton/neutron identification (possibly through neutron capture tagging) and extend the energy region below 200 MeV, where the contribution from irreducible backgrounds is less.

# Chapter 9

# Conclusions

Neutrino-nucleon neutral current elastic scattering has recently gained a lot of interest among the nuclear physicis community because it is a fundamental probe of the nucleon structure. In particular it is sensitive to the strange quark contribution to the nucleon spin ($\Delta s$), which is important to measure due to the ongoing proton spin crisis problem, as described in Section 3.4.1. The current measurement of $\Delta s$ from neutrino data came from one experiment only, namely BNL E734 [62], which used an accelerator-based neutrino beam; 951 $\nu_\mu p \rightarrow \nu_\mu p$ and 776 $\bar{\nu}_\mu p \rightarrow \bar{\nu}_\mu p$ events were used for the $\Delta s$ fit. The neutrino flux at the detector was obtained from the CCQE events observed in the detector divided by the predicted cross-section.

This thesis describes the neutrino-nucleon neutral current elastic scattering in the MiniBooNE experiment. A reconstruction package for proton events in MiniBooNE has been developed and described as well as its performance. It is shown that because protons above Cherenkov threshold (350 MeV of kinetic energy) produce a directional prompt light it is possible to reconstruct their direction. A known particle's direction gives a great tool for a reliable particle identification.

Using the world largest sample of 94,531 NCE candidate events with a relatively high (65%) signal fraction, the flux-averaged neutral current elastic differential cross-section has been measured in the range of $Q^2$ from 0 GeV$^2$ to 1.8 GeV$^2$ (see Chapter 6). This cross-section is averaged over three NCE processes: scattering off free protons in hydrogen, bound protons in carbon, and bound neutrons in carbon with the corresponding coefficients as described in Section 6.9. The cross-section is not sensitive to small values of $|\Delta s|$, but is sensitive to the value of the axial vector mass when using a dipole approximation of the axial form factor, which is the dominating contribution to the NCE cross-section at low $Q^2$. $M_A$ fits to the MiniBooNE NCE cross-section have been performed

using an absolute (POT) normalization of the energy spectrum, which is related to the differential cross-section (see Chapter 7). The fitted $M_A$ value slightly depends on the $\Delta s$ value used in the MC. Using $\Delta s = 0.0$ the allowed value of $M_A$ was obtained:

$$M_A = (1.39 \pm 0.11) \text{ GeV},$$

which is in agreement with the latest $M_A$ measurement from the MiniBooNE CCQE channel of $M_A = (1.35 \pm 0.17)$ GeV [126].

MiniBooNE NCE events above Cherenkov threshold have been studied extensively for a possible proton/neutron particle identification, which would allow to measure $\Delta s$ (see Chapter 8). A special class of NCE proton events have been obtained – events that have only one proton in the final state. A series of cuts have been applied to select two samples of events: NCE proton and NCE proton+neutron in the reconstructed energy range from 350 MeV to 800 MeV. The NCE proton+neutron data sample has 24,004 events with a predicted NCE events fractions of 45%. The NCE proton data sample, where an additional proton/neutron particle identification cut and a cut on $\theta_p$ (reconstructed nucleon direction with respect to the beam direction) were used, has 7,616 events with a predicted NCE proton events fraction of 55%. A lot of systematic errors are reduced by using the ratio of these two samples, which is sensitive to $\Delta s$, as shown in Section 8.4. The result of the $\Delta s$ fit to the MiniBooNE ratio data, which is described in Section 8.5, shows a slight dependence on the value of $M_A$ used in the MC. Using $M_A = 1.35$ GeV the allowed value for $\Delta s$ yields

$$\Delta s = 0.08 \pm 0.26,$$

which is in agreement with the BNL E734 result of $\Delta s = -0.21 \pm 0.10$ [62]. The biggest error which limits our $\Delta s$ sensitivity is due to the uncertainty in the optical model. In particular a large uncertainty in the optical model multisims is due to the scintillation light production. Because there is no direct proton calibration used in MiniBooNE, a large variation in the scintillation light production is assigned. A way to constrain the latter would be to use a proton energy calibration. A potential proton energy scaling problem in MiniBooNE and ways to measure it are described in Appendix C.

Last but not least, one should mention that there is an alternative way to report the MiniBooNE results (the NCE differential cross-section and the $\nu p \to \nu p$ over $\nu N \to \nu N$ ratio) which is described in Appendix B. There we report the results in the reconstructed energy spectrum and also describe

the procedure to convert the predicted flux-averaged cross-sections to the MiniBooNE reconstructed energy spectrum.

# Part III

# Appendices

# Appendix A

# The Unfolding Problem

Whenever a physical quantity is measured there are distortions to the original distribution in the observed quantity. The procedure of correcting these distortions is called unfolding. While studying the unfolding problem for the neutral current elastic nucleon scattering kinetic energy distribution, the direct matrix method of unfolding has been developed and studied. Here we formulate the unfolding problem and also discuss different solutions for it and compare their performances.

## A.1 Formulation of the Unfolding Problem

In any experiment there is always a distortion to the distribution of a variable subject to measurement due to the limited resolution of the detector and the detection efficiency. The procedure of correcting these distortions is generally called unfolding.

We consider a true kinetic energy distribution of nucleons $E_{true}$ of the MiniBooNE NCE events as the variable that we would like to measure. We allow for a limited resolution in the measurement, as well as the detection efficiency to be less than 100%.

As a simplification, we assume the MC to be perfect in terms of describing particle propagation and detection. The only error that we consider here is the error in the $E_{true}$ spectrum (or a cross-section error effectively, since we don't consider flux error). The data may have a different $E_{true}$ distribution than MC due to a different cross-section, and we want to measure it. Also, we do not consider any backgrounds. Thus, we consider only with NCE events taken from the MiniBooNE MC.

Each observed event is characterized by two quantities: the true value $E_{true}$ and the reconstructed

value $E_{rec}$ (the reconstruction is based on the NCFitter package, which assumes the event to be single proton). Also, since some events may not pass the selection cuts, we must allow for the possibility to have events that do not result in any measured value at all. Thus, if an event doesn't pass the quality cuts, it is characterized by only one quantity, $E_{true}$.

In this appendix we use a set of matrices and histograms with the following notation:

- $\mu_i$ – the true nucleon kinetic energy histogram
- $\nu_j$ – the reconstructed kinetic energy histogram
- $\epsilon_i$ – the efficiency histogram as a function of the true nucleon kinetic energy
- $M_{ij}$ – the migration matrix
- $R_{ij}$ – the response matrix

The probability that an event leads to a measured value is called the detection efficiency, which in general depends on the true value of the event $E_{true}$, $\epsilon(E_{true})$. It could also depend on other variables too, for example the true value of the radius of the event and/or its direction, but we neglect all other possible dependences here.

For each NCE event in the MC the total kinetic energy of nucleons is known. The distribution of this variable for all events in the MC is the predicted true (kinetic) energy spectrum of nucleons, which is represented in form of a histogram:

$$\mu_i^{MC}, \qquad i = 1, ..., m. \tag{A.1}$$

For each bin $i$ the efficiency is defined as follows. We fill another histogram $\mu_i^{MC,passed\ cuts}$, which is filled only with the events that pass the cuts. The efficiency then defined simply through these histograms by dividing them bin by bin, namely

$$\epsilon_i = \frac{\mu_i^{MC,passed\ cuts}}{\mu_i^{MC}}, \qquad i = 1, ..., m. \tag{A.2}$$

$\epsilon_i$ is the probability for an event with the true energy in the bin $i$ to pass the selection cuts. For the MC events that pass the cuts, there is also the observed (reconstructed) energy histogram:

$$\nu_j^{MC}, \qquad j = 1, ..., n.$$

In general, one needs to impose the following constrain: $n \geq m$, because we reconstruct the true energy distribution in $m$ bins using the information from the observed $n$ bins. Otherwise, there is not enough information and, as a result, the unfolding would have had an infinite number of solutions.

Another definition that we use in this appendix is the migration matrix

$$M_{ij}, \qquad i = 1, ..., m, \qquad j = 1, ..., n. \tag{A.3}$$

This $m \times n$ matrix defines the correlation between the reconstructed and true energy of the events that pass the cuts according to the MC. $M_{ij}$ is the number of events with the true energy in bin $i$ and the reconstructed energy with bin $j$.

The migration matrix and the efficiency together give a full description of the MC as far as unfolding goes, because one can express the true energy $(\mu_i^{MC}, i = 1, ..., m)$ and the reconstructed energy $(\nu_j^{MC}, \qquad j = 1, ..., n.)$ for the MC in terms of the migration matrix and the efficiency. The projection of the migration matrix on the reconstructed energy axis gives the reconstructed energy:

$$\nu_j^{MC} = \sum_{i=1}^{m} M_{ij}, \qquad j = 1, ..., n. \tag{A.4}$$

The projection of the migration matrix on the true energy axis divided by efficiency gives the true energy spectrum before any cuts:

$$\sum_{j=1}^{n} M_{ij} = \mu_i^{MC,passed\ cuts} = \epsilon_i \mu_i^{MC} \Rightarrow \mu_i^{MC} = \frac{1}{\epsilon_i} \sum_{j=1}^{n} M_{ij} \qquad i = 1, ..., m. \tag{A.5}$$

We denote the reconstructed data spectrum as

$$\nu_j^{DATA}, \qquad j = 1, ..., n. \tag{A.6}$$

The task is to estimate what was the underlying true energy spectrum of the data that led to the reconstructed spectrum in (A.6). This defines the unfolding problem.

Now, since one would also like to compare the goodness of different methods of unfolding, we need to know the true energy spectrum. Thus, we will construct "fake data" with a known true energy spectrum

$$\mu_i^{DATA}, \qquad i = 1, ..., m, \tag{A.7}$$

which may be different from (A.1) and generate the reconstructed spectrum (A.6). After unfolding,

we get the unfolded distribution

$$\mu_i^{unf}, \qquad i = 1, ..., m. \tag{A.8}$$

This way, one can compare the unfolded spectrum (A.8) and true data spectrum (A.7) and see how close they are to each other.

## A.2 Event Selection.

Only in-tank NCE events are considered. The following selection cuts are used for the NCE events in this study (an early version of the NCE cuts):

- 1 subevent
- $25 < Tank\ PMTs < 150$
- $Veto\ PMTs < 6$
- reconstructed event time between 4400 ns and 6500 ns
- reconstructed radius is less than 4.5 m

Each event is characterized by its true energy $E_{true}$, which is defined as the sum over the kinetic energies of all nucleons that are produced in the event. If an event passes the selection cuts, then it is also characterized by the reconstructed energy $E_{rec}$. The distributions of $\mu^{MC}$, $\mu^{MC,passed\ cuts}$, and $\nu^{MC}$ are shown in Fig. A.1. The efficiency as a function of $E_{true}$ is shown in Fig. A.2.

Finally, the migration matrix $M$ for the NCE events that passed the cuts, is shown in Fig. A.3. As one can see from the plot, most of the events can be found close to the $E_{rec} = E_{true}$ line with the energy resolution of about 20%.

## A.3 The Inverse Matrix Method

The method is fully described in Ref. [121]. In this reference, one can also find the proof that this method leads to an unbiased estimator of the true original spectrum; in other words, with infinite statistics for both MC and data, the unfolded distribution and the true original spectrum are identical regardless of what the original spectrum was (again, a perfect MC is assumed, which means that there are no systematic errors). Furthermore, one can show that this method has the least variance among all unbiased estimators. Thus, any other method of unfolding is either less efficient than the

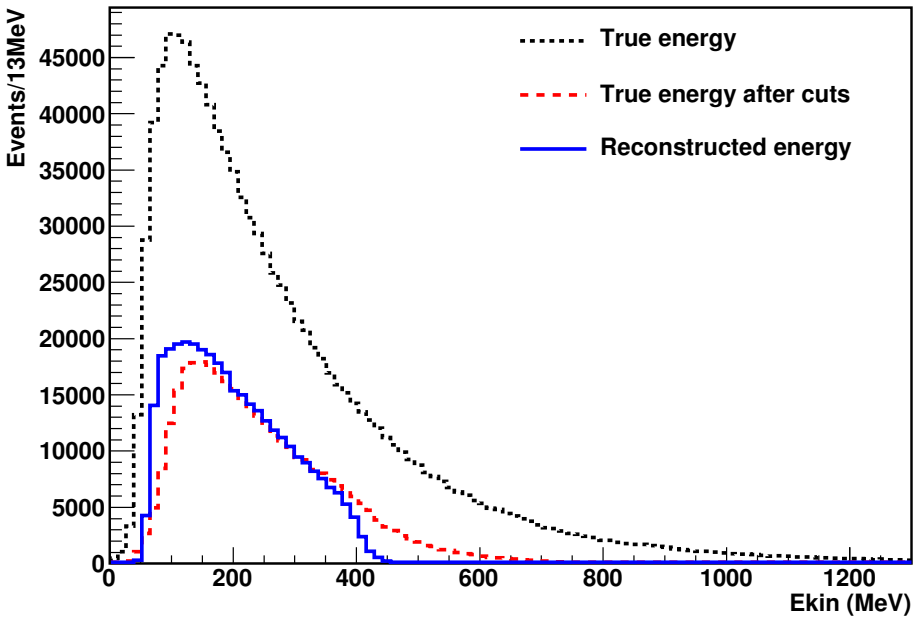


Figure A.1: The true energy before cuts, the true energy after cuts and the reconstructed energy distributions for the NCE event sample.

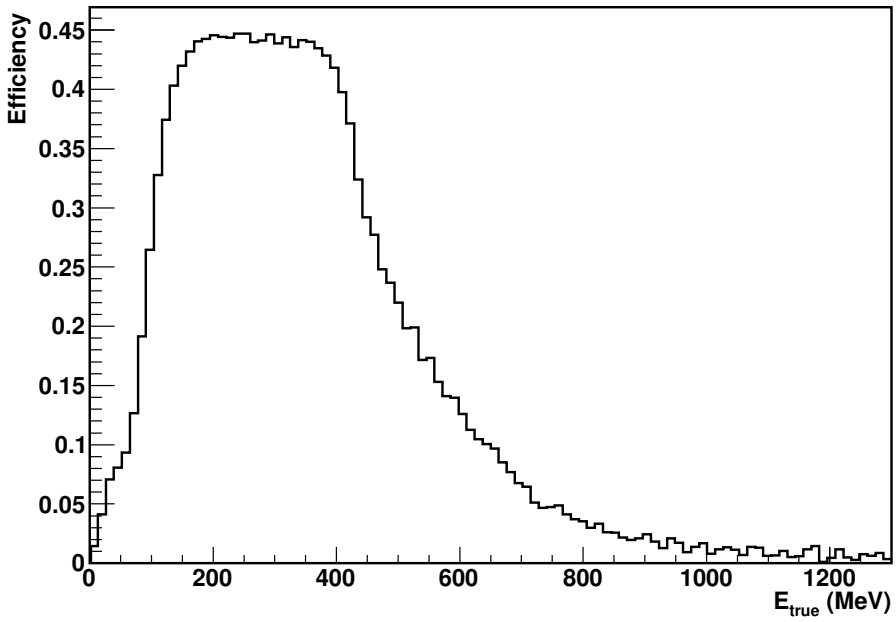


Figure A.2: Selection cuts efficiency as a function of the true kinetic energy of nucleons.

inverse matrix method or it is biased, which means that that the unfolded distribution (A.8) depends on the MC prediction (A.1). The only problem with this method is the inverse matrix calculation. As we will find out, this method leads to large statistical errors.

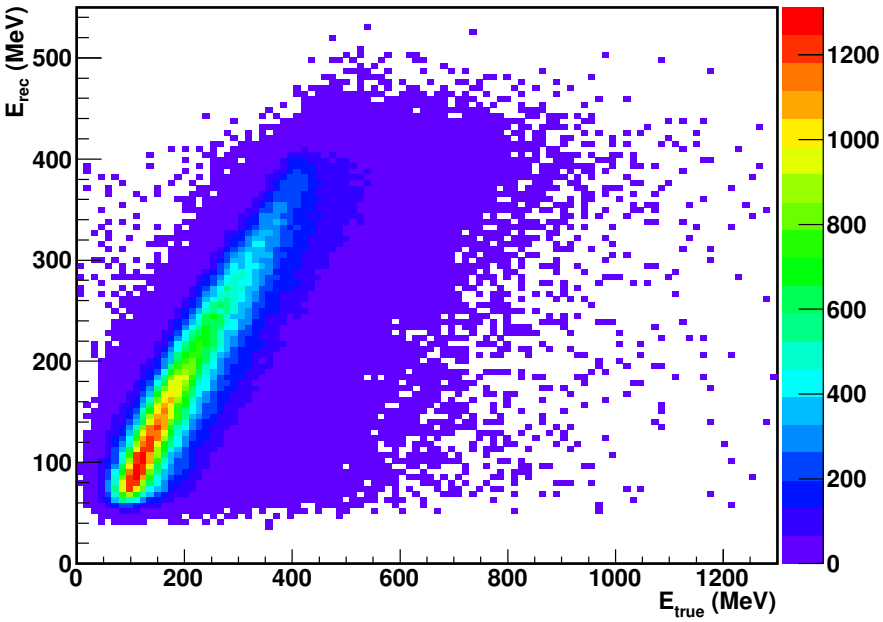


Figure A.3: The migration matrix.

### A.3.1 The Response Matrix

According to the definition in Ref.[121], the response matrix is defined as:

$$R_{ij} = Prob(observed\ in\ bin\ j | true\ value\ in\ bin\ i), \qquad i = 1, ..., m, \qquad j = 1, ..., n. \tag{A.9}$$

One can express it in terms of the migration matrix (A.3) and efficiency (A.2):

$$R_{ij} = \frac{M_{ij}\epsilon_i}{\sum_{k=1}^{n} M_{ik}}, \qquad i = 1, ..., m, \qquad j = 1, ..., n. \tag{A.10}$$

Physically, we normalize the columns of the migration matrix so that the sum of each column of the response matrix is equal to the efficiency:

$$\sum_{j=1}^{n} R_{ij} = \frac{\sum_{k=1}^{n}(M_{ik}\epsilon_i)}{\sum_{l=1}^{n} M_{il}} = \epsilon_i \ , \qquad i = 1, ..., m.$$

### A.3.2 Inverting the Response Matrix

The relation between the true and the reconstructed energy spectra is:

$$\nu_j = \sum_{i=1}^{m} Prob(observed\ in\ bin\ j | true\ value\ in\ bin\ i)\mu_i = \sum_{i=1}^{m} R_{ij}\mu_i \ , \qquad j = 1, ..., n. \qquad \text{(A.11)}$$

However, in the real data all we see is $\nu_j$, and thus one needs to find a solution $\mu_i$ for Eq.(A.11). The obvious solution is to find the inverse matrix $R^{-1}$, such that

$$\sum_{l=1}^{n} R^{-1}_{kl} R_{lr} = \delta_{kr} \ , \qquad k = 1, ..., m, \qquad r = 1, ..., m,$$

where $\delta_{kr}$ is the Kronecker delta. Multiplying by $R^{-1}_{kj}$ the expression (A.11) and summing over $j$, one obtains

$$\mu_k = \sum_{j=1}^{n} R^{-1}_{kj} \nu_j \ , \qquad k = 1, ..., m.$$

In summary, the inverse matrix method requires the response matrix as defined by (A.10), where the migration matrix $M$ and the efficiency $\epsilon$ are taken from MC. For the data, the unfolded distribution using the inverse matrix method is expressed in the following way:

$$\mu^{unf}_k = \sum_{j=1}^{n} R^{-1}_{kj} \nu^{DATA}_j, \qquad k = 1, ..., m,$$

or in the matrix notation:

$$\begin{pmatrix} \mu^{unf}_1 \\ \mu^{unf}_2 \\ \vdots \\ \mu^{unf}_m \end{pmatrix} = \begin{pmatrix} r^{-1}_{11} & r^{-1}_{12} & \cdots & r^{-1}_{1n} \\ r^{-1}_{21} & r^{-1}_{22} & \cdots & r^{-1}_{2n} \\ \vdots & \vdots & \ddots & \vdots \\ r^{-1}_{m1} & r^{-1}_{m2} & \cdots & r^{-1}_{mn} \end{pmatrix} \begin{pmatrix} \nu^{DATA}_1 \\ \nu^{DATA}_2 \\ \vdots \\ \nu^{DATA}_n \end{pmatrix} .$$

### A.3.3 Results of Unfolding with the Inverse Matrix Method

Let us see how the inverse matrix method works for NCE events in MC. We have seen from Fig. A.1 that the true and the reconstructed energy spectra have different range. In this case we take both distributions in 9 bins: 8 bins in $E_{true}$ from 0 to 600 MeV and everything greater than 600 MeV going into the 9-th bin (overflow), and 8 bins in $E_{rec}$ from 0 to 400 MeV and everything greater than 400 MeV going into the 9-th bin. The generated and the reconstructed energy distributions

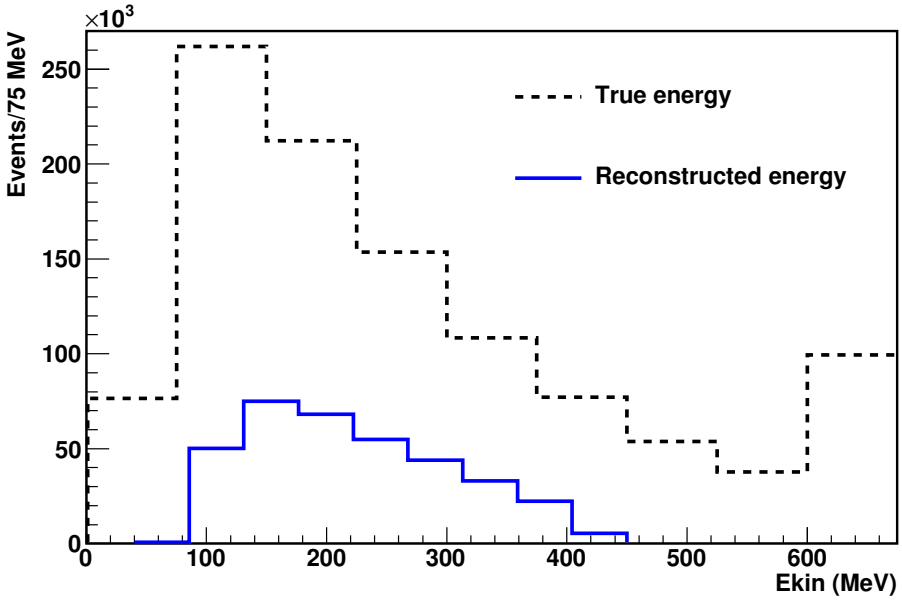


Figure A.4: The true energy and the reconstructed energy of the MC in 9 bins used for the test of the inverse matrix method unfolding.

for this case are shown in Fig. A.4.

When we invert the response matrix, the result is a matrix with large alternating positive and negative entries. To illustrate what it looks like, the positive and negative entries are shown separately on a logarithmic scale in Fig. A.7.

The efficiency is shown in Fig. A.5 and the response matrix is shown in Fig. A.6.

In order to check that this $R^{-1}$ is indeed the inverse of the response matrix, we multiply them to see that the product is a unitary matrix, which is given by:

$$\begin{pmatrix}
-1.29\times10^{-16} & -1.57\times10^{-16} & -5.31\times10^{-16} & -3.46\times10^{-16} & -2.73\times10^{-17} & -5.90\times10^{-17} & -2.43\times10^{-17} & -1.39\times10^{-17} & 1.00 \\
3.35\times10^{-18} & -7.53\times10^{-17} & -1.57\times10^{-16} & -1.35\times10^{-17} & -6.01\times10^{-17} & 1.73\times10^{-18} & -8.67\times10^{-18} & 1.00 & -1.73\times10^{-18} \\
6.47\times10^{-18} & 1.11\times10^{-17} & 8.24\times10^{-18} & 4.61\times10^{-18} & -1.11\times10^{-17} & -1.52\times10^{-18} & 1.00 & 1.00\times10^{-30} & 1.00\times10^{-30} \\
-2.02\times10^{-17} & -9.05\times10^{-17} & -6.65\times10^{-17} & -2.06\times10^{-17} & 2.70\times10^{-17} & 1.00 & 4.34\times10^{-18} & -8.67\times10^{-19} & 1.00\times10^{-30} \\
4.97\times10^{-18} & 3.94\times10^{-17} & 3.51\times10^{-17} & 2.33\times10^{-17} & 1.00 & 3.47\times10^{-18} & 1.30\times10^{-18} & -2.17\times10^{-19} & 3.25\times10^{-19} \\
-1.21\times10^{-19} & -9.03\times10^{-20} & 4.78\times10^{-20} & 1.00 & -1.37\times10^{-19} & -1.49\times10^{-19} & 5.42\times10^{-20} & 1.36\times10^{-20} & 1.00\times10^{-30} \\
-3.05\times10^{-20} & -4.58\times10^{-19} & 1.00 & 1.74\times10^{-19} & -2.87\times10^{-19} & 7.12\times10^{-20} & -2.71\times10^{-20} & -3.39\times10^{-20} & -6.78\times10^{-21} \\
5.25\times10^{-20} & 1.00 & 2.18\times10^{-19} & -2.31\times10^{-19} & -6.56\times10^{-20} & -2.24\times10^{-20} & -1.63\times10^{-20} & -5.29\times10^{-21} & -1.48\times10^{-21} \\
1.00 & -1.86\times10^{-19} & 9.49\times10^{-20} & 5.67\times10^{-19} & 4.73\times10^{-19} & 1.02\times10^{-19} & 8.13\times10^{-20} & 4.07\times10^{-20} & 1.02\times10^{-20}
\end{pmatrix}.$$

We indeed see that it is a unitary matrix.

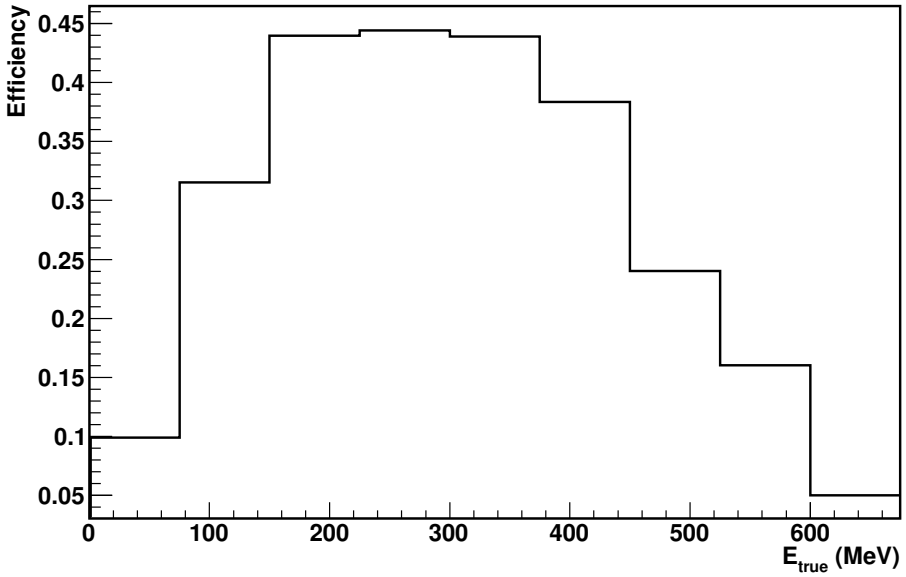


Figure A.5: The efficiency in 9 bins of energy.

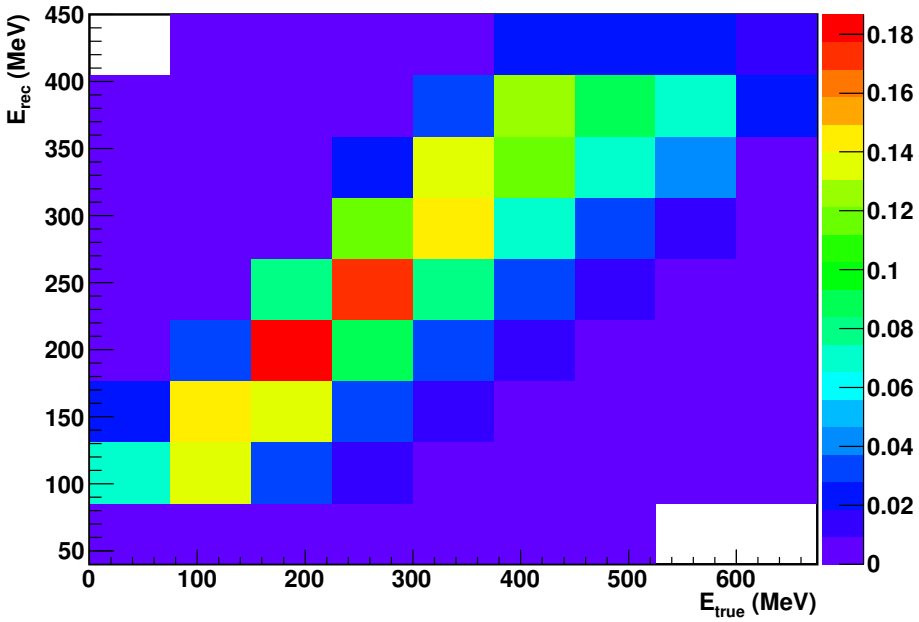


Figure A.6: The response matrix in 9 bins of energy.

### A.3.4 Consistency Test

Next, a consistency test is performed, in which the reconstructed spectrum of the original MC is taken as the input for data:$\nu^{DATA} = \nu^{MC}$. In this case, obviously, the unfolded distribution has to be equal to the MC generated spectrum, $\mu^{unf} \simeq \mu^{DATA}$, where the only deviations may be of

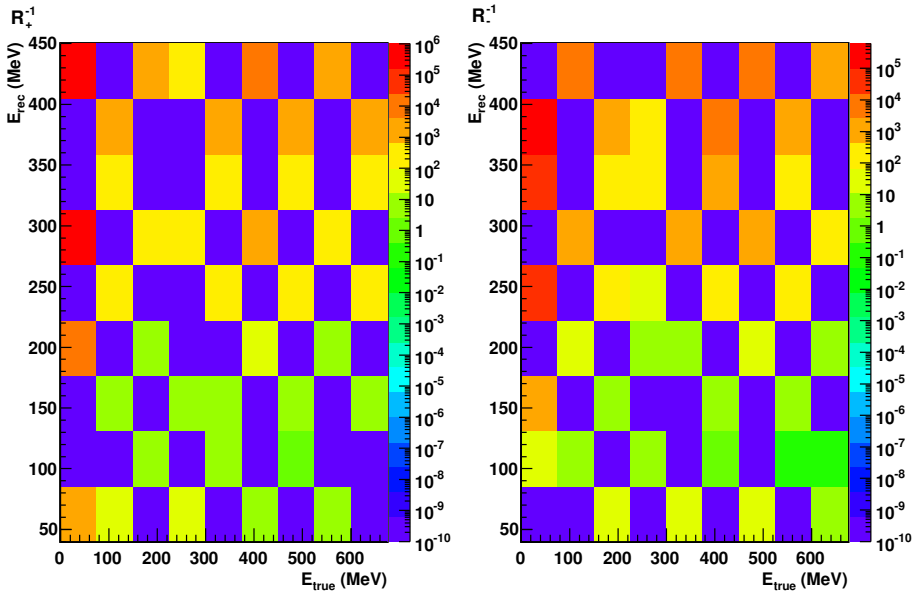


Figure A.7: The inverse matrix in 9 bins of energy. Positive (left plot) and negative entries (right plot) of $R^{-1}$.

numerical nature.

This is basically to check that there is no mistake in the unfolding procedure, in addition we checked that $RR^{-1} = I$. In other words, we check if the following relation is true:

$$\sum_{j=1}^{n} R_{ij}^{-1} \nu_j^{MC} \simeq \mu_i^{MC} \qquad i = 1, ..., m.$$

The result of the unfolding is shown in Fig. A.8. As expected, the unfolded distribution with the inverse matrix (red solid) is identical to the generated energy (black dashed) distribution. However, the method is unstable. Because elements of the inverse matrix are large, the unfolded spectrum is very sensitive to the input reconstructed energy spectrum. Thus, statistical errors in the reconstructed energy spectrum may induce large variations in the unfolded energy spectrum in the inverse matrix method. We now test the statistical error for the inverse matrix method, in which we unfold a modified reconstructed spectrum $\nu'$ which is greater than $\nu^{MC}$ by $\sqrt{\nu^{MC}}$:

$$\nu_i' = \nu_i^{MC} + \sqrt{\nu_i^{MC}} \qquad i = 1, ..., m. \tag{A.12}$$

The result of the unfolding of $\nu'$ is the blue dotted histogram in Fig. A.8. As one can see, it is very different from the original spectrum.

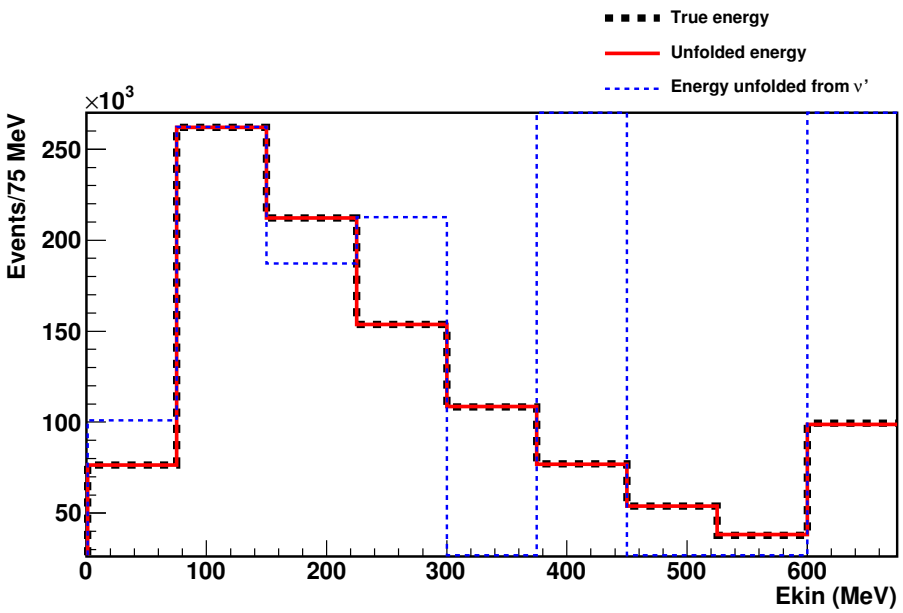


Figure A.8: The result of the consistency test and statistical error estimation. True energy distribution (black dashed), unfolded energy distribution (red solid) and unfolded from $\nu'$ (blue dotted).

## A.4 The Direct Matrix Method

Since the inverse matrix method is very sensitive to statistical variations, we are going to try to avoid the inverse matrix calculations. The direct matrix method is an alternative unfolding method. In this method we will find another matrix $U$ that relates the true and the reconstructed energy distributions such that:

$$\begin{pmatrix} \mu_1^{unf} \\ \mu_2^{unf} \\ \vdots \\ \mu_m^{unf} \end{pmatrix} = \begin{pmatrix} u_{11} & u_{12} & \cdots & u_{1n} \\ u_{21} & u_{22} & \cdots & u_{2n} \\ \vdots & \vdots & \ddots & \vdots \\ u_{m1} & u_{m2} & \cdots & u_{mn} \end{pmatrix} \begin{pmatrix} \nu_1^{DATA} \\ \nu_2^{DATA} \\ \vdots \\ \nu_n^{DATA} \end{pmatrix} .$$

### A.4.1 The $U$ Matrix

To construct the unfolding matrix $U$ we again use the migration matrix (A.3) and the efficiency (A.2), which describe the correlation between the true and the reconstructed energy spectra and the efficiency of the selection cuts. But now, instead of normalizing columns as we did to obtain the

response matrix, we normalize the rows:

$$U'_{ij} = \frac{M_{ij}}{\sum_{k=1}^{m} M_{kj}}, \quad i = 1, ..., m, \quad j = 1, ..., n.$$

Thus, now $(i, j)$-th element of the matrix $U'$ is the probability of an event to have $E_{true}$ in bin $i$ if $E_{rec}$ is in bin $j$:

$$U'_{ij} = Prob(true\ value\ in\ bin\ i | observed\ in\ bin\ j), \quad i = 1, ..., m, \quad j = 1, ..., n.$$

Obviously, the true energy spectrum of the events that pass the cuts is given by

$$\mu'_i = \sum_{j=1}^{n} Prob(true\ value\ in\ bin\ i | observed\ in\ bin\ j)\nu_j = \sum_{j=1}^{n} U'_{ij}\nu_j \ , \quad i = 1, ..., m.$$

To get the true energy spectrum before the selection cuts, one needs to correct the previous expression by the efficiency. Then, the true energy spectrum yields

$$\mu_i = \frac{1}{\epsilon_i}\mu'_i = \frac{1}{\epsilon_i}\sum_{j=1}^{n} U'_{ij}\nu_j \ , \quad i = 1, ..., m.$$

Thus, for unfolding with the direct matrix, the matrix $U$ will be used:

$$U_{ij} = \frac{1}{\epsilon_i}U'_{ij} = \frac{M_{ij}}{\epsilon_i \sum_{k=1}^{M} M_{kj}}, \quad i = 1, ..., m, \quad j = 1, ..., n,$$

and the relation between $\nu$ and $\mu$ for the original MC is simply

$$\mu_i = \sum_{j=1}^{n} U_{ij}\nu_j \ , \quad i = 1, ..., m.$$

### A.4.2 Stability Under Fluctuations

In Fig. A.9 the result of the consistency test is shown in order to check for any possible numerical errors: the true energy distribution coincides with the unfolded one. Furthermore, we study if the method is stable to statistical variations of the reconstructed energy spectrum. Just like we did before, we unfold a fluctuation spectrum $\nu'$ which is defined in (A.12). As one can see from

Fig. A.9, the blue histogram is close to the true spectrum; thus, this method is stable to statistical variations. In other words, small changes of the reconstructed spectrum do not affect much the unfolded spectrum.

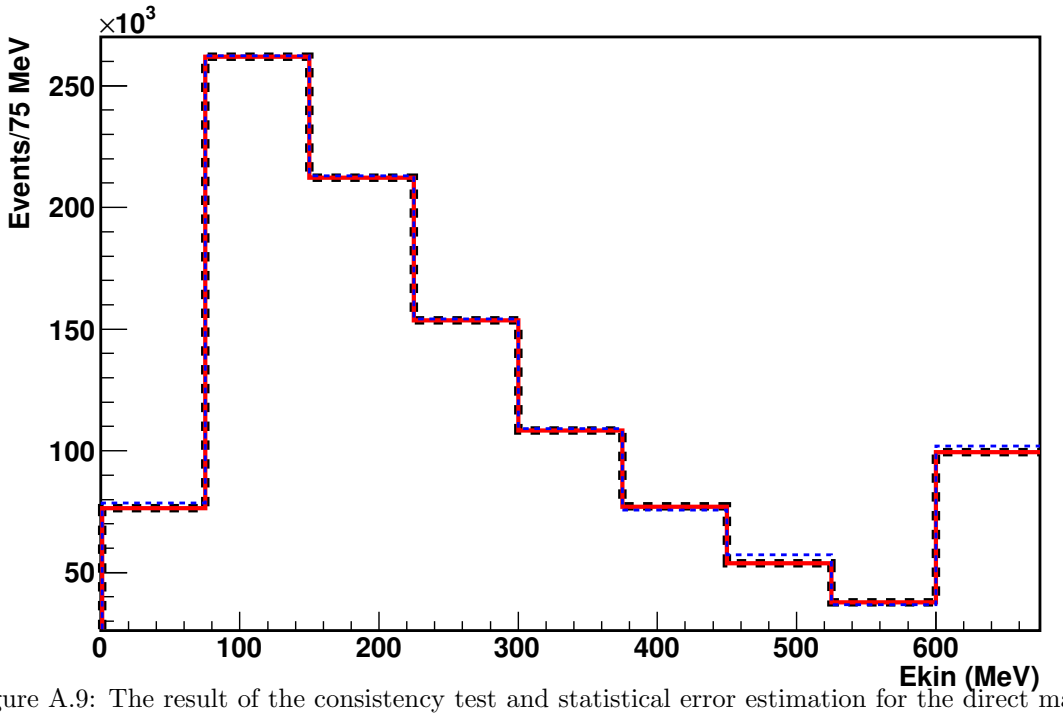


Figure A.9: The result of the consistency test and statistical error estimation for the direct matrix method. True energy distribution (black dashed), unfolded energy distribution (red solid) and unfolded from $\nu'$ (blue dotted).

### A.4.3 Data Construction

Now we would like to study what would happen if we did apply this method to the data. First, we form some MC-based "data" by reweighting the MC events depending on their generated energy with a weighting function of our choice. For example, if one wants the data spectrum to be close to the MC, then the reweighting function should be close to 1.0 at any true energy. After this procedure the new histograms of the true and the reconstructed energies are obtained.

This procedure simulates a data sample with a cross-section that is different from the predicted MC cross-section (if the weighting function is not 1.0 everywhere). We would like to study if it is possible to measure this cross-section assuming a perfect MC. Again the perfect MC means that there are no systematic errors. That is the MC correctly predicts all other MC parameters except the cross-section (like optical model, flux, light propagation parameters, etc.). Since the data are

constructed from the MC, then this is a perfect MC.

The diagram of the data construction is shown on Fig. A.10. Two histograms are filled for the events: the reconstructed and the true energy. Both are filled with the same weight function which depends on the true energy. The true energy histogram is always filled. The reconstructed energy histogram is filled only when the event passes the selection cuts.

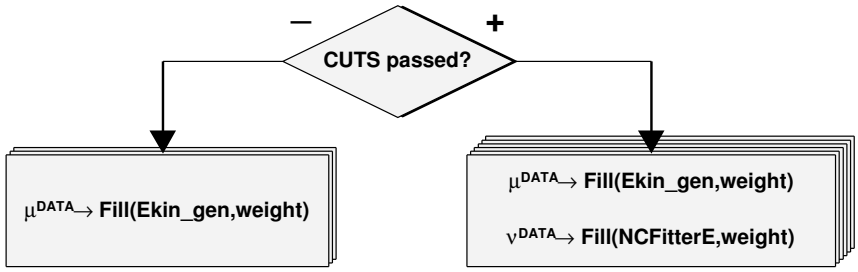


Figure A.10: Data construction diagram.

### A.4.4 Iterations with Direct Matrix Method.

Once we unfold the data with the direct matrix method, the unfolded distribution is still biased. Indirectly it depends on the MC reconstructed energy spectrum, because we normalized the rows for the unfolding matrix $U$. If the MC generated energy spectrum were different, we would have a different $U$ matrix.

However, one can reweigh the migration matrix according to the new unfolded distribution. Assuming that the unfolded distribution is always closer to the true data than the original MC, then one can reweigh the MC events according to their true energy with the following weight function bin by bin:

$$weight_i = \frac{\nu_i^{unf}}{\nu_i^{MC}}, \quad i = 1, ..., m.$$

This way a new migration matrix is constructed for the 2-nd iteration:

$$M_{ij}^{(2)} = weight_i M_{ij}, \quad i = 1, ..., m, \quad j = 1, ..., n,$$

and then we repeat the procedure of unfolding.

### A.4.5 Results of Unfolding with the Direct Matrix Method.

Now, one can test the unfolding with the direct matrix method. Four different reweighting functions were generated that change the original MC spectrum. Then, the unfolding with 1000 iterations is used to see if we are able to recover the reweighted true energy spectra. Also, the number of bins was increased to 50 in this case.

The results of the unfolding are shown in Fig. A.11 for the four modified input spectra. As one can see, in each case the unfolded distribution describes the reweighted spectrum well enough.

## A.5 Toy Model

In Section A.4.5 it was shown that for some reweighting functions of the MC true spectrum the direct matrix method appears to converge to the correct reweighted solution. One would like to understand what the conditions are for this convergence, and try to estimate the rate of the convergence.

First, we form the simplest possible unfolding problem, which we then try to solve. Let us take the MC as having only two bins of both true and reconstructed energy. Suppose the true energy bins have values $N_1$ and $N_2$, so that the MC true energy spectrum is:

$$\begin{cases} \mu_1^{MC} = N_1 \\ \mu_2^{MC} = N_2. \end{cases} \tag{A.13}$$

Let us assign the probabilities of events to have different true and reconstructed energy bins (migration probability):

$$\begin{cases} p_1 = Prob(Reconstructed\ bin\ 2 | True\ bin\ 1) \\ p_2 = Prob(Reconstructed\ bin\ 1 | True\ bin\ 2). \end{cases} \tag{A.14}$$

We also assume the efficiency to be 100% for simplicity. Then, the reconstructed spectrum $\nu$ is:

$$\begin{cases} \nu_1 = (1-p_1)N_1 + p_2 N_2 \\ \nu_2 = p_1 N_1 + (1-p_2)N_2 \quad . \end{cases} \tag{A.15}$$

The 2-dimensional matrices: migration, response, $R^{-1}$ and $U$ for this simple case are:

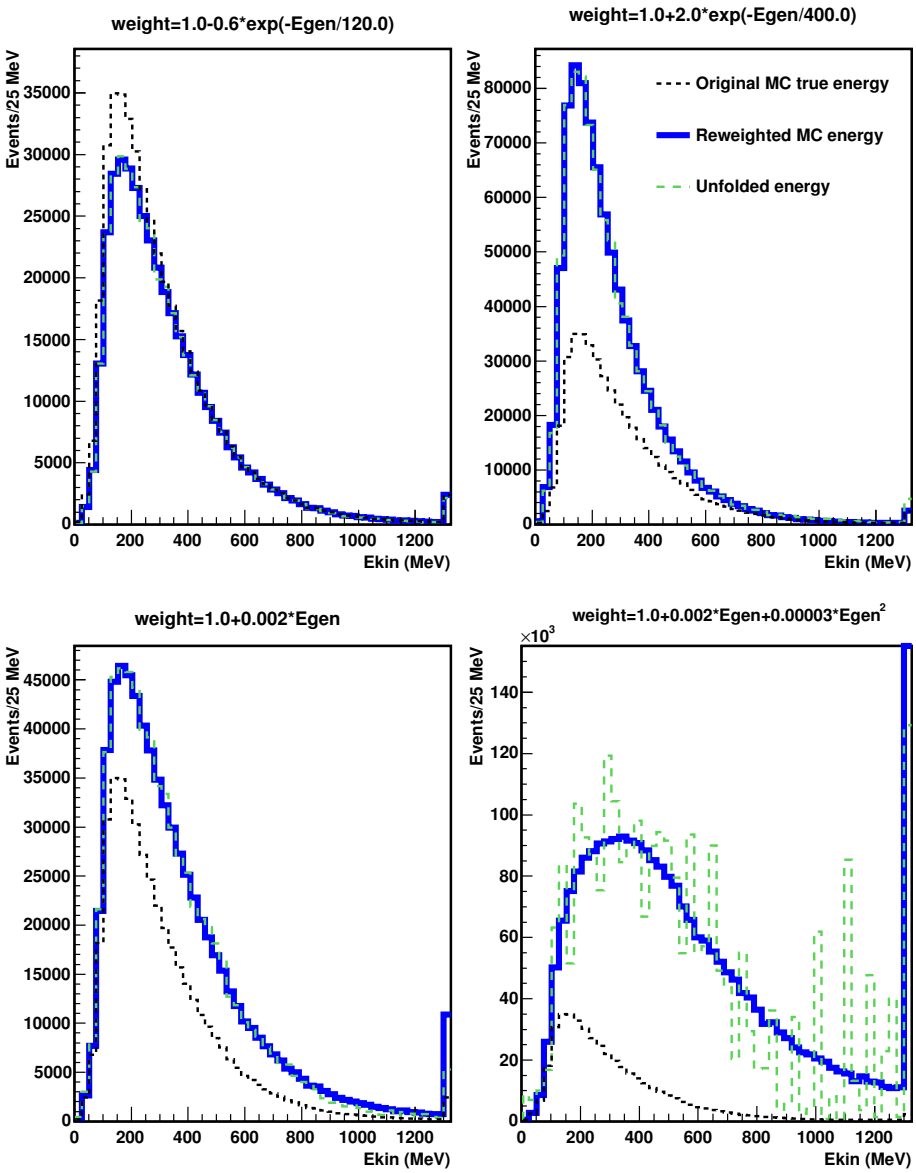


Figure A.11: Results of unfolding with direct matrix method for the MC-based data with four different reweighting functions. The original MC, the reweighted, and the unfolded spectra for four different reweighting functions.

$$M = \begin{array}{c} \\ \text{j=2} \\ \text{j=1} \end{array} \begin{array}{c} \begin{array}{cc} \text{i=1} & \text{i=2} \end{array} \\ \begin{pmatrix} N_1 p_1 & N_2(1-p_2) \\ N_1(1-p_1) & N_2 p_2 \end{pmatrix} \end{array}$$

$$U = \begin{array}{c} \\ \text{j=2} \\ \text{j=1} \end{array} \begin{array}{c} \begin{array}{cc} \text{i=1} & \text{i=2} \end{array} \\ \begin{pmatrix} \frac{N_1 p_1}{N_1 p_1 + N_2(1-p_2)} & \frac{N_2(1-p_2)}{N_1 p_1 + N_2(1-p_2)} \\ \frac{N_1(1-p_1)}{N_1(1-p_1)+N_2 p_2} & \frac{N_2 p_2}{N_1(1-p_1)+N_2 p_2} \end{pmatrix} \end{array}$$

where, as usual, the index $i$ goes over the true energy bins and $j$ over the reconstructed energy bins.

As one can see right away, the response matrix $R$ and, consequently, $R^{-1}$ do not depend on the MC true energy spectrum ($N_1$ and $N_2$ bins). Thus, the inverse matrix method is indeed unbiased (as expected). The unfolding matrix $U$, on the other hand, does depend on $\nu$, which means that the direct matrix method is biased.

And this is how we do unfolding in this case:

1. Unfolding with the inverse matrix method $\mu = R^{-1}\nu$:

$$\begin{cases} \mu_1^{unf} = \dfrac{1-p_2}{1-p_1-p_2}\nu_1 - \dfrac{p_2}{1-p_1-p_2}\nu_2 \\ \mu_2^{unf} = \dfrac{-p_1}{1-p_1-p_2}\nu_1 + \dfrac{1-p_2}{1-p_1-p_2}\nu_2 \end{cases} \tag{A.16}$$

2. Unfolding with the direct matrix method $\mu = U^T\nu$:

$$\begin{cases} \mu_1^{unf} = \dfrac{N_1(1-p_1)}{N_1(1-p_1)+N_2p_2}\nu_1 + \dfrac{N_1p_1}{N_1p_1+N_2(1-p_2)}\nu_2 \\ \mu_2^{unf} = \dfrac{N_2p_2}{N_1(1-p_1)+N_2p_2}\nu_1 + \dfrac{N_2(1-p_2)}{N_1p_1+N_2(1-p_2)}\nu_2 \end{cases} \tag{A.17}$$

Notice that the two expressions in the equations (A.13)-(A.17) are symmetric under the exchange of the lower indices $1 \leftrightarrow 2$. Thus, in the following calculations one only needs to solve one of the equations. For the other equation one would just need to change the indices from the first one.

### A.5.1 Consistency Test

For the consistency test, we put the MC reconstructed spectrum in Eq.(A.15) into the unfolding Eq.(A.16) and (A.17) to get the unfolded distribution $\mu^{unf}$ and compare it to the predicted MC true energy spectrum (A.13). This allows to see if the true energy spectrum is recovered when the "Data" and the MC reconstructed spectra are identical.

1. *Consistency test for unfolding with the inverse matrix method.* Putting (A.15) into (A.16), we get the first bin of the unfolded distribution:

$$\mu_1^{unf} = \frac{1-p_2}{1-p_1-p_2}(N_1(1-p_1)+N_2p_2) - \frac{p_2}{1-p_1-p_2}(N_1p_1+N_2(1-p_2)) = N_1$$

From the symmetry, $\mu_2^{unf} = N_2$. Thus, the consistency test succeeds.

2. *Consistency test for unfolding with the direct matrix method*:

$$\mu_1^{unf} = \frac{N_1(1-p_1)}{N_1(1-p_1)+N_2p_2}\left[N_1(1-p_1)+N_2p_2\right] + \frac{N_1p_1}{N_1p_1+N_2(1-p_2)}\left[N_1p_1+N_2(1-p_2)\right] = N_1$$

Again, $\mu_2^{unf} = N_2$ and the consistency test succeeds.

### A.5.2 Test of a Modified Data Distribution

In this case we take a true energy distribution for the data different than the MC true spectrum. Without loss of generality, we take it to be of this form:

$$\begin{cases} \mu_1^{Data} = w_1N_1 \\ \mu_2^{Data} = w_2N_2, \end{cases}$$

where $w_1$ and $w_2$ are the weights for the respective bins to the MC spectrum. This way, our data is of the form of the reweighted MC from Section A.4.3.

Now, applying the migration probabilities (A.14), the reconstructed spectrum for the Fake Data becomes

$$\begin{cases} \nu_1^{Data} = & w_1N_1(1-p_1) & + & w_2N_2p_2 \\ \nu_2^{Data} = & w_1N_1p_1 & + & w_2N_2(1-p_2) \end{cases} \tag{A.18}$$

Now, let us see what happens if we plug the reconstructed energy spectra (A.18) to the unfolding schemes, as given by Eqs. (A.16) and (A.17).

1. *the inverse matrix method:*

   This has to give the input spectrum, by definition, and it definitely does:

$$\mu_1^{unf} = \frac{1-p_2}{1-p_1-p_2}(w_1N_1(1-p_1)+w_2N_2p_2) - \frac{p_2}{1-p_1-p_2}(w_1N_1p_1+w_2N_2(1-p_2)) = w_1N_1$$

   From the symmetry, $\mu_2^{unf} = w_2N_2$. So, the inverse matrix method gives the right solution.

2. *the direct matrix method:*

$$\mu_1^{unf} = \frac{N_1(1-p_1)}{N_1(1-p_1)+N_2p_2}\left[w_1N_1(1-p_1)+w_2N_2p_2\right]+\frac{N_1p_1}{N_1p_1+N_2(1-p_2)}\left[w_1N_1p_1+w_2N_2(1-p_2)\right].$$

Introducing $\delta w$:

$$\begin{cases}\delta w_1 = w_1 - 1\\ \delta w_2 = w_2 - 1,\end{cases}$$

then the expression for $\mu_1$ becomes:

$$\begin{aligned}\mu_1^{unf} = \quad & N_1 + \frac{N_1(1-p_1)}{N_1(1-p_1)+N_2p_2}\left[\delta w_1N_1(1-p_1)+\delta w_2N_2p_2\right] \\ & +\frac{N_1p_1}{N_1p_1+N_2(1-p_2)}\left[\delta w_1N_1p_1+\delta w_2N_2(1-p_2)\right].\end{aligned} \tag{A.19}$$

Now, we change the variables:

$$\begin{cases}\delta w_1 = \delta w_N + \delta w_S\\ \delta w_2 = \delta w_N - \delta w_S.\end{cases} \tag{A.20}$$

We can always do this substitution. The physical meaning of these variables is now: $\delta w_N$ - normalization weight change (both bins go up or down, depending on the sign) and $\delta w_S$ - shape weight change (if one of the bins goes up, the other goes down). The true energy for the data in terms of these variables:

$$\begin{cases}\mu_1^{Data} = w_1N_1 = N_1 + N_1\delta w_1 = N_1 + N_1\delta w_N + N_1\delta w_S\\ \mu_2^{Data} = w_2N_2 = N_2 + N_2\delta w_2 = N_2 + N_2\delta w_N - N_2\delta w_S.\end{cases}$$

Next, we plug in (A.20) into the last expression for $\mu_1$ (A.19) to get:

$$\begin{aligned}\mu_1 = \quad & N_1 + N_1\delta w_N + \frac{N_1(1-p_1)}{N_1(1-p_1)+N_2p_2}\left[N_1(1-p_1)-N_2p_2\right]\delta w_S \\ & +\frac{N_1p_1}{N_1p_1+N_2(1-p_2)}\left[N_1p_1-N_2(1-p_2)\right]\delta w_S \\ = \quad & N_1 + N_1\delta w_N + N_1\delta w_S\underbrace{\left(1-\frac{2N_2p_2(1-p_1)}{N_1(1-p_1)+N_2p_2}-\frac{2N_2(1-p_2)p_1}{N_1p+N_2(1-p_2)}\right)}_{A}\end{aligned} \tag{A.21}$$

We can see that after the first iteration of unfolding with the direct matrix method the unfolded

distribution has the right normalization as the unfolding picks up the normalization difference $\delta w_N$, but the shape error may be wrong (if $A \neq 1$). However, if the unfolded distribution has a shape error closer to the data, then with iterations it will eventually converge to the data because in the next iteration the unfolded distribution becomes the new MC and the same procedure applies.

The condition for the direct matrix method to converge to the data is

$$0 < A < 2.$$

Four cases of A and the behavior of the solutions as the number of iterations increases are shown in Fig.A.12. The actual values of A for these plots are shown on top in square brackets. As one can

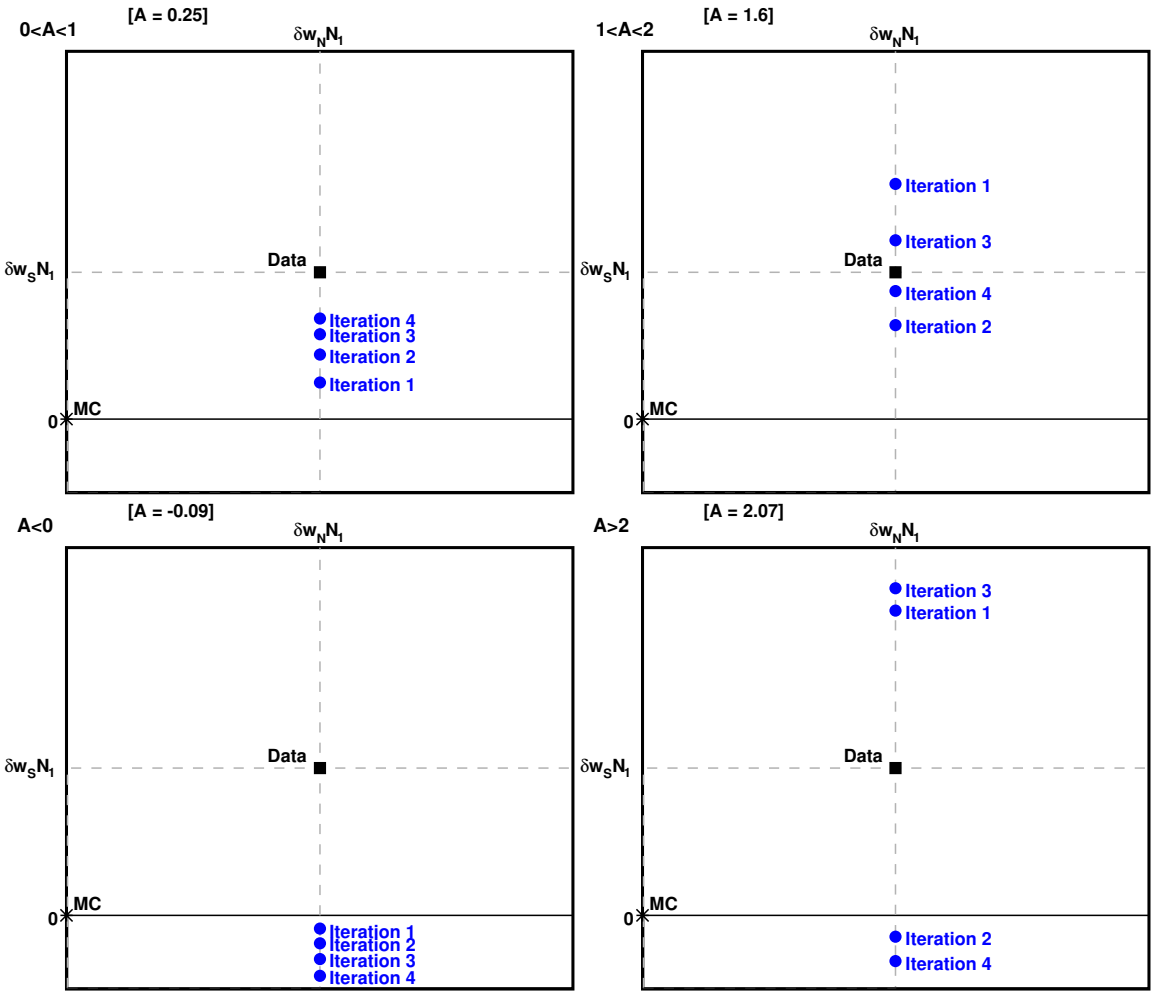


Figure A.12: The behavior of the direct matrix method solution with iterations.

see from the plot, the normalization error naturally goes away already after the first iteration.

In case of $0 < A < 1$, the solution of the direct matrix method converges to the data after each iteration. If $1 < A < 2$, the solution still converges to the data, only now not monotonically, but always switching the shape error sign with each iteration. In the other two cases, the solution diverges from the data. From Eq.(A.21) we can see that for the 2 bins case, $A \leq 1$. Thus, the convergence condition simplifies to

$$A > 0$$

Then, in order to simplify it by getting rid of the denominators for the terms of A, we multiply A by the product of the denominators of the second and third term for A in (A.21) to get the parameter B:

$$B = A(N_1(1-p_1) + N_2 p_2)(N_1 p + N_2(1-p_2)).$$

After some simplification of B, the convergence condition is:

$$B = N_1^2(1-p_1)p_1 - N_2^2(1-p_2)p_2 + N_1 N_2(1-2p_1)(1-p_1-p_2) > 0$$

Obviously, the same should be applied to the second bin. Thus, exchanging indices, the convergence condition for the second bin is:

$$B' = N_2^2(1-p_2)p_2 - N_1^2(1-p_1)p_1 + N_1 N_2(1-2p_2)(1-p_1-p_2) > 0$$

As one can see, it is possible in principle to make such conditions, where the direct matrix method would not converge to the data. In order for this to happen for example one can make the third term in the expression for $B$ or $B'$ to be negative.

But in reality, the first two terms should nearly cancel each other. Moreover, the migration probabilities $p_1$ and $p_2$ should be at least less than $\frac{1}{2}$, which makes the third term to be positive. Also, $p_1$ and $p_2$ should be small, which makes the second term much smaller than the third, even if the first one doesn't cancel it. So, under these reasonable assumptions, the direct matrix method should converge. The rate of convergence depends on the value of $A$ – the closer it is to 1, the faster the convergence.

## A.6 Direct Matrix and Inverse Matrix Methods Comparisons

One last test was to compare the direct and the inverse matrix methods for some samples of simulated data in 9 bins. Five different functions of the true energy spectrum were generated for these unfolding tests. Three of them represent large deviations from the original MC spectrum, while the other two represent only small variations. The results of the unfoldings for these two sets are shown in Figs. A.13 and A.14. As one can see, if a spectrum is somewhat close to the MC, the direct matrix method is good enough.

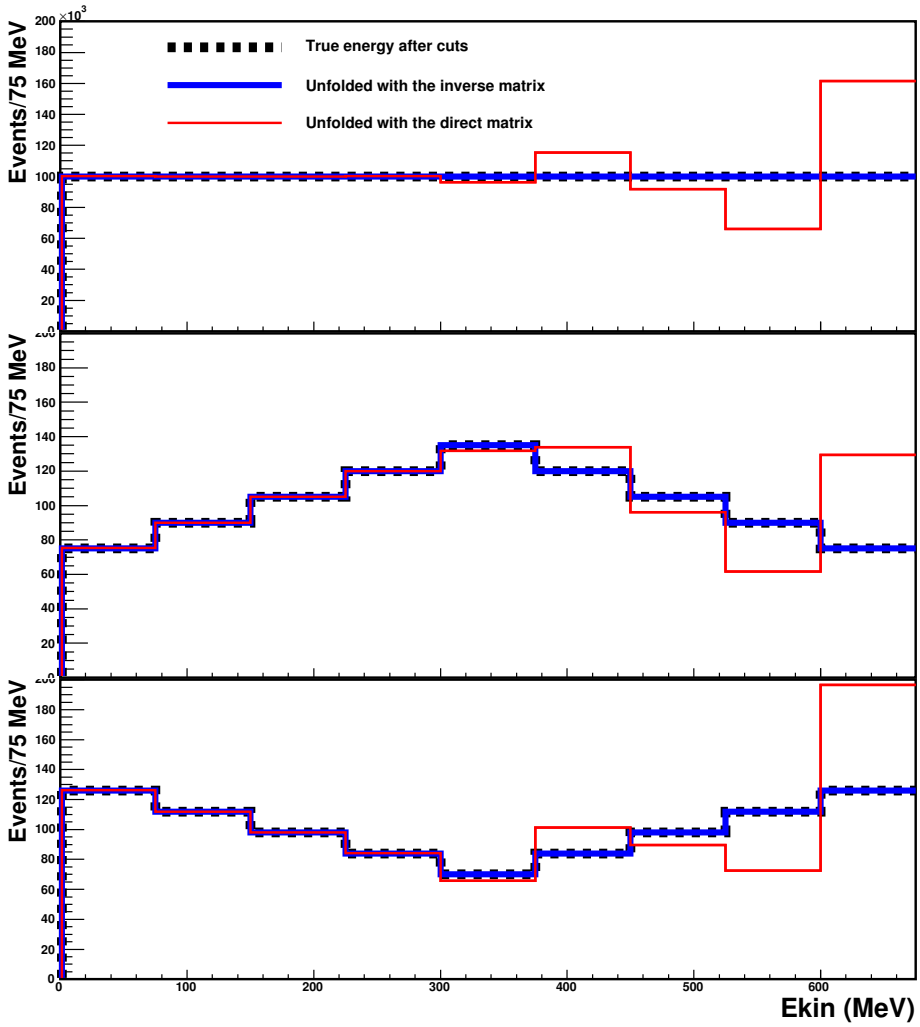


Figure A.13: Unfolding tests for the first three modified data samples (tests number 1,2, and 3) which are small deviations from the original MC spectrum. The true energy, the unfolded with inverse matrix, and the unfolded direct matrix solution.

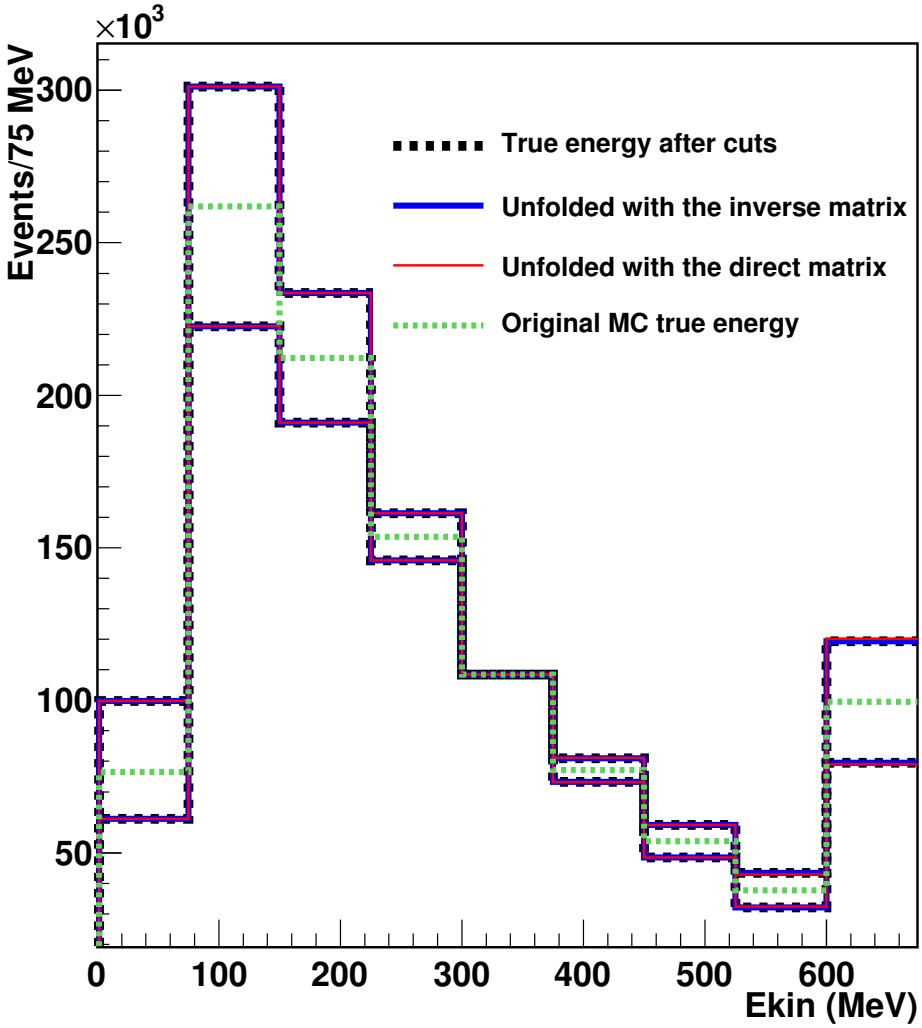


Figure A.14: Unfolding tests for the first last two modified data samples (tests number 4 and 5) which are small deviations from the original MC spectrum. The true energy for simulated data, the unfolded with inverse matrix, and the unfolded direct matrix solution, and the original MC true energy. The data distribution are taken as a superposition of the original MC and a linear function.

## A.7 Convergence with Iterations

In the true spectrum we looked at the behavior of the $\chi^2$ distributions between the simulated data and the unfolded energy distribution as a function of the number of iterations:

$$\chi^2_{true}(it) = \sum_{i=1}^{m} \frac{\left(\mu_i^{Data} - \mu_i^{unf}(it)\right)^2}{\mu_i^{Data}},$$

where $\mu_i^{unf}$ is the unfolded energy distribution and "$it$" is the iteration number.

To test the goodness of the convergence in the reconstructed energy spectrum, first of all, one needs to calculate the predicted MC reconstructed spectrum that gives the unfolded energy $\mu_i^{unf}(it)$. For that, the latter is multiplied by the response matrix (like in Eq.(A.11)):

$$\nu_j^{pred}(it) = \sum_{i=1}^{m} R_{ij}\mu_i^{unf}(it).$$

Now, the behavior of the $\chi^2$ distribution between the simulated data reconstructed energy spectrum and the predicted MC reconstructed energy for the unfolded distribution:

$$\chi^2_{rec}(it) = \sum_{j=1}^{n} \frac{\left(\nu_j^{Data} - \nu_j^{pred}(it)\right)^2}{\nu_j^{Data}}.$$

Looking at these quantities one can define whether the unfolding method converges and decide when to stop the iteration.

For the five tests that we looked at before, the $\chi^2_{rec}$ and $\chi^2_{true}$ values are shown as a function of the number of iterations in Figures A.15-A.17. In Fig. A.15 they are shown in the range 0-10000. However, the distributions have features which are hidden on this scale. These features are shown on the other two plots with different number of iterations ranges, where we concentrate on them.

One can see that apart from these small features both $\chi^2_{true}$ and $\chi^2_{rec}$ normally decrease with increasing the number of iterations. However, test number 1 slowly goes up after reaching the minimum at 250 iterations. Moreover, as one can see in Fig. A.16 for the tests number 4 and 5 (small variations from the original MC), the biggest drop in both $\chi^2_{rec}$ and $\chi^2_{true}$ is in the first $\sim$10 iterations; after that the change is very slow.

Also, on the next set of Figures A.18–A.22, one can see how the method physically converges to the data in both the true and reconstructed energy spectra. From Figures A.21 and A.22 one can see that if the true energy spectrum is not too far from the original MC, then the unfolding converges to the right solution. Within several iterations, the unfolded energy spectrum approaches the true energy spectrum very close.

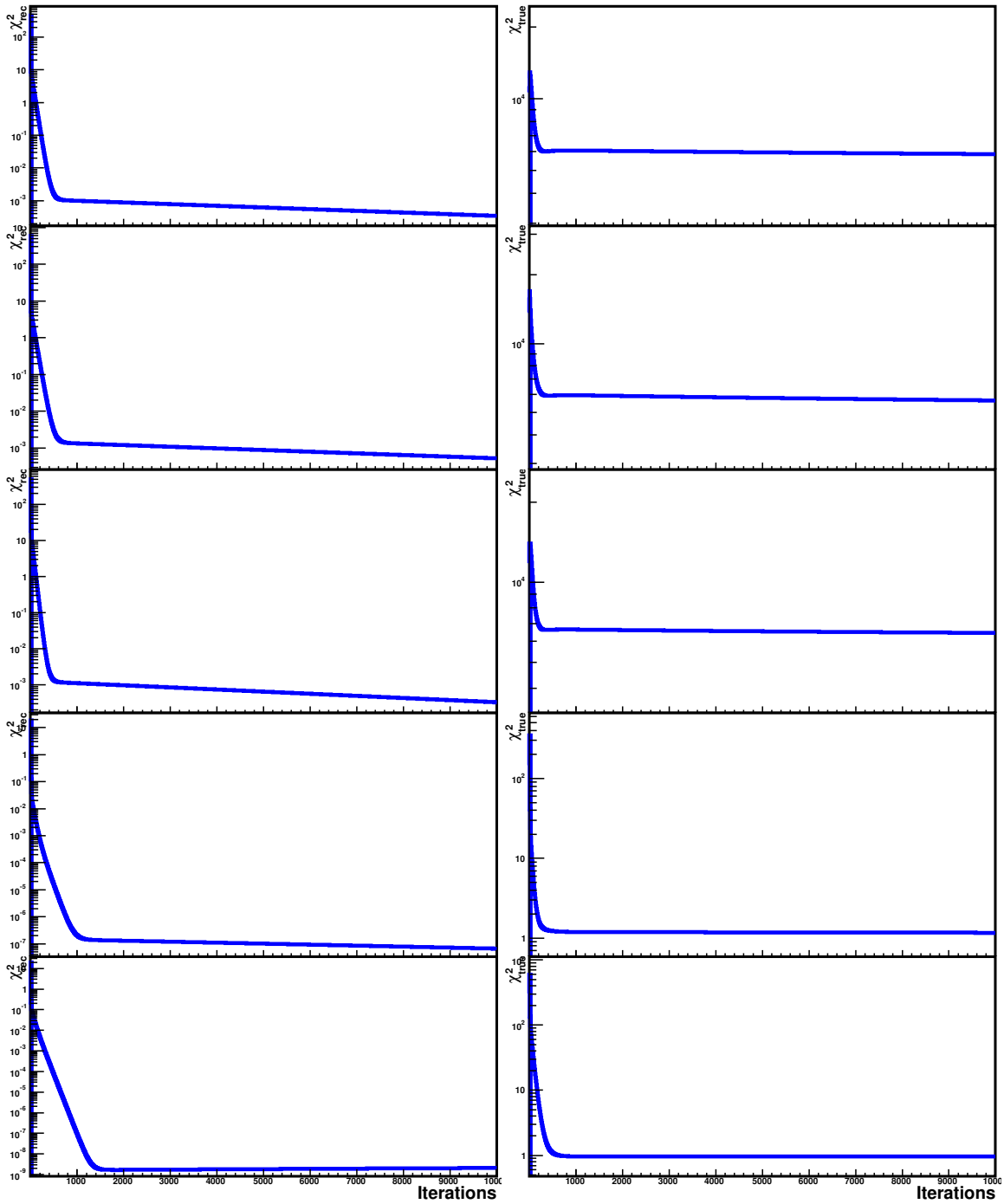


Figure A.15: $\chi_{rec}$ (left plots) and $\chi_{true}$ (right plots) as a function of the number of iterations for the five unfolding tests. From top to bottom: tests from number 1 through number 5.

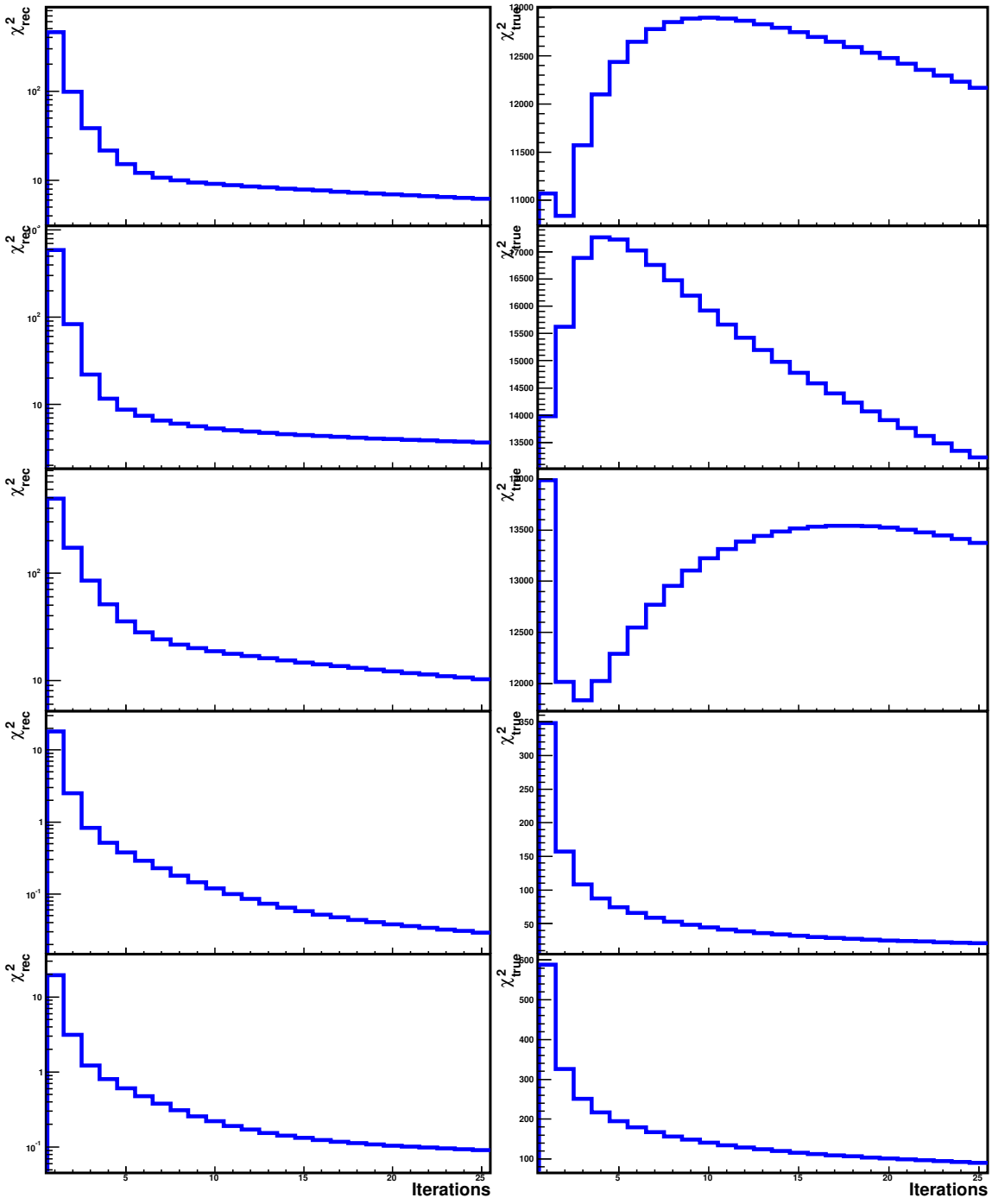


Figure A.16: $\chi_{rec}$ (left plots) and $\chi_{true}$ (right plots) as a function of the number of iterations for the five unfolding tests. From top to bottom: tests from number 1 through number 5.

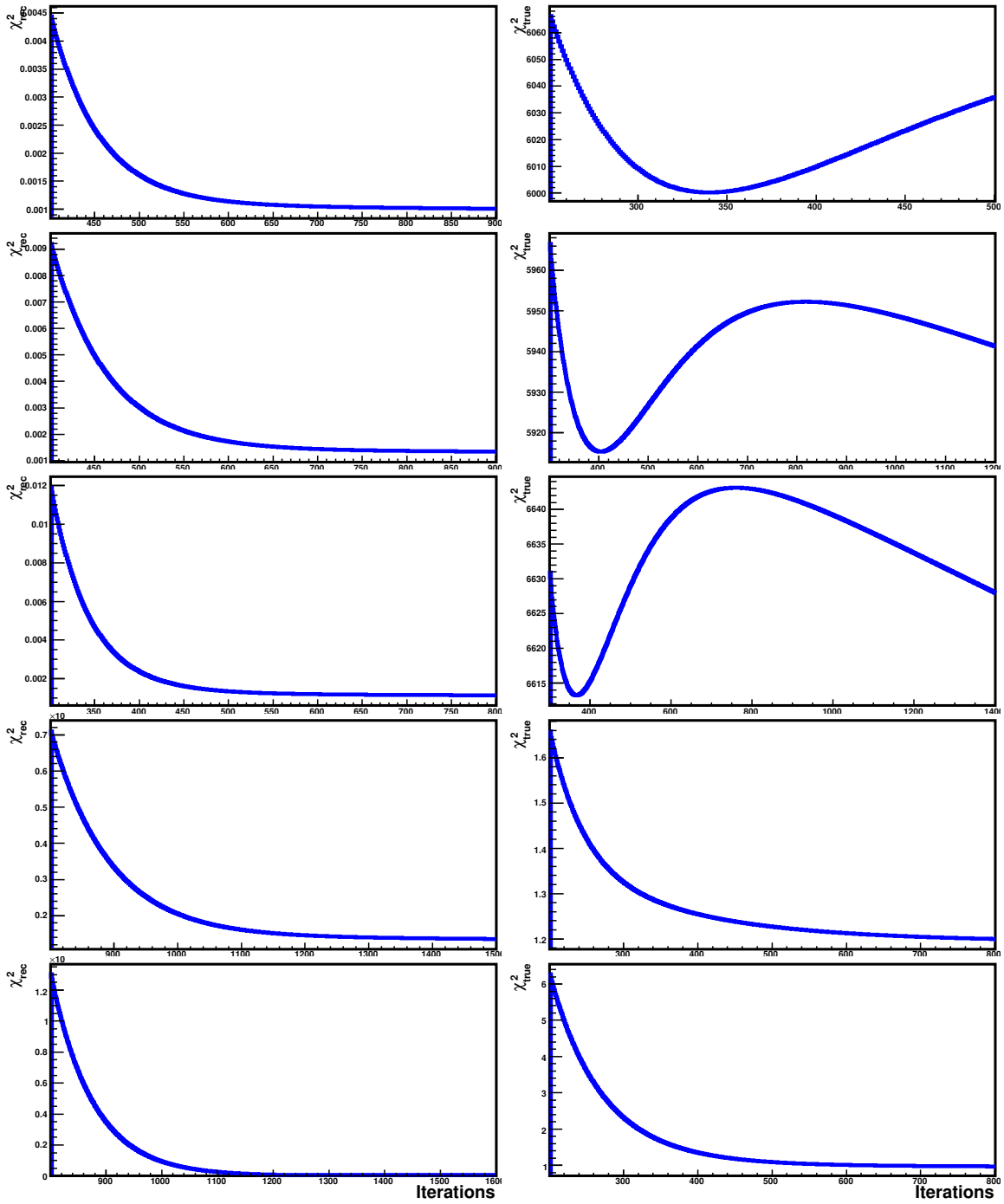


Figure A.17: $\chi_{rec}$ (left plots) and $\chi_{true}$ (right plots) as a function of the number of iterations for the five unfolding tests. From top to bottom: tests from number 1 through number 5.

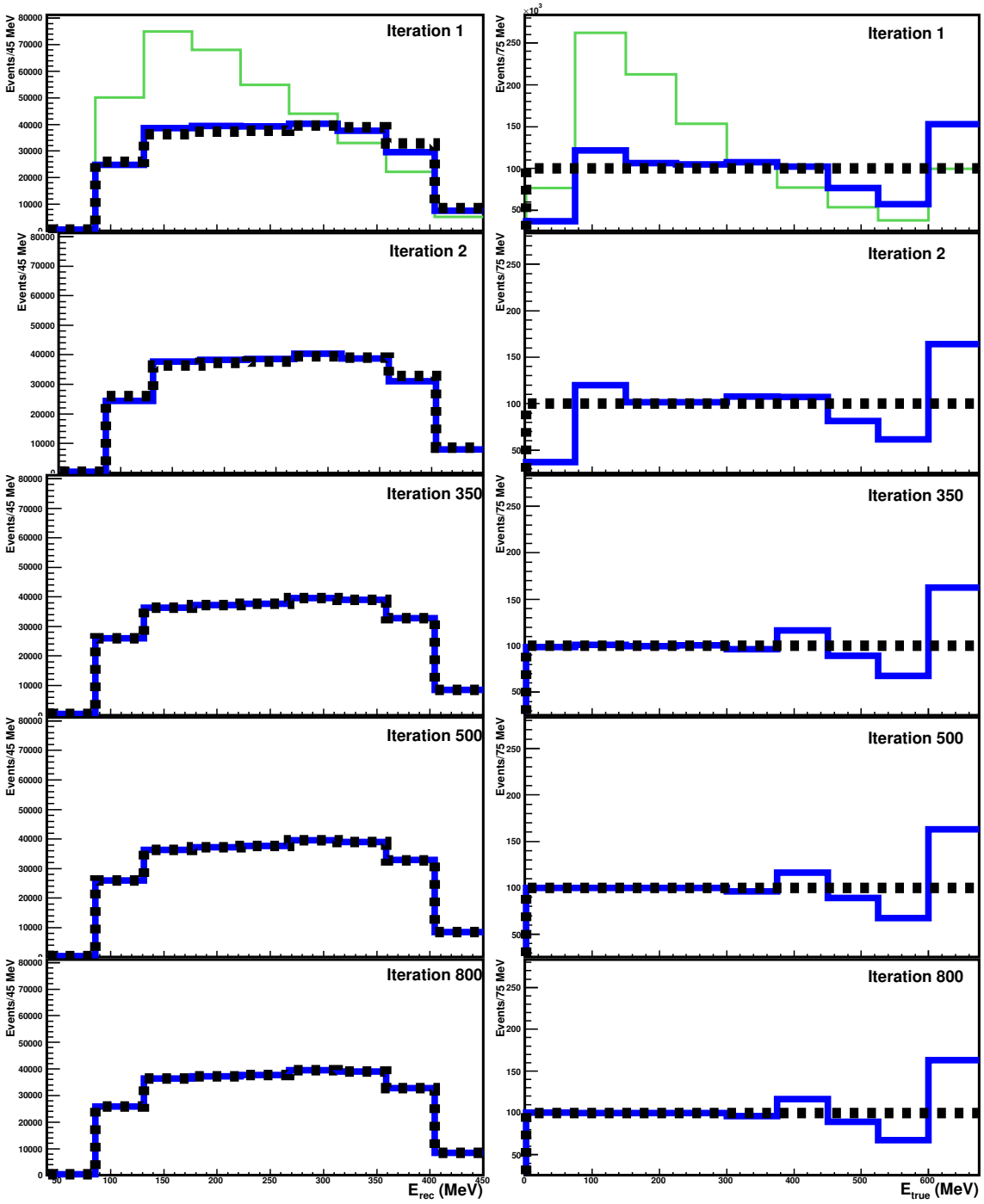


Figure A.18: Unfolding Iterations for the test number 1. The reconstructed spectrum (left plots) and the true spectrum (right plots). Data (black dashed), Original MC (green), Unfolded spectrum (blue solid on the right) $\nu^{pred}$ (blue solid on the left).

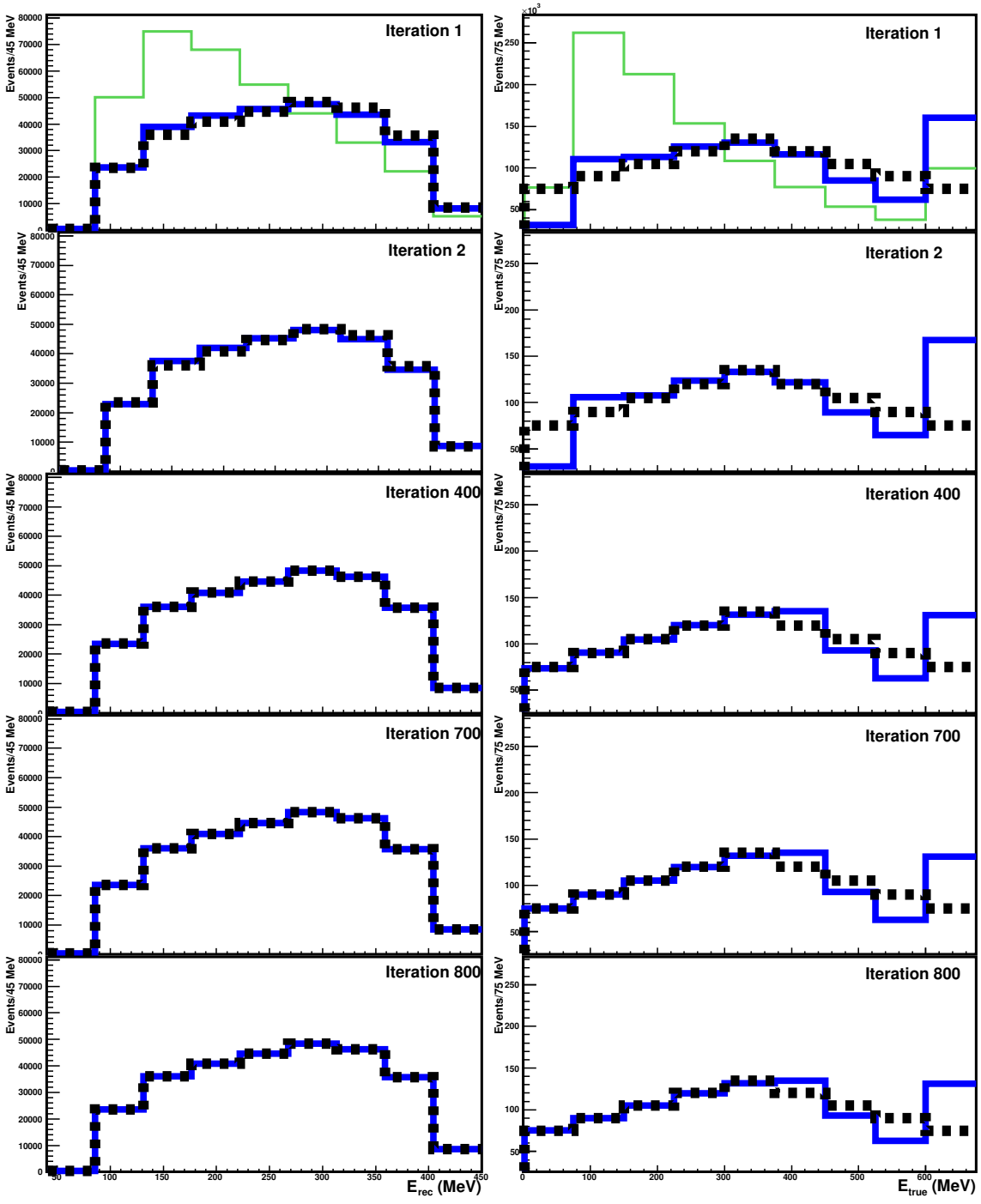


Figure A.19: Unfolding Iterations for the test number 2. The reconstructed spectrum (left plots) and the true spectrum (right plots). Data (black dashed), Original MC (green), Unfolded spectrum (blue solid on the right) $\nu^{pred}$ (blue solid on the left).

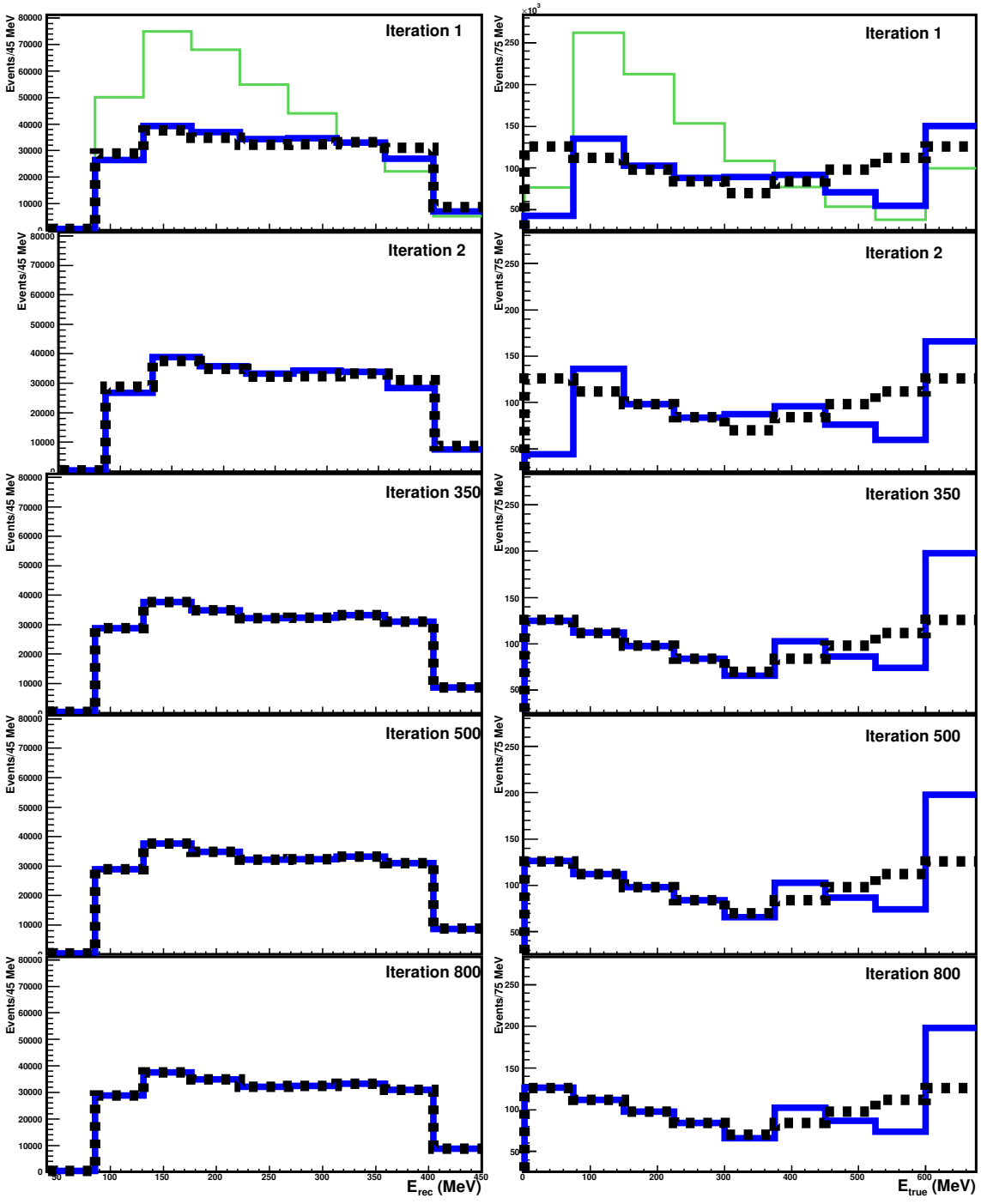


Figure A.20: Unfolding Iterations for the test number 3. The reconstructed spectrum (left plots) and the true spectrum (right plots). Data (black dashed), Original MC (green), Unfolded spectrum (blue solid on the right) $\nu^{pred}$ (blue solid on the left).

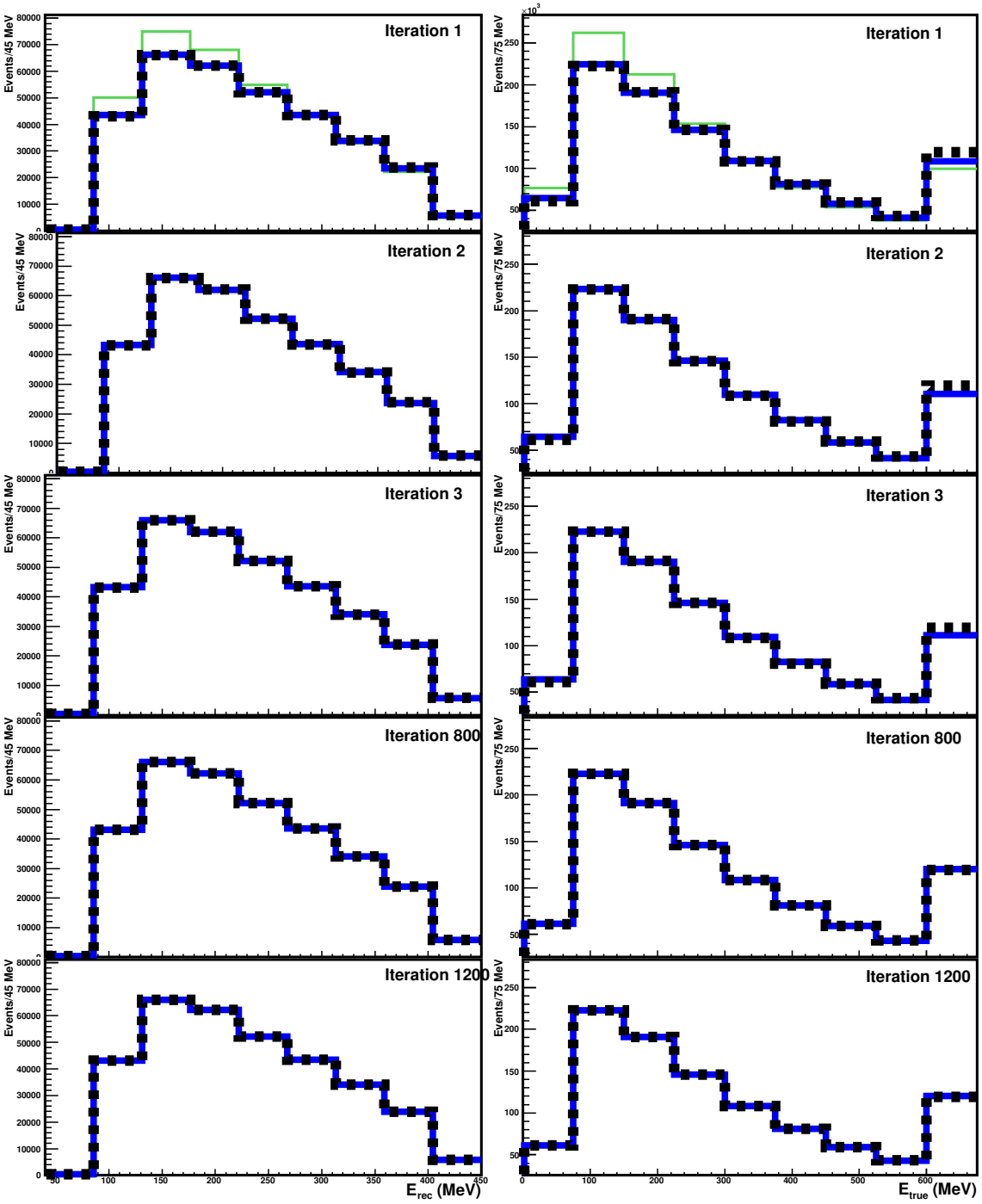


Figure A.21: Unfolding Iterations for the test number 4. The reconstructed spectrum (left plots) and the true spectrum (right plots). Data (black dashed), Original MC (green), Unfolded spectrum (blue solid on the right) $\nu^{pred}$ (blue solid on the left).

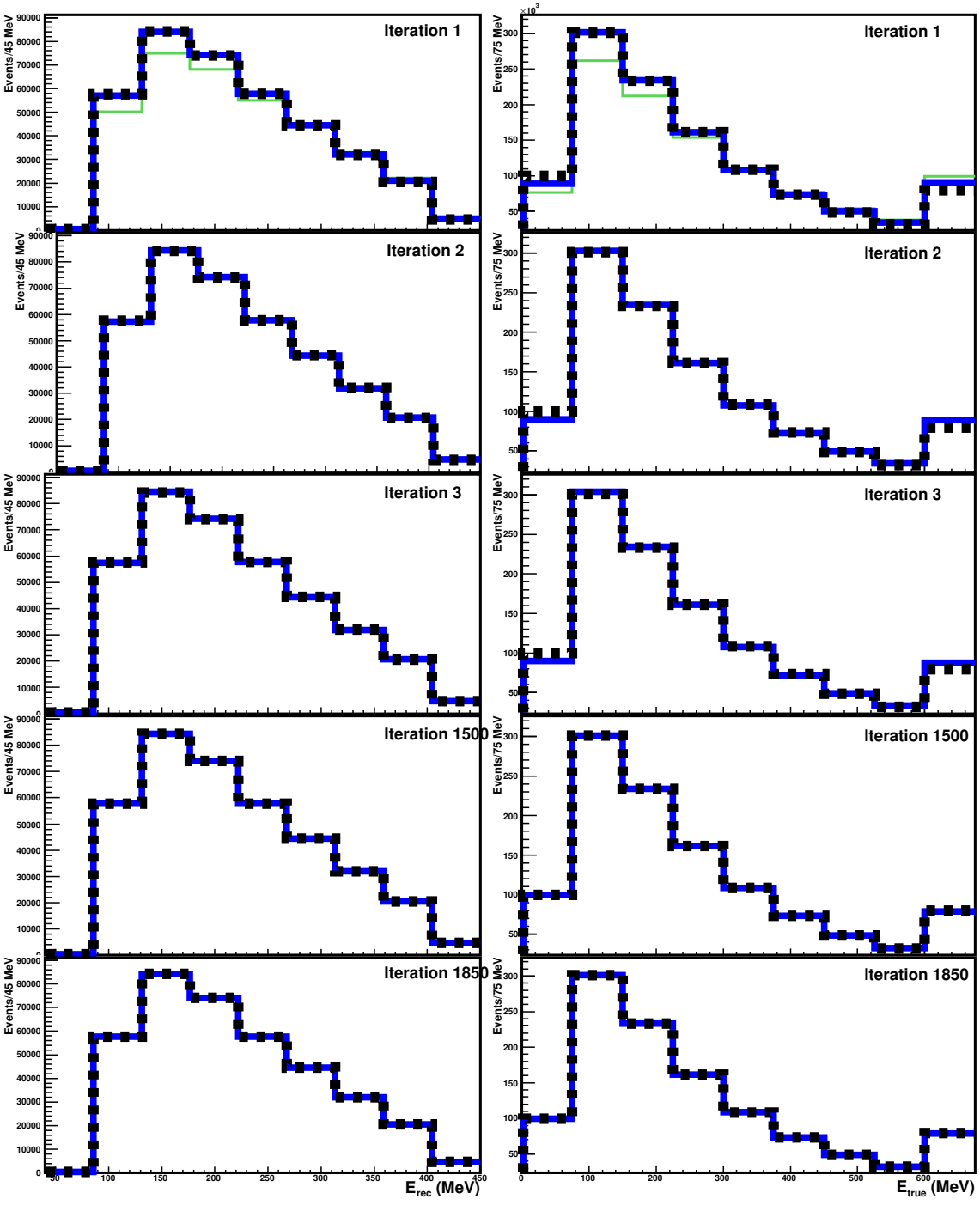


Figure A.22: Unfolding Iterations for the test number 5. The reconstructed spectrum (left plots) and the true spectrum (right plots). Data (black dashed), Original MC (green), Unfolded spectrum (blue solid on the right) $\nu^{pred}$ (blue solid on the left).

## A.8 Conclusions

In this appendix we formulated the unfolding problem for the NCE cross-section measurement and described possible solutions for it using the inverse and direct matrix methods.

In Section A.3 we showed that the inverse matrix method gives mathematically right solution, which is unbiased (doesn't depend on MC). However, it is very sensitive to statistical fluctuations, thus it can not be applied for our purpose of measuring the NCE cross-section.

In Section A.4 we described an alternative, the direct matrix method, and showed that it is stable to the small fluctuations of the reconstructed energy spectrum. The disadvantage of the method is that it is biased. However, there is an iterative procedure to eliminate this bias, but we could not theoretically show that it should always converge to the right solution in general case. We did, however, solve exactly the simplest toy model, the 2-bin case, in Section A.5. In the toy model we showed that under reasonable assumptions, the direct matrix method always converges to the right solution. In Section A.4.5 for the 50-bin case we showed that direct matrix method appears to converge to a solution that is close enough to data. Also, in Section A.6 for the 9-bin case, we studied how the direct matrix method converges and showed that if the deviations from MC are not too big, the direct matrix method converges. It has been shown that within 10 iterations, the unfolded energy is close enough to the data.

# Appendix B

# MiniBooNE Neutral Current Elastic Analysis Results in the Reconstructed Energy

Because of the energy smearing and limited efficiency one needs to correct for these effects; in general, experiments choose to correct the data distribution using unfolding techniques described in Appendix A and report results in the true (unsmeared) energy distribution in order to compare them to the MC prediction. However, there is an alternative method for reporting results, which is to report them in the reconstructed nucleon energy, without applying the unfolding procedure. These results would still be useful for Data/MC comparison

Let us forget about backgrounds for a moment. In terms of the matrices defined in Sections A.1–A.3, the reconstructed energy and the true energy distributions are related through

$$\nu_j = \sum_{i=1}^{m} R_{ij}\mu_i \ , \quad j = 1, ..., n. \tag{B.1}$$

The response matrix $R_{ij}$ simulates the energy smearing in the detector and the efficiency, transforming the true energy into the reconstructed energy.

The unfolding procedure finds the solution to Eq.(B.1) for the data ($\mu_i^{DATA}$) in terms of $R_{ij}$ and

$\nu_j^{DATA}$ (which is known). If the MC prediction is $\mu_i^{MC}$, then we can compare the histograms

$$\sum_{j=1}^{n} R_{ij}^{-1} \nu_j^{DATA} \qquad \text{and} \qquad \mu_i^{MC}.$$

The histogram on the left is the MiniBooNE cross-section and the histogram on the right is a theorist cross-section prediction. This is the Data/MC comparison in the true energy distribution.

In the alternative method the idea here is instead of correcting data for comparison with the MC, one can correct the MC. In this case, we calculate $\nu_j^{MC}$:

$$\nu_j^{MC} = \sum_{i=1}^{m} R_{ij} \mu_i^{MC} \ , \quad j = 1, ..., n.$$

After this, one can compare it to the data; in this case one would compare:

$$\nu_j^{DATA} \qquad \text{and} \qquad \sum_{i=1}^{m} R_{ij} \mu_i^{MC}.$$

The expression on the right is the predicted MC reconstructed spectrum of the events after the same selection cuts that were applied for the data.

This alternative method has advantages and disadvantages. The advantages are related to eliminating the unsmearing procedure, i.e., no unsmearing bias or complications in the ratio measurement. Also we have provided the inverse total error matrices $Err^{-1}$ in reconstructed energy bins, so that it can be used to calculate the $\chi^2$ of the data with a theory prediction. The disadvantages are that it is a little more complex to deal with, and the resulting plot in the reconstructed energy distribution cannot be directly compared to other experimental data; for that one would have to smear the other experiments data with the MiniBooNE response matrices.

## B.1 Brief Method Description

Since some matrices that are reported here are too big, we decided to organize them in the form of ASCII files. This way the files are easy to read from and are platform independent. We report the matrices and histograms for the three samples of NCE events:

- NCE sample: NCE proton and neutron sample for 40 MeV $< Ekin_{rec} <$ 650 MeV.
- High energy NCE $p$: NCE proton-enriched sample for 350 MeV $< Ekin_{rec} <$ 800 MeV.

- High energy NCE ($p + n$): NCE proton and neutron sample for 350 MeV $< Ekin_{rec} <$ 800 MeV.

The first sample was used to produce the cross-section and the $M_A$ and $\kappa$ fits. The second and the third samples are used in the $NCE\ p/NCE\ (p + n)$ ratio measurement and the subsequent $\Delta s$ fit. For each sample, there are *potential signal* events and the *background* events. The potential signal events include the following types of events:

(1) $\nu p \to \nu p$ on $H_2$

(2) $\nu p \to \nu p$ on $^{12}C$ with FSI

(3) $\nu p \to \nu p$ on $^{12}C$ without FSI

(4) $\nu n \to \nu n$ on $^{12}C$

(5) Irreducible backgrounds.

We call it potential signal because some theorists have a freedom not to calculate cross-sections for some of these processes (for example (1) or (5) or both). In this case they consider them as a background. Alternatively, they may choose to combine some of them (for example (2) and (3)) together and calculate the combined cross-section. For each of these potential signal events we report the migration matrix $M_{ij}^{(k)}$ and the MC true energy before any cuts ($\mu^{(k)}$). With this information, one can form the response matrices $R_{ij}^{(k)}$, which may be different for different processes. If needed, it is easy to combine some of the signals together (for example if a theorist predicts only $\nu p \to \nu p$ on $^{12}C$, regardless of FSI, then one can combine items (2) and (3)). Also, if a theorist needs to count some of these events as background (for example the irreducible backgrounds), then it is also easy to obtain the reconstructed spectrum for them.

For the background events including dirt, beam-unrelated and other one only needs the reconstructed energy spectrum $\nu_j^{BKG}$ predicted by the MiniBooNE MC. They need to be added to the MC signal spectrum to get the total energy spectrum.

Again, the idea is to calculate the predicted reconstructed energy spectrum for all MC processes $\nu_j^{MC}$ and compare it to the data $\nu_j^{DATA}$. The total reconstructed energy spectrum for MC events

is the sum of the reconstructed spectra for individual processes:

$$\begin{aligned}\nu_j^{MC} &= \underbrace{\sum_{i=1}^{m} R_{ij}^{(1)}\mu_i^{(1)}}_{\nu_j^{(1)}} + \underbrace{\sum_{i=1}^{m} R_{ij}^{(2)}\mu_i^{(2)}}_{\nu_j^{(2)}} + \underbrace{\sum_{i=1}^{m} R_{ij}^{(3)}\mu_i^{(3)}}_{\nu_j^{(3)}} \\ &+ \underbrace{\sum_{i=1}^{m} R_{ij}^{(4)}\mu_i^{(4)}}_{\nu_j^{(4)}} + \underbrace{\sum_{i=1}^{m} R_{ij}^{(5)}\mu_i^{(5)}}_{\nu_j^{(5)}} + \nu_j^{BKG},\end{aligned} \quad , \qquad j = 1, ..., n, \tag{B.2}$$

where $\mu^{(k)},\ k = 1, ..., 5$ is the theoretical prediction of the true energy distribution for the $k$-th potential signal.

If, for example, a theorist calculates $\nu p \to \nu p$ on $^{12}C$ regardless of FSI and does not calculate the irreducible backgrounds, then one needs to combine (2) and (3) and treat (5) as a background and use the MiniBooNE prediction, in this case the reconstructed energy for MC:

$$\nu_j^{MC} = \sum_{i=1}^{m} R_{ij}^{(1)}\mu_i^{(1)} + \sum_{i=1}^{m} R_{ij}^{(2\&3)}\mu_i^{(2\&3)} + \sum_{i=1}^{m} R_{ij}^{(4)}\mu_i^{(4)} + \nu_j^{(5),MC} + \nu_j^{BKG,MC}, \quad j = 1, ..., n.$$

Thus, if a theory predicts a potential signal type of event, then one needs to use $R_{ij}$ for it and replace a respective term in Eq.(B.2). Otherwise, one needs to use the MiniBooNE $\nu_j$ prediction.

## B.2 Files Description

There are 4 files which contain the needed information to use the MiniBooNE NCE data:

- Table_NCE.tab: tables for the NCE sample.
- Table_highe_p.tab: tables for the high energy NCE $p$ sample.
- Table_highe_pn.tab: tables for the high energy NCE $(p + n)$ sample.
- ErrorMatrix.tab: tables of the error matrices for the NCE sample and the ratio of high energy NCE $p$ to $(p + n)$.

As described, the last file contains tables with the two error matrices for the NCE sample and the ratio of high energy NCE $p$ to $(p+n)$. The first three files have the same structure, but for different event samples. There are following tables in the files:

- True nucleon MC kinetic energy spectra before any cuts for different possible signal events, $\mu_i^{(k)}$.

- Reconstructed nucleon kinetic energy spectra for the data and the MC background prediction, $\nu_j^{DATA}$ and $\nu_j^{BKG,MC}$.

- MC migration matrices (Ttrue vs Trec) for the neutral current elastic for different possible signal events, $M_{ij}^{(k)}$.

All these matrices are illustrated on Figures B.1–B.22. Notice that the variables which have the true energy on one of the axes always have an overflow bin – the events with the true kinetic energy greater than 900 MeV go in the last (overflow) bin. Also, for both high energy samples, the true energy has an underflow bin – the events with the true kinetic energy less than 300 MeV go in the first (underflow) bin.

## B.3 Calculating $R_{ij}$ or $\nu_j$ for the Possible Signal Events

Using $M_{ij}^{(k)}$ and $\mu_i^{(k)}$ , it is easy to calculate the needed $R_{ij}^{(k)}$ or $\nu_j^{(k)}$. $\nu_j^{(k)}$ is calculated using the property of the migration matrix Eq.(A.4) by projecting $M_{ij}^{(k)}$ onto the reconstructed energy axis. Using Eq.(A.10) and the property of the migration matrix Eq.(A.5), $R_{ij}^{(k)}$ can be calculated in the following way:

$$R_{ij}^{(k)} = \frac{M_{ij}^{(k)}}{\mu_i^{(k)}} \quad i = 1, ..., m, \quad j = 1, ..., n. \tag{B.3}$$

If the signal events are combined together, for example (2&3), then the response matrix is calculated the following way:

$$R_{ij}^{(2\&3)} = \frac{M_{ij}^{(2)} + M_{ij}^{(3)}}{\mu_i^{(2)} + \mu_i^{(3)}} \quad i = 1, ..., m, \quad j = 1, ..., n.$$

## B.4 The $\nu^{MC}$ Calculation

For each of the signal processes that are predicted by a theory one has to follow several steps, in order to use the MiniBooNE data in the alternative reconstructed energy description:

- Calculate the flux-averaged differential cross-section as a function of the nucleon kinetic energy using any nuclear model. Then the cross-section needs to be converted to have the same energy bins as used for the true energy axis in the migration matrices $M_{ij}^{(k)}$:

- For the NCE sample, it is 50 bins from 0 MeV to 900 MeV plus the 51-st bin overflow, $E > 900$ MeV$MeV$.
- For the high energy NCE samples, 28 bins from 300 MeV to 900 MeV, plus the 1-st underflow bin $E < 300$ MeV and 30-th overflow bin, $E > 900$ MeV.

- Convert the cross-section into the expected true energy histogram. This is a simple multiplication by factor, which can be calculated using Eq.(6.3), but now expressing $\sigma_i$:

$$\sigma_i = \left[ \left( \frac{dQ^2}{dT_N} \Delta T_N \right) N_N N_{POT} \int \Phi_\nu dE_\nu \right] \times \frac{d\sigma_i^{NCE}}{dQ^2}$$

- Calculate $R_{ij}^{(k)}$ as in Eq.(B.3) using the corresponding $M_{ij}^{(k)}$ and $\mu_i^{(k)}$ from the MC.

For the signal process that theory doesn't predict, calculate $\nu_j^{(k)}$ as described in Appendix B.3. The last part is to calculate $\nu^{MC}$ by combining the predicted MC energy spectra by using Eq.(B.2).

## B.5 Data/MC Comparison

Now one can make use of the MiniBooNE data for the data/MC comparison. Using the error matrices for the NCE event sample, one can calculate the $\chi^2$ in order to compare the theory prediction with the MiniBooNE data:

$$\chi^2 = \sum_{i=1}^{n} \sum_{j=1}^{n} \left( \nu_i^{DATA} - \nu_i^{MC} \right) M_{ij}^{-1} \left( \nu_j^{DATA} - \nu_j^{MC} \right),$$

where $M_{ij}$ is the error matrix for the NCE sample.

For the ratio measurement one has to calculate $\nu^{MC,NCE(p)}$ and $\nu^{MC,NCE(n+p)}$ for the high energy $NCE$ $p$ and $NCE$ $(p+n)$ samples. Then the $\chi^2$ between data and MC is

$$\chi^2 = \sum_{i=1}^{n} \sum_{j=1}^{n} \left( \frac{\nu_i^{DATA,NCE(p)}}{\nu_i^{DATA,NCE(p+n)}} - \frac{\nu_i^{MC,NCE(p)}}{\nu_i^{MC,NCE(p+n)}} \right) M_{ij}^{-1} \left( \frac{\nu_j^{DATA,NCE(p)}}{\nu_j^{DATA,NCE(p+n)}} - \frac{\nu_j^{MC,NCE(p)}}{\nu_j^{MC,NCE(p+n)}} \right)$$

with $M_{ij}$ being the error matrix of the ratio in this case.

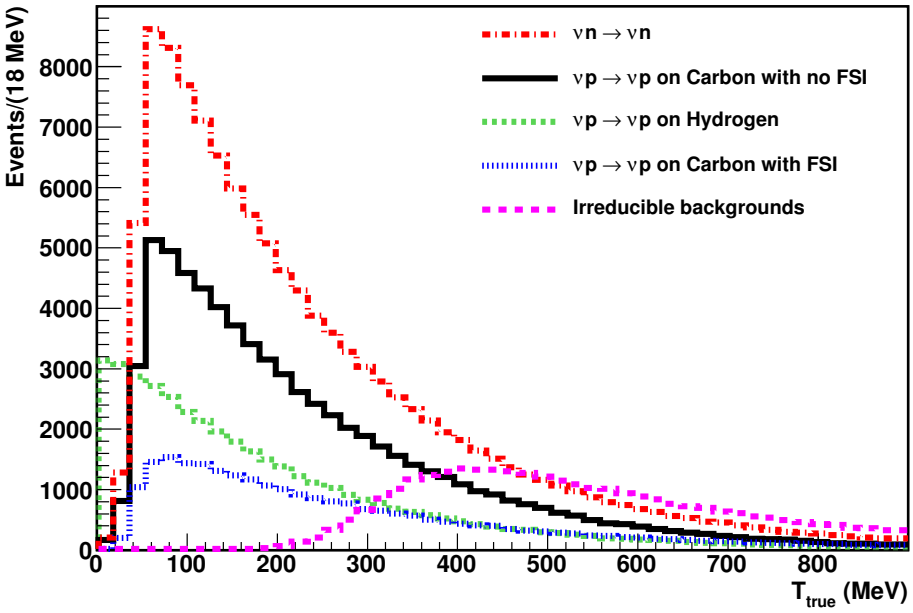


Figure B.1: True energy histograms for possible signal events before any cuts are applied, used in the NCE cross-section measurement.

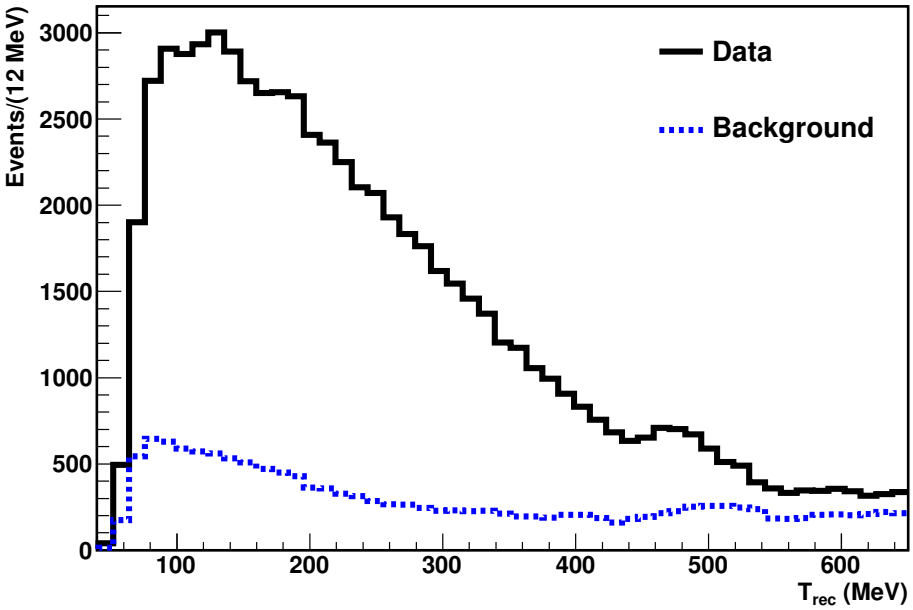


Figure B.2: Reconstructed energy histograms for the data the background MC after the NCE cuts are applied.

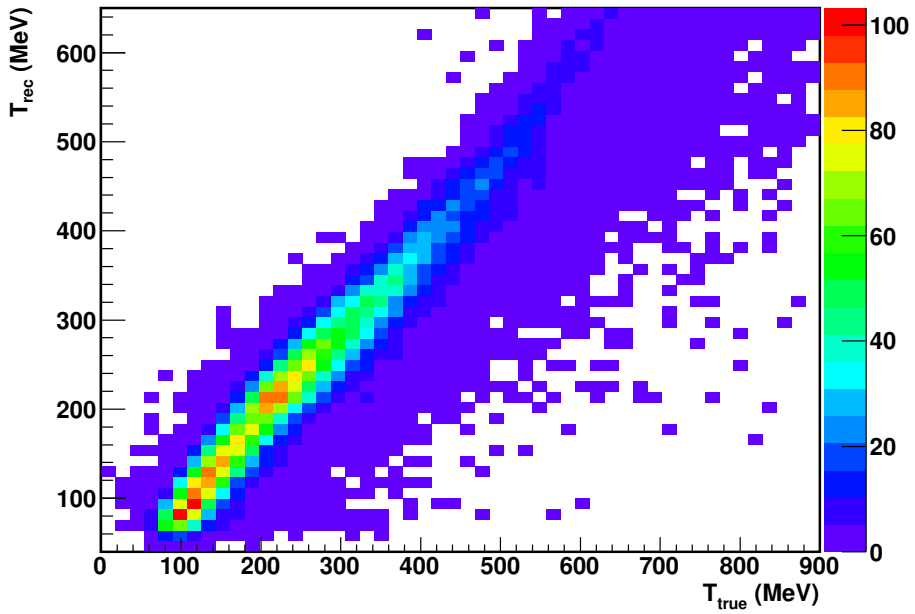


Figure B.3: Migration matrix for the NCE events on hydrogen in the NCE event sample.

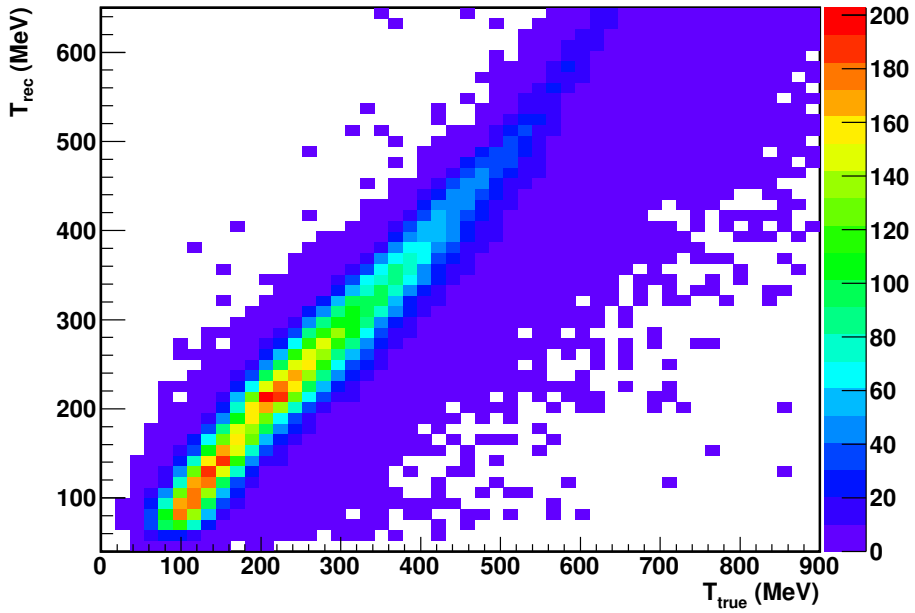


Figure B.4: Migration matrix for the NCE events on single protons (with no FSI) in carbon in the NCE event sample.

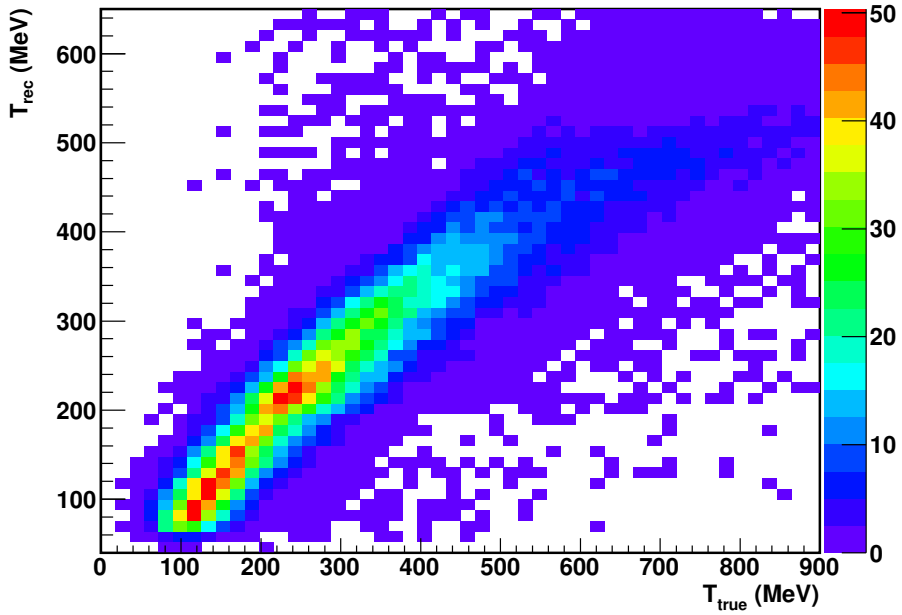


Figure B.5: Migration matrix for the NCE events on protons with FSI in carbon in the NCE event sample.

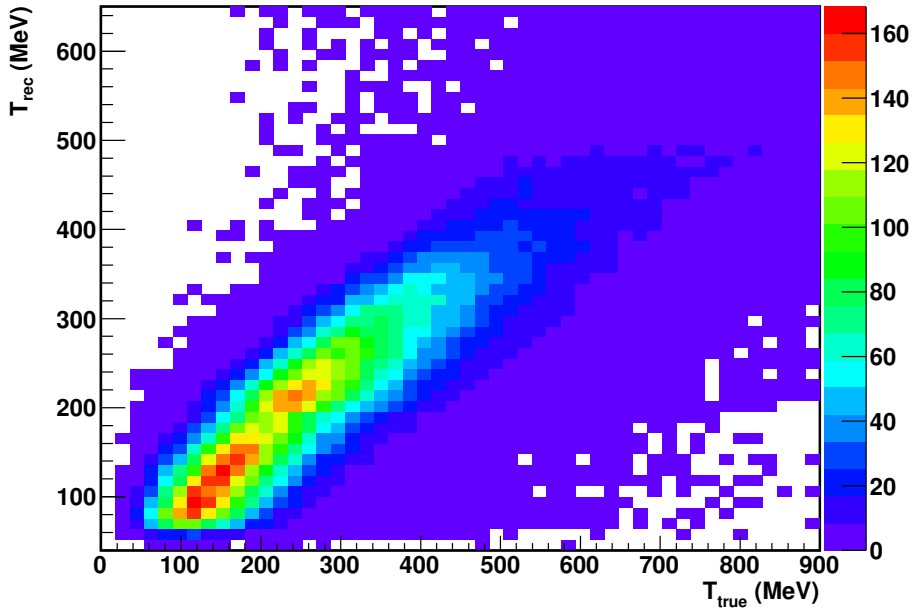


Figure B.6: Migration matrix for the NCE events on neutrons in carbon in the NCE event sample.

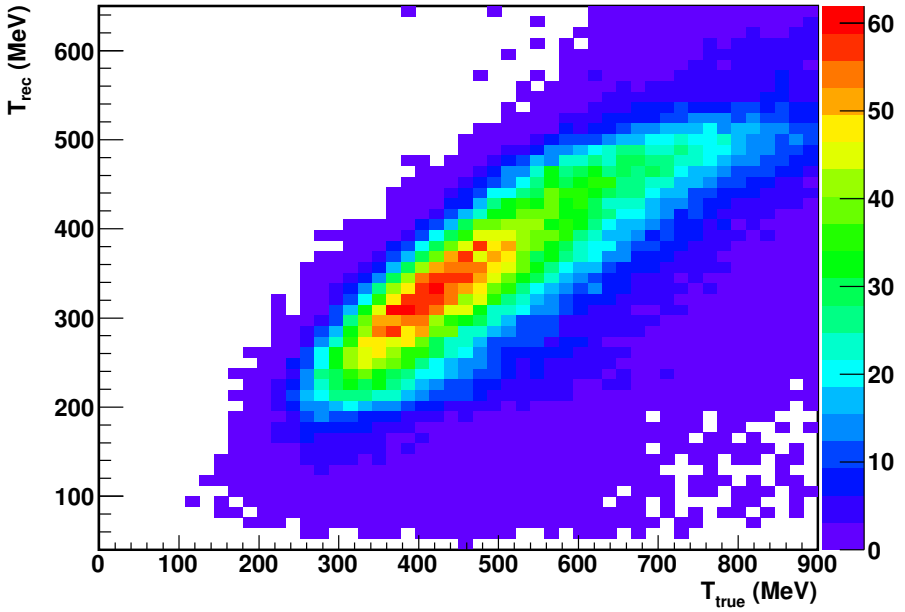


Figure B.7: Migration matrix for the irreducible backgrounds in the NCE event sample.

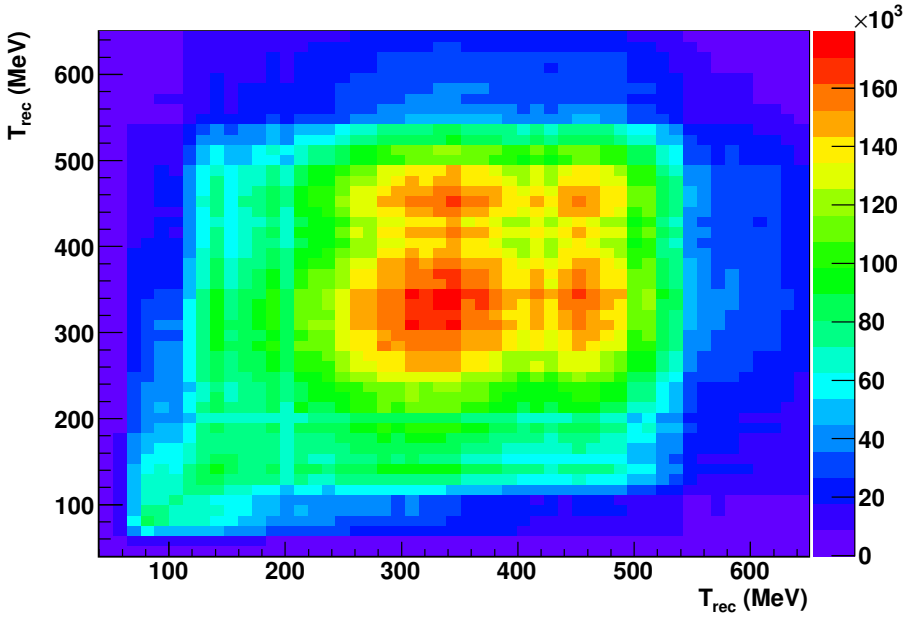


Figure B.8: Error matrix for the NCE event sample.

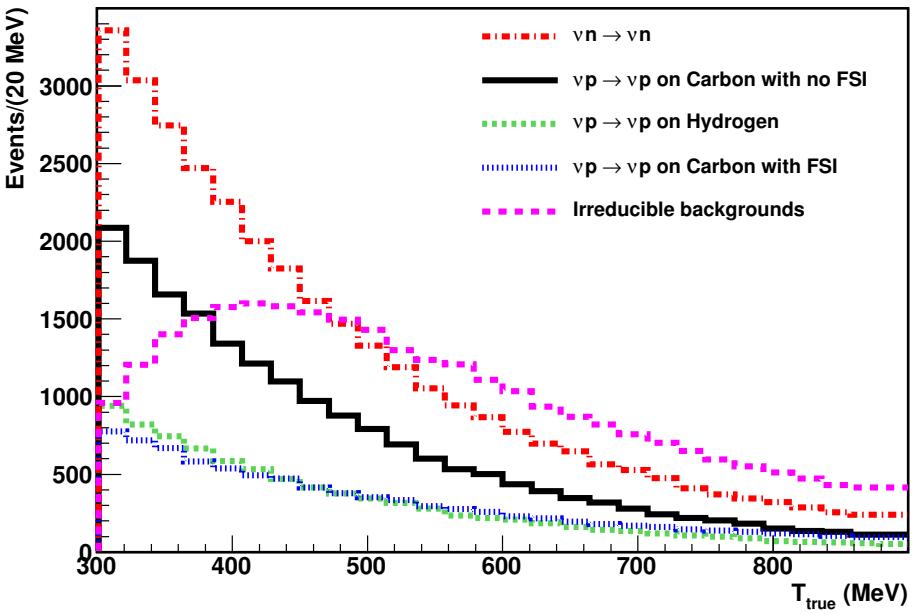


Figure B.9: True energy histograms for possible signal events before any cuts are applied, used for both high energy NCE samples ($p$ and $p+n$).

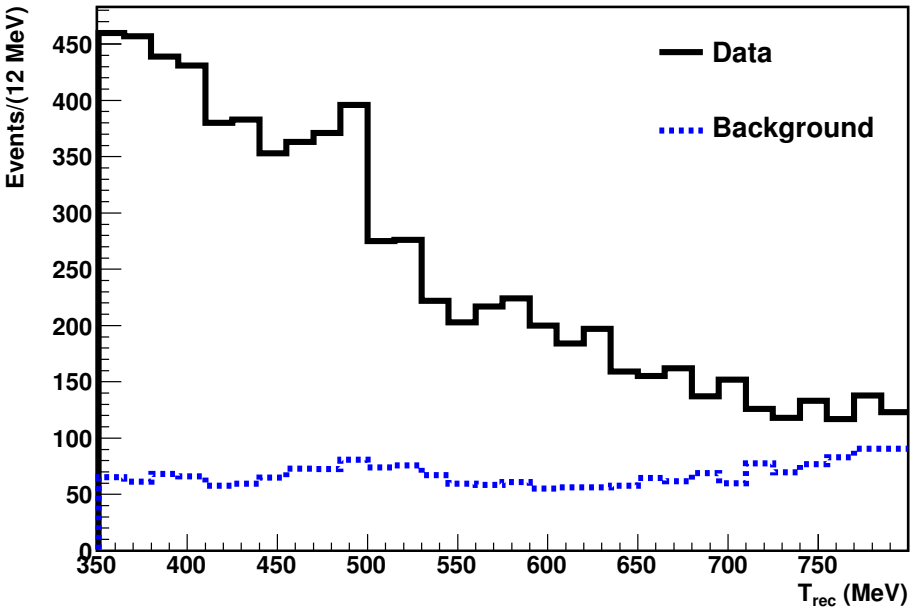


Figure B.10: Reconstructed energy histograms for the data the background MC after the high energy NCE $p$ cuts (numerator of the ratio) are applied.

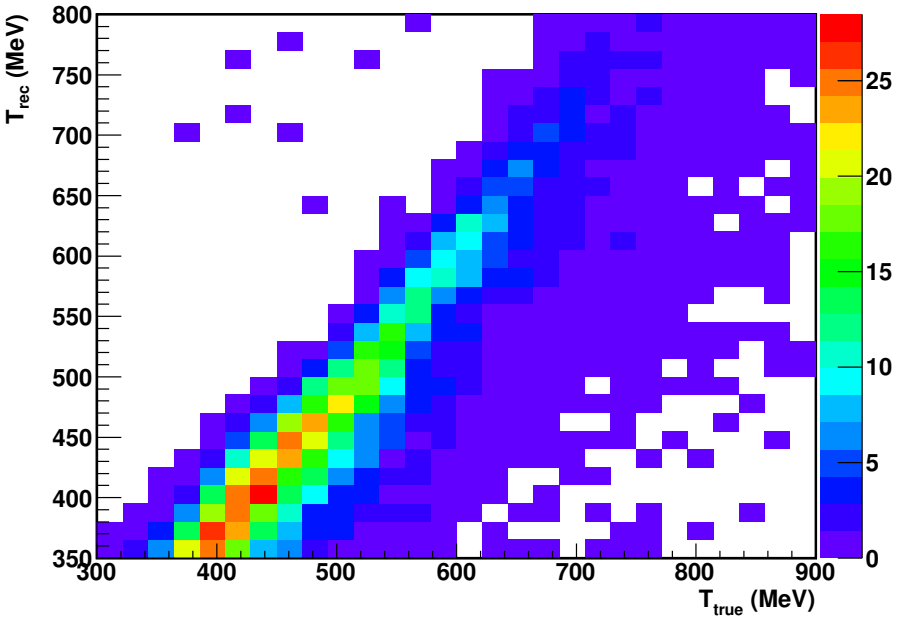


Figure B.11: Migration matrix for the NCE events on hydrogen in the high energy NCE $p$ event sample (numerator of the ratio).

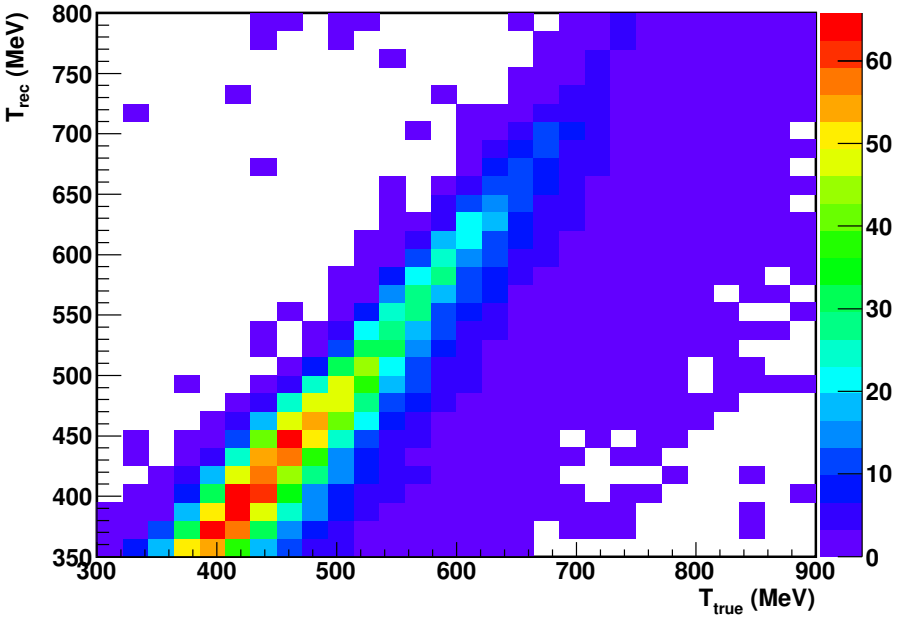


Figure B.12: Migration matrix for the NCE events on single protons (with no FSI) in carbon in the high energy NCE $p$ event sample (numerator of the ratio).

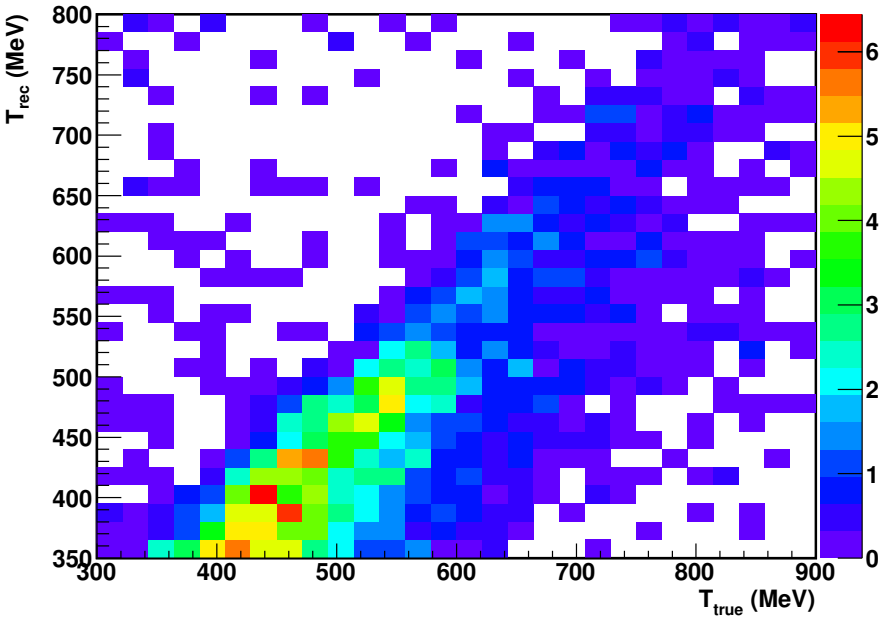


Figure B.13: Migration matrix for the NCE events on protons with FSI in carbon in the high energy NCE $p$ event sample (numerator of the ratio).

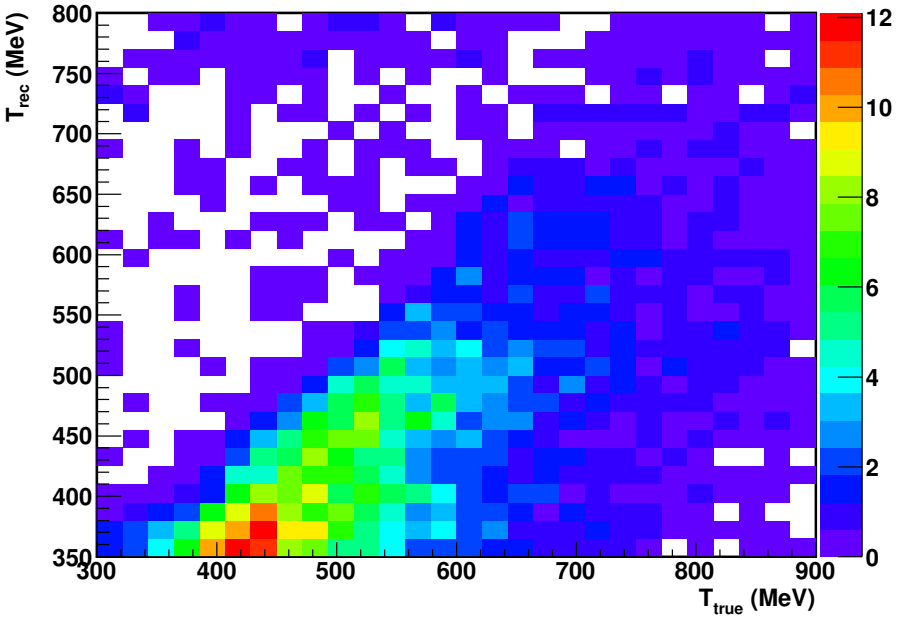


Figure B.14: Migration matrix for the NCE events on neutrons in carbon in the high energy NCE $p$ event sample (numerator of the ratio).

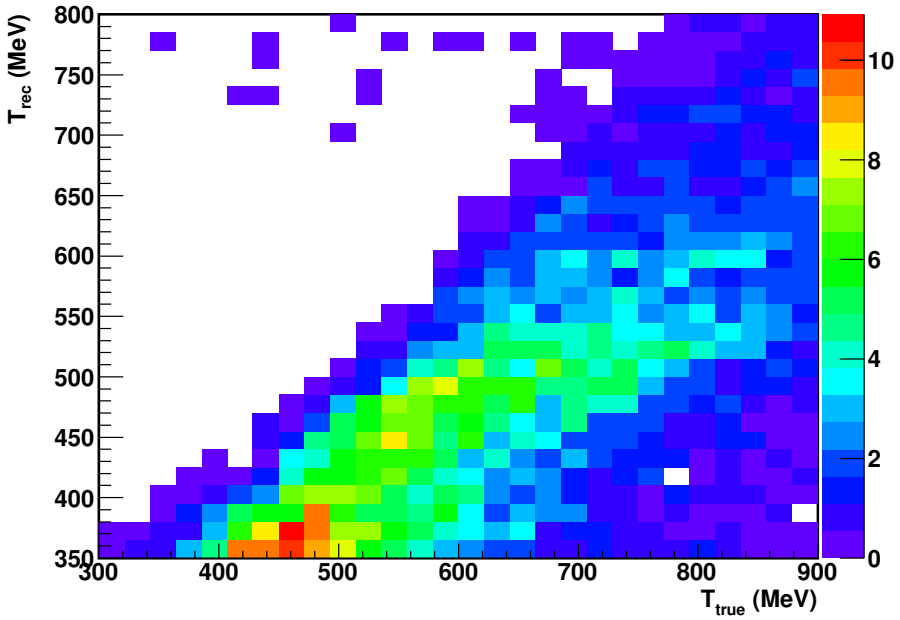


Figure B.15: Migration matrix for the irreducible backgrounds in the high energy NCE $p$ event sample (numerator of the ratio).

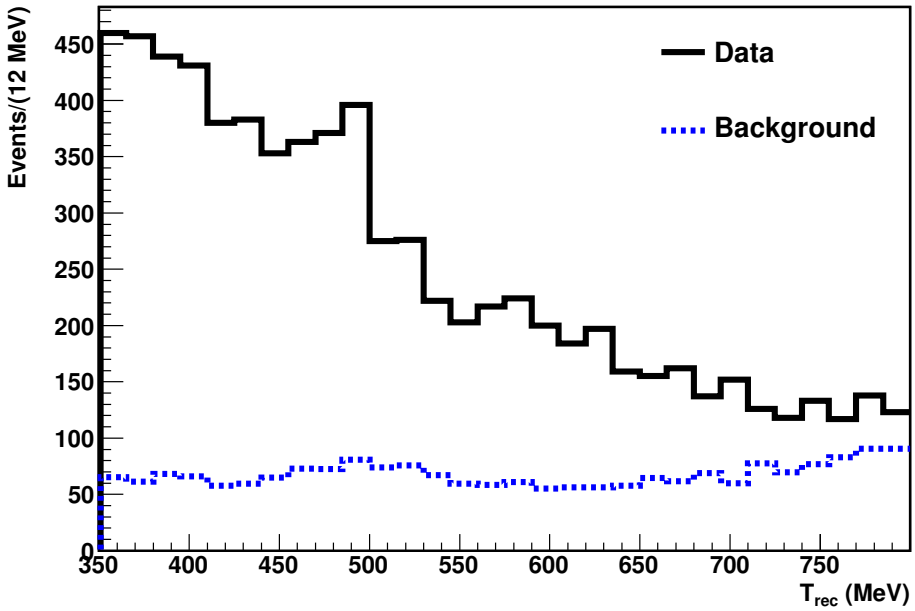


Figure B.16: Reconstructed energy histograms for the data the background MC after the high energy NCE $p + n$ cuts (denominator of the ratio) are applied.

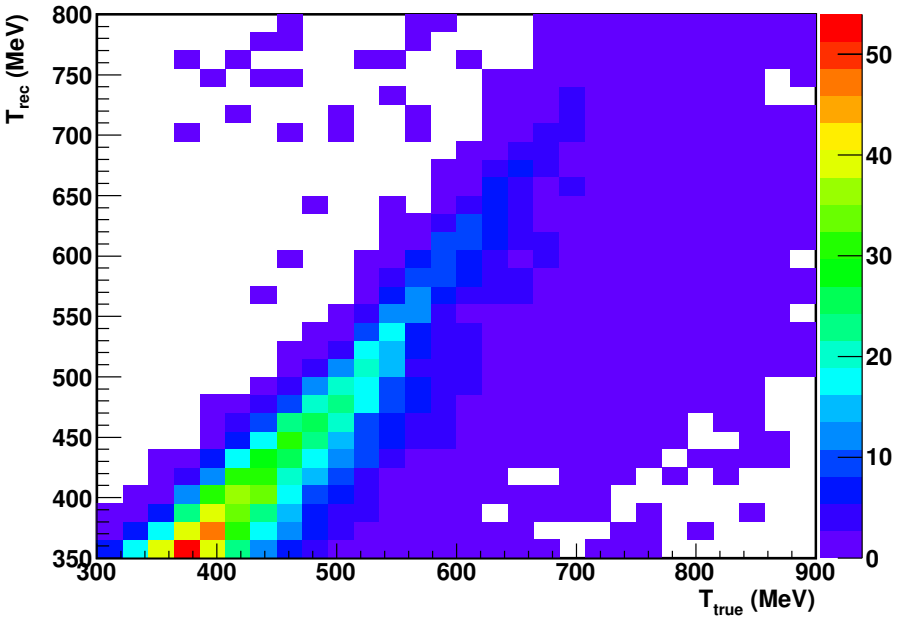


Figure B.17: Migration matrix for the NCE events on hydrogen in the high energy NCE $p+n$ event sample (denominator of the ratio).

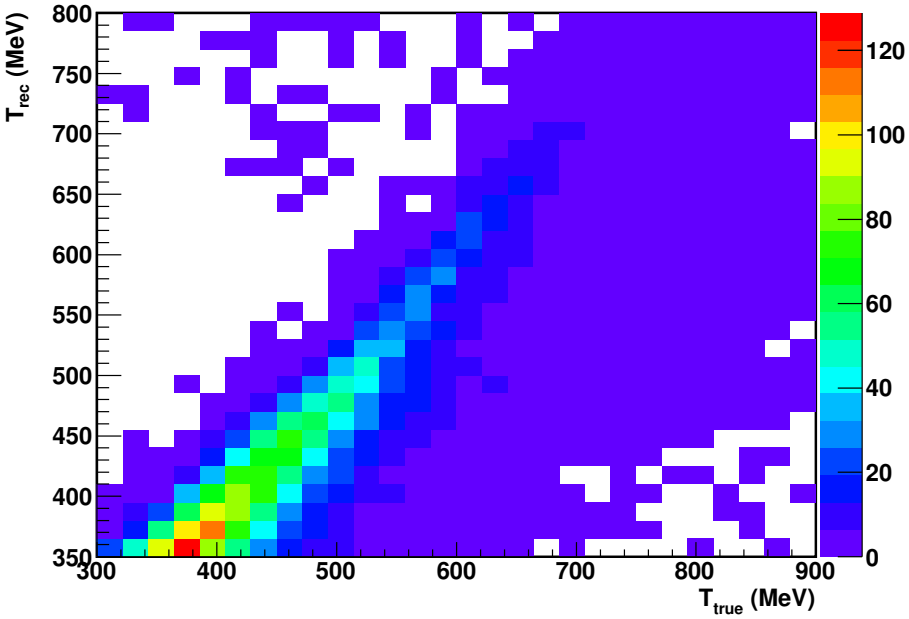


Figure B.18: Migration matrix for the NCE events on single protons (with no FSI) in carbon in the high energy NCE $p+n$ event sample (denominator of the ratio).

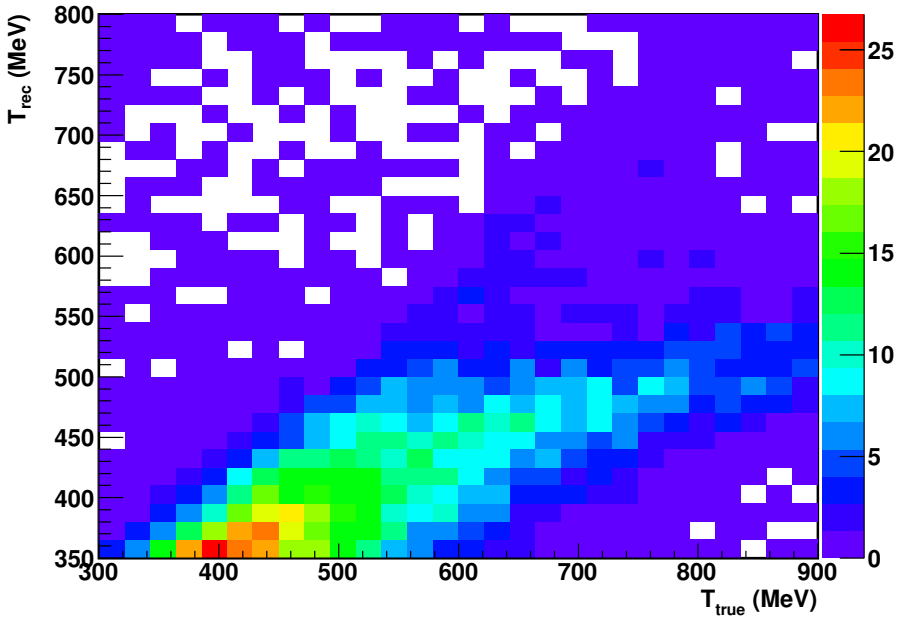


Figure B.19: Migration matrix for the NCE events on protons with FSI in carbon in the high energy NCE $p + n$ event sample (denominator of the ratio).

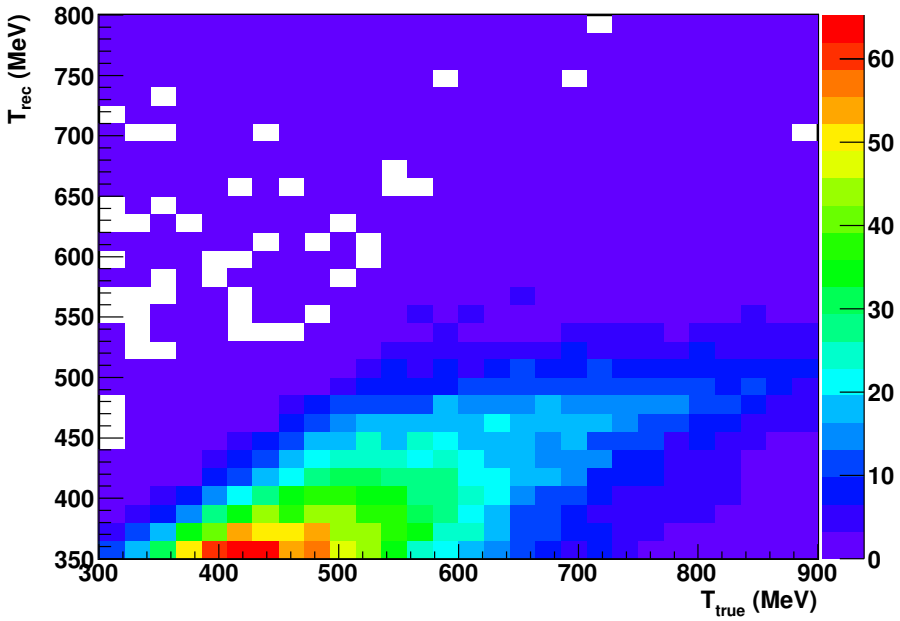


Figure B.20: Migration matrix for the NCE events on neutrons in carbon in the high energy NCE $p + n$ event sample (denominator of the ratio).

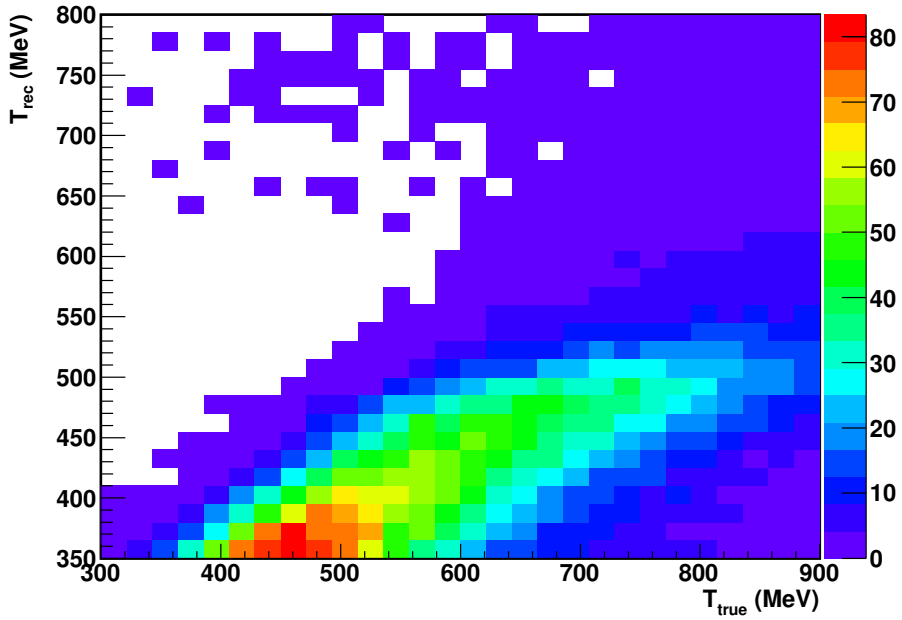


Figure B.21: Migration matrix for the irreducible backgrounds in the high energy NCE $p + n$ event sample (denominator of the ratio).

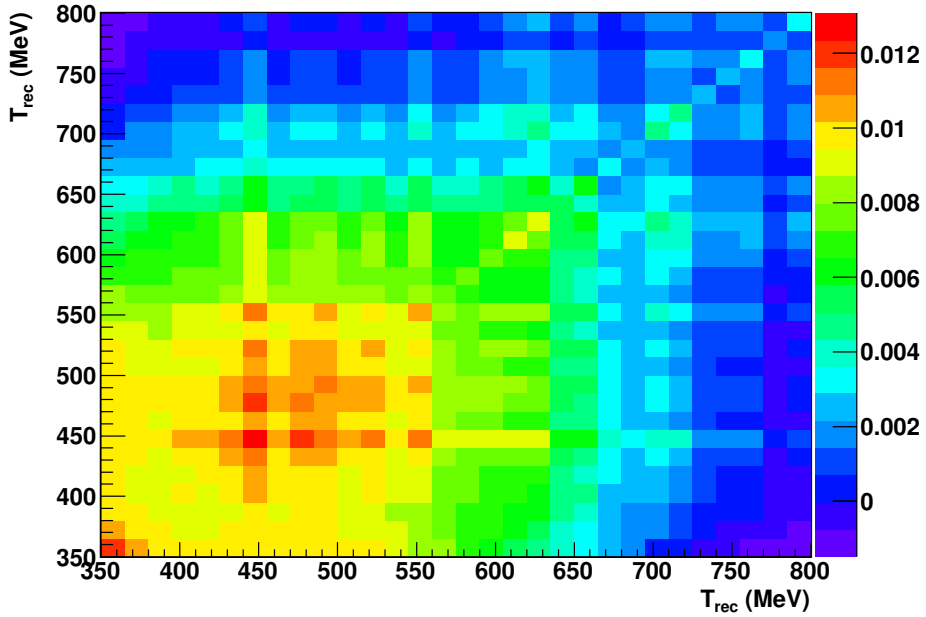


Figure B.22: Error matrix for the ratio of high energy NCE $p$ to $p + n$ samples.

# Appendix C

# Proton Energy Calibration

## C.1 Proton Energy Scaling Using Scintillation Fraction

Unfortunately, in MiniBooNE there was no direct proton energy calibration. The light yield was tuned on other particles, namely muons and electrons.

A potential energy scaling problem for the NCE events has been investigated. The idea is to look for a variable that gives an evidence of the prompt light as a function of the reconstructed nucleon energy; The scintillation fraction in the StancuFitters was chosen as such variable, called "$scifra$" henceforth.

The nucleon reconstructed energy, $Erec$, is a complex variable, which is an output of the NCFitter after maximizing charge and time likelihoods. However, in the first approximation, it depends mostly on the total charge on all PMTs. $scifra$ is also a complex variable, which is an indirect output from the StancuFitters (electron hypothesis): it represents the reconstructed fraction of the scintillation flux in the total flux.

When plotting $scifra$ as a function of $Erec$, one should expect a good agreement between the data and the MC for energies below the proton Cherenkov threshold because protons produce only scintillation light there. However, around the proton Cherenkov threshold and above, there may be a data/MC disagreement due to a possible energy scaling problem (or some other problem, a wrong FSI model [125], for example).

The $scifra$ variable for the NCE data and the central value MC is shown in Fig. C.1. Normally, one would expect the $scifra$ value for NCE events to be about 1 for energies below 350 MeV and then to drop above that energy. However, the $scifra$ is the scintillation fraction under electron

hypothesis, not for proton hypothesis. The StancuFitter algorithm assumes the event is an electron and expects a big prompt peak in the corrected time distribution (the Cherenkov to scintillation ratio is 3 to 1 for electrons) which would minimize the electron time likelihood. When there are very few tank hits (as is the case of the NCE events, where we typically observe about 50-100 tank hits depending on energy), it is easier for the fitter to find such a vertex with a reconstructed prompt peak in the corrected time distribution. We can see that in Fig. 6.6 – the corrected time for the NCE events has a bigger prompt peak in the StancuFitters (bottom plot) than that in the NCFitter (top plot). The lower energy of the proton, the fewer the number of PMT hits and, thus, the easier for the StancuFitter to put a bigger fraction of events in the prompt peak of the corrected time distribution (for example, in the extreme case of say 2 PMT hits, StancuFitter would always find at least one PMT hit to be prompt). This is why $scifra$ goes down as the energy decreases when the energy is below 350 MeV. If there were no Cherenkov light for protons, one would expect $scifra$ to go up with energy and eventually stabilize at 1.

Above 350 MeV, $scifra$ goes down as the energy increases, which shows that the events in the NCE sample start producing more and more Cherenkov light. One can see that $scifra$ has lower values in data for energies above 350 MeV. This disagreement could be explained, for example, by a wrong energy scaling, which means that the central value MC overpredicts scintillation light coming from protons in the detector.

Assuming a wrong energy scaling for protons, one can either apply the energy scaling either to the MC or to the data and try to match data/MC in the $scifra$ plot. After applying an energy rescaling of 11%, the disagreement in $scifra$ plot becomes good at high energies, as we can see from Fig. C.2. This 11% energy rescaling also improves a shape energy disagreement between data and MC for NCE event sample, as we can see in Fig. C.3, compared to the reconstructed energy spectrum before the energy rescaling shown in Fig. 6.8.

However, if we look at the $scifra$ plot for the optical model multisims in Fig. C.4, one can see that the disagreement is covered with this error. In the end we decided not to perform the rescaling and take the MC central value as is and claim that the systematic errors cover the $scifra$ spread, but we are aware of the possible energy rescaling problem for protons. Doing it the right way one would need to redefine the MC central value, reduce the optical model error spread and retune all fitters, etc., which is potentially years of additional work. A proton energy scaling would significantly reduce the optical model error, which dominates all measurements presented in this thesis.

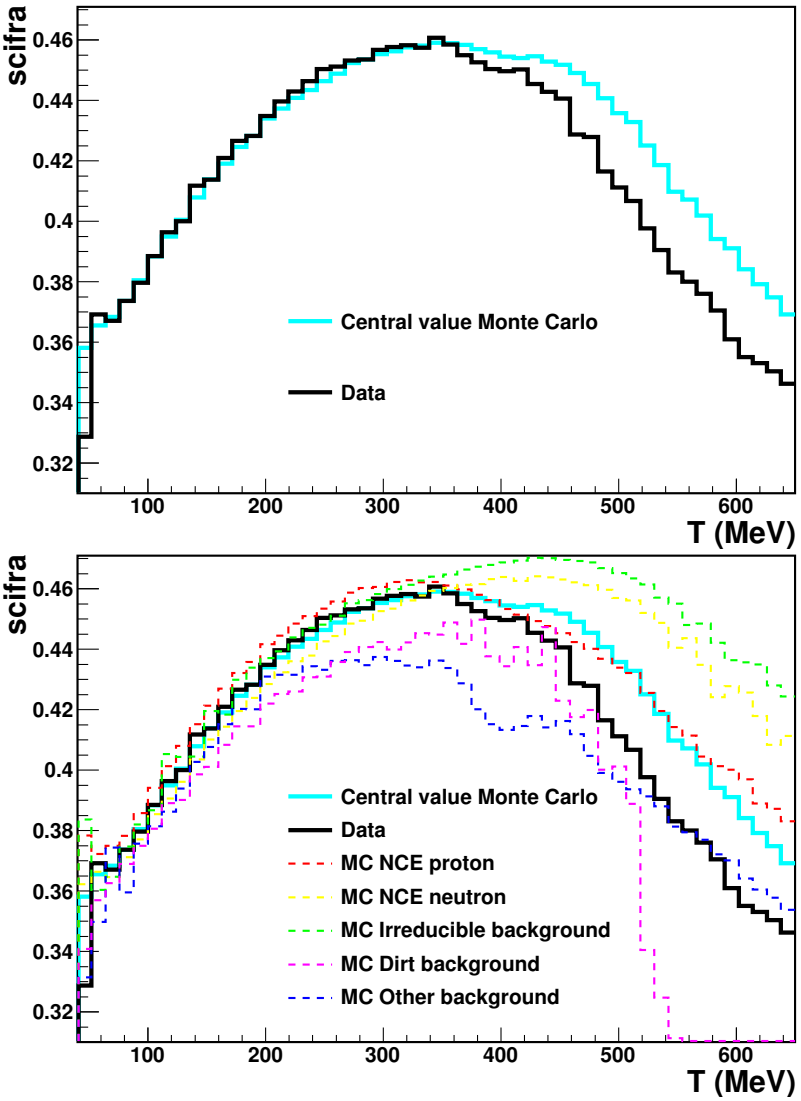


Figure C.1: *scifra* as a function of reconstructed nucleon energy for the data and the MC. Also individual scifra contributions from different channels are as labeled.

## C.2 Proton Energy Using the Charge-Current Quasi-Elastic Channel

Although it is not conclusive to use the MiniBooNE NCE channel for the proton energy scaling, one should mention the possibility to use the MiniBooNE CCQE channel in neutrino mode for this purpose. In CCQE , $\nu_\mu + n \rightarrow \mu^- + p$, a muon and a proton is produced. Muons usually produce enough light (mostly Cherenkov) to reliably reconstruct its kinematics – the vertex, direction and energy. For CCQE events with high $Q^2$ values (above 0.7 GeV$^2$) it should be possible also to

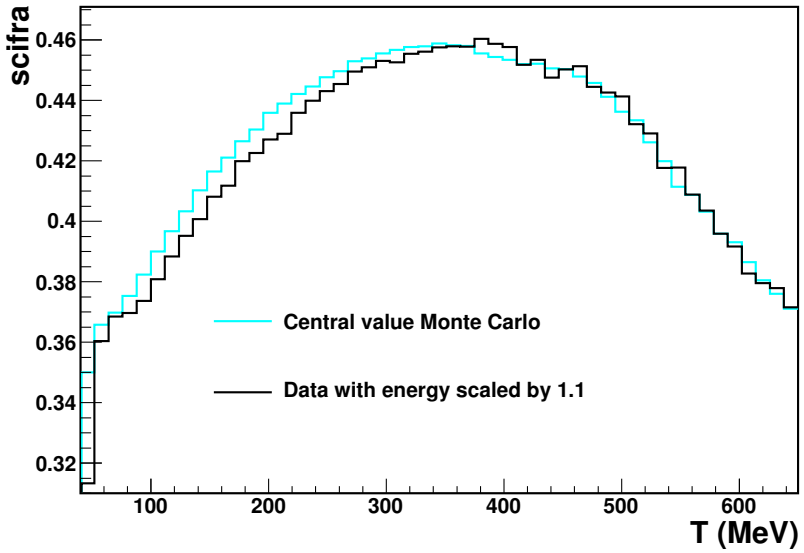


Figure C.2: *scifra* as a function of reconstructed nucleon energy for the MC and the data after applying 11% energy rescaling.

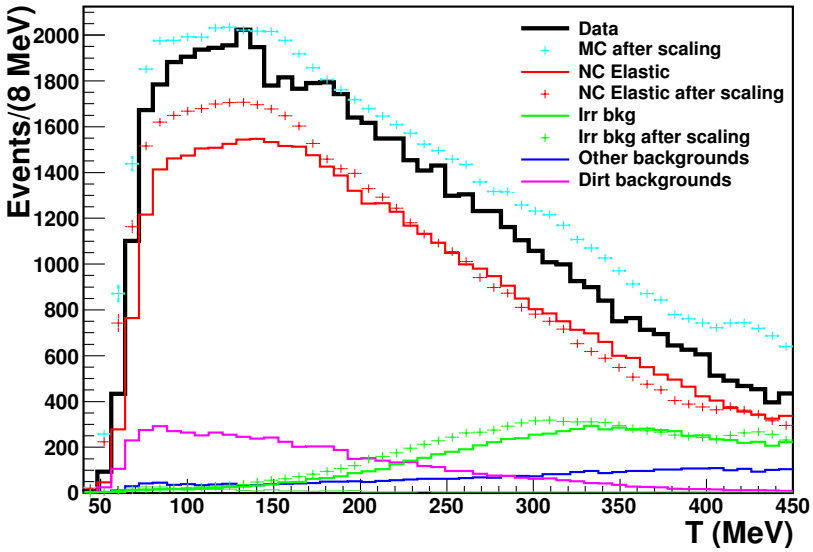


Figure C.3: Reconstructed energy after applying 11% energy rescaling to NCE and irreducible events. Individual channel contributions including before and after the energy rescaling are as labeled.

reconstruct the proton direction and energy. In principle, for a stationary target neutron, muon kinematics define the outgoing proton kinematics. Of course, nuclear effects smear the predicted proton kinematics. By measuring both proton and muon in the same CCQE event, one may compare the predicted proton kinematics (from the reconstructed muon kinematics) to the measured proton kinematics. This way one can conclusively measure the proton energy scaling. My plan is to work on this measurement after graduation together with Joe Grange, Ph.D. student at the University of

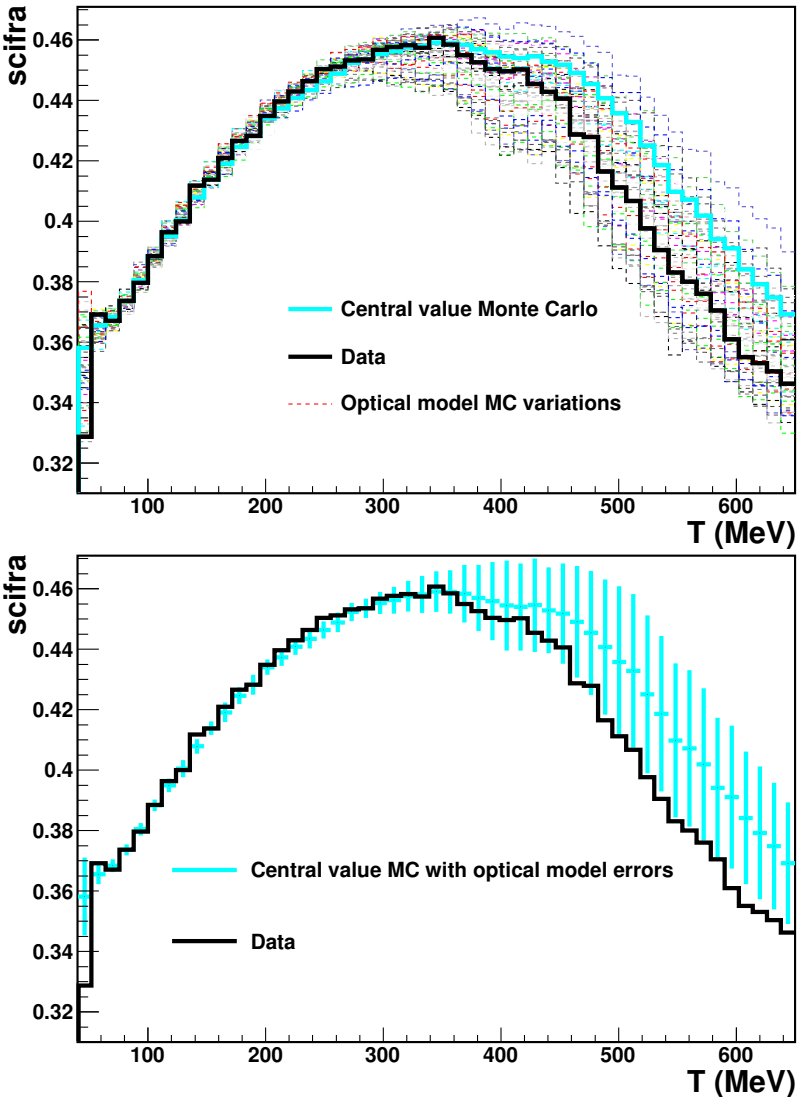


Figure C.4: *scifra* as a function of reconstructed nucleon energy. The data (black), the total MC (cyan), optical model multisims (colored). The bottom plot shows the error bars from the optical models taken about the MC central value.

Florida and Heather Ray, professor at the University of Florida (Joe's supervisor).

# References


[1] A. H. Becquerel, Compt. Rend. Math. **122**:420–421 (1896).

[2] P. Curie and M. Curie, Comptes rendus **127**:175–8 (1898).

[3] E. Rutherford, Philosophical Magazine **ser. 5, xlvii**:109–163 (1899).

[4] P. Villard, Comptes rendus **129**:244 (1899).

[5] P. Villard, Comptes rendus **130**:1010–1012, `http://gallica.bnf.fr/ark:/12148/bpt6k3086n.image.f1010` (1900).

[6] P. Villard, Comptes rendus **130**:1178–1179 (1900).

[7] P. Villard, Seances de la Societe francaise de physique, p.45–46 (1900) .

[8] H. Becquerel, Comptes rendus **130**:809–815, `http://gallica.bnf.fr/ark:/12148/bpt6k3086n.image.f809` (1900).

[9] C. Ellis, Proc. Roy. Soc. **A99**:261 (1921).

[10] Ellis and Skinner, Proc. Roy. Soc. **A105**:185 (1924).

[11] L. Meitner, Ergebnisse der Exakten Naturwissenschaften **3**:160 (1924).

[12] K. Emeleus, Proc. Camb. Phil. Soc. **22**:400 (1924).

[13] R. Gurney, Proc. Roy. Soc. **A109**:540 (1925).

[14] Ellis and Wooster, Proc. Roy. Soc. **A117**:313 (1927).

[15] W. Pauli, Phys. Today **31N9**:27 (1978).

[16] J. Chadwick, Nature **129**:312 (1932).

[17] F. Perrin, Comptes Rendus **197**:1625 (1933).

[18] E. Fermi, Z. Phys. **88**:161–177 (1934).

[19] H. Bethe and R. Peierls, Nature **133**:532–533 (1934).

[20] C. L. Cowan, F. Reines, F. B. Harrison, E. C. Anderson, and F. N. Hayes, Phys. Rev. **90**:493–494 (1953).

[21] F. Reines and C. L. Cowan, Phys. Rev. **92**:830–831 (1953).

[22] C. L. Cowan, F. Reines, F. B. Harrison, H. W. Kruse, and A. D. McGuire, Science **124**:103–104 (1956).

[23] F. Reines and C. L. Cowan, Phys. Rev. **113**:273–279 (1959).

[24] G. Danby *et al.*, Phys. Rev. Lett. **9**:36–44 (1962).

[25] J. Davis, Raymond, D. S. Harmer, and K. C. Hoffman, Phys. Rev. Lett. **20**:1205–1209 (1968).

[26] J. N. Bahcall, Phys. Rev. Lett. **12**:300–302 (1964).

[27] [KAMIOKANDE-II collaboration], K. S. Hirata *et al.*, Phys. Lett. **B205**:416 (1988).

[28] [IMB collaboration], W. Gajewski In *Munich 1988, Proceedings, High energy physics* 1305-1306. (see Conference Index).

[29] [Working Group on LEP Energy collaboration], L. Arnaudon *et al.*, Phys. Lett. **B307**:187–193 (1993).

[30] [OPAL collaboration], R. Akers *et al.*, Z. Phys. **C65**:47–65 (1995).

[31] [DELPHI collaboration], P. Abreu *et al.*, Z. Phys. **C74**:577–586 (1997).

[32] [L3 collaboration], M. Acciarri *et al.*, Phys. Lett. **B431**:199–208 (1998).

[33] [Super-Kamiokande collaboration], Y. Fukuda *et al.*, Phys. Lett. **B433**:9–18 (1998). [arXiv:hep-ex/9803006]

[34] [Super-Kamiokande collaboration], Y. Fukuda *et al.*, Phys. Lett. **B436**:33–41 (1998). [arXiv:hep-ex/9805006]

[35] [DONUT collaboration], K. Kodama *et al.*, Phys. Lett. **B504**:218–224 (2001). [arXiv:hep-ex/0012035]

[36] [SNO collaboration], Q. R. Ahmad *et al.*, Phys. Rev. Lett. **89**:011301 (2002). [arXiv:nucl-ex/0204008]

[37] [KamLAND collaboration], K. Eguchi *et al.*, Phys. Rev. Lett. **90**:021802 (2003). [arXiv:hep-ex/0212021]

[38] [K2K collaboration], M. H. Ahn *et al.*, Phys. Rev. Lett. **90**:041801 (2003).

[39] [Particle Data Group collaboration], C. Amsler *et al.*, Phys. Lett. **B667**:1 (2008).

[40] C. Kraus *et al.*, Eur. Phys. J. **C40**:447–468 (2005). [arXiv:hep-ex/0412056]

[41] K. Scholberg (2003). [arXiv:hep-ex/0308011]

[42] V. M. Lobashev *et al.*, Nucl. Phys. Proc. Suppl. **91**:280–286 (2001).

[43] B. Pontecorvo, Zh. Eksp. Teor. Fiz. **33**:549 (1957).

[44] E. Pachos, *Electroweak Theory*, cambridge University Press (2007).

[45] F. M. F. Soler, C. Froggatt, *Neutrinos in Particle Physics, Astrophysics and Cosmology*, cRC Press (2008).

[46] S. L. Glashow, Nucl. Phys. **22**:579–588 (1961).

[47] S. Weinberg, Phys. Rev. Lett. **19**:1264–1266 (1967).

[48] A. Salam Originally printed in *Svartholm: Elementary Particle Theory, Proceedings Of The Nobel Symposium Held 1968 At Lerum, Sweden*, Stockholm 1968, 367-377.

[49] P. W. Higgs, Phys. Lett. **12**:132–133 (1964).

[50] P. W. Higgs, Phys. Rev. **145**:1156–1163 (1966).

[51] C. Quigg, *Gauge Theories of the Strong, Weak and Electromagnetic Interactions*, benjamin-Cummings Publishing Company, Inc. (1983).

[52] M. Kobayashi and T. Maskawa, Prog. Theor. Phys. **49**:652–657 (1973).

[53] T. D. Lee, M. Rosenbluth, and C.-N. Yang, Phys. Rev. **75**:905 (1949).

[54] M. M. Block *et al.*, Phys. Lett. **12**:281–285 (1964).

[55] F. J. Hasert *et al.*, Phys. Lett. **B46**:121–124 (1973).

[56] [Gargamelle Neutrino collaboration], F. J. Hasert *et al.*, Phys. Lett. **B46**:138–140 (1973).

[57] A. C. Benvenuti and e. al., Phys. Rev. Lett. **32**:800–803 (1974).

[58] W.-Y. Lee *et al.*, Phys. Rev. Lett. **37**:186–189 (1976).

[59] D. Cline *et al.*, Phys. Rev. Lett. **37**:252–255 (1976).

[60] D. Cline *et al.*, Phys. Rev. Lett. **37**:648 (1976).

[61] A. Entenberg *et al.*, Phys. Rev. Lett. **42**:1198 (1979).

[62] L. A. Ahrens *et al.*, Phys. Rev. **D 35**:785 (1987).

[63] [European Muon collaboration], J. Ashman *et al.*, Nucl. Phys. **B328**:1 (1989).

[64] G. Garvey, E. Kolbe, K. Langanke, and S. Krewald, Phys. Rev. **C48**:1919–1925 (1993).

[65] E. D. Commins and P. H. Bucksbaum, *Weak interactions of leptons and quarks*, cambridge university press (1983).

[66] F. J. Ernst, R. G. Sachs, and K. C. Wali, Phys. Rev. **119(3)**:1105–1114 (1960).

[67] T. Katori, *A Measurement of the Muon Neutrino Carged Current Quasielastic Interaction and a Test of LorentZ Violation with the MiniBooNE Experiment*, Ph.D. thesis, Indiana University (2008).

[68] V. Bernard *et al.*, J. Phys. **G 28**:R1 (2002).

[69] [MiniBooNE collaboration], A. A. Aguilar-Arevalo *et al.*, Phys. Rev. Lett. **100**:032301 (2008). [arXiv:0706.0926]

[70] [K2K collaboration], R. Gran *et al.*, Phys. Rev. **D 74**:052002 (2006).

[71] [K2K collaboration], X. Espinal and F. Sanchez, AIP Conf. Proc. **967**:117 (2007).

[72] M. E. Dorman FERMILAB-THESIS-2008-72.

[73] G. Garvey, W. C. Louis, and D. H. White, Phys. Rev. **C 48**:761 (1993).

[74] [HAPPEX collaboration], A. Acha *et al.*, Phys. Rev. Lett. **98**:032301 (2007). [arXiv:nucl-ex/0609002]

[75] G. M. Shore (1998). [arXiv:hep-ph/9812355]

[76] J. R. Ellis and R. L. Jaffe, Phys. Rev. **D9**:1444 (1974).

[77] A. W. Thomas (2009). [arXiv:0904.1735]

[78] [HERMES collaboration], A. Airapetian *et al.*, Phys. Rev. **D75**:012007 (2007). [arXiv:hep-ex/0609039]

[79] [COMPASS collaboration], V. Y. Alexakhin *et al.*, Phys. Lett. **B647**:8–17 (2007). [arXiv:hep-ex/0609038]

[80] J. Monroe and P. Fisher, Phys. Rev. **D76**:033007 (2007). [arXiv:0706.3019]

[81] [FINeSSE collaboration], L. Bugel *et al.* (2004). [arXiv:hep-ex/0402007]

[82] [LSND collaboration], A. Aguilar *et al.*, Phys. Rev. **D64**:112007 (2001). [arXiv:hep-ex/0104049]

[83] [The MiniBooNE collaboration], A. A. Aguilar-Arevalo *et al.*, Phys. Rev. Lett. **98**:231801 (2007). [arXiv:0704.1500]

[84] [MiniBooNE collaboration], A. A. Aguilar-Arevalo *et al.*, Phys. Rev. Lett. **103**:111801 (2009). [arXiv:0904.1958]

[85] [MiniBooNE collaboration], A. A. Aguilar-Arevalo *et al.*, Phys. Rev. **D79**:072002 (2009). [arXiv:0806.1449]

[86] M. Sorel, *Search for Sterile Neutrinos Using the MiniBooNE Beam*, Ph.D. thesis, Columbia University (2005).

[87] [GEANT4 collaboration], S. Agostinelli *et al.*, Nucl. Instrum. Meth. **A506**:250–303 (2003).

[88] [HARP collaboration], M. Catanesi *et al.*, Eur. Phys. J. C **52**:29 (2007).

[89] I. Chemakin *et al.*, Nucl. Phys. A **639**:407 (1998).

[90] [E-802 collaboration], T. Abbott *et al.*, Phys. Rev. **D45**:3906–3920 (1992).

[91] D. Dekkers *et al.*, Phys. Rev. **137**:B962–B978 (1965).

[92] T. Eichten *et al.*, Nucl. Phys. **B44**:333–343 (1972).

[93] G. J. Marmer *et al.*, Phys. Rev. **179**:1294–1300 (1969).

[94] R. A. Lundy, T. B. Novey, D. D. Yovanovitch, and V. L. Telegdi, Phys. Rev. Lett. **14**:504–507 (1965).

[95] *MiniBooNE April 2007 Data Release*, `http://www-boone.fnal.gov/for_physicists/data_release/`.

[96] [MiniBooNE collaboration], A. A. Aguilar-Arevalo *et al.*, Nucl. Instrum. Meth. **A599**:28–46 (2009). [arXiv:0806.4201]

[97] S. J. Brice *et al.*, Nucl. Instrum. Meth. **A562**:97–109 (2006).

[98] H. Meyer, *Index of Refraction of Marcol 7*, miniBooNE Technical Note N190.

[99] [the MiniBooNE collaboration], B. C. Brown *et al.*, IEEE Nucl. Sci. Symp. Conf. Rec. **1**:652–656 (2006).

[100] R. Patterson, *A Search for Muon Neutrino to Electron Neutrino Oscillations at* $\Delta m^2 > 1\ eV^2$, Ph.D. thesis, Princeton University (2007).

[101] [MiniBooNE collaboration], Z. Djurcic (2009). [arXiv:0901.1648]

[102] I. Stancu and Y. Liu, *The MiniBooNE Charge Likelihoods and Light Scattering in Michel Electron Events*, miniBooNE Technical Note N126.

[103] I. Stancu, *The Single-PE Time Resolution with Ryan Patterson's QT-Algorithms*, miniBooNE Technical Note N81.

[104] L. Michel, Poudres Annexe **35**:77 (1953).

[105] D. E. Groom, N. V. Mokhov, and S. I. Striganov, Atom. Data Nucl. Data Tabl. **78**:183–356 (2001).

[106] P. Lipari, Nucl. Phys. B (Proc. Suppl.) **112**:274 (2002).

[107] D. Casper, Nucl. Phys. B (Proc. Suppl.) **112**:161, `http://nuint.ps.uci.edu/nuance/` (2002).

[108] C. H. Llewellyn-Smith, Phys. Rep. **3**:261 (1972).

[109] R. A. Smith and E. J. Moniz, Nucl. Phys. B **43**:605, Erratum-ibid. **B101**:547 (1975) (1972).

[110] H. Budd, A. Bodek, and J. Arrington (2003). [arXiv:hep-ex/0308005]

[111] D. Rein and L. M. Sehgal, Nucl. Phys. B **223**:29 (1983).

[112] M. J. Wilking .

[113] R. Brun *et al.* CERN-DD/EE/84-1 (1987).

[114] C. Zeitnitz and T. A. Gabriel, Nucl. Inst. & Meth. **349**:106 (1994).

[115] A. Bazarko *et al.*, *Studies of Scattering in Marcol 7 Mineral Oil*, miniBooNE Technical Note N144.

[116] D. Toptygin, *Time-Resolved Fluorecence of MiniBooNE Mineral Oil*, miniBooNE Technical Note N122.

[117] M. Abramowitz and I. A.Stegun, *Handbook of Mathematical Functions with Formulas, Graphs, and Mathematical Tables.*, new York: Dover (1972).

[118] MINUIT, CERN Program Library entry **D506**. Available at `http://wwwasdoc.web.cern.ch/wwwasdoc/minuit/minmain.html`.

[119] T. Suzuki, D. F. Measday, and J. P. Roalsvig, Phys. Rev. **C35**:2212 (1987).

[120] J. E. Rothberg *et al.*, Phys. Rev. **132**:2664–2678 (1963).

[121] G. Cowan, *Statistical Data Analysis*, oxford science publications (1998).

[122] G. D'Agostini, Nucl. Instrum. Meth. **A362**:487–498 (1995).

[123] D. C. Cox, *A measurement of the neutral current neutrino-nucleon elastic cross section at MiniBooNE*, Ph.D. thesis, fERMILAB-THESIS-2008-08.

[124] L. Lyons, *Statistics for nuclear and particle physicist*, cambridge university press (1992).

[125] G. P. Zeller, (private communication).

[126] [MiniBooNE collaboration], T. Katori (2009). [arXiv:0909.1996]